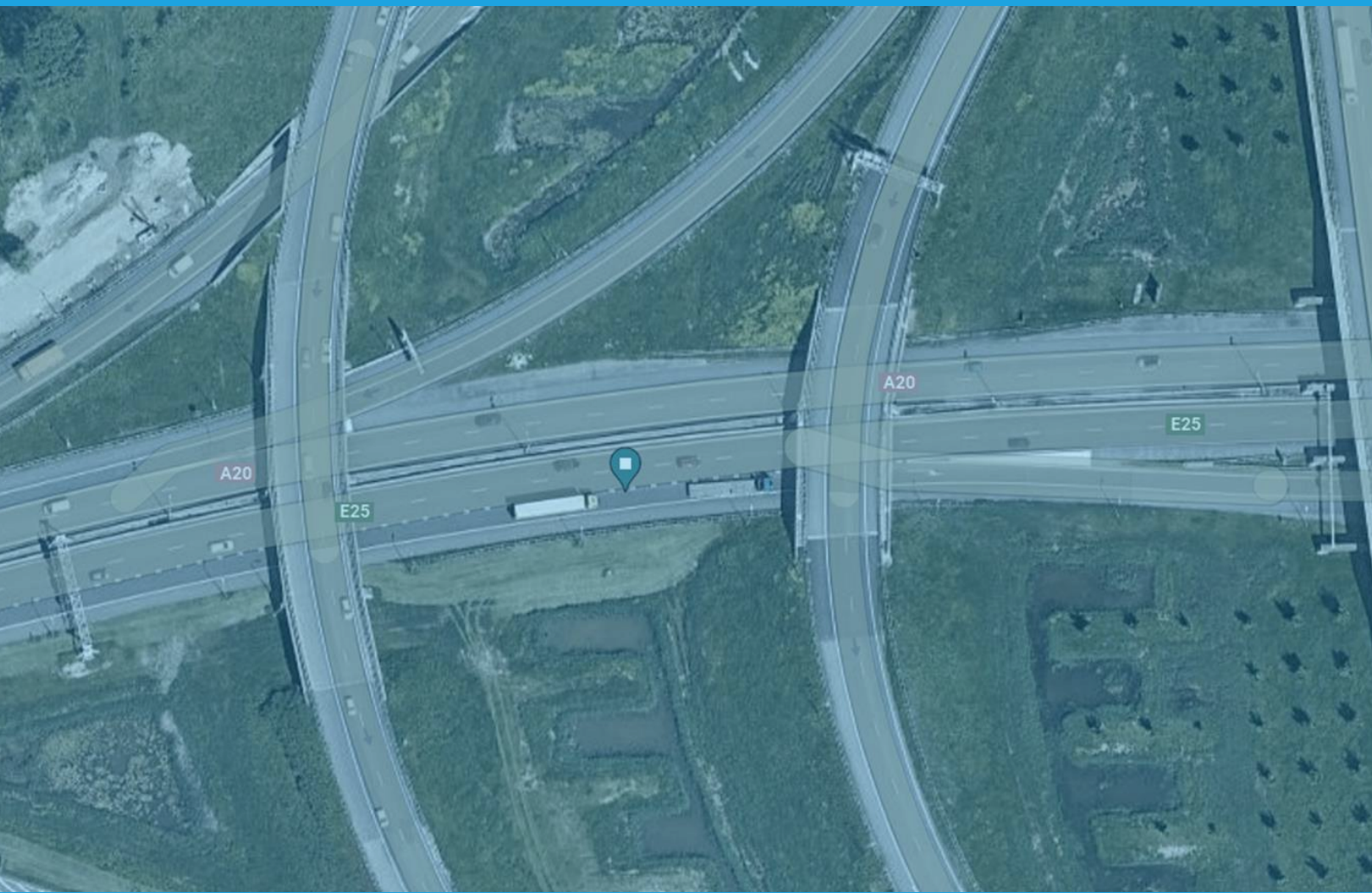# Optimizing the assessment of fatigue in inverted T-girder bridges

A parametric study of the factors influencing the fatigue analysis of concrete under compression

Athanasia Noukari

TUDelft

Witteveen + Bos

Optimizing the assessment of fatigue in inverted T-girder bridges

A parametric study of the factors influencing the fatigue analysis of concrete under compression

by

Athanasia Noukari

to obtain the degree of Master of Science in Structural Engineering at the Delft University of Technology, to be defended publicly on 29 December 2023.

Student number: 5576431
Project duration: December 1, 2022 - November 29, 2023

Supervisors:
Dr. ir. Y. (Yuguang) Yang (TU Delft)
Prof.dr.ir. M.A.N. (Max) Hendriks (TU Delft)
Ir. C. (Cor) Kasbergen (TU Delft)
Ir. P. (Pieter) Schoutens (Witteveen+Bos)

An electronic version of this thesis is available at `http://repository.tudelft.nl/`.

A thesis submitted in fulfilment of requirements

for the degree of Master of Science

in

Civil Engineering

Structural Engineering

Faculty of Civil Engineering and Geosciences

Technishe University of Delft

Stevinweg 1

2628 CN Delft

The Netherlands

Acknowledgement

This journey has come to its end, and it was full of challenges, new experiences and unforgettable moments. I will never forget these last years as a student at TU Delft University. Writing this final part of my thesis, I am overwhelmed by many emotions - happiness, tiredness, a sense of accomplishment, and above all, gratitude for all the people who supported me through this endeavour.

I would like to express my sincere appreciation to Pieter Schoutens, my supervisor at Witteveen+Bos, for his unyielding support throughout my graduation process. He was always there to help me, answer my numerous questions, and, most importantly, motivate me to overcome any obstacles I faced during my project. My experience at Witteveen+Bos has helped me grow both personally and professionally, and it has given me the confidence to tackle any future challenges. I am also thankful to the Infra constructies group at Witteveen+Bos for creating a welcoming environment and making me feel like a part of their team.

Furthermore, I would like to thank all my committee members, namely Yuguang Yang, Max Hendriks, and Cor Kasbergen, for their excellent communication during the thesis period and for providing valuable feedback and guidance when needed. Your contribution was invaluable and encouraged me to improve and make the most of my work.

However, my deepest gratitude goes to my family, including my mother, Anna; my grandfather and grandmother, Athanasios and Sofia; my sisters, Sofia and Despoina; my aunt and uncle, Anastasia and Eleftherios and lastly, Elena, Michalis and Thanos. Each one of them played a crucial role in this journey. Without their unwavering support, trust, and unconditional love, I wouldn't have been able to fulfil this dream. They always believed in me, motivated me to become the best version of myself, and encouraged me to pursue my aspirations. This thesis is dedicated to my grandparents, Athanasios and Sofia. I am grateful to have such wonderful people in my life who have taught me valuable lessons and instilled in me the values that make me the person I am today.

Finally, I want to thank my boyfriend, Vassilis, for supporting and tolerating me throughout this process, but mostly for listening to me, even though he had no clue what I was talking about most of the time. And, of course, I would like to thank my old and new friends. This experience would not have been the same without them.

Abstract

With the continuous increase in transportation volume, bridges face the challenge of carrying higher traffic loads. As a result, bridges undergo fatigue due to repeated and increasing loads, leading to progressive deterioration of their structural reliability. While existing codes already account for several variables affecting the concrete's ability to withstand compression fatigue, some critical factors are still not considered. Furthermore, the modelling aspects of Finite Element Analysis (FEA) are often simplified or disregarded in practical applications, leading to an inaccurate estimation of fatigue life for concrete. As a result, a considerable number of bridges may be rejected for fatigue despite the possibility that they are not susceptible to this issue.

To address these issues, this thesis presents a parametric study that explores and quantifies the influence of various parameters on the fatigue life of inverted T-girder bridges, focusing on modelling aspects and material degradation. For this reason, a special case study was specifically designed to fail in fatigue within its lifespan. The fatigue analysis process employed both analytical and numerical methods, with the fatigue failure of the beams determined based on the bending failure at the beam's midspan criterion. A basic case was established as a basis for analysis, and the effect of each parameter was evaluated by incorporating it into the basic case and calculating the fatigue life of the bridge.

The analysis results demonstrate that stress distribution affecting parameters are significantly important in determining the fatigue performance of a bridge. The analysis identified that accounting for the gradual development of prestress losses, rather than instantaneous losses, and utilising area loads for vehicle modelling are critical aspects that substantially prolong the bridge's fatigue life. Furthermore, performing a historical lane configuration analysis is crucial for accurately assessing fatigue, as it significantly impacts the fatigue life of the bridge and identifies its critical components. The inclusion of material degradation caused by cyclic loading in the fatigue analysis is highly advantageous. It can even result in the bridge no longer being susceptible to fatigue. It is worth noting that accounting for the cracking of the slab in the lateral has a major negative effect on the fatigue life of the bridge. However, it is necessary to include it in the analysis to avoid an inaccurate and overly optimistic fatigue assessment. The study also provides specific equations to calculate the effect of time-dependent traffic volume on fatigue life. Lastly, the research investigated other parameters, such as the composite action of the structural components, which had a minor effect on the fatigue life of the bridge.

It is important to note that the influence percentage of most parameters cannot be generalised to all bridges, as they are contingent on specific factors unique to each case. Nevertheless, this research provides insights into the magnitude and contribution of the

investigated parameters on the fatigue life of concrete bridges, outlining those that must be necessarily included in the fatigue assessment.

Contents

List of Figures

List of Tables

'This thesis is dedicated to my grandparents

Athanasios Delimanolis and Sofia Delimanoli'

1   Introduction

1.1   Problem statement

Transportation has always been an integral part of the development of modern societies. Infrastructure works, especially bridges, are used to traverse geographical constraints. Bridges are complex structures that signify technological advancement. Their complexity lies in their structural system and loading conditions. Being subjected to increasing and repeated loads, bridges experience a progressive deterioration of their structural reliability, namely fatigue. According to the definition, fatigue is the process of progressive, permanent internal structural changes occurring in a material subjected to repetitive stresses (Rilem Committee 1984). In other words, fatigue refers to the number of loading cycles that the material or a structural element can sustain before failure (Lee and Barr 2004).

The booming transportation volume resulted in a constant growth of traffic load that needs to be carried from the existing transport network. As part of the highways, bridges are required to sustain higher axle and average vehicle loads in combination with increasing traffic intensity over their lifetime. Considering the fact that their design has been based on former codes that are no longer valid and on traffic models that are not representative of the current demands, the assessment of the fatigue life of concrete bridges is necessary to be conducted. In order to properly study a structural element in fatigue, the contribution of each material is individually assessed over the cross section (Blasón et al. 2019; Tilly 1979). Numerous experimental, numerical and analytical studies have been conducted to provide codes and models that determine the residual life of steel and concrete subjected to cyclic loading. However, the scope of this thesis is limited to the fatigue assessment of the concrete compressive zone of the prefabricated prestressed beams of girder bridges.

Girder bridges are one of the most popular types of prestressed bridges. Disregarding box girder bridges, the composition of their deck includes a number of I-shaped or inverted T-beams, which are placed in parallel, maintaining a constant distance. The beams are connected in the transverse direction through diaphragm beams at the position of supports and occasionally in

the midspan when this is required based on the length. The erection of the beams and the construction of the diaphragms is followed by the in-situ casting of the deck slab on top of the beams (Fernández-Ordóñez Hernández 2005). Understanding the individual construction stages of this bridge type is highly important since they are responsible for the stress distribution along the beam.

According to the Eurocode, National Annex's regulations, and RBK (Richtlijnen Beoordeling Kunstwerken) regulations by the Dutch Ministry of Public Works, the concrete compressive zone of the beams needs to be checked for fatigue. This is also confirmed in Appendix A, based on which high-stress values are noted on the top fibre of the prestressed beams. Since fatigue is affected by the level and range of stress, prestressed bridges are prone to fatigue.

The analysis of practical case studies has shown that even though fatigue is an important factor contributing to the deterioration of structures, collapses of concrete structures solely due to fatigue have not been reported (Chapter 2). Without a doubt, current codes and suggested modified methods (Chapter 3) provide a close estimation of the investigated structure's fatigue life. However, simplifications that are often adopted in the analysis process or excluding the effect of time-dependent parameters from the analysis can result in an inaccurate stress distribution and, consequently, estimation of the remaining fatigue life.

The rejection of the structural reliability of large-scale concrete structures would lead to high investment costs, extensive use of material, high levels of carbon emissions and disruption of traffic. Consequently, the need arises for a more accurate and sustainable fatigue assessment, which will comply with the current code regulation without being overly conservative.

The problem that is addressed in this study is stated as follows:

Problem statement

During the fatigue assessment of prestressed concrete bridges, a considerable number of bridges are being rejected for fatigue despite the possibility that they may not be susceptible to this issue.

1.2 Research objectives

To address the previously described problem, this research's first objective concerns identifying the parameters that influence the fatigue life of the bridge. Having specified these parameters, the study examines the extent to which these parameters are incorporated in the fatigue assessment of concrete bridges based on existing codes and methods. The research also determines the various analysis aspects that are often simplified or disregarded in the fatigue assessment of these structures. Once the influencing parameters have been determined, the research aims to quantify the impact of the analysed parameters on the fatigue analysis and fatigue life of the bridge.

The overall objective of this thesis is to gain insight into the influence of material properties, time-dependent parameters, loading conditions and analysis aspects on fatigue verification checks. This way, the study aims for a more accurate and sustainable evaluation of the fatigue assessment of existing bridges, providing a more detailed estimation of their expected lifetime.

1.3 Research questions

The primary research question that is addressed in this thesis is

---

Research question

In which way do variable analysis aspects and time-dependent parameters influence the fatigue life of an inverted T-girder bridge, and can this be used for a more sustainable fatigue assessment?

In order to answer the main research question, the following questions are also required to be considered.

Sub-questions:

- How do the considerations taken into account for the calculation of prestress losses impact the fatigue life of the bridge?

- How does the consideration of the traffic increase volume influence the fatigue life of the

bridge?

- In what manner are the results of the fatigue analysis affected by the inclusion of orthotropic slab properties?

- How might the use of different load types in the modelling of fatigue moving loads influence the fatigue life of the bridge?

- What effect will different loading configurations have on the fatigue performance of the bridge?

- To what extent will the consideration of the composite action of structural components affect the fatigue life of the structure?

- How does cyclic loading influence the material properties of concrete and, consequently, the fatigue performance of the bridge?

1.4   Scope

This survey is carried out based on the following points that describe the scope:

- The investigated bridges are highway prestressed concrete girder bridges that are part of the Dutch national infrastructure.

- The design of the bridge has been based on Eurocode and Dutch Annexes provisions and with the Dutch guidelines for designing infrastructure (ROK) and for assessing infrastructure (RBK).

- The fatigue assessment of the bridge is conducted based on the Eurocode and Dutch Annexes provision and with the Dutch guidelines for assessing infrastructure (RBK).

- The investigated bridge is assumed to intersect with the undergoing road at a 90° angle, resulting in a bridge geometry of an orthogonal parallelogram.

- The bridge is modelled as a single span and simply supported on discrete bearing pads, which are positioned maintaining a constant centre-to-centre distance.

- The bridge is subjected to permanent loads (self-weight and additional loads), traffic loads

and fatigue live loads, while thermal, wind, seismic and impact loads are not considered in the analysis.

- Linear global analysis of the whole structure is conducted using 3D elements.

- Nonlinear cross-sectional analysis is performed for the critical cross-section of the beams.

- The failure criterion for this study is the failure due to bending at the midspan of the beams.

1.5   Thesis outline

In the following steps, the thesis outline is roughly described, depicting the applied methodology for the execution of this survey.

1. Literature study

2. Design a case study that does not satisfy fatigue verification checks of concrete in compression at the time of assessment

   - Linear global analysis of the structure without including the effect of the studied parameters.

   - Determine the influence line (resulting bending moment for the positions of vehicles along the bridge deck) at the critical cross-section for every vehicle of the fatigue model.

   - Obtain the maximum and minimum values of internal forces (M_{max}, M_{min}).

   - Insert the internal forces obtained for every beam at the IDEA Statica models of the beams.

   - Nonlinear cross-sectional analysis of the beams to determine the stress distribution without including the effect of the studied parameters (σ_{max}, σ_{max}).

   - Fatigue verification of the concrete in compression or calculation of the remaining fatigue life.

3. Determine the investigated parameters and analysis aspects that influence the fatigue performance of the bridge.

4. For every time step:

   - Implement the influence of the parameters in the Finite Element Models (global and cross-sectional).

   - Linear global analysis of the structure, including the effect of the studied parameters.

   - Determine the influence line (the resulting bending moment values for the positions of vehicles along the bridge deck) at the critical cross-section for every vehicle of the fatigue model.

   - Obtain the maximum and minimum values of internal forces (M_{max}, M_{min})

   - Insert the internal forces obtained for every beam at the IDEA Statica models of the beams.

   - Nonlinear cross-sectional analysis of the beams to determine the stress distribution without including the effect of the studied parameters (σ_{max}, σ_{max})

   - Fatigue verification of the concrete in compression or calculation of the remaining fatigue life.

5. Comparison of the obtained fatigue life of the bridge with and without the influence of the studied parameter.

6. Draw conclusions and discussion of the results.

2   Literature study

2.1   Fatigue phenomena

Fatigue is a phenomenon characterised by high complexity since it is related to cyclic loads, stress level and range during the structure's lifetime, flaws and weak points initially existing in the materials and external mechanical and environmental factors. The presence and action of the following parameters have a significant influence on the behaviour of the structural elements and, by extension, on the behaviour of the structure (CEB-FIP 1988):

1. Constant deflections result in the development of secondary stresses.

2. High traffic stresses and high magnitude or frequency rolling loads applied on slabs, pavements and bridge decks.

3. Stresses caused by live loads are significantly larger than the stresses of dead loads.

4. Impact and other repeated forces presented on pavement joints and bridge bearings.

5. Vibrations, especially in the case of dynamically active elements and contaminants.

6. Inadequately confined or unconfined application points of repeated loads.

7. Chemical attack, pitting and fretting, notably in prestressed concrete.

8. Carbonation attack, particularly in the case of reinforced concrete.

Taking into account the importance of the investigated structures, namely bridges, and the magnitude of the possible consequences, understanding the fatigue mechanism of concrete is critical for the design of concrete structures, as well as for the assessment of existing structures (Gao and C.-T. T. Hsu 1998).

Fatigue cyclic loading involves repeated load cycles, while static, permanent loads are characterised by long-duration actions that do not significantly accelerate the structures. The type of applied loads determines the difference between the two. Rilem Committee 1984 distinguish two categories of fatigue loading: low-cycle and high-cycle loading. Specifically, low-cycle cyclic loading refers to high amplitude loading that includes a small number of load cycles. In contrast,

in high-cycle fatigue loading, numerous load repetitions are conducted that reach lower stress levels. Based on T. T. Hsu 1981, the spectrum of fatigue loading is broader, also including the super-high cycle loading. This way, the fatigue loading classes are finally formed, as presented in Table 2.1.

Table 2.1: Classes of fatigue loading (T. T. Hsu 1981)

Classes of fatigue load, after [2]

Low-cycle fatigue			High-cycle fatigue				Super-high-cycle fatigue		
1	10^1	10^2	10^3	10^4	10^5	10^6	10^7	10^8	10^9
Structures subjected to earthquakes			Airport pavements and bridges		Highway and railway bridges, highway pavements		Mass rapid transit structure		Sea structures

One of the most popular approaches to assess the fatigue life of a material, structural element or structure is based on the empirical Wöhler curves, also known as S-N curves. These curves are a semi-log graphical representation of the fatigue performance that depicts the relationship between the maximum stress level S_{max} that the structure is subjected to and the logarithmic number of cycles to failure N. In order to predict and represent the fatigue performance of the material under investigation, fatigue tests are conducted. The tests present a large scatter regarding their result (Rilem Committee 1984). Therefore, many specimens are required to be tested to create the S-N curve of a particular type of concrete.

According to the definition, fatigue strength is a fraction of static strength that the structure can withstand for multiple load cycles. In concrete, determining the static strength is influenced by the shape of the tested specimens and the rate of the applied loading, which is significantly lower than the rate of loading applied in the fatigue tests. As a result, the maximum stress values obtained are nominal values related to conventional strength properties that may deviate from the reality of the structure subjected to loading (Rilem Committee 1984).

The S-N curves are usually plotted based on two procedures specifically, for a constant minimum stress level (S_{min}) or for constant minimum and maximum stress level ratio ($R=S_{min}/S_{max}$). Maximum and minimum stress levels have a noteworthy influence on the fatigue life of concrete, which is clearly in the Goodman diagram (Figure 2.1a), for constant minimum stress level (S_{min}), and in the Smith diagram (Figure 2.1b), for constant mean stress level ($S_m=1/2$ ($S_{min}+ S_{max}$)).
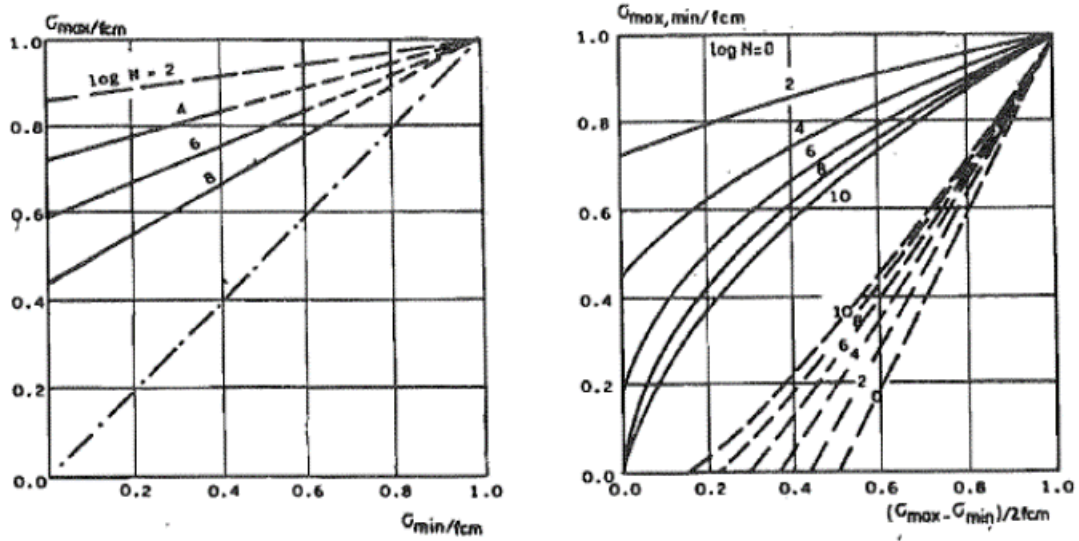
Figure 2.1: (a). Goodman diagram, (b). Smith diagram (Tepfers and Kutti 1979)

Including the minimum and maximum stress level ratio in the S-N relationship, both Wöhler curves and Smith-diagram can be described by a standard equation (Tepfers and Kutti 1979, Aas-Jakobsen 1970), namely

$$S_{max} = 1 - \beta(1 - R)\log_{10} N \tag{1}$$

where,

$R \qquad\qquad = \frac{S_{min}}{S_{max}}$, the stress level ratio
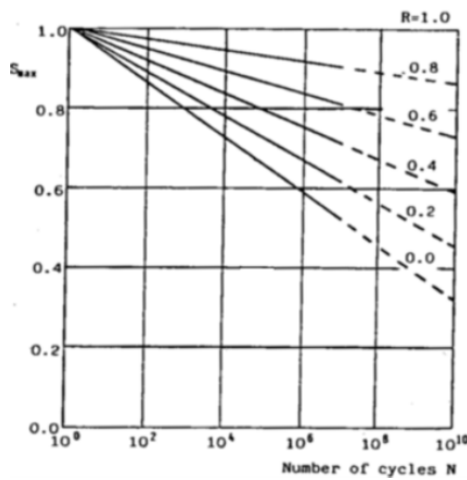
Figure 2.2: S-N curves for constant R-values (Tepfers and Kutti 1979)

2.2   Fatigue damage hypotheses

The previous section (2.1) provides an overview of fatigue life models used to investigate the fatigue phenomenon. While most of the research on the concrete's fatigue characteristics has focused on the effect of constant amplitude loading, the stress cycles in actual structures often present significant variations in magnitude and frequency. Consequently, when addressing more complex loading histories, fatigue damage hypotheses are employed to better understand the behaviour of the material (Rilem Committee 1984).

The structural impact of loading histories is frequently analysed through linear damage theories, with the Palmgren-Miner (P-M) hypothesis being the most commonly used. This hypothesis was initially proposed by Palmgren 1924 regarding ball bearings and then utilised by Miner 1945 for tests conducted on notched aluminium specimens. Based on this theory, the structure reaches its failure when:

$$\sum_{i=1}^{k} \left(\frac{N_i}{N_{Fi}} \right) = 1 \tag{2}$$

where,

N_i the number of cycles at the stress level i

N_{Fi} the number of cycles to failure at the stress level i

Multiple-stage-block loading experimental studies have reported both conservative and unsafe predictions of the P-M hypothesis (Holmen 1979, Weigler and Klausen 1979, Awad 1971, Tepfers and Kutti 1979).

Research conducted by Singh 2003 has listed a few significant limitations of the P-M hypothesis:

1. The sequence effect is not taken into consideration.

2. At low load levels, the magnitude of damage is underestimated since low load levels are considered non-damaging.

3. The amount of damage is considered constant in every load cycle, where this belongs to the initial or the final stages of the fatigue loading.

In order to address these limitations and better approach the fatigue performance of the material, alternative theories have been proposed. Marco and Starkey 1954 modification of the P-M hypothesis shows that the accumulated damage due to constant amplitude loading is non-linear. The damage (D_i) is expressed using the following equation,

$$D_i = \left(\frac{n_i}{N_i}\right)^{x_i} \tag{3}$$

where, as illustrated in Figure 2.3, the value x_i is determined by the stress level S_i.
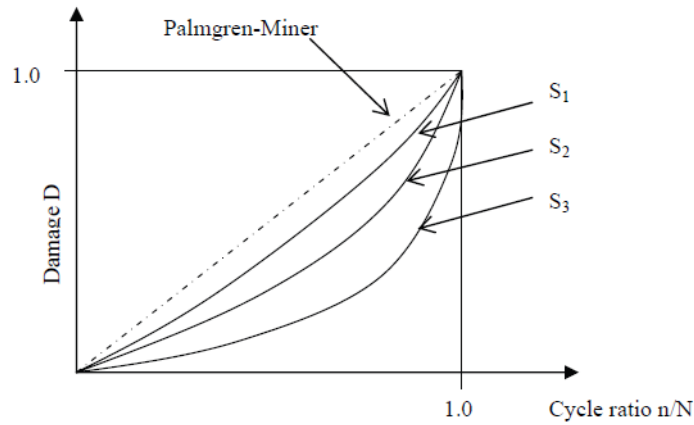
Figure 2.3: Damage/cycle ratio relationship dependent on stress level (Marco and Starkey 1954)

Developing the theory for two stages of cycling loading having constant amplitudes, as presented in Figures 2.4 and 2.5, has shown that the accumulative damage differs based on the loading sequence. Specifically, the application of a higher stress level in the first stage followed by lower stress cycles (Figure 2.4) results in accumulated damage less than unity:

$$\sum_{i=1}^{k} \frac{N_i}{N_{Fi}} = \frac{n_1}{N_1} + \frac{n_2}{N_2} < 1 \tag{4}$$

In contrast, when the lower stress precedes the high-stress stage (Figure 2.5),

$$\sum_{i=1}^{k} \frac{N_i}{N_{Fi}} = \frac{n_1}{N_1} + \frac{n_2}{N_2} > 1 \tag{5}$$
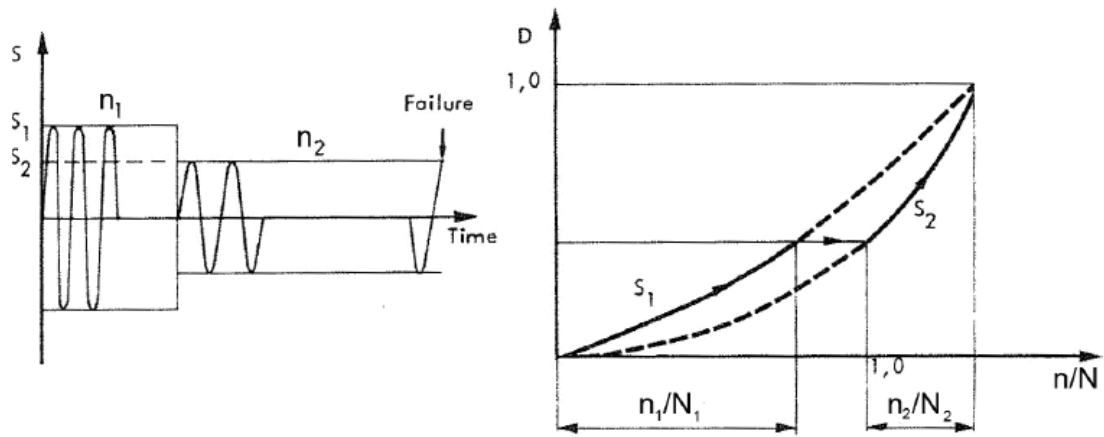
Figure 2.4: Case of high-low sequence in two-stage constant amplitude tests with corresponding stress-dependent damage accumulation (Marco and Starkey 1954).
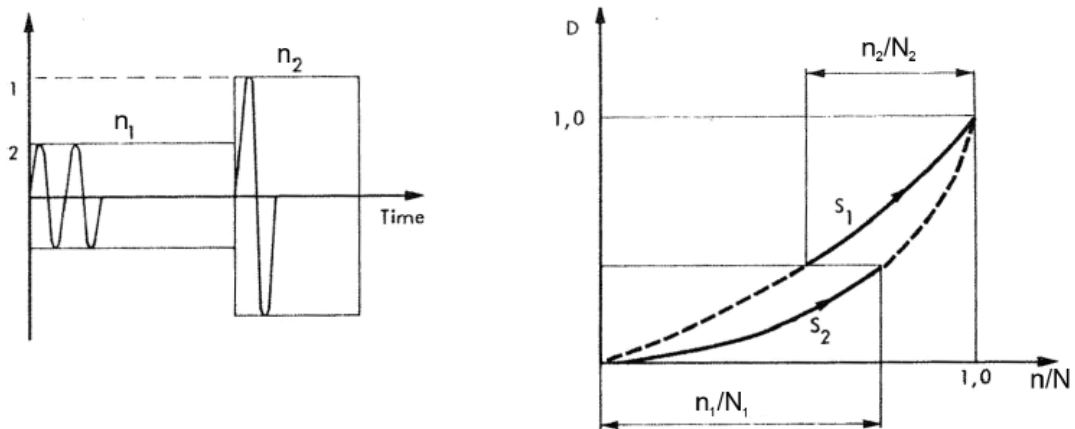
Figure 2.5: Case of low-high sequence in two-stage constant amplitude tests with corresponding stress-dependent damage accumulation (Marco and Starkey 1954).

A different modification suggested the introduction of the ω factor in the failure criterion, which is therefore given as (Rilem Committee 1984),

$$\frac{1}{\omega}\sum_{i=1}^{k}(\frac{N_i}{N_{Fi}}) = 1.0 \tag{6}$$

12

or

$$\sum_{i=1}^{k} (\frac{N_i}{N_{Fi}}) = \omega \tag{7}$$

where the loading parameters determine ω.

Finally, Oh 1991 proposed a theory that outlines the sequence and magnitude of cyclic loading. The theory is described by the following equation,

$$\left(\frac{n_1}{N_1}\right) + \left(\frac{n_2}{N_1}\right)\left(\frac{S_2}{S_1}\right) + ... + \left(\frac{n_i}{N_1}\right)\left(\frac{S_i}{S_1}\right)^P = 1 \tag{8}$$

where,

n_i	the number of cycles in stage i
S_i	the stress level in stage i
N_1	the reference number of cycles
S_1	the reference stress level
P	factor calculated based on experimental data

2.3   Fatigue of plain concrete

2.3.1   Mechanism of fatigue in plain concrete

As previously stated, fatigue is a gradual process of internal structural changes that occur in a material when subjected to repetitive stresses (Rilem Committee 1984). The occurring changes often lead to the growth of cracks and eventually to the complete fracture of the concrete in case the stress repetitions are significant enough (Shah and Chandra 1970, Raju 1970). At a macro-level, these internal changes in the material caused by the fatigue compressive loading significantly affect its mechanical properties. Understanding and quantifying their effect is necessary to accurately predict the fatigue life of the investigated structures. However, describing the fatigue mechanism of concrete can often be proven challenging due to the complexity of the phenomenon. Over the years, many researchers have proposed several hypotheses regarding the initiation and propagation of cracks due to fatigue loads.

Murdock 1960 suggested fatigue loading results in the deterioration of the bond between the matrix and the aggregates that happens alongside the reduction of the section of the loaded specimen. The specimen ultimately fails when the matrix undergoes fracture. If the modulus of elasticity of the coarse aggregate exceeds that of the binding matrix, the development of cracks may be intensified.

An alternative theory was proposed by Antrim 1967. According to this hypothesis, repetitive loads cause the development of small cracks that propagate in the cement paste, forming a crack pattern. Over time, this pattern of cracks can compromise the structural integrity of the section, which is unable to sustain the applied loads. The development of this damaging crack pattern is primarily influenced by the water-cement (W/C) ratio of the cement paste, as well as the presence of shrinkage stresses in the cement paste. Specifically, increasing the W/C ratio increases the number of capillary pores in the cement paste, reducing the concrete strength. Moisture content can also influence the concrete strength since, due to shrinkage, tensile stresses are developed as water is withdrawn from the gel.

According to Rilem Committee 1984, numerous studies conducted have revealed evidence supporting both hypotheses, which highlights the complex nature of concrete fatigue mechanisms. Nevertheless, it can be concluded that concrete fatigue is associated with the development of internal micro-cracking, which is likely to occur at the interface between the cement matrix and the aggregate, as well as within the matrix itself. It is noted that the fatigue crack system is more extensive compared to the cracking experienced during static compressive failure (Bennett and Raju 1969).

Based on a different approach, the fracture mechanism also differs on the basis of loading class (T. T. Hsu 1984):

- Low-cycle fatigue: the fracture mechanism is governed by cracks formed in the concrete matrix forming a crack network.

- High-cycle fatigue: repeated loading results in bond cracks, which are gradually formed in the concrete.

2.3.2   Development of microcracking and inelastic strain

In static monotonic concrete compression, the deformation response is categorised into three stages, namely linear, nonlinear hardening, and post-peak softening. Similarly, fatigue microcracking in concrete is developed in three stages, as illustrated in Figure 2.6. In the first stage, a rapid increase of microcracks is noted at the weak points within the concrete or mortar (0 - 10 % of fatigue life). Following, the second stage is known as the propagation stage, in which the microcracking uniformly and progressively increases, reaching a critical size (10 - 80 % of fatigue life). In the final stage, a sufficient number of cracks has been developed, reducing the cross-section to such a degree that the propagating cracks easily penetrate, leading to failure (80 % to failure)(Rilem Committee 1984, Gao and C.-T. T. Hsu 1998 and Lee and Barr 2004).

The process of fatigue crack growth can be divided into two distinct stages (Hideyuki Horii, Shin, and Pallewatta 1992). The first stage is characterised by a deceleration in the crack growth rate as the crack expands. The second stage is the acceleration stage, in which there is a steady increase in the crack growth rate until the component fails (Kolluru et al. 2000).
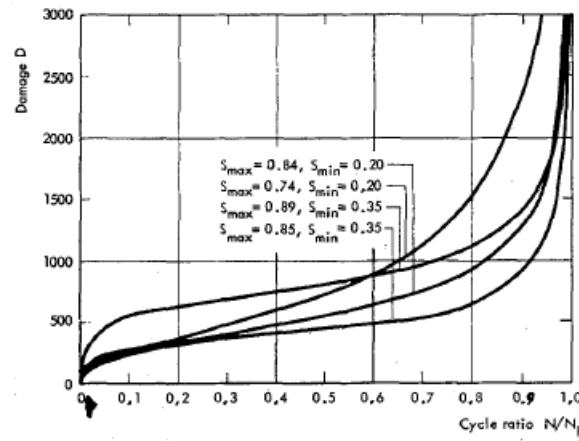
Figure 2.6: Crack development under constant amplitude cyclic loading measured using the acoustic emission method (Weigler and Klausen 1979)

Current research has provided more insight into the damage evolution due to compressive fatigue. Using new technological means (X-rays, 3D Industrial Computed Tomography (ICT)), researchers were able to understand the development of the fatigue phenomenon better, quantify

the fatigue damage in concrete and express the fatigue behaviour of concrete subjected to cyclic loading through constitutive models. In their study, Marzec, Tejchman, et al. 2019 examine the fracture evolution in concrete due to compressive fatigue. As depicted in Figures 2.7a and 2.8a, the concrete initial state presents a significant number of microcracks. Over the course of 10,000 cycles, thin, irregular-shaped cracks were observed, primarily concentrated along the vertical edges of the specimens. Analysis revealed that all micro-cracks were present in the Interfacial Transition Zones (ITZs) between the matrix and aggregate particles and then propagated further into the cement matrix. After 30,000 cycles, the internal cracks continued to develop and extended deeper into the cement matrix, and new macro-cracks emerged (Figure 2.7b and 2.8b). At 60,000 cycles, the existing vertical macro-cracks persisted along the lateral edges, with two of those cracks propagating through the height of the specimen (Figure 2.7c and 2.8c). Next, at 70,000 cycles, the vertical cracks throughout the specimen's height were predominant, with diagonal cracks also noticeable. These macro-cracks were interconnected through a network of smaller cracks (Figure 2.7d and 2.8d). Finally, the specimen damage occurred in the corner where the dominant vertical macro-crack was located.
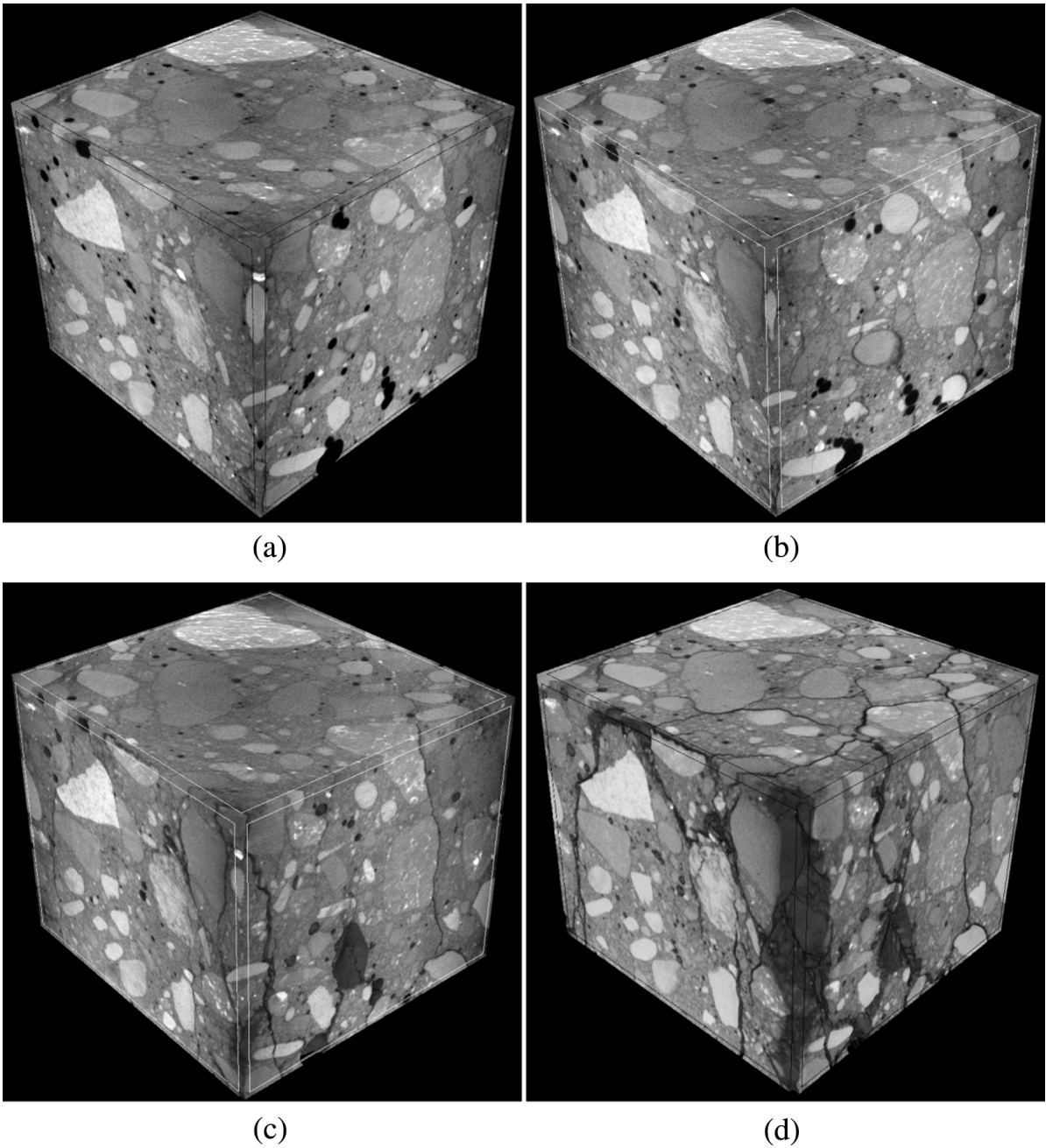
Figure 2.7: Evolution of cracking in concrete specimen subjected to compressive fatigue loading, using 3D micro-CT images: (a) before the test, (b) at $N = 30,000$ cycles, (c) at $N = 60,000$ cycles and (d) at $N = 70,000$ cycles. (Marzec, Tejchman, et al. 2019)
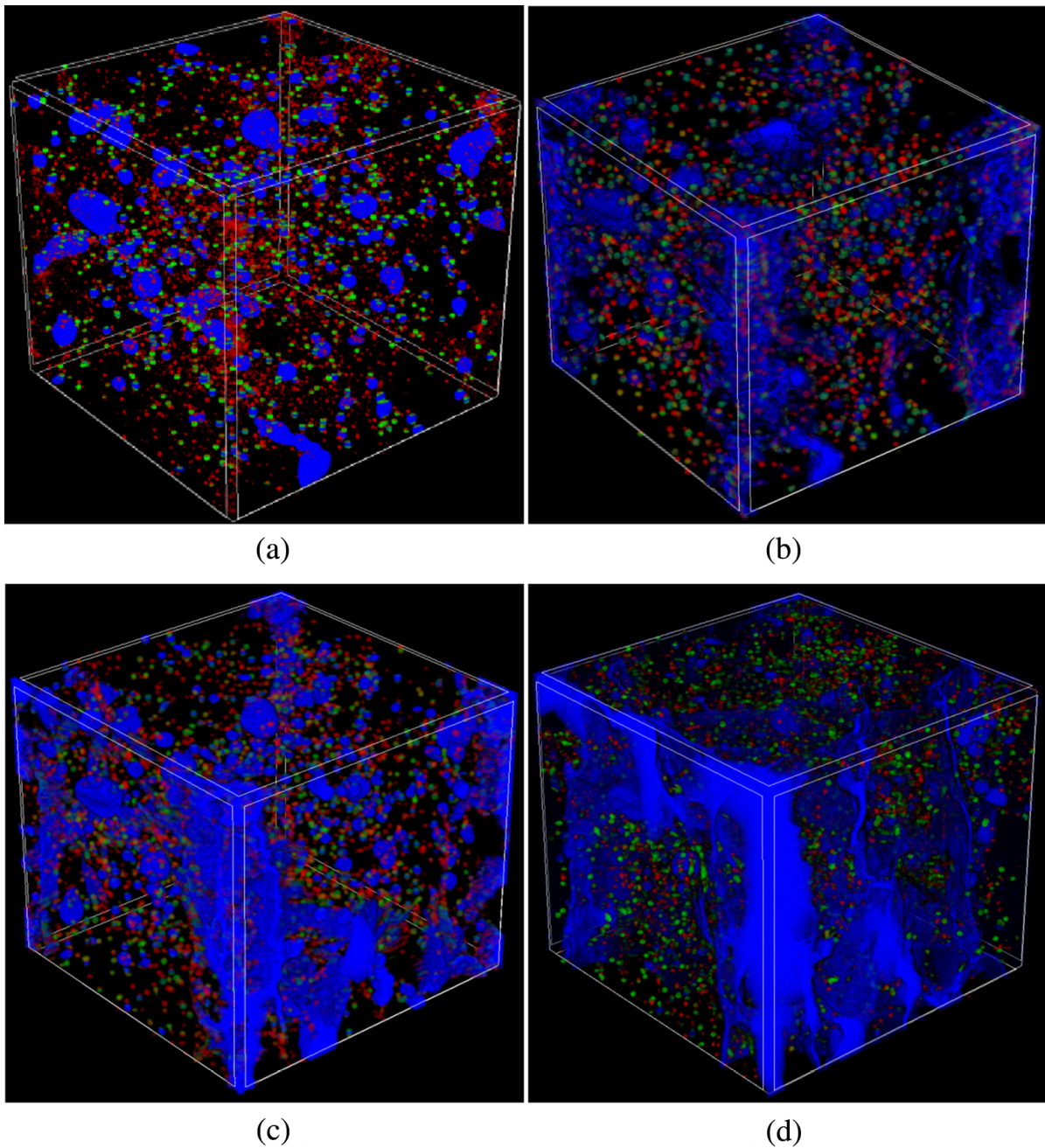
Figure 2.8: Pores and cracks distribution in concrete specimen subjected to compressive fatigue loading, using 3D micro-CT images: (a). before the test, (b). at $N = 30,000$ cycles, (c). at $N = 60,000$ cycles and (d). at $N = 70,000$ cycles. The colours indicate the diameter of pores within a specific range: $\leq 1.0mm$ (red colour), $1.01mm - 2.0mm$ (green colour) and $\geq 2.0mm$ (blue colour)) (Marzec, Tejchman, et al. 2019)

The gradual expansion of microcracking significantly increases the irrecoverable strains. On a

larger scale, this is expected to affect the material's mechanical properties (Lee and Barr 2004).

As illustrated in Figure 2.9, the strain - cycle ratio diagram follows a three-stage pattern similar to the one of the crack growth. According to Gao and C.-T. T. Hsu 1998, the first stage is defined as the cyclic creep stage since irreversible strains are predominantly caused by the cyclic creep effect. In this stage, irreversible strains display a rapid increase, similar to that observed during crack growth. The second stage, known as the creep-fatigue stage, is characterised by the coupling of cyclic creep and fatigue, which determines the accumulation of irreversible strain at a slower rate. Finally, the third stage, the fatigue stage, is marked by strain development, which is determined by factors such as width, distribution, and propagation of existing cracks. Again, the fatigue strain change is divided into two distinct stages (Figure 2.10). During the first stage, the fatigue strain range remains relatively stable and does not significantly fluctuate with the increase of the load cycle. However, the second stage sees a rapid increase in fatigue strain range, as it is directly linked to the formation and propagation of fatigue cracks. As the density of fatigue cracks increases and they continue to propagate, the fatigue strain range becomes increasingly unstable.
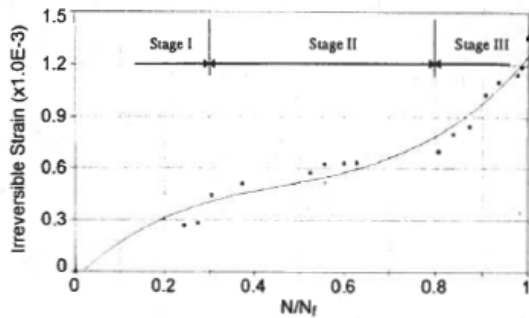
Figure 2.9: Irreversible strain development stages
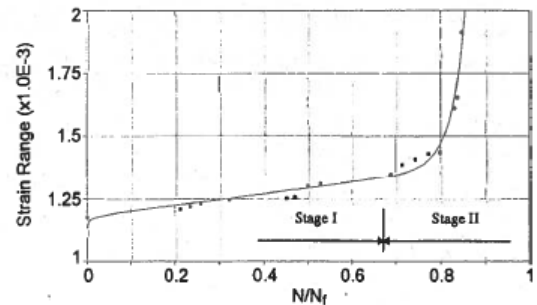
Figure 2.10: Variation of fatigue strain range

As categorised by Bazant and Hubler 2014 in their study, there are five types of cracks that result in inelastic strains. The five types of cracks are depicted in Figure 2.11.

1. Crushing band propagating transversely to compression (S. Suresh, Tschegg, and Brockenbrough 1989, Subra Suresh 1998, Eliáš and Le 2012) (Figure 2.11a)

2. Wedge-splitting cracks at hard inclusions, parallel to compression (Bažant and Xiang 1997) (Figure 2.11b)

3. Interface cracks at inclusions (Figure 2.11c)

4. Pore-opening cracks parallel to compression (Fairhurst and Cornet 1981, Sammis and MF Ashby 1986) (Figure 2.11d)

5. Wing-tip frictional cracks inclined to compression direction (Ingraffea 1977, Nemat-Nasser and H. Horii 1982, Kachanov 1982, M.F. Ashby and Hallam 1986, Schulson and Nickolayev 1995) (Figure 2.11e)
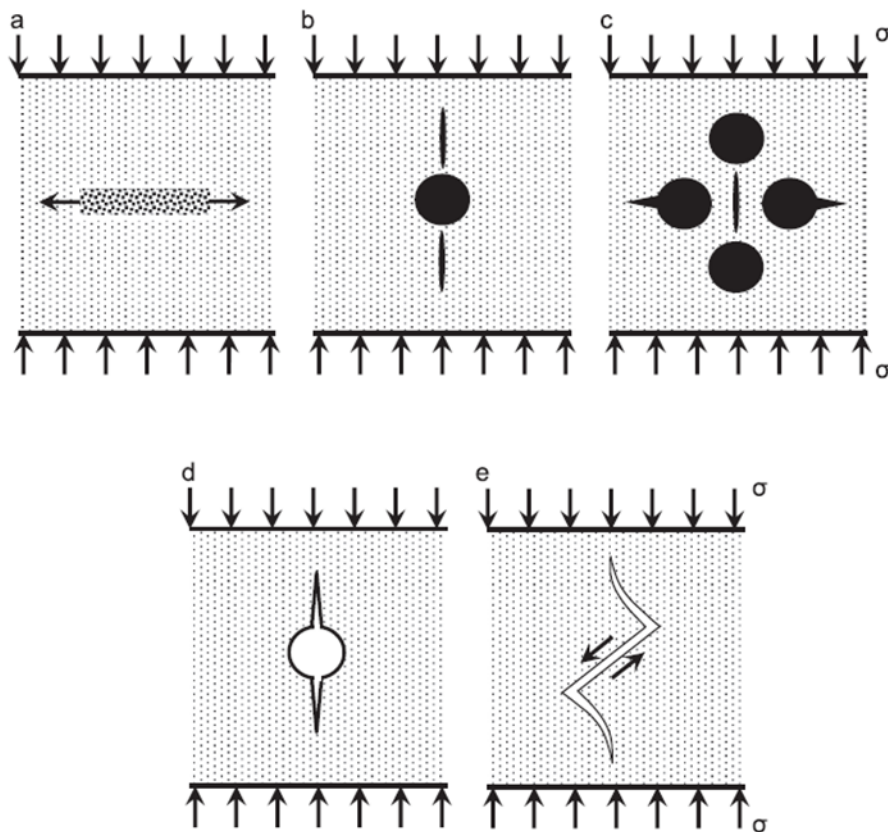
Figure 2.11: Types of crack that result in the inelastic strain development (Bazant and Hubler 2014)

Generally, determining fatigue failure in any material largely depends on the extent of the crack pattern since the final fracture is directly influenced by it. Fatigue fracture mechanism is similar to brittle fracture as both depend on the random distribution of imperfections or weak points within the material (Antrim 1967). The brittle fracture occurs when the material's strength is exceeded at one or more of these locations, resulting in little to no yielding before failure

(Richards 1961). Even if it presents a brittle fracture mechanism, the fatigue failure process presents significant differences from that of static situations, as it depends on a series of random events that may vary from case to case. As a result, there is considerable variation in fatigue data. Additionally, compressive cyclic loading results in a crack system with wider distribution (Holmen 1979) and lower strength than the statically determined ones. It is worth mentioning that since the fatigue failure is initiated at the weak points of the material, delaying the crack propagation can significantly prolong the fatigue life of the structure.

2.4   Case studies of fatigue failure of concrete structures

The fatigue life of reinforced and prestressed beams has been frequently studied under controlled laboratory conditions. Nonetheless, many real-life structures exhibit signs of fatigue over time. While the fatigue in steel structures presents an easily identifiable crack pattern, concrete fatigue cracking does not display a distinctive surface topology. For this reason, the assessment of the concrete structures for fatigue requires detailed data from the service life of the structures, carefully considering the existing cracks and the crack pattern developed. Further information regarding the construction methods, dates, and loading conditions during the structures' lifetime are integral parts of detailed reporting and essentials for assessing their fatigue life (CEB-FIP 1988).

Over the years, plenty of concrete structures have progressively deteriorated, with fatigue being the primary or essential contributory factor, along with other factors such as fretting fatigue and corrosion. Several case histories have been reported by CEB-FIP 1988 in which the aforementioned factors lead to the distortion of the concrete structures. As evident from the following examples, pure fatigue cannot be solely attributed to the deterioration of the structures. In most cases, fatigue is accompanied by other factors, such as repeated deflections, increased loading, and higher frequencies or vibrations. Additionally, chemical attacks like fretting, pitting, or carbonation attack can further worsen the fatigue-induced degradation, particularly in prestressed concrete.

Case study 1 - Throgs Neck Bridge, New York

The Throgs Neck bridge is an 887 m long suspension bridge which has been in service since 1961.

The bridge's deck is supported by longitudinal beams, which are placed on transverse beams with cantilever brackets at 7.3 m intervals. Just ten years after its opening, the bridge showed signs of severe concrete deterioration, an issue that only worsened over time. The cantilevers' repetitive deflection caused secondary tensile and fatigue stresses, identified as the primary cause of the bridge's failure. Other factors contributing to the bridge's unreliability include insufficient reinforcement in accordance with more recent standards, corrosion caused by de-icing salt, and the loss of concrete cover.

Case study 2 - Japanese bridge decks

Incidents of fatigue failure have been reported on Japanese bridge decks since 1965. The characteristics of such failures include concrete spalling under the bottom reinforcement layer at the soffit or depressions of the running surface caused by punching failure. The failure was localised to the concrete following a grid-like pattern, while the steel reinforcement displayed no evident damage. This type of failure indicates that fatigue caused by traffic loads is the primary reason for the distortion of the bridge, even in the early stages of its service life. Fatigue due to repetitive loads and increasing traffic volume was not considered in the design process at the time of the bridges' construction. The reason for their failure became clear only later when researchers classified that the repetition of shear and torsional effects reduces the structures' fatigue strength, inducing their failure. Similar failures have also been observed in bridges in Sweden.

Case study 3 - Bridge decks in the Netherlands

From 1935 to 1950, around thirty trussed-girder bridges were built in the Netherlands. These bridges were parted by a cast in-situ, reinforced concrete deck placed on longitudinal and transverse steel girders, with main spans ranging from 50 to 200 m in length. The deck width varied from 6 to 12 m, having no structural connection to the steel.

In the following period, the concrete decks of all the bridges needed to be replaced because of their severe condition. The damage was caused by the formation of numerous small cracks that eventually led to complete concrete deterioration. In the initial stages, the cracks were primarily longitudinal and occurred beneath the wheel tracks. During the demolition of the

decks, no damage was observed on the reinforcing steel, and the concrete strength was found to be high, with a cube strength of $50 N/mm^2$ or more.

According to the Bridge Building Department of Rijkswaterstaat (RWS) in the Netherlands, the fatigue of the concrete was the primary reason for the concrete failure, given that the previous Dutch code did not include regulations related to fatigue loading. The following observations supported this conclusion:

1. The concrete damage was mainly concentrated beneath the wheel tracks of the heavy vehicles.

2. The traffic volume and axle loads are significantly higher than what was initially considered in the design process.

3. The live load stresses were significantly larger than those induced by the permanent loads, and the variation of stresses was the least favourable.

4. There was no evidence of damage to the steel reinforcement.

5. The concrete next to the cracked area presented high cube strength.

Case study 4 - Bridge over Tarnaforsen, Sweden

The bridge, located in Vasterboten, Sweden, was built in 1943 and has a maximum allowed total load of 514 kN. Over time, vertical and inclined shear cracks have been observed on the bridge beams. These cracks were believed to be caused by heavy vehicles passing over the bridge when the permissible load was exceeded. In 1950, a 2200 kN weight truck crossed the bridge and nearly caused a collapse, which served as the start of fatigue cracking problems. Additionally, the bridge was not sufficiently reinforced for shear, as the shear resistance of the concrete was thought to be higher until the 1960s. Despite attempts to repair the cracks, they have reappeared (Figure 2.12).
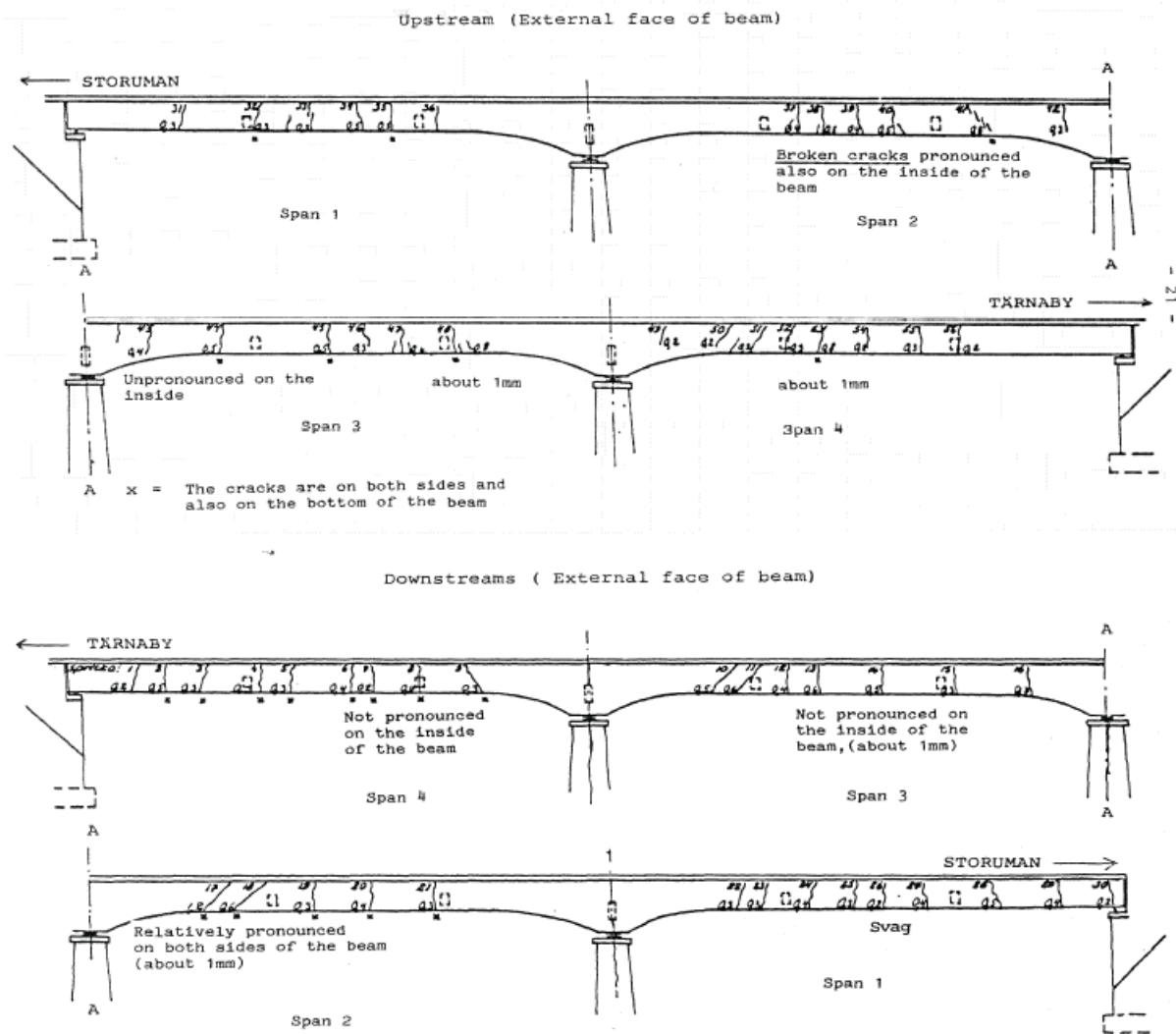
Figure 2.12: Recorded cracks on the main beam. Road E79, Bridge Ume River at Tärnafors, Tärnaby-Storuman. (CEB-FIP 1988)

Case study 5 - Traveling crane track, Sweden

Tracks are distinguished into two types: the first type is upheld by a steel beam that rests on concrete columns, while the second type rests on steel plates which are supported by the columns. In both cases, the track structure is supported by nuts and the load is transferred to the columns through hold-down bolts and mortar beneath the steel members. In the investigated track that was built in 1976, it was noticed that the concrete around the bolts had spalled, the mortar had cracked, and the bolts had been sheared. It was considered that the damage occurred by

the repeated loads from the cranes acting on the columns and were not structurally confined.
The tops of the columns underwent repair with extra compressive and confining reinforcement
(Figures 2.13 and 2.14).
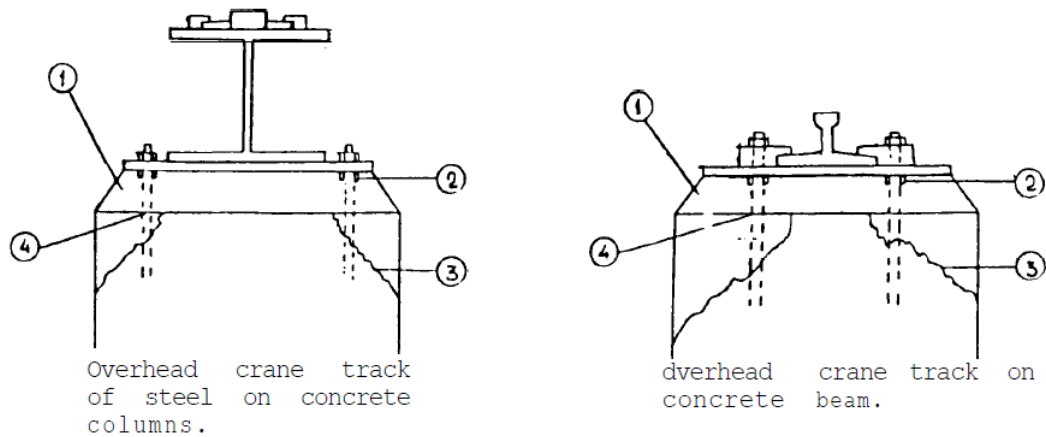
Figure 2.13: Failure pattern of the concrete column under the travelling crane. (CEB-FIP 1988)
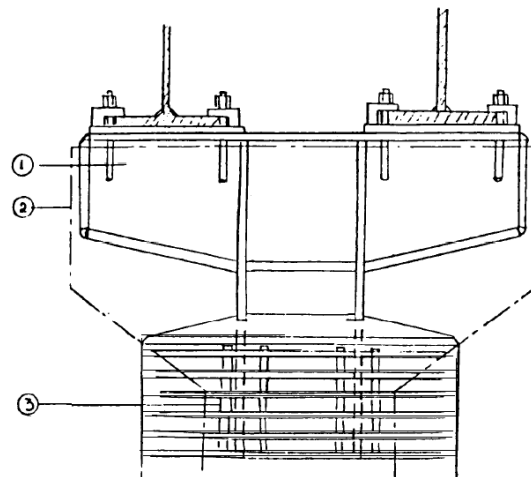
Figure 2.14: Strengthening arrangement of the column. (CEB-FIP 1988)

Case study 6 - Viaduct over railway, Sweden

The viaduct, constructed in 1934 using steel beams and a continuous concrete slab, has been observed to have transverse cracks on the underside of the slab. Part of the concrete cover has also fallen away from the free span. Through cracks have also been found in the slab near the two middle supports. Despite repair attempts, the damage keeps resurfacing.

Similar to the Japanese bridges, it is considered that the repeated live loads resulted in the formation of wide cracks since it is unlike that static loads could cause those. In addition, the concrete cover has been dislodged due to the carbonation of the concrete, which, combined with the cracks, has allowed corrosion of the reinforcing steel. The presence of these factors finally led to the deterioration of the structure.

Case study 7 - Reconstruction of concrete pavement, The Netherlands

It has been observed that unreinforced concrete motorways, which have been in use for longer than their intended lifespan, experience fatigue problems. These issues result in transverse cracks forming in the most heavily used lanes and smaller longitudinal cracks appearing between them. Fatigue is believed to be a significant contributing factor to this deterioration. For the reconstruction of motorways, the principle of reflection cracks is used, where fatigue and reflection cracks are caused by existing cracks in the lower layers. This reduces the life of the structures. The problem is addressed by constructing soft stress interlayers to prevent the formation and propagation of cracks between the surface and the stabilised base.

Case study 8 - Factory floor, United Kingdom

The factory floor experienced fatigue failure due to deflection and excessive cracking. It was constructed using precast, prestressed planks topped with a thick, continuous, reinforced, cast in-situ concrete slab. After the factory was occupied, cracks appeared at the joints between the precast and cast in-situ concrete members. The cracking was initially suspected to be due to shrinkage, but the pattern and distribution of the cracks did not suggest shrinkage or temperature effects. Additionally, the in-situ concrete did not show any spalling at the construction joints from the use of folklift trucks.

The cracking was mainly caused by the repetitive movements of the folklift trucks. Based on the original design, the load would be distributed over three units, allowing each unit to share the applied load with adjacent units. However, the crack pattern that was caused by fatigue resulted in each unit becoming isolated and causing excessive sagging of the slab. Finally, the increasing deflection was worsened by the onset of vibration, accelerating the fatigue of the floor.

Case study 9 - Wood chip processor in Korsnasverken, Sweden

This particular concrete building was constructed in 1967. After only one year, cracks were discovered in the slab. Despite attempts to repair and strengthen the structure in 1969, the cracks reappeared. The equipment attached to the structure was operated in a manner that prevented the amplification of vibrations through resonance. This helped to reduce the vibrations, but the cracks still returned. The building was then reinforced with concrete walls and steel beams, but this did not fix the problem, and the cracks resurfaced at the beginning of 1971. Unfortunately, a thorough analysis of the issue was not conducted due to the complex combinations of loads. These loads included hydraulic jacks in the machinery, the weight of wood chips, forces from the chips caused by changes in moisture content, and the increasing size of tractors that were used to push the chips. It was believed that the cracks were caused by fatigue.

Case study 10 - Papermill, Finland

The building was constructed in the late 1930s using concrete beams and columns. However, some areas were found to have low concrete strength, resulting in transverse and vertical cracks in the structure. It is considered that the damage was caused due to fatigue since the structure was not designed to withstand fatigue. Additionally, no ground settlements were observed in the structure despite being subject to long-term load, vibrations, and penetrating oil.

2.5 Fatigue in concrete bridges

Many experimental studies are focused on examining the fatigue behaviour of concrete when subjected to axial compression. This fact raises the question of whether the findings associated with the fatigue of concrete under uni-axial compression can also be applied to the fatigue assessment of the compressive zone of the concrete beams.

Lambotte and Baus 1963 compared the response of prisms subjected to uni-axial compression and over-reinforced beams that were constructed having the exact dimensions and quality of concrete. After 10^7 cycles, the beams reached failure due to fatigue of the compressive zone, being able to sustain 70% of their ultimate static strength. At the same time, the equivalent value of the compressed prisms reached approximately 60%. In addition, in the research conducted by Ople and Hulsbos 1966, the concrete compressive zone of the beams was simulated by applying eccentric loads on concrete prisms. In order to ascertain the fatigue strength of the specimens, the stress at the compression fibre was calculated using the specimen's stress-strain graph under uni-axial static compression. Based on the results, increasing the eccentricity positively affected the fatigue strength but did not influence the relative fatigue strength regarding the total applied load. Consequently, the effect of eccentricity on the fatigue and the static strength was of the same proportion, meaning that the fatigue values of concrete under uni-axial compression can be safely applied to the compressive zone of the beams.

A different approach is suggested by Jiang et al. 2017, whose research focuses on cyclic creep. Based on this study, considering that the structural elements of the instigated bridges are subjected to both axial force and bending moment would result in a more realistic approach that reflects the stress gradient occurring in each cross-section. As the number of load cycles rises, the structural elements present a redistribution of stresses along the cross-section caused by the gradual degradation of the mechanical and material properties. Therefore, conducting fatigue experiments by assessing the concrete behaviour under both uni-axial and eccentric loads is necessary to better understand fatigue's structural influence.

2.6   Parameters affecting fatigue of concrete

2.6.1   Composition and quality of concrete

According to Rilem Committee 1984, the influence of the composition and quality of the concrete on the fatigue strength is uncertain. Variables such as water-cement ratio (W/C), cement content, curing conditions, entrained air quantity, aggregate type, and loading age appear not to have an impact on fatigue strength when this is expressed in terms of static strength (Nordby 1958, Tepfers and Kutti 1979). In fact, in flexural fatigue tests conducted on three concrete

types, aged for up to five years and subjected to different curing methods, the obtained results expressed in terms of the static strengths were almost identical (Raithby 1979).

However, a different theory is suggested by Antrim 1967. As previously mentioned (Chapter 2.3), concrete is a heterogeneous material whose fatigue life is highly dependent on the development of internal microcracking. Microcracking is initiated at the weak points of the concrete when the applied stress surpasses the concrete strength. One of the main parameters influencing crack pattern development is the water-cement (W/C) ratio. Its increase results in the formation of more capillary pores in the cement paste, adversely affecting the strength of the concrete. Additionally, moisture content can impact the strength of concrete since shrinkage leads to the development of tensile stresses as water is removed from the gel.

According to Powers 1959, the shrinkage process occurs within the gel, and the degree of shrinkage depends on the amount of water extracted. This means that a paste with few capillary pores (low W/C ratio) will experience a shrinkage directly proportional to water loss. Conversely, a paste with a significant number of capillary pores (high W/C ratio) will undergo minimal shrinkage. As the drying continues, the shrinkage becomes directly proportional to water loss. It is noted that the effect is higher in concrete specimens having a lower W/C ratio and, consequently, a denser structure from which water cannot easily escape.

Finally, as cement content is associated with the strength of the concrete, it affects the cracking mechanism and, consequently, its fatigue life (Zanuy, Albajar, and De la Fuente 2009).

2.6.2   Stress level and stress variation

The fatigue life of concrete is significantly impacted by the maximum and minimum stresses it experiences. Specimens subjected to high maximum stress present a shortened lifespan. Moreover, an increase in the stress range ($R = \sigma_{min}/\sigma_{max}$) decreases the number of cycles to failure.

Current X-rays and CT imaging methods have shown that the morphology and propagation of fatigue cracks are notably affected by the stress magnitude during fatigue loading. As obtained by the Fan and Sun 2019, the damage evolution in concrete specimens under compressive cycling loading is depicted in Figures 2.15 and 2.16. Comparing the results for the two different stress

levels, it is clear that the primary fatigue crack propagation was highly associated with the loading level. During the initial stages of cyclic loading, the micro-cracks exhibited some degree of widening, yet no noteworthy expansion was observed. Upon completion ($n/N = 0.15$), no significant changes were noted in the higher loading levels, while in specimens where the loading levels were lower, the primary crack had already appeared. As loading cycles increased, the development of the main fatigue crack accelerated gradually and had fully formed by the end of the stage. It was noted that higher stress levels resulted in a brittle fracture occurring after fewer load cycles. Conversely, lower loading levels presented more obvious fatigue characteristics in the specimen.

Finally, variation of the stress level in the duration of the cyclic loading highly affects the fatigue performance of concrete. As analytically explained in Chapter 2.2, the stress sequence can either prolong or shorten the material's fatigue life.

(a) n/N=0   (b) n/N=0.15   (c) n/N=0.9
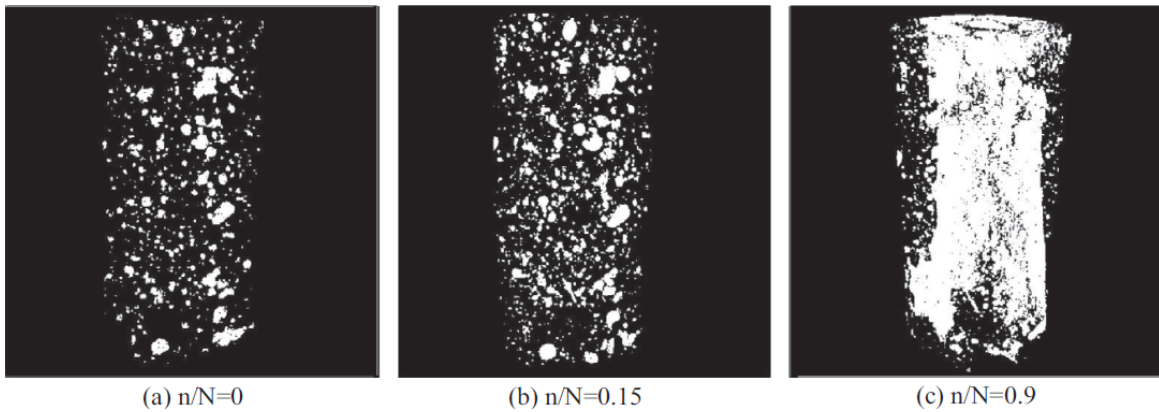
Figure 2.15: Damage evolution at $S_{max} = 0.85$. (Fan and Sun 2019)

(a) n/N=0   (b) n/N=0.15   (c) n/N=0.9
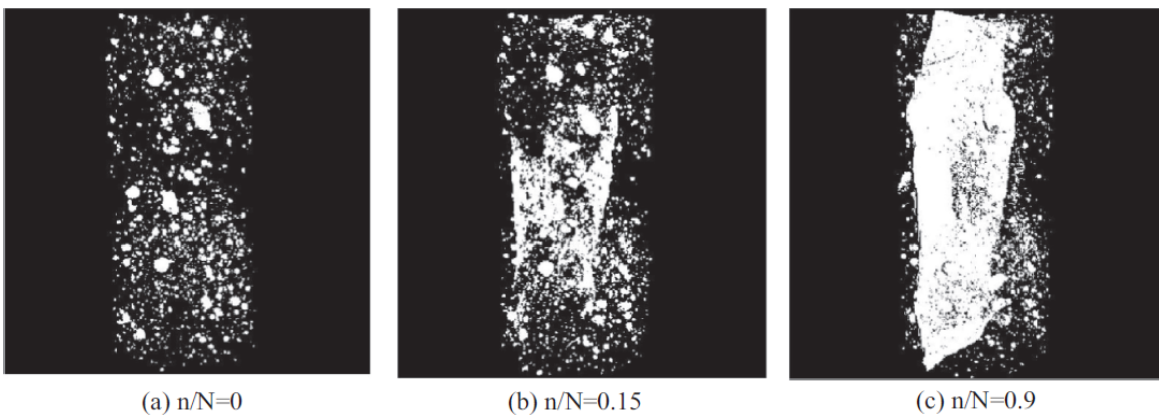
Figure 2.16: Damage evolution at $S_{max} = 0.80$. (Fan and Sun 2019)

2.6.3   Frequency of loading and stress rate

Several researchers have conducted studies on the impact of loading frequency as presented by Rilem Committee 1984. Based on these, it was widely acknowledged that changes in loading frequency do not significantly affect fatigue strength, provided that the maximum stress level remains below approximately 75% of the static strength (Hanson, Ballinger, and Linger 1974). This effect differs at high-stress levels, where the decrease in the loading frequency results in lower fatigue strength (Holmen 1979).

The effect of the loading rate on the fatigue strength of plain concrete subjected to compression was studied by Sparks and Menzies 1973. The study showed that altering the loading rate from 0.5 to 50 MPa/s significantly increased the average fatigue life for stresses exceeding approximately 75% of the static compressive strength. This indicates that, for high cyclic stresses, accelerated fatigue tests may overestimate the fatigue life of concrete structures compared to the loading rates that may arise during their service life.

2.6.4   Rest periods

Hilsdorf and Kesler 1966 conducted a study to examine the impact of rest periods on fatigue flexure tests for plain concrete. The study showed that taking repeated rest periods of up to 5 minutes after the loading cycles can increase fatigue strength as it allows for recovery during the rest period. However, a different series of tests where shorter rest periods were applied presented decreased fatigue life at a specific stress level. Similar findings were obtained by Siemes 1985, showing that resting periods of 1.5 to 10 min can prolong the fatigue life when the maximum and minimum applied stresses remain constant. The noted improvement in both studies was considered insignificant due to the large scatter in the resulting values. Despite the scatter, it is accepted that applying longer resting periods can extend the fatigue life of the specimens, as it provides time for self-healing, relaxation of stresses at the crack tip and finally, stress redistribution in the concrete.

2.6.5   Moisture content

Understanding the influence of moisture conditions on the fatigue life of concrete has been proven complex. To assess its effect, Galloway, Harding, and Raithby 1979 performed fatigue flexural experiments using concrete beams that had dried from various periods after being saturated in water. Their findings indicate notable differences in both rapture modulus and fatigue performance. However, when the fatigue stress was expressed as a proportion of concrete flexural strength, the obtained fatigue strength presented no considerable differences. Similar conclusions have been drawn by testing using saturated, surface dry, or oven-dried following prolonged immersion. Generally, moisture gradients within the specimens are believed to have played a more critical role in the observed differences in fatigue performance than the moisture percentage. The gradient can lead to high initial strains at the specimen's surface and the potential development of shrinkage cracking (CEB-FIP 1988).

Other experimental studies examining the fatigue performance of concrete specimens in dry and wet conditions have shown that dry concrete can sustain a larger number of loading cycles in compression (Van Leeuwen and Siemes 1979, Waagaard 1981) and tension (Cornelissen and Reinhardt 1984), as presented in Figure 2.17. It has been observed that dry concrete exhibits less creep compared to wet concrete. This characteristic can be attributed to its substantial impact on the propagation of cracks in concrete when subjected to cyclic loads.
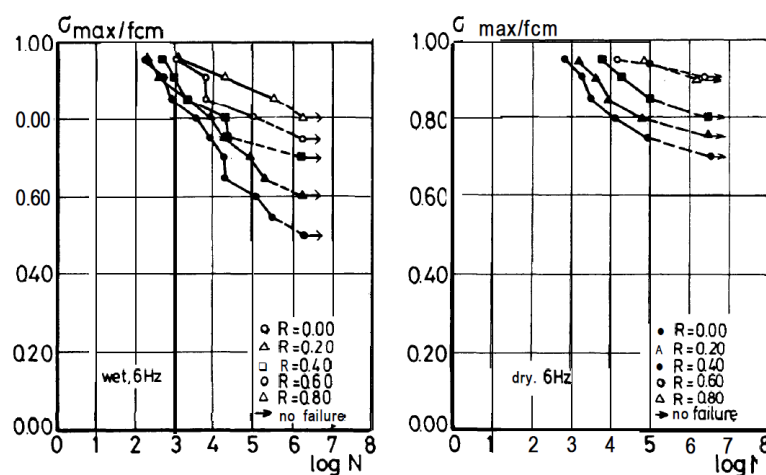
Figure 2.17: Effect of moisture conditions on fatigue life of concrete subjected to compression for (a). dry, and (b). wet concrete (Van Leeuwen and Siemes 1979).

2.6.6   Lateral confining pressure

The findings of fatigue tests conducted on sealed cylindrical specimens have revealed that lateral confining pressure has a significant impact on their fatigue strength on lower stress levels (Takhar, Jordan, and Gamble 1974). As depicted in Figure 2.18, the specimens subjected to lateral pressure presented a remarkable extension in their fatigue life. It is also noted that the maximum stress level of the fatigue load influences this prolongation effect (Rilem Committee 1984).
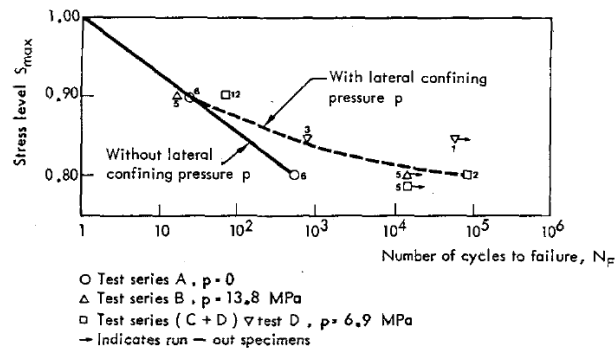
Figure 2.18: Effect of lateral confining on fatigue life of concrete subjected to compression. (Takhar, Jordan, and Gamble 1974)

Based on a different study (Petkovic 1993), Figure 2.19 illustrates how the fatigue life N is affected by mean stress S_m and stress range R. It is clear that at every lateral to longitudinal stress ratio $(S_{m,1}/S_{m,2})$, the positive impact of lateral confinement on fatigue performance diminishes after the specimen undergoes more than approximately 50 loading cycles.
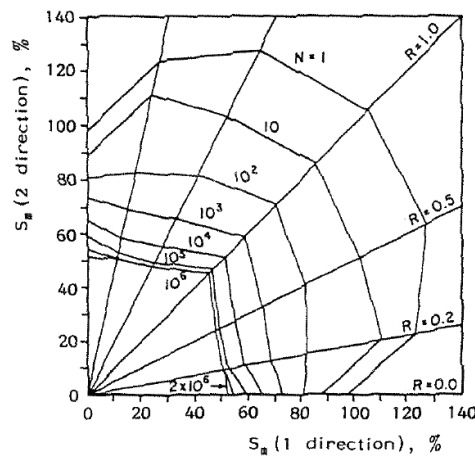
Figure 2.19: Influence of biaxial loading on fatigue life of concrete. (Petkovic 1993)

2.6.7   Different waveforms

Most of the experimental studies are conducted by subjecting a structure to repeated sinusoidal loading, replicating the wave and wind loads experienced in practical applications (Rilem Committee 1984). However, specific structures may be exposed to other loading patterns, which requires investigating the effect of different waveforms. In their research, Tepfers and Kutti 1979 studied the influence of rectangular, triangular and sinusoidal loading patterns on the fatigue life of concrete prisms. The findings indicate that the rectangular waveform results in a shorter fatigue life than the sinusoidal waveform. In contrast, the greatest number of loading cycles can be sustained when triangular waveforms are applied. Figures 2.20 and 2.21 present the number of load cycles sustained by the concrete specimens for the different load types.

It is noted that strain velocity is an additional factor influencing the performance of specimens exposed to different waveforms. In particular, rectangular waveforms with higher velocities exhibit more significant effects compared to triangular waveforms with lower velocities. It is, therefore, essential to account for time-dependent effects when assessing the fatigue life of concrete under varying waveforms.
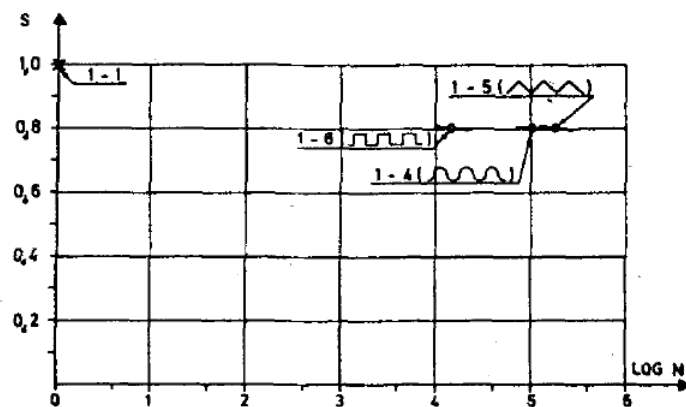
Figure 2.20: Effect of loading using different waveforms on the fatigue life of concrete - Wöhler diagram. (Tepfers and Kutti 1979)
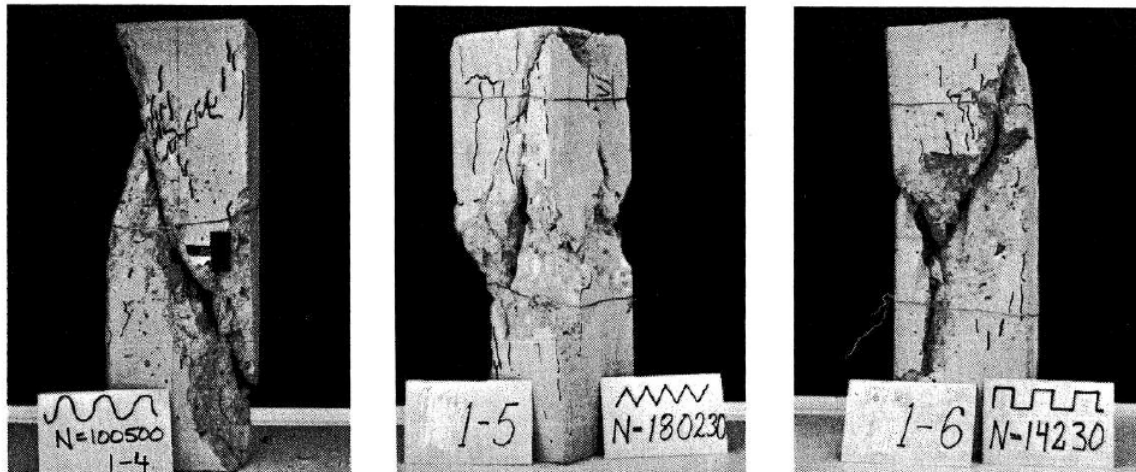
Figure 2.21: Effect of loading using different waveforms on the fatigue life of concrete - Concrete prisms after fatigue failure (Tepfers and Kutti 1979).

2.6.8   Strengthening effect

The effect of the strengthening effect of concrete on the fatigue performance of concrete is analysed by Rilem Committee 1984. Even though the fatigue concrete strength is expressed as a fraction of its static strength withstanding repetitive loading, it is important to note that a specimen's residual static strength after a certain number of cycles is not an accurate indicator of the extent of damage it has sustained. Numerous researches (Bennett and Raju 1969, Awad 1971, Holmen 1979) have indicated that a specimen subjected to cyclic loading with a specific cycle ratio (N/N_f) shows improved strength by up to 15% when tested statically.

Several theories have emerged to explain this strengthening effect (Bennett and Raju 1969). First, the elevation in temperature caused by energy dissipation in the form of heat may be linked to the increase in strength. The temperature rise may result in slightly greater maturity of the specimen as well as increased loss of capillary moisture, leading to a small increase in strength. The loss of gel moisture could also be a contributing factor to the increased rigidity and strength. In addition, the strengthening effects may be associated with the release of residual stresses caused by repeated loads or with the strain-hardening effects.

2.6.9   Eccentricity and stress gradient

The eccentricity of the applied loads is an additional influencing factor (Rilem Committee 1984). Considering that uniaxial compression is not always representative of the loads imposed on the structures, it is necessary to assess its contribution to the fatigue life of the concrete. Figure 2.22, obtained by Ople and Hulsbos 1966, illustrates the fatigue performance of concrete prisms subjected to compressive load cycles for different stress gradients. The stress level is determined by the ratio of the maximum stress, noted at the extreme fibre, over the concrete strength. When expressed this way, it is clear that eccentric loads have a positive impact on fatigue strength. However, when fatigue strength is measured in terms of static strength, the S-N curves of centrically and eccentrically loaded specimens overlap, suggesting that they are similarly affected.

The effect of eccentricity on fatigue performance has often been used to study the compression zone of concrete beams, as further discussed in Chapter 2.5.
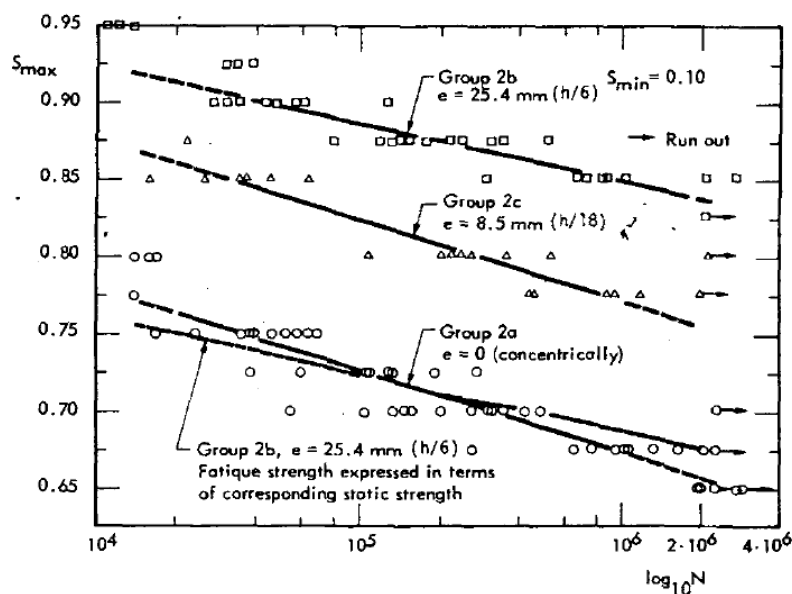
Figure 2.22: Effect of eccentricity on the fatigue life of concrete. (Ople and Hulsbos 1966)

36

2.6.10   Material degradation

According to Zanuy, Albajar, and De la Fuente 2009, concrete subjected to repeated loading undergoes alternation that leads to its progressive damage. This damage is characterised by an increase in the overall strain as the number of loading cycles increases, as discussed in the previous section. In addition to this, other changes in the material properties of the loaded specimens can also be observed. When subjected to cyclic loading, both the loading and unloading branches of each cycle become curved, as illustrated in Figure 2.23. The stress-strain curves deviate from the initial linear path, indicating a change in material properties, specifically, a reduction in the modulus of elasticity.

In the experimental study conducted by Jiang et al. 2017, data on eccentrically loaded concrete specimens have been utilised to investigate the distribution of strains in the cross-section during fatigue loading. According to their findings, the evolution of the neutral axis location measured from the tensile side revealed that, as cyclic loading continued, the neutral axis' position deviated from the tensile side. The change in the neutral axis shows a redistribution of stresses during fatigue loading, significantly affecting the concrete's fatigue life.
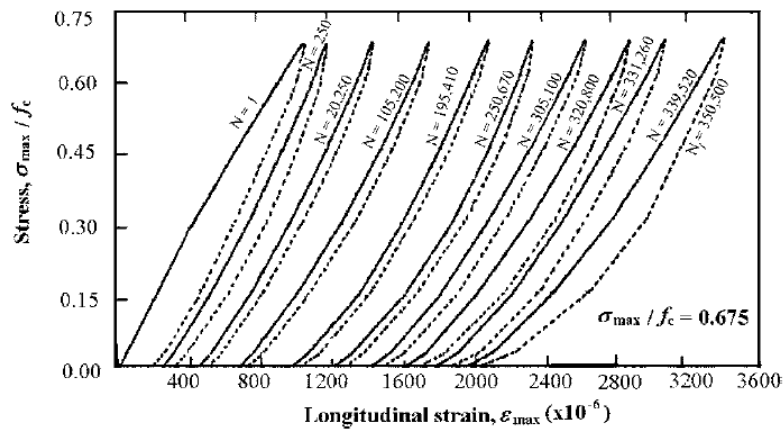
Figure 2.23: Stress-strain curve evolution with the fatigue loading (Bennett and Raju 1969).

3   Codes and methods for fatigue verification of concrete subjected to compression

3.1   Introduction

Various codes and modified methods have been proposed to ensure the concrete can withstand compressive cyclic loading. These codes are specifically intended to provide an accurate assessment of the fatigue life of concrete when subjected to compression. The following chapters present the current code provisions and some alternative methods, as reviewed by Lantsoght 2014, specifically intended to provide an accurate assessment of the fatigue life of concrete when subjected to compression.

3.2   NEN 6723:2009

According to the regulation of the previous Dutch national code NEN 6723: 2009 for concrete bridges, the fatigue assessment of concrete should comply with the Miner's rule, namely

$$\sum_{i=1}^{m} \frac{N_i}{N_{Fi}} \leq 1 \tag{9}$$

where,

m	the number of considered intervals
N_i	the number of cycles at the stress level i
N_{Fi}	the number of cycles to failure at the stress level i

As stated in §9.6.2.1, for varying compressive stresses, the number of loading cycles that can be sustained by concrete is given by

$$Log(N_i) = \frac{10}{\sqrt{1-R}} \left(1 - \frac{\sigma'_{b,d,max}}{f'_{b,v}} \right) \text{ for } \frac{\sigma'_{b,d,max}}{f'_{b,v}} > 0.25 \tag{10}$$

and

$$N_i = \infty \text{ for } \frac{\sigma'_{b,d,max}}{f'_{b,v}} \leq 0.25 \tag{11}$$

where,

R $= \frac{\sigma'_{b,d,min}}{\sigma'_{b,d,max}}$, the stress rate

$\sigma'_{b,d,min}$ the design value of the minimum compressive stress in the concrete, in N/mm^2

$\sigma'_{b,d,max}$ the design value of the maximum compressive stress in the concrete, in N/mm^2

In the limit fatigue state, the design value of the compressive strength of concrete ($f'_{b,v}$) is calculated as follows,

$$f'_{b,v} = \frac{f_{b,rep,v}}{\gamma_m} \tag{12}$$

$$f_{b,rep,v} = 0.5(f'_{b,rep,k} - 0.85 \cdot 30) + 0.85 + 30 \tag{13}$$

where,

γ $= 1.2$

$f'_{b,rep,k}$ the characteristic value of the uniaxial short-term concrete compressive strength $0,85f'_{ck}$, in N/mm^2

$f'_{b,rep,v}$ the characteristic value of the concrete compressive strength in the limit state of fatigue, in N/mm^2

3.3 NEN-EN 1992-1-1+C2:2011 and Dutch National Annex

Based on §6.8.7 of NEN-EN 1992-1-1+C2:2011/NB:2016+A1:2020, the fatigue resistance of concrete subjected to compressive cyclic loading can be considered sufficient when

$$E_{cd,max,equ} + 0.43\sqrt{1 - R_{equ}} \leq 1 \tag{14}$$

where,

R_{equ} $= \frac{E_{cd,min,equ}}{E_{cd,max,equ}}$, the stress ratio

$E_{cd,min,equ}$ $= \frac{\sigma_{cd,min,equ}}{f_{cd,fat}}$, the minimum compressive stress level

$E_{cd,max,equ}$ $= \frac{\sigma_{cd,max,equ}}{f_{cd,fat}}$, the maximum compressive stress level

$f_{cd,fat}$ the design fatigue strength of concrete

$\sigma_{cd,min,equ}$ the upper stress of the ultimate amplitude for N cycles

$\sigma_{cd,max,equ}$ the lower stress of the ultimate amplitude for N cycles.

The design fatigue strength of concrete is given by,

$$f_{cd,fat} = k_1 \cdot \beta_{cc}(t_0) \cdot f_{cd} \cdot \left(1 - \frac{f_{ck}}{250}\right) \tag{15}$$

where,

$\beta_{cc}(t_0)$ concrete strength coefficient at first load application

t_0 the starting time of the cyclic loading on concrete in days

f_{ck} the characteristic concrete strength

f_{cd} $= \frac{f_{ck}}{\gamma_{c,fat}}$, the design concrete strength

$\gamma_{c,fat}$ =1.5, for fatigue of concrete

For the calculation of the concrete strength coefficient at the first loading application,

$$\beta_{cc}(t) = e^{s\left[1-\left(\frac{28}{t}\right)^{\frac{1}{2}}\right]} \tag{16}$$

where,

t the age of the concrete in days

s a coefficient which depends on the type of cement:

$= 0.20$, for cement of strength Classes CEM 42,5 R, CEM 52,5 N and CEM 52,5

R (Class R)

$= 0.25$, for cement of strength Classes CEM 32,5 R, CEM 42,5 N (Class N)

$= 0.30$, for cement of strength Classes CEM 32,5 N (Class S)

It is noted that the recommended number of cycles is $N = 10^6$ cycles, which corresponds to k_1
value equal to 0.85.

Alternatively, it is possible to assume the fatigue verification of concrete under compression if

the following criterion is met,

$$\frac{\sigma_{c,max}}{f_{cd,fat}} \leq 0.5 + 0.45 \frac{\sigma_{c,min}}{f_{cd,fat}} \tag{17}$$

$$\leq 0.9 \text{ for } f_{ck} \leq 50 MPa \tag{18}$$

$$\leq 0.8 \text{ for } f_{ck} > 50 MPa \tag{19}$$

where,

$\sigma_{c,max}$	the maximum value of compressive stress at a fibre under the frequent load combination, in which the compression measured positive
$\sigma_{c,min}$	the minimum compressive stress value at the same fibre where $\sigma_{c,max}$ is noted.
The	value is taken equal to zero when $\sigma_{c,min}$ is a tensile stress

3.4 NEN-EN 1992-2+C1:2011 and Dutch National Annex

According to the NEN-EN 1992-2+C1:2011/NB:2016, associated with the design of concrete
bridges, the fatigue resistance of concrete is satisfactory when

$$\sum_{i=1}^{m} \frac{n_i}{N_i} \leq 1 \tag{20}$$

where,

m	the number of considered intervals
n_i	the actual number of cycles at the stress level i
N_i	the ultimate number of constant amplitude cycles in interval "i" that can be carried before failure.

As stated in §6.8.7, the maximum number of compressive loading cycles is obtained by the

following equations,

$$N_i = 10^{14 \frac{1 - E_{cd,max,i}}{\sqrt{1 - R_i}}} \tag{21}$$

$$R_i = \frac{E_{cd,min,i}}{E_{cd,max,i}} \tag{22}$$

$$E_{cd,min,i} = \frac{\sigma_{cd,min,i}}{f_{cd,fat}} \tag{23}$$

$$E_{cd,max,i} = \frac{\sigma_{cd,max,i}}{f_{cd,fat}} \tag{24}$$

where,

R_i	the stress ratio
$E_{cd,min,i}$	the minimum stress level
$E_{cd,max,i}$	the maximum stress level
$f_{cd,fat}$	the design fatigue strength of concrete
$\sigma_{cd,min,i}$	the lower stress in a cycle
$\sigma_{cd,max,i}$	the upper stress in a cycle

Taking into account the regulations of the Dutch National Annex, the design fatigue strength
of concrete is calculated as

$$f_{cd,fat} = k_1 \cdot \beta_{cc}(t_0) \cdot f_{cd} \cdot \left(1 - \frac{f_{ck}}{400}\right) \tag{25}$$

where,

$\beta_{cc}(t_0)$	coefficient for concrete strength at first load application, that is given by the Eq.16
t_0	the starting time of the cyclic loading on concrete in days
k_1	= 1, according to the Dutch National Annex

f_{ck}	the characteristic concrete strength
f_{cd}	$= \frac{f_{ck}}{\gamma_{c,fat}}$, the design concrete strength
$\gamma_{c,fat}$	=1.5, for fatigue of concrete

The aforementioned equations will be employed at a later stage to verify the fatigue of the precast beams in the bridge under investigation. It is noteworthy that the fatigue load models utilized in the assessment of the bridge are analytically presented in Section 5.5.

3.5   fib Model Code 2010

According to the fib Model Code 2010, §7.4.1, the S-N curves for concrete under compression are obtained by the following equation. For $0 \leq S_{cd,min} \leq 0.8$:

(a). if $logN_1 \leq 8$, then $logN = logN_1$

$$logN_1 = \frac{8}{Y-1}(S_{cd,max} - 1) \tag{26}$$

(b). if $logN_1 > 8$, then $logN = logN_2$

$$logN_2 = 8 + \frac{8ln(10)}{Y-1}(Y - S_{cd,min})log\left(\frac{S_{cd,max} - S_{cd,min}}{Y - S_{cd,min}}\right) \tag{27}$$

with,

$$Y = \frac{0.45 + 1.8S_{cd,min}}{1 + 1.8S_{cd,min} - 0.3S_{cd,min}^2} \tag{28}$$

where,

$\sigma_{c,min}$	the minimum compressive stress
$\sigma_{c,max}$	the maximum compressive stress
$S_{c,min}$	$= \frac{\gamma_{Ed}\sigma_{c,min}\eta_c}{f_{cd,fat}}$, the minimum compressive stress
$S_{c,max}$	$= \frac{\gamma_{Ed}\sigma_{c,max}\eta_c}{f_{cd,fat}}$, the design fatigue reference strength for concrete in compression
η_C	an averaging factor considering the stress gradient

In order to account for the stress gradient present in the compression zone of a cracked section

of concrete, the maximum stress is multiplied with a factor η_c that equals:

$$\eta_c = \frac{1}{1.5 - 0.5\,|\sigma_{c1}|\,/\,|\sigma_{c2}|} \tag{29}$$

where,

$|\sigma_{c1}|$ the minimum absolute compressive stress within a 300mm distance

     from the surface under the relevant load combination of actions

$|\sigma_{c2}|$ the maximum absolute compressive stress within a 300mm distance

     from the surface under the relevant load combination of actions

The fatigue reference strength is determined as

$$f_{cd,fat} = 0.85 \cdot \beta_{cc}(t) \cdot f_{ck} \cdot \left(1 - \frac{f_{ck}}{400}\right) / \gamma_{c,fat} \tag{30}$$

where,

f_{ck} the characteristic concrete compressive strength

$\beta_{cc}(t)$ $= e^{s\left[1-\left(\frac{28}{t}\right)^{\frac{1}{2}}\right]}$, the coefficient depending on the age t of concrete in days and

     the beginning of the fatigue loading with,

s depends on the strength class of the cement

t the corrected for temperature age of concrete in days, given by

     $t_T = \sum_{i=1}^{n} \Delta t_i e^{13.65 - \frac{4000}{273+T(\Delta t_i)}}$, with

     Δt_i : the number of days with temperature T

     $T(\Delta t_i)$: the temperature during time period Δt_i

For $S_{cd,min} > 0.8$, the above S-N relation are applying for $S_{cd,min} = 0.8$.

3.6   Proposal by Hans Bongers

Hans Bongers developed a new approach for determining the S-N curves based on NEN-EN
1992-2+C1:2011. This method aimed to address the issues with the S-N curves produced by
earlier Eurocode regulations. However, according to Lantsoght 2014, the proposal has proven
impractical due to difficulties in achieving convergence. In this proposal, the number of loading

cycles is given by Eq.21, which is described by the following expressions,

$$E_{cd,max,i} = \frac{\sigma_{cd,max,i}}{0.9f_{cd} - (0.9f_{cd} - f_{cd,fat})\frac{1}{6}log(N_i)} \text{ for } N_i \leq 10^6 \tag{31}$$

and

$$E_{cd,max,i} = \frac{\sigma_{cd,max,i}}{f_{cd,fat}} \text{ for } N_i > 0^6 \tag{32}$$

3.7   Proposal by Kim & Kim

J.-K. Kim and Y.-Y. Kim 1996 conducted an experimental study to investigate the influence of concrete strength on the fatigue performance of structures. They proposed an expression for the S-N curves in the following manner:

$$S_{max} = -7.6 \left(\frac{f'_c}{f_1}\right)^{0.066} logN_f + 126 \left(\frac{f'_c}{f_1}\right)^{-0.025} \tag{33}$$

where,

N_f the number of loading cycles

f'_c the design compressive strength

f_1 $= 1MPa$

3.8   Proposal by Lantsogth

Two fatigue analysis methods for both new and existing structures have been proposed by Lantsoght 2014. These methods were based on the NEN EN1992-2 regulations, which have been adjusted to align with experimental findings for high-strength concrete. The equations for assessing fatigue behaviour in newly designed structures are identical to those outlined in NEN-EN 1992-2+C1:2011/NB:2016 (Section 3.4). A different proposal is given for the fatigue assessment of existing structures based on which,

(a). for $N_i \leq 10^6$:

$$logN_i = \frac{6(S_{max} - 1)}{S_{max,EC} - 1} \text{ for } S_{max} \geq S_{max,EC} \tag{34}$$

with $S_{max,EC}$ the maximum stress level at 10^6 loading cycles that equals,

$$S_{max,EC} = \left(1 - \frac{f_{ck}}{400}\right)\left(1 - \frac{3}{7}\sqrt{1 - R'_i}\right) \tag{35}$$

(b). for $N_i > 10^6$, the maximum number of compressive loading cycles is calculated using the Eq. 21 to 25 presented in Chapter 3.4.

3.9   Review of the codes and methods

The preceding sections have outlined the various codes and methods employed to verify the fatigue performance of concrete under compression. Upon review, it is clear that many of the parameters that affect the fatigue performance of concrete are taken into account. These variables include the levels of stress applied, concrete strength, type of cement utilised, age of the concrete, strength evolution, and initiation of fatigue loading. Notably, Eurocode regulations incorporate the value of the k_1 factor, and the fib Code Model accounts for the temperature age of concrete, indicating that moisture conditions and temperature are also contemplated in certain codes and proposals.

This study aims to evaluate the fatigue assessment of an inverted T-girder concrete bridge based on the provisions of the NEN-EN 1992-2+C1:2011/NB:2016 code. While this code incorporates most factors that affect the fatigue performance of concrete, it does not consider critical parameters such as time-dependent material degradation due to cyclic loading.

4 Hypothesis

Reviewing the previous chapters, it becomes evident that there are multiple variables that can significantly impact the ability of concrete to withstand compression fatigue. Many of these factors have already been taken into account through existing code provisions and methodologies, as discussed in Section 3.9.

With regards to the structure under investigation and the repeated loads it endures, it is assumed that parameters associated with cyclic loading have already been incorporated into the fatigue load models utilised for bridge fatigue analysis. As will be later discussed in the thesis (Section 5.5), current codes propose specific fatigue loading models that take into consideration the yearly number of loading cycles, the type and dimensions of vehicles, and the contribution of each vehicle to the fatigue damage, simulating the traffic that corresponds to the traffic category of the structure. Therefore, it is believed that parameters such as frequency, rate of application, and rest periods have already been factored into these models.

The existing concrete codes do not consider critical factors, namely the material degradation caused by repeated loading cycles. The concrete's capacity for redistribution is often overlooked because most code provisions are not based on time-dependent material behaviour. Various researchers have addressed this issue by employing path-dependent modelling. For instance, Kindrachuk, Thiele, and Unger 2015 have proposed a constitutive model to describe the cyclic creep effect in concrete under compression. However, the proposed model's complexity can make its application challenging in practical scenarios. Other studies by Maekawa, Toongoenthong, et al. 2006, Maekawa, Gebreyouhannes, et al. 2006 have suggested an embedded into finite element code fatigue model that yields promising results but requires significant computational time. Hence, it is important to have a model that can accurately replicate the material changes and the stress-strain evolution while being applicable to practical problems.

Furthermore, the modelling aspects of Finite Element Analysis (FEA) can significantly influence the fatigue life assessment of concrete, which is often simplified or disregarded in practical applications. Several examples of such simplifications include the selection of load type, calculation of prestress losses, increased rate of traffic loads, modelling of orthotropic properties of the cast

47

in-situ slab, constraining action of regular reinforcement, and relative creep and shrinkage in composite structures. The design and computational time required are integral components of the decisions made in the numerical analysis of the structures, which can significantly impact the fatigue analysis outcomes. Therefore, fatigue analysis must be approached with utmost attention to detail to ensure the accuracy of results.

Excluding the effect of various parameters and oversimplifying the fatigue analysis can lead to inaccurate predictions of the fatigue life of structures. When assessing the concrete fatigue of existing bridges in engineering practice, the fatigue resistance of structural members is often proven insufficient. This leads to the rejection of their structural reliability, even though many of the examined bridges are fully functional and present no evidence of possible collapse. Considering these, this thesis aspires to explore and quantify the influence of various factors and analysis parameters on the fatigue life of inverted T-bridges, with an emphasis on modelling aspects and material degradation. Specifically, the investigated parameters that are part of this thesis scope are:

- the calculation of prestress losses,

- the increase in traffic rate,

- the cracking of the slab,

- the type of applied loads,

- the position of fatigue loads on the bridge deck,

- the fatigue load model,

- the relative creep and shrinkage of the composite structure and

- the material degradation due to cyclic creep.

The selection of the aforementioned parameters was based on the premise that they could potentially have a positive impact on the fatigue life of the bridge if a more comprehensive approach is followed during their analysis. In fact, starting from the calculation of the prestress losses, engineers tend to opt for a rough estimation of prestress losses, which can lead to an over-

estimation of losses. These losses, in turn, substantially contribute to the stress distribution and, consequently, to the fatigue life of the bridge. This thesis endeavours to investigate how a more detailed calculation can influence the fatigue of concrete. As stated, the load modelling simplifications in the Finite Element Analysis are anticipated to impact fatigue as they affect the distribution of forces within the structure. This research also evaluates the accuracy of the traffic conditions modelling. In engineering practice, simpler load models are often preferred, requiring less design and computational time. However, such considerations can be conservative and significantly underestimate the fatigue life of the structure. Accounting for material degradation caused by cyclic loading is expected to positively influence fatigue. The repetition of loads can modify material properties over the cross-section, leading to a redistribution of stresses. Lastly, parameters such as the cracking of the slab in the transverse direction can influence the load distribution and, by extension, the concrete fatigue. It is expected that this factor will have a significant impact on the fatigue performance of the structure, the magnitude of which is investigated in this parametric study. These factors will be analytically presented in Chapter 7.

Summarizing, the study of the above parameters on the fatigue life of concrete aims for a more accurate and sustainable fatigue assessment, which will comply with the current code regulation without being overly conservative.

5   Case study

5.1   Case study

The central objective of this study is to assess the compressive fatigue of prestressed concrete beams utilised in girder bridges. Girder bridges consist of precast concrete beams arranged in a parallel configuration while maintaining a constant centre-to-centre distance. The beams are interconnected at their edges by diaphragm beams, and the primary structure is finalised by adding the cast in-situ slab at the top of the beams.

A special case study was designed to investigate the influence of the examined parameters on the concrete fatigue life. The case study centred on a precast, inverted T-beam concrete bridge that was specifically designed to fail in fatigue within its lifespan. It is important to note that bending failure at the beam midspan is the failure criterion for this study, whereas shear is deemed irrelevant and is thus beyond the scope of the investigation.

It is considered that the structure was built in 1974, making the bridge relatable to actual cases that are investigated for their structural integrity. Being in service for approximately 50 years, the bridge is assessed to determine its remaining life. The assumed timeline of its erection was intentionally chosen to align with the objective of this research (Figure 5.1). Specifically, ten days after the casting of the beams ($t_0 = 0$ days), the concrete had developed sufficient strength and the prestressing tendons were cut, transferring the prestressing force to the beams. Then, the beams were transferred to the site, where the casting of the top slab took place 28 days after the beam casting. The fatigue loading started at 56 days, after the strength of the cast in-situ slab had fully developed. Although fatigue loading usually occurs later in most practical cases, the chosen timeline was deliberate to ensure that the bridge would fail within its anticipated lifespan. However, it is worth mentioning that keeping the initiation of fatigue loading constant in the fatigue analyses of the beams does not impact the study results related to the investigated parameters.

In order to have a better understanding of the analysed factors' impact, complex geometries have been avoided, and the structure was designed as a simply supported single-span bridge,

which crosses that undergoing road at a 90°angle.
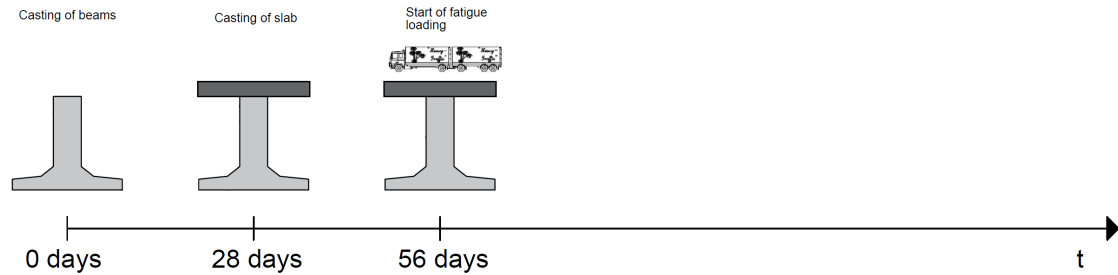
Figure 5.1: Timeline of the bridge erection process and start of the fatigue loading

The selection of starting points and design details has often been based on the codes and guidelines:

- Eurocode: NEN-EN 1990:2002/A1:2006/C2:2010, NEN-EN 1990+A1+A1/C2:2019/NB:2019, NEN-EN 1991-1-1:2002/C1:2009, NEN-EN 1991-1-1+C1+C11:2019/NB:2019, NEN-EN 1991-2:2003/C1:2010, NEN-EN 1991-2+C1:2015/NB:2019, NEN-EN 1992-1-1:2005/C2:2010, NEN-EN 1992-1-1+C2:2011/NB:2016+A1:2020, NEN-EN 1992-2:2005/C1:2008 and NEN-EN 1992-2+C1:2011/NB:2016

- Richtlijnen Ontwerp Kunstwerken (ROK) - Guidelines for the Design of Structures: RTD 1001: 2021 2.0 and RTD 1010:2019-2.0

- Richtlijnen Beoordeling Kunstwerken (RBK) - Guidelines for the Assessment of Existing Structures: RTD 1006:2022-1.2.1

- NEN 8701: NEN 8700:2011+A1:2020 and NEN 8701:2011+A1:2020

5.2   Bridge geometry

The dimensions of the bridge were selected based on practical cases. To begin with, the bridge length is established considering the size of the obstacle that we need to traverse, and for this case, it was set at 30 meters. In simply supported structures, the span length is determined as the centre-to-centre distance (ctc) between the supports. For this bridge, the supports were

positioned at a distance of $l_{cantilever} = 0.5$ m, forming cantilevering sections at the edges of each beam, as depicted in Figure 5.2. As a result, the span length of the beams is $l_{span} = 29$ m.
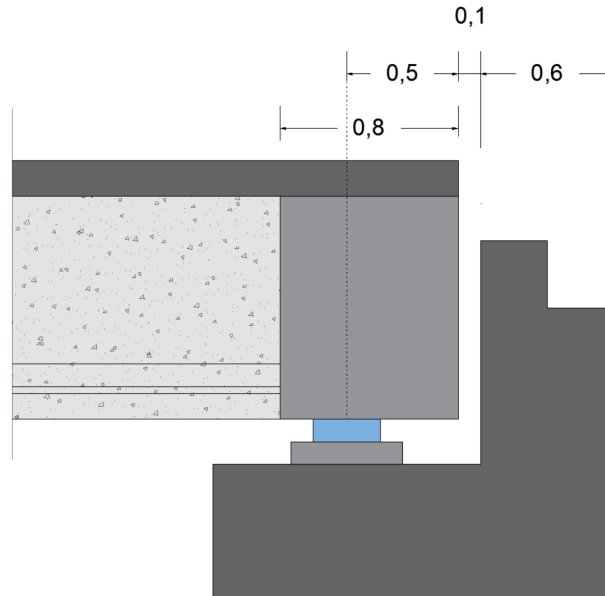
Figure 5.2: Geometry of the bridge above the supports

The width of the bridge, on the other hand, is defined as the distance between the bridge's free edges, perpendicular to its length, and it is determined by the lane configuration and the additional distances considered. The road configuration of the examined bridge features two traffic lanes and an emergency lane. Standard traffic lanes have a width of 3.5 m, while emergency lanes are 3.7 m wide. In addition, according to the guidelines outlined in the RWS Informatie, 'Richtlijn Ontwerp Autosnelwegen - Veilige Inrichting van Bermen,' a minimum distance of 0.5 m must be present between the side of the emergency lane and the right-side guide rail. On the left side, the minimum distance between the side of the road and the guide rail is 1.5 m. Additional distances of 1.4 m are added to the bridge sides, as illustrated in Figure 5.3 (excluding the cosmetic side facing). The total required width of the bridge is then calculated as,

$W_{required} = 2 * 3.5 + 3.7 + 0.5 + 1.5 + 2 * 1.4 = 15.5 m$
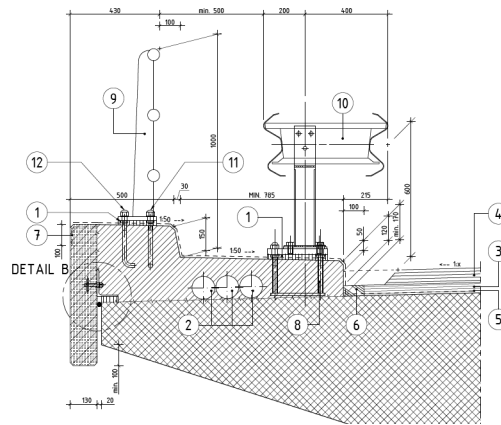
Figure 5.3: Cross-section of the edge structure (the cosmetic element 7 is not accounted for in the edge distance). RTD 1010:2019-2.0

The final width of the bridge was defined by the number and geometry of the precast beams. Taking into account the date of the bridge's erection, the beam profile was chosen from edition Nr. 2.2.1 of the Spanbeton Bulletin technical series. The structure was built using a HIP beam profile produced by Spanbeton, presented in Figure 5.4. The beams maintain a 1.2 m centre-to-centre distance, which is parted by a beam flange width of 1180mm and an intermediate distance of 20mm between the flanges. To support the width of the bridge, 13 beams were utilised, as illustrated in Figure 5.5. This way, the width of the bridge is finally determined as (Figure 5.6),

$$W_b = 13 * 1.18 + 12 * 0.02 = 15.58m$$

It is considered that the lane configuration of the bridge has remained constant throughout its service life.
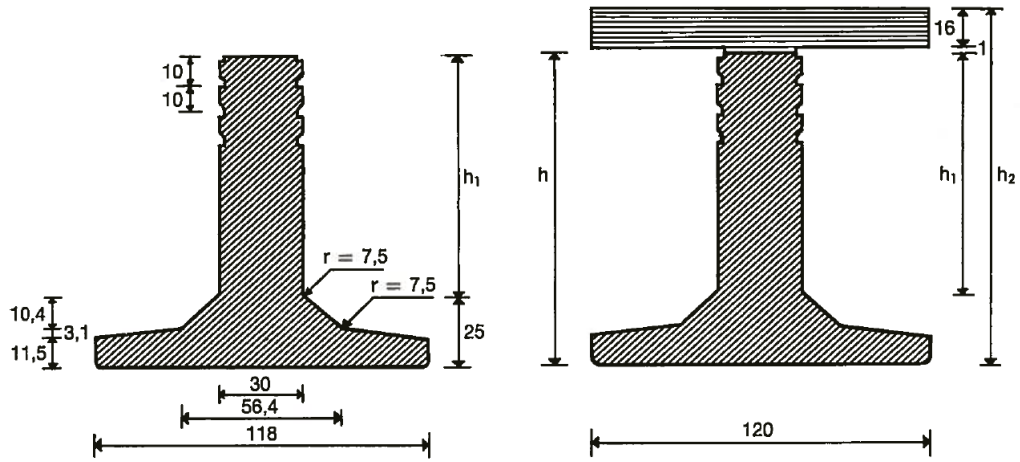
Figure 5.4: (a). Cross-section of the HIP beam profile, (b). Cross-section of the composite beam. (Nr. 2.2.1 of the Spanbeton Bulletin technical series)
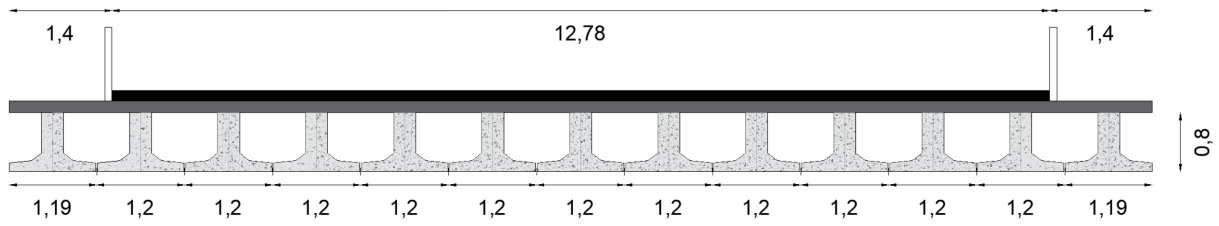
Figure 5.5: Cross-section of the bridge
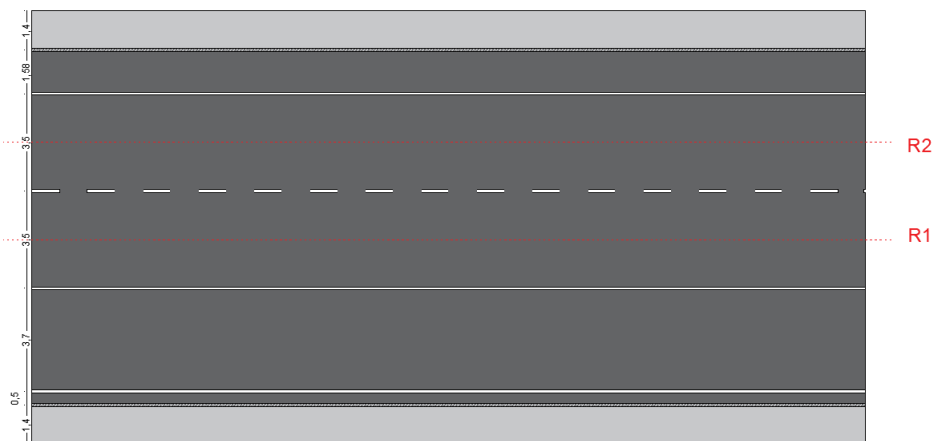
Figure 5.6: Road configuration of the investigated bridge

The beam height and the prestressing strands' number were selected based on the following criteria:

- A preliminary check was conducted according to the previous Dutch code to ensure that the original bridge's design satisfies the stress control and bending moment resistance checks (Appendix B).

- In the Ultimate Limit State (ULS), the occurring bending moments at the beams are lower than their bending moment capacity. The bending moment resistance of the beams is verified based on current code regulations (Appendix E).

- The structure fails due to fatigue of concrete under compression within its service life.

The above criteria were satisfied for the beam profile with height $H_b = 810mm$. For the prestressing, $25\varnothing12.5$ ($A = 93mm^3$) strands are used, having the configuration depicted in Figure 5.7.
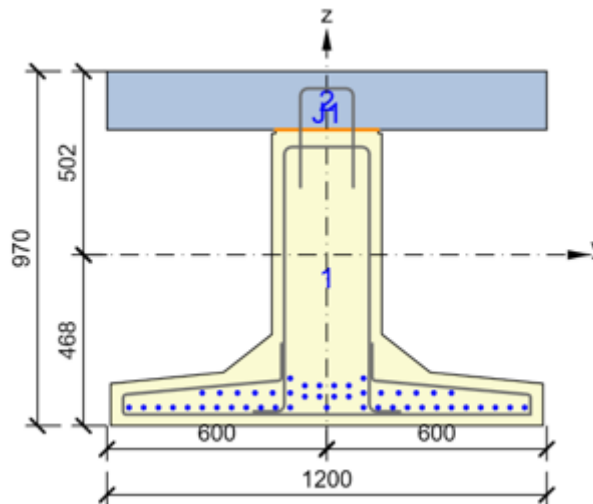
Figure 5.7: Prestressing strand configuration at the midspan of the precast beams (image generated by IDEA Statica).

In older bridge designs, the thickness of the cast in-situ slab was thinner compared to new structures. Following the edition Nr. 2.2.1 of the Spanbeton Bulletin technical series, the slab thickness was chosen equal to 160 mm. At the top of the slab, an asphalt layer is poured, for

which the minimum value of thickness is calculated based on RTD 1001: 2021 2.0 as,

$$H_a = (140 + a) \qquad (36)$$

with

$$a = \frac{L - 30}{4}, \text{ for } 0 \le a \le 30mm \qquad (37)$$

where,

L	the size of span in m
a	spacing in mm

Therefore, in this case study (L_{span} = 29 m), the thickness of the asphalt layer is chosen equal to the minimum value, namely 140mm.

As illustrated in Figure 5.2, transverse beams are cast at the edge of the beams, with a width equal to 0.8m. Finally, self-supporting prestressed edge structures are used at the free edges of the bridge, as presented in Figure 5.8. Since the structures are self-carrying, they do not contribute to the loading, and neither are included in the Finite Element Model, as will later be discussed in the thesis.
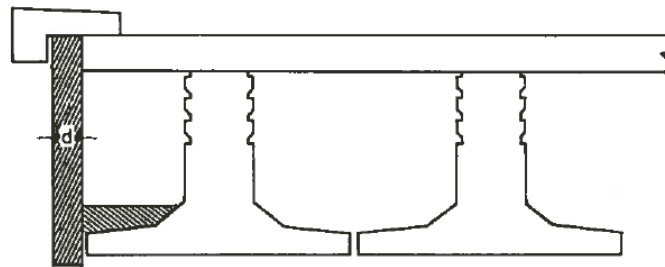
Figure 5.8: Self-supporting edge structure (Nr. 2.2.1 of the Spanbeton Bulletin technical series).

5.3   Supporting conditions

The boundary conditions of a bridge can significantly impact its internal force and stress distribution. The investigated case study examines a simply supported bridge that utilizes discrete

bearing pads to support its beams. These bearing pads consist of either natural rubber or neoprene and are reinforced with steel plates, which increase the bearing's compressive and rotational stiffness. While the bearing pads permit horizontal movement of the deck through the shear deformation of the rubber, it is important to note that such movements are restricted by their stiffness in those directions. Nonetheless, these bearing pads provide several advantages, such as their resistance to corrosion, cost-effectiveness, and minimal maintenance requirements. The dimensions of the bearing pads used for the support of this structure are:

$(length \cdot width \cdot thickness) = (400 \cdot 300 \cdot 80)mm$
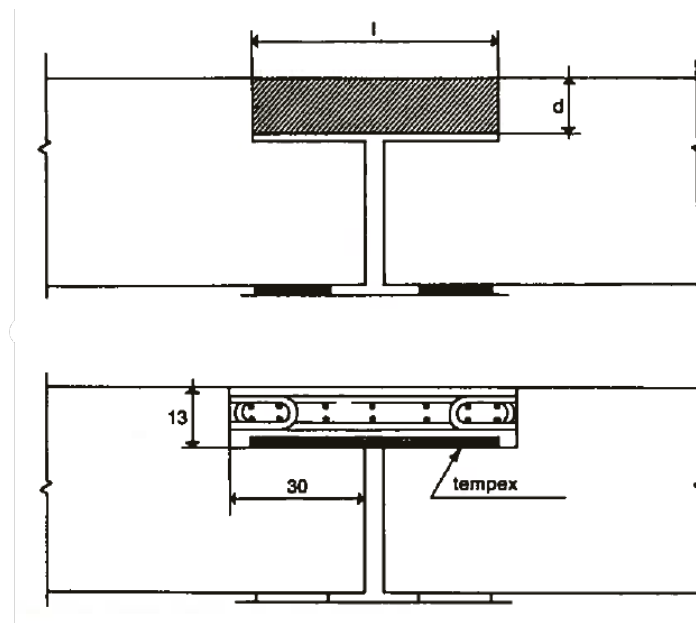
Figure 5.9: Support detail of simply supported deck (Nr. 2.2.1 of the Spanbeton Bulletin technical series).

5.4   Materials

The bridge is a composite structure that comprises several structural components. For the construction of these, different materials have been utilised. Starting from the concrete components, the concrete classes were determined according to the RTD 1001: 2021 2.0 guidelines as follows,

- Prefabricated beams: C55/67

- Cast in-situ slab: C25/30

- Cast in-situ cross beams: C35/45

The prestressing forces are applied through pre-tensioned steel strands featuring a steel grade of FeP 1860. Finally, a FeB500 (=B500B) steel grade was used for the normal reinforcement of the reinforced concrete slab and the shear reinforcement of the precast beams.

5.5   Loads

5.5.1   Introduction

The analysis of the structural integrity of the structures investigates their capacity to withstand different types of loads and load combinations throughout their lifespan. Accurate estimation of the magnitude of these loads is an important component of the analysis process. European and national codes provide design models and guidelines that assist in this regard.

The action of moving vehicles produces stress gradients that may eventually cause fatigue of the structural components. In this investigation, the failure criterion is the bending failure at the midspan of the precast beams comprising the bridge. Based on this criterion, the fatigue analysis of concrete beams is performed after having verified their cross-section capacity. The bending moment capacity at the Ultimate Limit State (ULS) evaluates the bridge's capacity to withstand the permanent and variable loads applied to the structure. The live loads used for the bending moment resistance of the bridge are described in the traffic Load Model 1. The results of this analysis are presented in Appendix E. Subsequently, the fatigue life of the precast beams is then examined using the Fatigue Load Models described in the following sections.

Regarding other types of loads, the action of thermal loads can be expressed as imposed deformations. In the analysis of statically determined structures, it is generally assumed that thermal component-induced deformation can occur freely without causing additional stress. Even though this assumption holds true to some extent, in the case of simply supported bridges, the horizontal movement is partially constrained due to the stiffness of the discrete bearings used for support. For the purpose of this investigation, it is considered that the supports can fully accommodate the deformation of the bridge deck in the horizontal longitudinal direction. As the structure is not simply supported in the transverse direction, horizontal deformation cannot be fully developed. However, thermal loads have a relatively low frequency compared to traffic loads and are

thus excluded from the fatigue analysis. It is also worth noting that impact loads and variable wind loads have a negligible impact on concrete fatigue and are thus not taken into account in the fatigue assessment.

5.5.2   Dead loads

Concrete self-weight

The self-weight of the concrete structural components is automatically calculated by the software used for the global analysis (Diana FEA), taking into account the dimensions of each member. According to NEN-EN 1991-1-1:2002/C1:2009, the value of concrete self-weight is $24kN/m^3$ for unreinforced concrete and $25kN/m^3$ for reinforced and prestressed concrete. It is noted that the default value used in Diana FEA for the acceleration of gravity is equal to $9.81m/s^2$.

Asphalt layer dead load

As previously stated (Section 5.2), the cast in-situ concrete slab is covered by an asphalt layer having a $140mm$ thickness. Accounting for the weight of the asphalt, which equals $23kN/m^3$, the resulting permanent load is calculated as:

$23kN/m3 * 0.14m = 3.22kN/m^2$

Additional dead weight

Additional permanent loads are caused by the elements of the edge structure presented in Figure 5.8. As mentioned above, the prestressed edge structure is self-supported and does not cause additional loads on the bridge. However, it is considered that the load of the concrete corner detail is entirely taken by the concrete slab. By considering the dimensions provided in Figure 5.10 and accounting for the self-weight of the unreinforced concrete, the dead load of the corner structure is

$0.1m^2 * 24 = 2.4kN/m.$
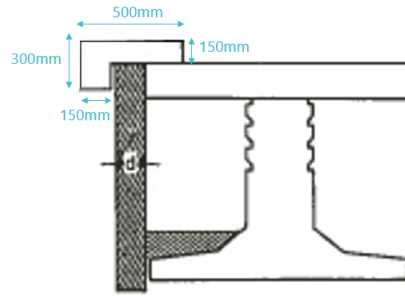
Figure 5.10: Dimensions of the edge structure's concrete concrete corner detail (Nr. 2.2.1 of the Spanbeton Bulletin technical series).

Other structural details, such as traffic barriers and handrails, contribute to the loading of the bridge, for which the loads are equal to $1kN/m$ and $0.5kN/m$, respectively. This way, the total load applied at the free edges of the top slab is $3.9kN/m$.

Finally, as illustrated in Figure 5.10, concrete is poured into the space between the inverted T-beams and the self-supporting edge structures, resulting in additional weight on the system. It is considered that the total load of this element is applied on the edge of the beam flange and is accounted for in the bridge analysis by applying a line load and distributed moment to the base of the modelled edge beams. Their values are calculated as follows,

$A_{con} = (318 * 140) + (0.5 * 132 * 104) + (0.5 * 318 * 31) = 56313mm^2$

$q_{con} = 0.0563m^2 * 24kN/m^3 = 1.35kN/m$

$M_{con} = 1.35kN/m * 0.59m = 0.797kNm/m$

5.5.3   Prestress

As outlined in Chapter 5, The precast beams were prestressed using 25 pretensioned strands made of steel class FeP1860, with a diameter of $\varnothing12.5$ ($A = 93mm^2$). The prestressing strand configuration depicted in Figure 5.7 refers to the midspan of the beam, consisting of both straight and deflected strands. For the deflected stands, the push-down points are located at $1/3$ and $2/3$ of the beam length, as illustrated in Figure 5.11. The prestressing was conducted by applying the maximum allowable prestress, which, according to RTD 1006:2022-1.2.1, equals $1394N/mm^2$ after the immediate losses. It should be noted that the strand configuration at the beam edges

is not presented, as the internal forces and stress distribution at the edges of the beams are deemed irrelevant to the scope of this thesis.
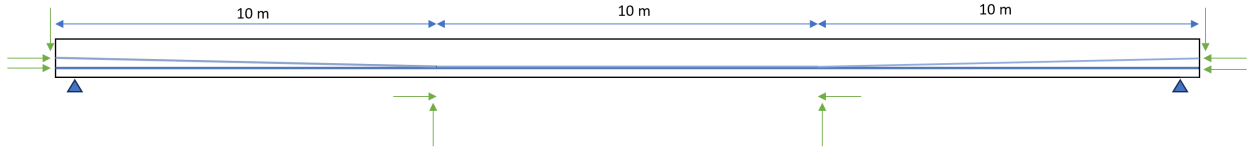
Figure 5.11: Prestressing stand profile - Push-down points.

To calculate the prestressing effect, the strand geometry and configuration, initial prestress, and prestress losses were input into the cross-sectional model created in IDEA Statica. This approach allowed for the automatic calculation of internal forces and stress distribution resulting from the prestress during cross-sectional analysis. An analytical calculation of the prestress losses used in the parametric study is presented in Appendix F.

5.5.4   Live loads

5.5.4.1   Introduction

Traffic loads on bridges are influenced by various factors such as the bridge composition and type, traffic density, and vehicle types that use the bridge. To accurately analyse these structures, loading models that account for these variables and align with the specific traffic conditions of the bridge in question are necessary.

For the present case, the structure is a long-distance highway bridge, categorised under traffic class 1 for roads with at least two traffic lanes per direction and high flow rates for heavy vehicles. Given that one of its two lanes is considered a slow lane, the anticipated number of heavy vehicles per slow lane for bridges of this traffic category is $2.0 * 10^6$ (Table 5.1).

Table 5.1: Number of heavy vehicles annually expected per slow lane (NEN-EN 1991-2:2003/C1:2010)

	Traffic categories	N_{obs} per year and per slow lane
1	Roads and motorways with 2 or more lanes per direction with high flow rates of lorries	$2{,}0 \times 10^6$
2	Roads and motorways with medium flow rates of lorries	$0{,}5 \times 10^6$
3	Main roads with low flow rates of lorries	$0{,}125 \times 10^6$
4	Local roads with low flow rates of lorries	$0{,}05 \times 10^6$

According to NEN 8701:2011+A1:2020, Fatigue Load Models 1, 4, and 5 are utilised to conduct fatigue analysis of concrete structures. Since no recorded traffic data exists describing the moving loads applied on the bridge, only models 1 and 4 will be employed to ascertain the fatigue life of the precast beams.

5.5.4.2 Notional lanes

To represent the action of traffic loads on the structure, the carriageway is initially divided into notional lanes. The number and width of these lanes are determined in accordance with NEN-EN 1991-2:2003/C1:2010, §6.2.3, as described in Table 5.2.

Table 5.2: Number and width of notional lanes (NEN-EN 1991-2:2003/C1:2010)

Carriageway width w	Number of notional lanes	Width of a notional lane w_l	Width of the remaining area
$w < 5{,}4$ m	$n_1 = 1$	3 m	w - 3 m
$5{,}4$ m $\leq w < 6$ m	$n_1 = 2$	$\dfrac{w}{2}$	0
6 m $\leq w$	$n_1 = Int\left(\dfrac{w}{3}\right)$	3 m	$w - 3 \times n_1$
NOTE For example, for a carriageway width equal to 11m, $n_1 = Int\left(\dfrac{w}{3}\right) = 3$, and the width of the remaining area is 11 - 3×3 = 2m.			

Following the division of the carriageway into distinct lanes, each lane is assigned a specific number and position that will have the most significant adverse impact on the structure. Lane

1 is identified as having the most unfavourable influence, followed by Lane 2 and subsequent lanes. An illustration of lane numbering can be observed in Figure 5.12.
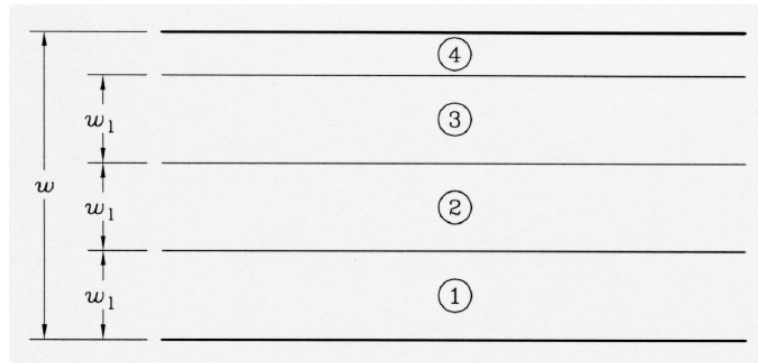
Key
w Carriageway width
w_l Notional lane width
1 Notional Lane Nr. 1
2 Notional Lane Nr. 2
3 Notional Lane Nr. 3
4 Remaining area

Figure 5.12: Example of the numbering of notional lanes (NEN-EN 1991-2:2003/C1:2010)

However, for the fatigue analysis of bridges, the lane configuration and numbering are determined based on the anticipated traffic loads in normal operating conditions.

5.5.4.3   Concentrated loads dispersal

According to NEN-EN 1991-2:2003/C1:2010, §6.3.6, the concentrated loads applied on the bridge should be dispersed horizontally through the cover layer and the concrete slab until reaching the level of the central axis of the slab. This distribution of loads should be achieved through a one-to-one spread-to-depth ratio, as illustrated in Figure 5.13.
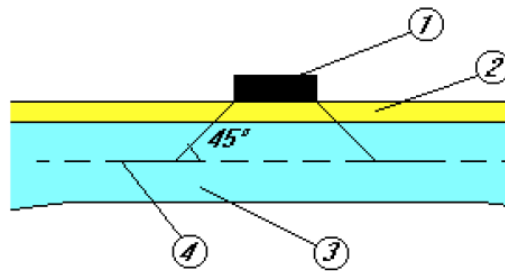
Key
1   Wheel contact pressure
2   Pavement
3   Concrete slab
4   Middle surface of concrete slab

Figure 5.13: Dispersal of concentrated loads (NEN-EN 1991-2:2003/C1:2010).

5.5.4.4   Load model 1

Load Model 1 is composed of both concentrated and uniformly distributed loads, which reflect the majority of traffic vehicles, including cars and lorries. It incorporates two loading systems, namely the Tandem System (TS) featuring double-axle concentrated loads and the Uniformly Distributed Loads (UDL). The characteristic values of the aforementioned loads are presented in Table 5.3.

Table 5.3: Characteristic values of traffic Load Model 1 (LM1) (NEN-EN 1991-2:2003/C1:2010)

Location	Tandem system *TS*	UDL system
	Axle loads Q_{ik} (kN)	q_{ik} (or q_{ik}) (kN/m^2)
Lane Number 1	300	9
Lane Number 2	200	2,5
Lane Number 3	100	2,5
Other lanes	0	2,5
Remaining area (q_{rk})	0	2,5
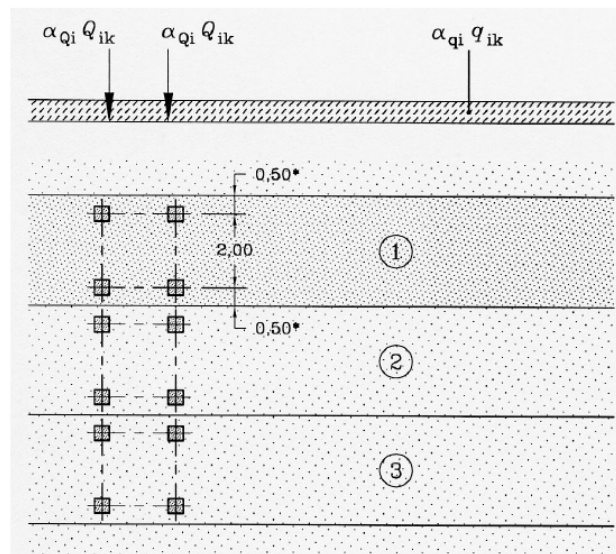
Key
(1) Lane Nr. 1 : Q_{1k} = 300 kN ; q_{1k} = 9 kN/m^2
(2) Lane Nr. 2 : Q_{2k} = 200 kN ; q_{2k} = 2,5 kN/m^2
(3) Lane Nr. 3 : Q_{3k} = 100 kN ; q_{3k} = 2,5 kN/m^2
* For w_l = 3,00 m

Figure 5.14: Application of traffic Load Model 1 (NEN-EN 1991-2:2003/C1:2010).
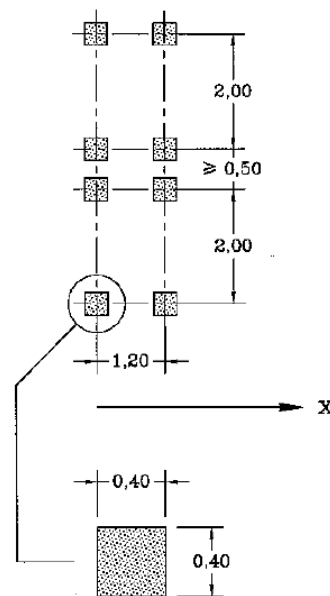
Figure 5.15: Application of tandem systems for traffic Load Model 1 (NEN-EN 1991-2:2003/C1:2010).

According to the guidelines of the Dutch National Annex NEN-EN 1991-2+C1:2015/NB:2019, correction factors are necessary to be applied to modify the loads of each lane. The lane bearing the heaviest load requires an adjustment factor of $a_{q1} = 1.15$, whereas, for the remaining lanes, the correction factor differs based on the number of theoretical lanes. In the case of two theoretical lanes, the correction factor employed is $a_{q2} = 1.0$, while for more than two lanes, it is $a_{q2} = 1.4$.

5.5.4.5   Fatigue Load model 1

According to NEN-EN 1991-2:2003/C1:2010, §4.6.1, Fatigue Load Model 1 (FLM1) is derived from Load Model 1, described in the previous section. This model's axle load values are equal to $0,7Q_{ik}$, while equivalent values for the uniformly distributed loads are given as $0,3q_{ik}$. By evaluating all possible loading configurations and taking into account the effect of simultaneously loaded lanes, the model determines the maximum and minimum stress levels required for fatigue analysis. It is worth noting that FLM1 is generally considered a conservative model and is primarily applied to determine whether the fatigue life tends to be unlimited when given a constant stress amplitude fatigue limit. Therefore, This model is deemed suitable for steel structures but not other materials.

5.5.4.6   Fatigue Load model 4b

The Fatigue Load Model 4 (FLM4) comprises a series of heavy vehicles that, when combined, simulate the effects of actual vehicles in the corresponding traffic category. To comply with the Eurocode and Dutch codes, the fatigue analysis of concrete structures must be based on the equivalent lorries of Fatigue Load Model 4b, presented in Table 5.4. Each heavy vehicle in this model is defined by its axle loads, the number and spacing of its axles, as well as the contact areas and configuration of its wheel types, illustrated in Figure 5.16.

Table 5.4: Fatigue Load Model 4b for concrete structures - Set of equivalent lorries (NEN-EN 1991-2+C1:2015/NB:2019)

Type voertuig			Verkeerstype			
Afbeelding van de vrachtwagen	Afstand tussen de assen m	Gelijkwaardige aslast kN	Lange afstand % [a]	Middellange afstand % [a]	Lokaal verkeer % [a]	Wiel-type
	4,5	70 130	20,0	50,0	80,0	A B
	1,50 2,40 1,30	70 120 120 120	7,0	4,0	4,0	A C B B
	3,20 5,20 1,30 1,30	70 130 100 100 90	37,0	20,0	5,0	A B C C C
	3,40 6,00 1,80	70 140 90 90	20,0	12,0	4,0	A B C C
	4,80 3,60 4,40 1,30	70 150 80 80 70	10,0	10,0	5,0	A B C C C
	3,20 1,30 4,40 1,80 1,80	80 160 100 100 100 100	4,5	3,0	1,5	A B C C C C
	3,20 1,40 4,40 1,30 1,30 1,30	70 180 170 80 80 80 90	1,5	1,0	0,5	A B B C C C C
[a] Percentage vrachtwagens.						

The calculation of the contribution of each lorry type to the concrete fatigue takes into account the lorry percentage, which is determined based on the traffic type of the structure being assessed. The total number of heavy vehicles expected to travel annually in the slow lane of the corresponding traffic category is then multiplied by this percentage.
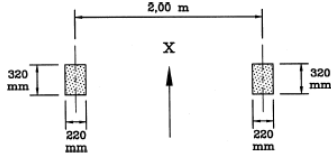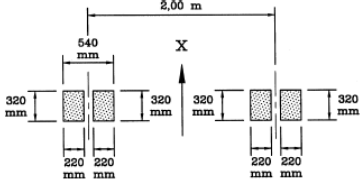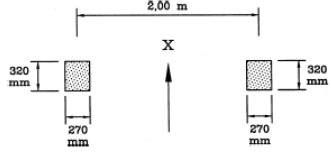
WHEEL/ AXLE TYPE	GEOMETRICAL DEFINITION
A	
B	
C	

Figure 5.16: Geometrical definition of wheels and axles (NEN-EN 1991-2:2003/C1:2010).

As per NEN-EN 1991-2+C1:2015/NB:2019, the fatigue analysis must also consider the presence of heavy vehicles in adjacent lanes. For bridges with traffic moving in the same direction, heavy vehicles are present on both lanes simultaneously in 10% of cases. The fatigue analysis of concrete structures, according to RTD 1006:2022-1.2.1, employs the equivalent trucks of FLM4b for the slow lane and the third vehicle of T0066 of the RTD 1001: 2021 2.0 for the loading of the adjacent lane (Table 5.5).

Table 5.5: Table T0066 from ROK - Set of equivalent lorries (RTD 1001: 2021 2.0)

Voertuig-type	Asafstand [m]	Equivalente aslast [kN]	Wieltype	Equivalent voertuiggewicht [kN]	Aantal per jaar
1	4,50	70 130	A B	200	750.000
2	4,20 1,30	70 120 120	A B B	310	600.000
3	3,20 5,20 1,30 1,30	70 150 90 90 90	A B C C C	490	600.000
4	3,20 1,30 4,40 1,30 1,30 1,30 1,30	70 90 70 70 70 70 70 70	A C A A A A A A	580	230.000
5	1,50 2,40 1,30 9,50 1,30 1,30 1,30	70 70 170 160 70 70 70 70	A A B B A A A A	750	66.000
6	1,70 3,30 1,30 3,50 3,50 1,30	70 70 180 190 70 180 190	A A B B A B B	950	3.100
7	2,40 1,30 5,50 1,30 1,30	170 170 200 180 180 190	B B B B B B	1.090	500
8	2,50 1,30 5,20 1,30 1,30 1,30	130 160 170 220 200 170 170	B B B B B B B	1.220	200
9	1,40 2,60 1,30 6,10 1,90 1,90	130 130 180 180 220 220 220	B B B B B B B	1.280	100
10	2,40 1,30 1,30 9,50 1,30 1,30 1,30	90 90 240 220 200 180 190 200	C C B B B B B B	1.410	100

5.5.5   Combinations

5.5.5.1   Structural reliability

The structures are categorised into five consequence classes to evaluate the potential impact of their failure on human life, injuries, and losses in social, economic and environmental domains. According to the regulation of NEN-EN 1990:2021, Table A.2.1 (NDP) (B), bridges that constitute part of the national infrastructure are classified as consequence class 3. In the event of such structures failing, the consequences could be severe in the aspects mentioned above. Furthermore, considering the consequence class of the structures being assessed and referring to Table A.2.2 (NDP), the expected service life is set at 100 years.

5.5.5.2   Load factors and combination factors

According to NEN-EN 1990:2002/A1:2006/C2:2010, §6.4, the structures are examined for Ultimate Limit State (ULS) based on the following equations:

(6.10a):

$$\sum_{j \geq 1} \gamma_{G,j} G_{k,j} \;"+" \; \gamma_P P \;"+" \; \gamma_{Q,1} \psi_{0,1} Q_{k,1} \;"+" \; \sum_{i > 1} \gamma_{Q,i} \psi_{0,i} Q_{k,i} \tag{38}$$

(6.10b):

$$\sum_{j \geq 1} \xi_j \gamma_{G,j} G_{k,j} \;"+" \; \gamma_P P \;"+" \; \gamma_{Q,1} \psi_{0,1} Q_{k,1} \;"+" \; \sum_{i > 1} \gamma_{Q,i} \psi_{0,i} Q_{k,i} \tag{39}$$

where,

Gk,j	the characteristic value of permanent load j,
P	the representative value of prestressing force,
$Q_{k,1}$	the characteristic value of predominant variable load, and
$Q_{k,i}$	the characteristic value of the secondary variable load i.

As per the provisions of EN 1991, the combination used to assess fatigue action is

$$\left(\sum_{j\geq 1} G, jG_{k,j} \; "+" \; P \; "+" \; \psi_{1,1}Q_{k,1} \; "+" \; \sum_{i>1} \psi_{2,i}Q_{k,i}\right) \; "+" \; Q_{fat} \tag{40}$$

where,

Q_{fat} the relevant cyclic load j

Load factors

According to RTD 1006:2022-1.2.1 the load factors are:

$\gamma_{G,j,sup}$ $=1.25$,

$\xi\gamma_{G,j,sup}$ $=1.15$,

$\gamma_{Q,traffic}$ $=1.25$.

Combination factors

The combination factors are determined by referring to table NB.9 - A2.1 of NEN-EN 1990:2002/A1:2006/C2:20...
as follows,

Table 5.6: Combination factors

Load case	ψ_0	ψ_1	ψ_2
Traffic loads - LM1 - vertical	0.8	0.8	0.4

5.5.5.3 Load combinations

The loads mentioned earlier have been calculated in order to assess the cross-sectional capacity of the structure. This has been accomplished by analyzing the bridge model for the load configurations specified in Appendix E. It should be noted that the structure under investigation corresponds to consequence class 3 and, as such, is subject to the load combinations presented in Table 5.7.

Table 5.7 also provides the load combination that has been utilised for the fatigue analysis of the bridge. This combination takes into account the action of permanent dead loads, prestressing,

and variable loads of the fatigue load models (Chapter 5.5). It is important to note that the fatigue analysis combination does not include the traffic loads of Load Model 1 due to the different frequencies of the variable traffic and fatigue load models.

Table 5.7: Load combinations

Ultimate Limit State (ULS) - Bending moment resistance	
6.10a - gr1a	$1.25 \cdot G_k + P + (\psi_0 = 0.8) \cdot 1.25 \cdot Q_k$
6.10b - gr1a	$1.15 \cdot G_k + P + 1.25 \cdot Q_k$
Fatigue loads	
	$G_k + P + Q_{fat}$

6   Finite Element Analysis (FEA)

6.1   Fatigue analysis procedure

In order to assess the influence of various parameters and analysis aspects on the fatigue life of the bridge, a specific analysis procedure is selected and followed for each individual beam. Both analytical and numerical methods are employed for the fatigue analysis process. This chapter will focus on explaining the process used for the fatigue assessment and outline the numerical considerations used in both the global and cross-sectional analysis models. The process comprises the following three parts: global linear analysis of the bridge, cross-sectional non-linear analyses at the midspan of the beams, and calculation of the fatigue life of the beams, as depicted in the workflow of Figure 6.1.
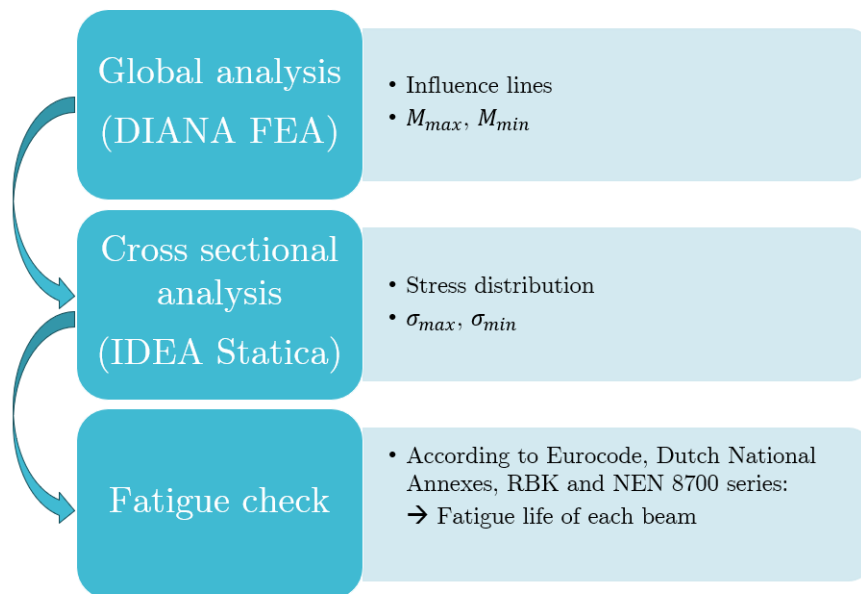
Figure 6.1: Workflow of the analysis process.

The global linear analysis of the bridge is carried out using the DIANA Finite Element Analysis software, in which the bridge is modelled based on the analysis aspects described in the subsequent sections. Once the bridge model is complete, fatigue load models presented in Chapter 5.5 are utilised to simulate the impact of heavy vehicles on the bridge. As these fatigue load model trucks traverse the bridge deck, the resulting bending moment values at the midspan of

each beam are used to form the influence lines of each load combination on the girders.

These influence lines provide the maximum and minimum bending moments (M_{max}, M_{min}), which are then input into the cross-sectional analysis. The values are used in each beam's non-linear, cross-sectional analysis using the software IDEA Statica to provide the stress distribution at the midspan of the beams.

As previously mentioned (Section 1.1), the critical stress values at the girder bridges are noted at their top compressive fibre. The cross-sectional analysis results in the stress levels $(\sigma_{max}, \sigma_{min})$ that are finally utilised to calculate the fatigue life of the beams following the code regulation outlined in Chapter 3.4. It is worth noting that the fatigue life of the bridge is determined by the fatigue life of the bridge beams and not the fatigue behaviour of the rest of the structural components.

The selection of DIANA FEA software was primarily based on its ability to accurately simulate the bridge geometry, material properties, supporting conditions, and types of loads applied to the structure. With its multiple modelling options, it was able to evaluate various design options and determine the most appropriate design decisions for this investigation. Additionally, the software's spacial functions allowed for an accurate representation of the bridge geometry while simplifying the analysis model, resulting in significant design and calculation time savings. This feature can also be used to model the variation of properties over the beam height, which may occur due to material degradation caused by cycling loading. Lastly, programming can be employed to create all necessary load cases required to easily model the live loads.

6.2   Global analysis

6.2.1   Modelling of structural components

6.2.1.1   Precast beams

For the modelling of the precast beams, various element types and design options were examined prior to selecting the final design. The analytical comparison between different beam designs is presented in Appendix C. Several factors, such as design and calculation time, bridge design accuracy, cross-sectional property representation, and analysis results, were taken into account

to make an informed decision. Ultimately, shell elements were selected to model the precast beams.

As shown in Figure 6.2, vertical shell elements with constant and variable thicknesses were utilised to model the beams to match the actual beam cross-sections. Varying shell element thickness was achieved using tapered shell elements whose properties were defined through spatial functions.
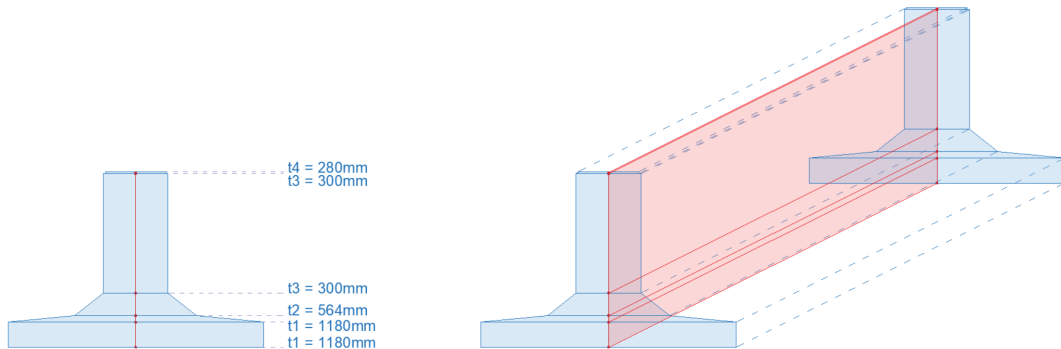
Figure 6.2: Modelling of the precast beams using vertical shell elements with varying thicknesses.

The beams' linear material properties are specified as:

- $E_{C55/67} = 38214.2 N/mm^2$

- $v = 0.2$

- $\rho_{beam} = 2548.42 Kg/m^3$

A consistent element type was employed to model the other structural components to ensure compatibility between the degrees of freedom at the nodes of the utilised elements. The regular flat shell elements have fundamental variables in the nodes, namely the translations u_x, u_y, and u_z, and the rotations ϕ_x and ϕ_y around the x and y-axis, respectively. However, as illustrated in Figure 6.3, the shell elements representing different structural components are not configured in the same plane. At the connection points, the shells meet in a perpendicular configuration, resulting in incompatibility of the degrees of freedom. The regular shell elements have two in-plane rotational degrees of freedom in each node. In order to address this issue, a special type of flat shell element with drilling rotation ϕ_z as an additional variable is utilised to model

the structural members. This results in nodes having three translational and three rotational degrees of freedom, as shown in Figure 6.4.
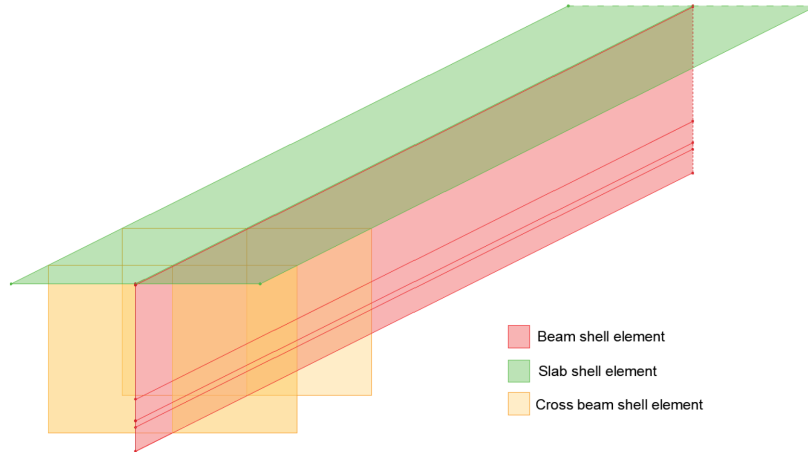
Figure 6.3: Perpendicular configuration of the shell elements used for the modelling of the structural components.
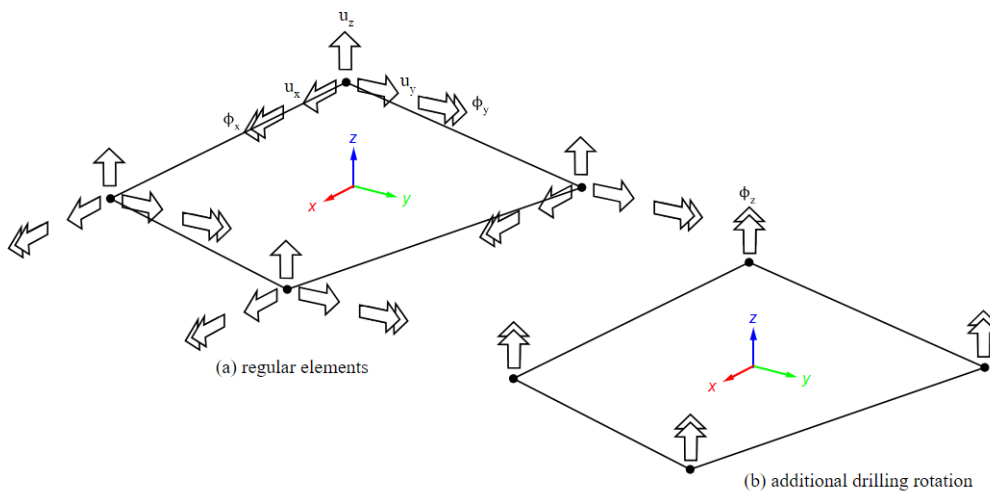
Figure 6.4: Node displacements of: a). regular flat shell elements, and b). flat shell elements with additional drilling rotation(DIANA FEA Release notes).

6.2.1.2   Cast in-situ slab

The cast in-situ slab was modelled as a two-dimensional flat shell element having an orthogonal shape. The thickness of the slab was assigned in the out-of-plane direction, enabling the two-

dimensional element to adequately represent the three-dimensional geometry. As displayed in Figure 6.3, the slab shell element is situated atop the beams. In DIANA FEA, the reference surface of the shell elements is located in the middle of its thickness, as depicted in Figure C.5. To accurately model the bridge geometry and avoid the double masses at the top parts of the beams, the slab thickness was eccentrically positioned. The eccentricity of the top slab shell element geometry in the z-direction equals $\frac{H_{slab}}{2} = \frac{160}{2} = 80mm$ (Figure 6.5). For the basis case study (Chapter 7.1), the cast in-situ slab is considered elastic isotropic, with the material properties specified as,

- $E_{C25/30} = 31475.81 N/mm^2$

- $v = 0.2$

- $\rho_{beam} = 2548.42 Kg/m^3$

It is noted that, as in the rest of the reinforced structural members, the steel reinforcement is not included in the global analysis model since a linear analysis is conducted.
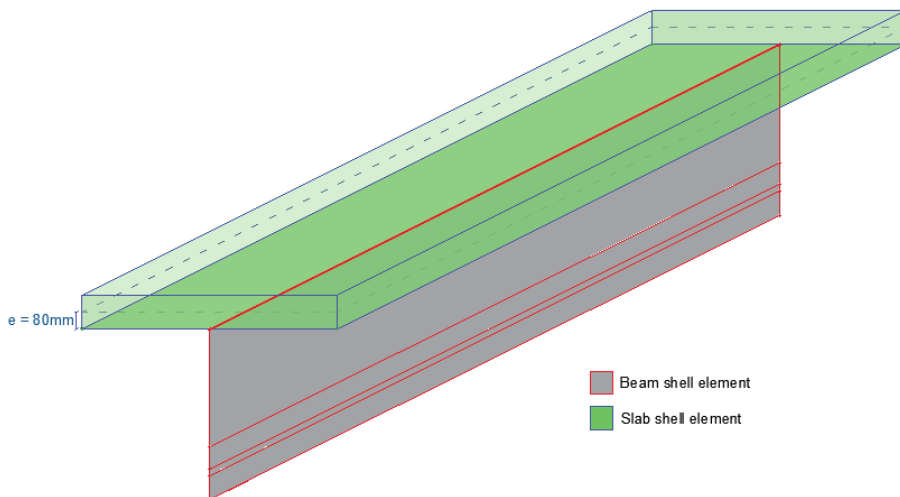
Figure 6.5: Eccentrically positioned slab thickness.

6.2.1.3   Cross beams

The cross beams in the bridge design were modelled with flat shell elements. The thickness of these elements was chosen to match the geometry of the diaphragm beam. However, utilizing a single shell element would not accurately simulate the confinement at the edge of the beam. This is due to the fact that the properties of the shell element at each height level are assigned to a single node in the longitudinal direction. To achieve the desired confinement, solid elements could be used for the cross-beam components. However, this approach would result in a significant increase in the number of nodes and calculation time. To avoid this, the transverse beam was modelled using two shells having half its thickness, as presented in Figure 6.6. This way, additional confinement is achieved without significantly increasing the computational time.
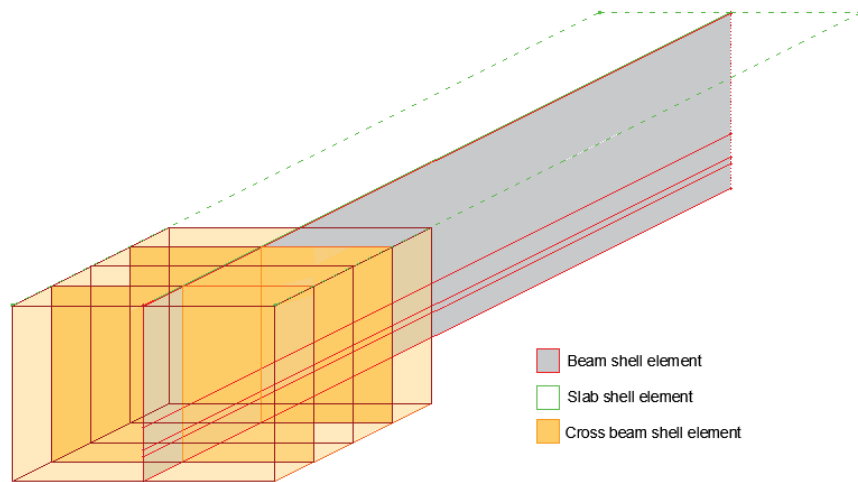
Figure 6.6: Modelling of the cross beams using two shell elements.

In addition, the asymmetrical loading of the bridge deck and the differential deflections of the beams lead to torsional cracks at the diaphragm beams. These cracks cause a decrease in the cross-beam stiffness, and consequently, the material properties of the cross-beams are determined as follows,

$E_{cm,C35/45} = 34077.15 N/mm^2$

$E_{C35/45,cracked} = \frac{E_{cm,C35/45}}{3} = 11359.05 N/mm^2$

$v_{cracked} = 0$

Modelling the precast beams using vertical shell elements has an impact on the design of the cross beams. As illustrated in Figure 6.7, the geometry of the diaphragm beams differs from the orthogonal shape used in the global analysis model. To account for this additional mass, the density mass of the cross beams was reduced based on the following calculations,

$A_1 = 0.594 m^2$

$A_2 = ctc \cdot h_{crossbeam} = 1.2 \cdot 0.695 = 0.834 m^2$

$\rho_{crossbeam} = \frac{A_1}{A_2} \cdot \rho_{concrete} = \frac{0.594}{0.834} \cdot 2548.42 = 1815.8 kg/m^3$

where,

A_1 the area of the actual geometry of the cross beams,

A_2 the area of the shell element used for the modelling of the cross beams,

$\rho_{crossbeam}$ the corrected mass density of the cross beams material,
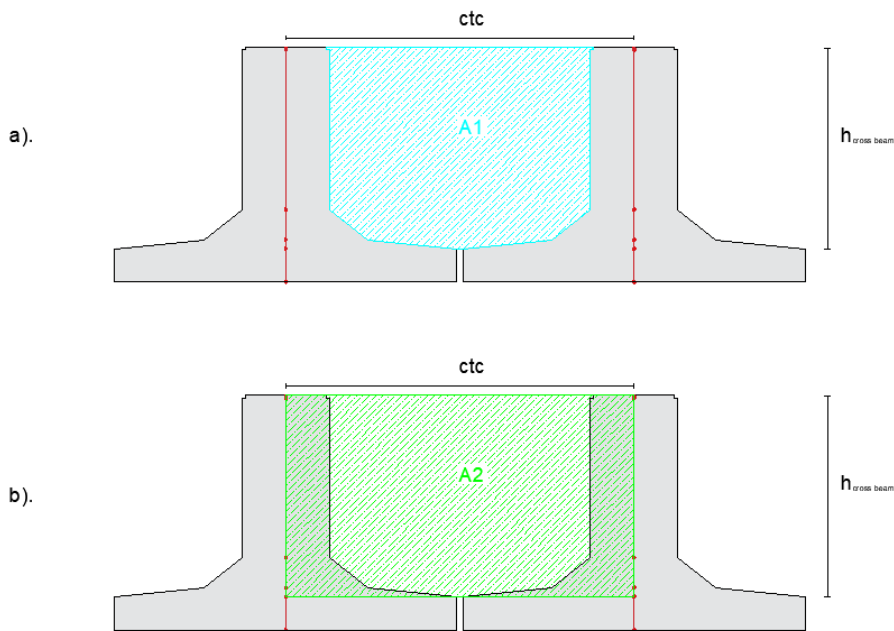
Figure 6.7: Correction of the diaphragm beams' mass density to compensate for the difference between the a). the actual geometry of the cross beams, and b). the modelled geometry of the cross beams using shell elements.

6.2.2   Supports

The investigated structure is supported by discrete bearing pads. As this research does not examine the influence of the other substructure components, the supports are modelled using boundary springs, a special type of spring that connects a vertex to the environment. The N6SPR element used in the global analysis model is a one-node generic spring element used in three-dimensional models, whose basic variables are the three-axis translations and rotations (Figure 6.8).
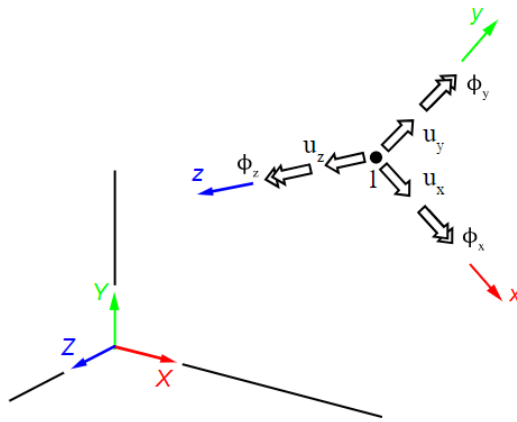
Figure 6.8: Degrees of freedom of the matrix spring element type N6SPR (DIANA FEA Release notes).

For the boundary spring element class, nodal springs have been selected. Nodal or matrix spring elements are defined in a matrix form based on stress-strain relationships, with or without cross terms. In this model, nodal springs without cross terms are implemented since there is no coupling between the six degrees of freedom. The stiffnesses in the springs are defined as material properties, while the equivalent translational and rotational stiffnesses simulate the supporting conditions of the bearing pads.

The springs are attached to the bottom of the shell elements, where the beams are connected to the bearings. The geometry of the support system is determined by specifying its local axes. Specifically, the local x and y axes are user-determined, while the z axis is automatically set by DIANA FEA perpendicular to the created plane. In this bridge model, the local axes of the

supporting springs were defined to coincide with the global coordinate system.

Equivalent stiffness

The equivalent support stiffness values were determined based on the dimensions and material properties of the utilised elastomeric bearing pads. As described in Section 5.3, their dimensions are $length \cdot width \cdot thickness = 400 \cdot 300 \cdot 80mm$, where the thickness corresponds only to the thickness of the elastomer. It is important to note that the calculation does not account for the thickness of the steel plates, as it is significantly larger than the equivalent stiffness of the rubber.

According to EN 1337-3:2005, the typical bulk modulus for the elastomeric material is $E_b = 2000N/mm^2$, while the shear modulus is $G = 1N/mm^2$. The compressive stiffness of the bearing pads is represented by the spring stiffness in the vertical (z) direction, which is calculated as,

$$k_z = \frac{A \cdot E_b}{t} = \frac{400 \cdot 300 \cdot 2000}{80} = 3 \cdot 10^6 N/mm \tag{41}$$

Similarly, the shear stiffness of the supports is represented by the spring stiffness in the horizontal directions, which equals,

$$k_x = k_y = \frac{A \cdot G}{t} = \frac{400 \cdot 300 \cdot 1}{80} = 1500N/mm \tag{42}$$

Lastly, it is considered that the elastomeric bearing pads do not restrain the rotational movements; hence, the rotational stiffnesses are taken equal to

$$k_{rotational} = 0 \tag{43}$$

6.2.3   Loads

Due to limitations of DIANA FEA Student Version 10.5, the load cases that represent the motion of moving vehicles are not automatically created. To address this, programming was used to generate the necessary load cases, encompassing all potential positions of the axle wheel

prints along the moving paths on the bridge deck. To minimise the number of load cases that need to be performed in the global analysis, axle loads of each wheel type were designed in various positions along the moving path (Figure 6.9). Each axle was loaded with a "unity" load divided between the contact areas. This load was subsequently multiplied to match the actual axle load of the trucks described in the loading models (Sections 5.5.4.5 and 5.5.4.6). Each axle load generates bending moments along the beams. Considering the number and spacing of the axles, the effect of each vehicle was obtained as a superposition of the resulting bending moments as depicted in Figure 6.10. Selecting a step size of 0.1m on a bridge with a length L = 30m corresponds to 304 load cases per wheel type that require analysis for each traffic route. This way, the influence lines of each vehicle were obtained, which, for this case, represents the variation of bending moment at the midspan of the beams as the vehicles traverse the bridge.
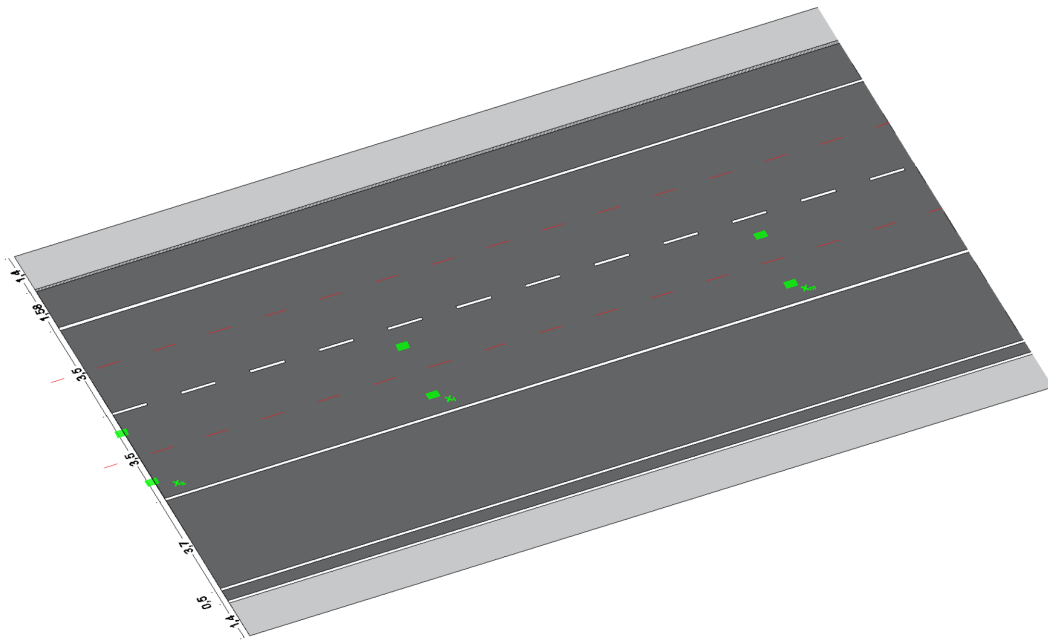
Figure 6.9: Modelling of the moving loads using areas loads traversing the bridge.
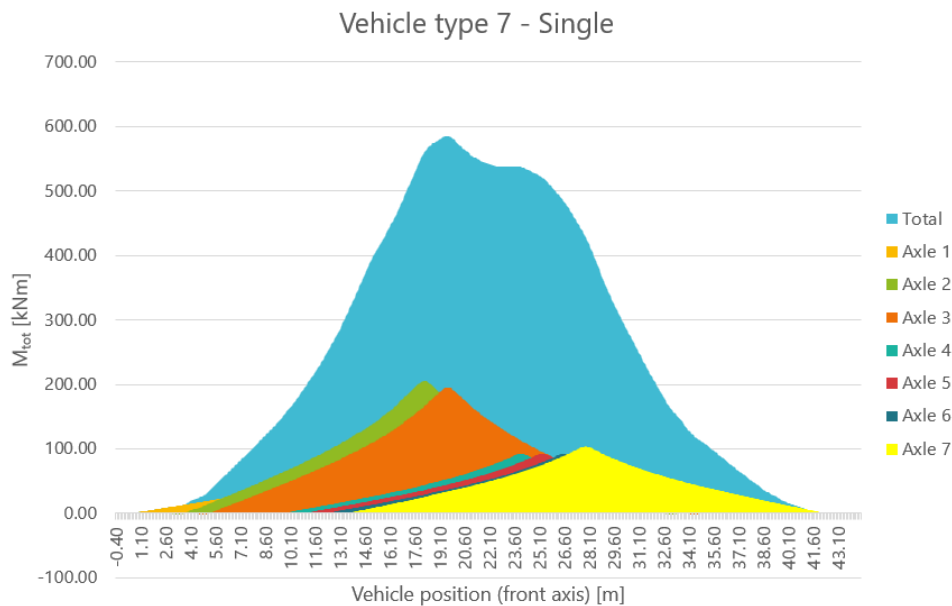
Figure 6.10: Influence line of vehicle 7 as a superposition of the bending moments generated by the axle loads.

Quadrilateral force loads

For the analysis of mobile loads, it was necessary to consider a wide range of wheel print loading positions. Since imprinting all these load areas on the bridge was not a feasible alternative, quadrilateral force loads were employed to model wheel loads (Figure 6.11). This load type distributes a force over a quadrilateral surface on a larger surface of flat shell, curved shell, plate bending, or solid elements. The edges of the quadrilateral area are not necessarily aligned with the element edges. This approach allowed for the analysis of moving loads without disrupting the meshing of loaded components. In the analysed model, quadrilateral force loads were defined as a series of rectangular surfaces that were configured identically to the respective wheel types depicted in Figure 5.16.
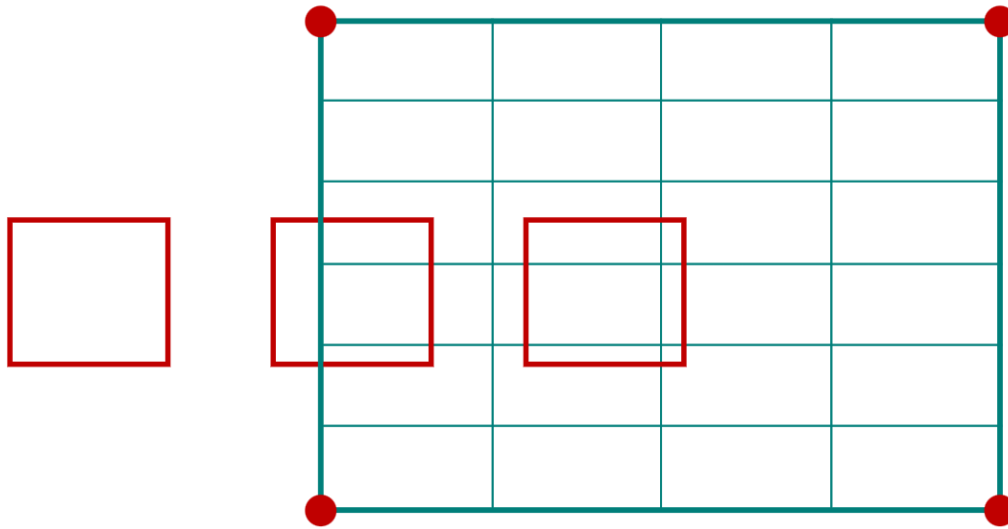
Figure 6.11: Quadrilateral force load defined as rectangular area (DIANA FEA Release notes).

The quadrilateral force loads are internally transformed into surface or point loads, ensuring that the summation of forces and moments precisely aligns with the user-defined force value and position of the quadrilateral force load.

In cases where the quadrilateral surface is partially situated outside the element area, the total force is scaled proportionally to the covered surface. This feature enabled the modelling of the entrance and exit of vehicles when only part of the first and last axle wheels were on the bridge deck.

6.2.4   Functions

Spatial functions are utilised to establish position dependency, which can be either one-, two-, or three-dimensional, depending on the global coordinate components upon which they rely. Each coordinate component combination is linked with a multiplication factor to define these functions. These functions are then connected to properties such as material, geometry, and load parameters through diagrams that illustrate how these properties vary in the x, y, and z global coordinates.

As described above, functions are utilised in this investigation to model the thickness (Figure

6.12). This feature can also be used to model the variation of properties over the beam height, which may occur due to material degradation caused by cycling loading. As outlined in the following chapter, cycling loading results in a decrease in material stiffness, which leads to redistribution of stresses. Incorporating this effect into the global bridge analysis was accomplished by utilizing spatial functions.
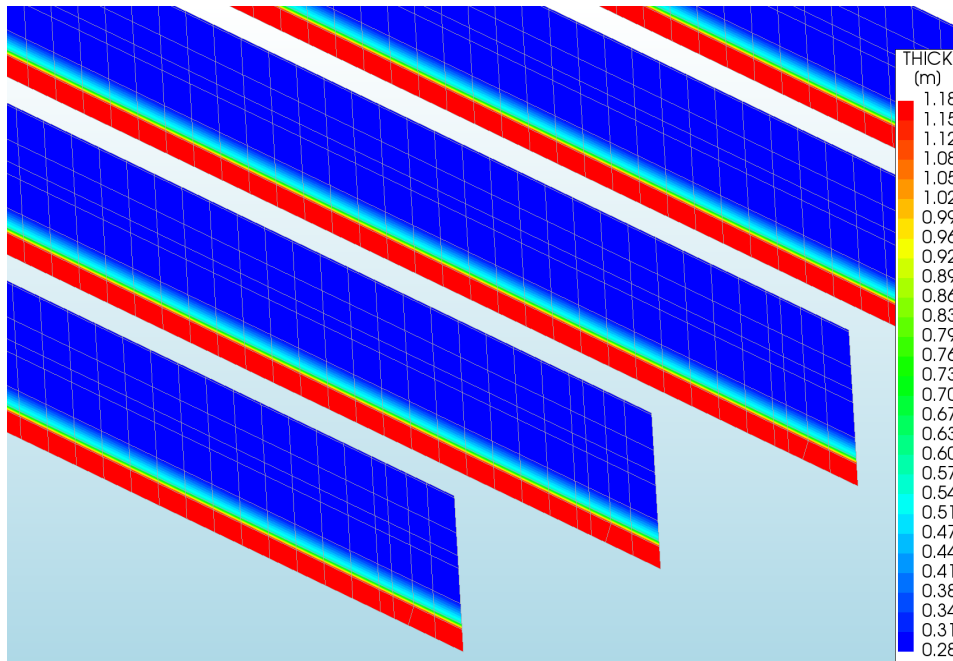
Figure 6.12: Modelling of the varying thickness using spacial functions (image generated by DIANA FEA).

6.2.5   Global analysis model results

6.2.5.1   Result processing

Coordinate system

As illustrated in Figure 6.13, the bridge's longitudinal orientation runs parallel to the x-global axis, while the transverse direction is parallel to the y-global axis. This orientation affects how the beams are identified in this analysis. Specifically, the beams are defined based on their transverse location, with the first beam, or Beam 1, positioned closest to the left free edge of the bridge, located at y=0. Furthermore, positive values in the vertical (z-) direction indicate an upward direction.
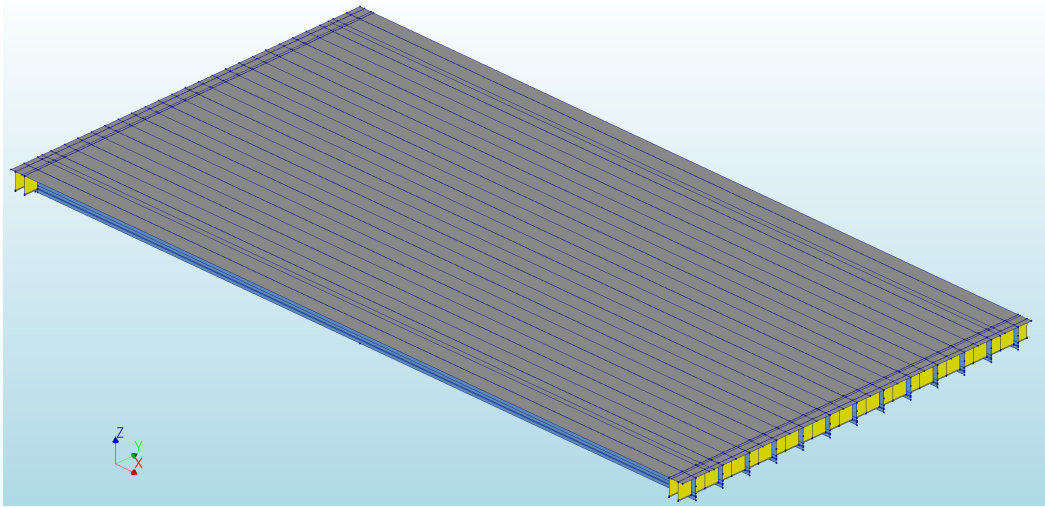
Figure 6.13: Coordinate system of the bridge (image generated by DIANA FEA).

Composed lines

The present study utilizes a failure criterion based on bending at the midspan of the beams. To determine the bending moment distribution of the composite section, the DIANA Finite Element Analysis (FEA) software's composite line feature is employed. Composite line elements are created parallel to the precast beams, as shown in Figure 6.14. This approach enables the integration of internal forces of each composite cross-section over a cross-section plane that is perpendicular to the defined line. The dimensions of the cross-section plane are determined by two values that define the nodes included in the calculation. It is important to note that the composite line does not need to be designed at the central axis of the examined section. DIANA FEA automatically shifts the composite line to coincide with the centroidal axis of the composite section. It is noteworthy that composite lines have no mechanical properties and, as a result, do not influence the results of the Finite Element Analysis.
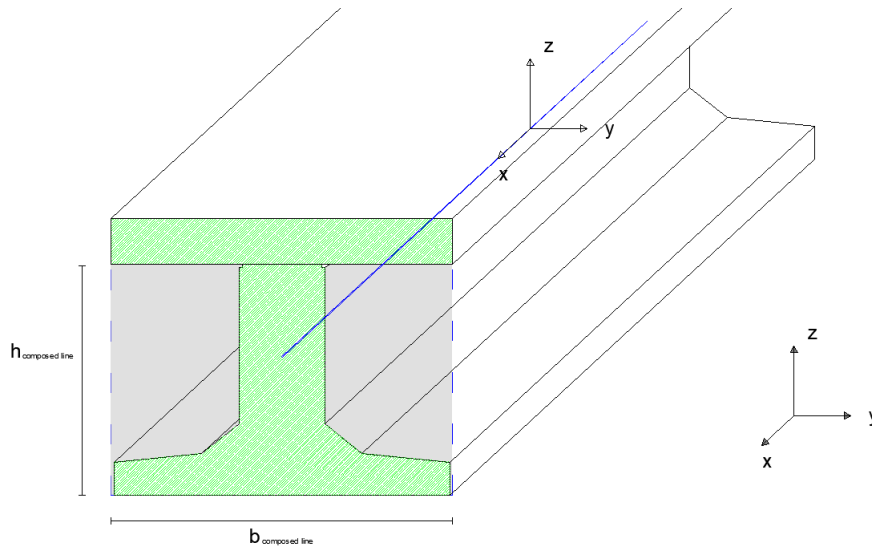
Figure 6.14: Dimensions of the composed lines.

6.2.5.2 Mesh element size effect

The determination of the appropriate mesh size for a given structure involves careful consideration of the balance between the accuracy of the model results and calculation time. Opting for larger mesh elements results in fewer elements required to represent the structure, thereby reducing the computational time in finite element analysis (FEA). However, this approach may not accurately capture the behaviour of the structure, leading to significant discrepancies between the model results and the actual behaviour. Conversely, a fine mesh model with more elements provides a more accurate representation of the structure's behaviour, but it requires a longer computation time. Ultimately, the decision on mesh size should be based on the desired level of accuracy and the available computational resources.

In the case of bridge analysis, the final mesh size was determined by comparing the results of two different mesh sizes, 0.1m and 0.2m. Table 6.1 illustrates the bending moments at the midspan of the beams for each mesh size. The two mesh sizes provided almost identical results, indicating that increasing the mesh element size did not compromise the accuracy of the results. Considering the size of the structure being investigated, a mesh element of 0.2m was selected for the Finite Element Analyses.

Table 6.1: Comparison of the results for different element sizes

| | Element size | | |
| | 0.1m | 0.2m | Difference |
Beam	$M_y(kNm)$	$M_y(kNm)$	%
1	1481.04	1481.11	0.00%
2	1482.48	1482.52	0.00%
3	1483.01	1483.02	0.00%
4	1485.48	1485.47	0.00%
5	1488.23	1488.20	0.00%
6	1490.22	1490.19	0.00%
7	1490.94	1490.90	0.00%
8	1490.22	1490.19	0.00%
9	1490.22	1490.19	0.00%
10	1485.48	1485.47	0.00%
11	1483.01	1483.02	0.00%
12	1482.48	1482.52	0.00%
13	1481.04	1481.11	0.00%
Number of nodes	549138	164610	
Analysis time (sec)	165	30	

6.2.5.3 Plate theories

When analyzing plate elements that undergo bending, two theoretical models are mainly applied, namely Kirchhoff and Mindlin theory. It is important to consider the specific circumstances involved when deciding which theory to use. Blaauwendraad 2010 provides analytical presentations of both methods, elucidating their differences and applications.

Mindlin theory, which is also referred to as thick plate theory, incorporates shear deformations in the analysis. In this theory, the cross-section is not assumed to be perpendicular to the vertical centre line of the plate, similar to Timoshenko beam theory. The edge degrees of freedom in

Mindlin theory include vertical displacement (w), normal (ϕ_n), and in-plane (ϕ_s) rotations, as illustrated in Figure 6.15. This corresponds to three load components - a vertically distributed force (f) equal to the shear force (v_n), a distributed torque (t_n) equal to the bending moment (m_{nn}), and a distributed torque (t_s) equal to the twisting moment (m_{ns}) in the direction of w, ϕ_n, and ϕ_s, respectively. Distributed torques t_n and t_s are typically zero, resulting in zero bending and twisting moments (m_{nn} and m_{ns}), as shown in the following equation,

$$\begin{Bmatrix} w \\ \phi_n \\ \phi_s \end{Bmatrix} \rightarrow \begin{Bmatrix} f \\ t_n \\ t_s \end{Bmatrix} \rightarrow \begin{Bmatrix} v_n \\ m_{nn} \\ m_{ns} \end{Bmatrix} \rightarrow \begin{matrix} v_n = f \\ m_{nn} = 0 \\ m_{ns} = 0 \end{matrix} \tag{44}$$
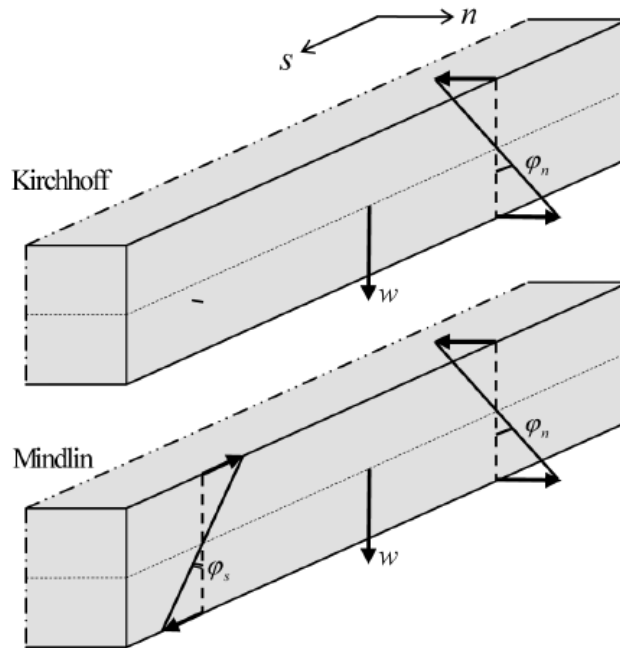
Figure 6.15: Boundary conditions for Kirchhoff and Mindlin bending plate theories (Blaauwendraad 2010).

On the other hand, Kirchhoff theory refers to thin plates in which shear deformations are ignored, resulting in only two degrees of freedom at the free edge - vertical deflection (w) and normal-to-the-edge rotation (ϕ_n). In line with the Euler-Bernoulli beam theory, the rotation within the plane of the edge is entirely dependent on the deflection, as described by the relation $\phi_s = \frac{\partial w}{\partial s}$.

Thus, two loads are applied to the plate edge - the vertical force (f), given by the equation $f = v_n + \frac{\partial m_{sn}}{\partial s}$., and the torque, t_n, equal to the bending moment, m_{nn}., and the torque t_n, equal to the bending moment $(m_n n)$. These relationships show that if there is no edge moment $(t_n$ equals zero), the corresponding quantity $m_n n$ is also zero. Conversely, if the vertical edge load is zero, internal quantities v_n, and $m_s n$ are not usually equal to zero, as described below:

$$
\begin{Bmatrix} w \\ \phi_n \end{Bmatrix} \rightarrow \begin{Bmatrix} f \\ t_n \end{Bmatrix} \rightarrow \begin{Bmatrix} v_n + \frac{\partial m_{ns}}{\partial s} \\ m_{nn} \end{Bmatrix} \rightarrow \begin{matrix} v_n \neq f \\ m_{nn} = 0 \\ m_{ns} \neq 0 \end{matrix} \tag{45}
$$

Subjecting the plate to a zero-edge load t_n results in a zero bending moment m_{nn}. However, it is important to note that a zero load at the plate's edge, represented by f, does not necessarily mean that the shear force v_n and twisting moment m_{ns} will also be zero. An unloaded free edge will still experience a twisting moment and a shear force despite the absence of f and t. This concentrated shear force, denoted as V_s, is only present in the Kirchhoff theory while is not accounted for in Mindlin theory. Instead, the theory calculates distributed shear forces v_s in a narrow edge zone.

To understand the difference between the two theories, it is helpful to examine the shear stress flow caused by a twisting moment in a section perpendicular to the free edge, as shown in Figure 6.16. Excluding the areas close to the edges, the shear stresses present a linear distribution due to the twisting moment, which equals zero at the middle plane $(h/2)$. A different distribution is observed near the edge, where the shear flow must turn around, which occurs over a plate length approximately equal to the thickness.

The stress state in this small end part of the plate can be described in terms of shear force (v_s) and twisting moment m_{ns}. The shear stresses are vertical and non-linear at the mid-plane of the plate. Specifically, they gradually increase from zero, reaching a maximum value at the edge. At the edge, the vertical shear stress is noted over the total plate thickness, with an almost parabolic distribution that becomes zero at the top and bottom. Regarding the stress state away from the edge section, two components can be distinguished. The vertical shear stress reduces

while moving away from the edge part. At the same time, the horizontal component follows the opposite trend and experiences a non-linear decrease until zero as we move towards the edge zone. The integration of the horizontal shear components results in the torsional moment m_{sn}, while integrating the vertical components yields the vertical shear force v_s.

The principal difference between the two theories lies in the fact that Mindlin's theory accurately depicts this distribution of shear force and twisting moment, while Kirchhoff's theory does not. The boundary condition $m_{ns} = 0$ is met in Mindin theory and not in Kirchhoff. In Kirchhoff theory, all local vertical stress components are integrated and condensed into a single shear force (V_s) at the edge. Additionally, the twisting moment remains constant up to the edge in Kirchhoff theory, as opposed to diminishing to zero, as demonstrated in Figure 6.16.
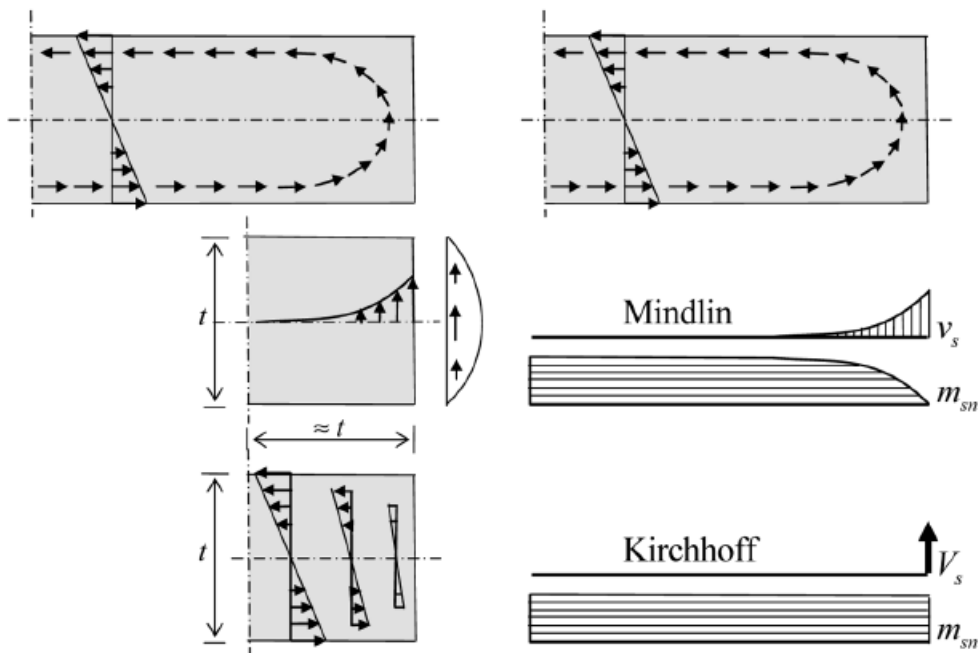
Figure 6.16: Stress state close to the free edge (Blaauwendraad 2010).

It should be noted that the majority of Finite Element Method (FEM) software does not account for the concentrated shear force. Consequently, the Mindlin theory has emerged as the preferred method for plate theory in most FEM software.

The global analysis of the bridge's structural members was carried out using the DIANA FEA software. The elements were modelled with flat shell components that can implement either

Kirchhoff or Mindlin-Reissner plate theories, depending on the element type. According to DIANA FEA Release notes, flat shell elements consist of a combination of a plane stress element and a plate bending element. The Mindlin-Reissner bending theory is predominantly employed for most of the element types, whereas the Kirchhoff plate bending theory is used for the T18SF and T18FSH three-noded flat shell components. In Mindlin plate bending elements, both transverse displacements and rotations of middle surface normals are independent and obtained via isoparametric interpolation from the nodes' displacements. In contrast, the Kirchhoff plate bending theory is based on the principle that zero transverse shear strain is encountered at several discrete points within the element. To expand the translational and rotational fields, shear constraints are introduced, thereby accounting for the effect of the shear deformation.

Based on Blaauwendraad 2010, the Kirchhoff theory is applied in plates where the deformation caused by shear forces can be neglected, which refers to cases with a span thickness ratio $l/t > 10$. Given the dimensions of the top slab, this ratio is calculated as,

$$\frac{l}{t} = \frac{29}{0.16} = 181.23 >> 10 \tag{46}$$

Using triangular elements for the top slab mesh that employs the Kirchhoff plate theory would significantly increase the number of nodes and, consequently, the computational time. Therefore, a comparison was made between the two methods to determine the bending theory used in the global analysis of the bridge. In this comparison, different element types were utilized for the top slab, as illustrated in Figures 6.17 and 6.18. Specifically, the first case utilized the Q24SF element, a four-node quadrilateral flat shell element following the Mindlin-Reissner bending plate theory (Figure 6.19). In contrast, the Kirchhoff theory employed the T18SF, a three-node triangular shell element (Figure 6.20). The analyses were conducted for the self-weight loads, and the resulting bending moment at the midspan of the precast beams is presented in Table 6.2. The obtained results did not exhibit significant differences between the analyses employing different theories. However, there was a notable increase in analysis time, which would have an impact on the required time considering the number of loading cases that need to be analyzed in this research. Therefore, the Mindlin-Reissner bending plate theory was selected for the global

analysis of the bridge, as it reduces the analysis time without compromising the accuracy of the obtained results.
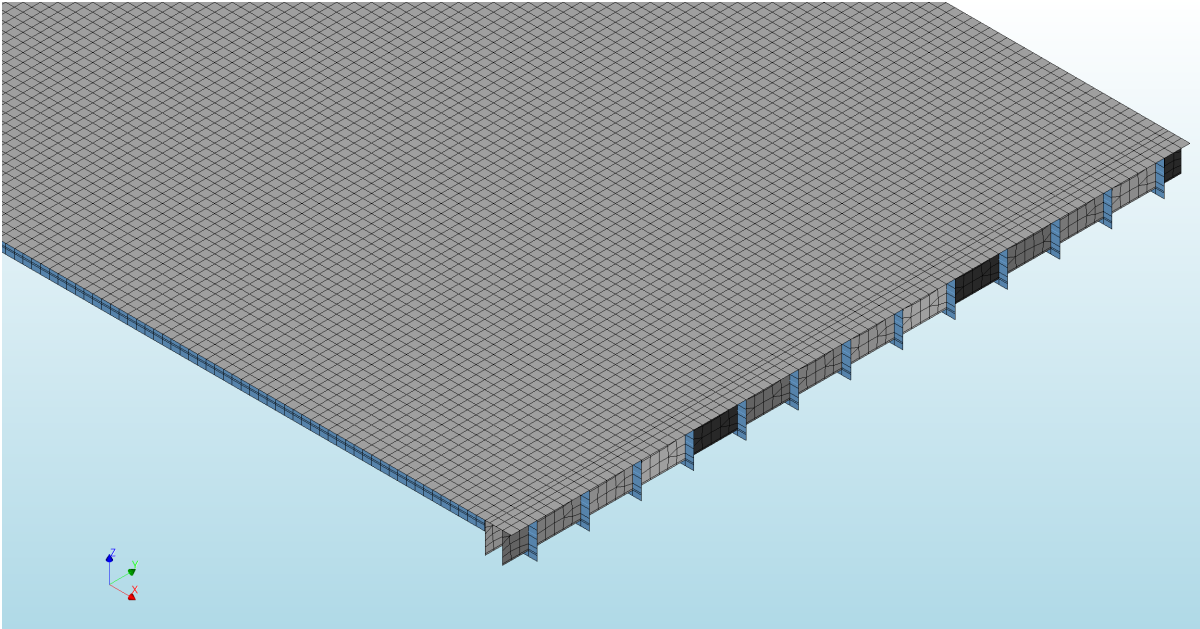
Figure 6.17: Modelling of the cast in-situ slab with four-node elements based on the Mindlin-Reissner theory (image generated by DIANA FEA).
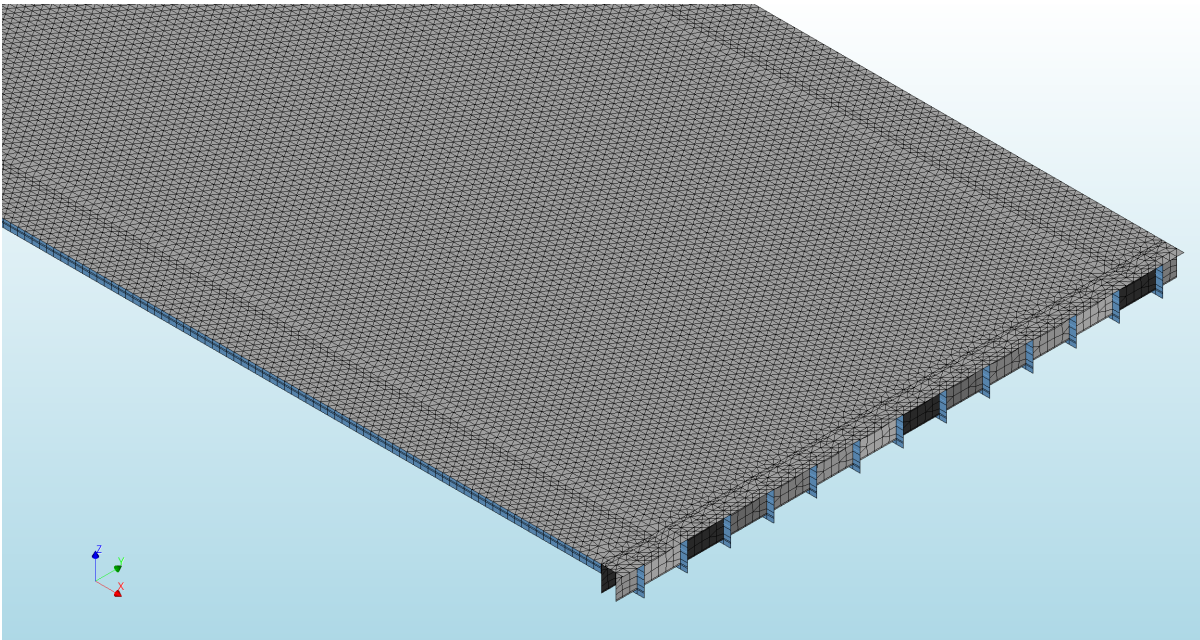
Figure 6.18: Modelling of the cast in-situ slab with three-node elements based on the Kirchhoff theory (image generated by DIANA FEA).
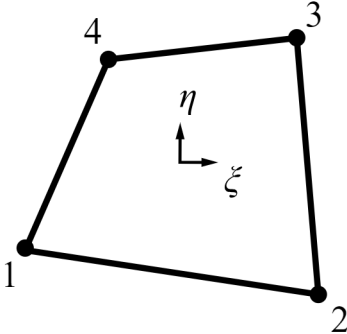
Figure 6.19: Four-node quadrilateral flat shell element - Q24SF (DIANA FEA Release notes).
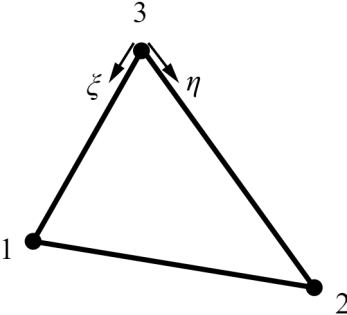
Figure 6.20: Three-node triangular flat shell element - T18SF (DIANA FEA Release notes).

Table 6.2: Comparison of the results for different Kirchhoff and Mindlin-Reissner

| | Bending plate theory | | |
| | Kirchhoff | Mindlin-Reissner | Difference |
Beam	$M_y(kNm)$	$M_y(kNm)$	%
1	1481.09	1481.11	0.00%
2	1482.5	1482.52	0.00%
3	1483.01	1483.02	0.00%
4	1485.46	1485.47	0.00%
5	1488.19	1488.20	0.00%
6	1490.18	1490.19	0.00%
7	1490.90	1490.90	0.00%
8	1490.18	1490.19	0.00%
9	1490.19	1488.20	0.00%
10	1485.47	1485.47	0.00%
11	1483.01	1483.02	0.00%
12	1482.5	1482.52	0.00%
13	1481.09	1481.11	0.00%
Number of nodes	188904	164610	
Analysis time (sec)	48	30	

6.3   Cross-sectional analysis

As aforementioned, the stress distribution over the beam height was obtained by the cross-sectional analysis conducted in IDEA Statica. The geometry of the composite section, the reinforcement and the prestressing configuration were initially determined along with their corresponding material properties. Additionally, the model was created by defining the construction stages, which finally determined the loads acting on the studied section. Regarding the internal forces, the moments caused by the self-weight of the structural components and the permanent loads on the structure were manually input into the model. On the other hand, axial forces

and moments due to prestress were automatically calculated by IDEA Statica, considering the geometry and configuration of the strands, the prestress applied and the prestress losses. Finally, the maximum and minimum stresses caused by the action of fatigue vehicles (FLM4b), as determined by the global analysis, were accounted for in the cross-sectional analysis.

Based on the above, the software calculated the maximum and minimum stress distributions. In both cases, the critical stress values were noted at the top fibre of the precast beams. These two stress values were then utilized to calculate the fatigue life of the concrete beams. It is important to note that the software also accounts for the increase in concrete stiffness caused by the ongoing hardening of the concrete. The stiffness evolution was automatically calculated by the software, using the secant E-modulus for the cross-sectional analysis.

7   Investigated parameters

7.1   Basic case

A basic case was established to investigate each parameter's impact as a basis for analysis. The effect of each parameter was assessed by implementing it in the basic case and calculating the fatigue life of the bridge using the analysis process previously described (Section 6.1). In each case, the resulting fatigue life of the bridge was then compared to the original value obtained from the basic case.

The finite element analysis (FEA) model for the basic case was created using the geometry, material properties, erection timeline of the bridge, and other analytical aspects outlined in the preceding chapters. The fatigue analysis of the model was performed using the fatigue load combination presented in Table 5.7. In this combination, variable actions were generated by the vehicles of Fatigue Load Model 4b, where the area loads were used to model wheel loads. The equivalent lorries traversed two defined routes located in the middle of each traffic lane. It is important to note that in this basic case, the traffic lane configuration did not match the actual lane layout. Instead, the two lanes were placed closer to the free edge of the bridge, as illustrated in Figure 7.1. This arrangement is often employed in engineering practice to induce the most unfavourable effect on the structure. Hence, this loading configuration was also utilised in this basic case to guarantee that the bridge would fail in fatigue within its lifespan. In the context of this study, the impact of traffic lane position on the bridge deck was analysed as an influential factor affecting the fatigue life of the bridge.

The calculation of prestress losses is presented in Appendix F.1. This calculation was conducted by taking into account the creep and shrinkage strains developed in the beam, as well as relaxation losses. It was considered that creep and shrinkage of the beam could develop freely without accounting for its interaction with the cast in-situ slab. Additionally, this simplified calculation includes only the axial loads to determine the creep strain, while bending moments were neglected. Accounting only for axial loads is a common practice, as the stress value at the prestress level is not constant along the length of the beam. In simply supported structures,
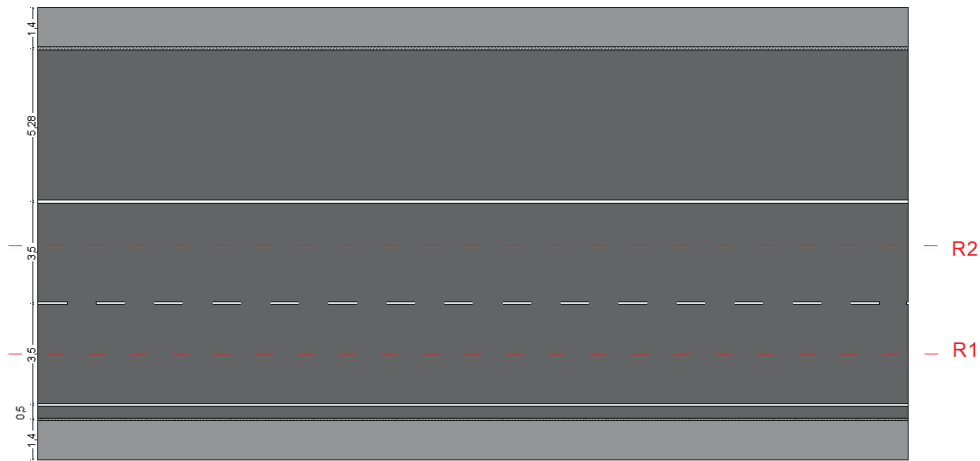
Figure 7.1: Positioning of the traffic lanes close to the free edge of the bridge.

the maximum moment is observed at the midspan of the beam. The stress gradient caused by the bending moments would lead to smaller stress values at the level of the strands. Thus, considering only axial loads is a conservative measure since higher stress levels lead to greater prestressing losses in the analysis. Finally, in the basic case, the fatigue analysis was performed, assuming that the maximum prestress losses had already occurred in the early stages of the bridge's lifespan.

It is worth mentioning that the effect of a more detailed calculation of the prestress losses is examined as part of the parametric study, as discussed in the next section.

7.2   Prestress losses

The loss of prestress is a highly consequential determinant of the fatigue life of bridges since it has a significant impact on the distribution of stress. Multiple calculation methods have been evaluated to investigate this parameter. As previously highlighted, the basic case involves a simplified calculation that assumes maximum prestress loss across the bridge's lifespan. In this section, three additional cases of prestress loss are presented: the first case assumes no losses, while the second case estimates the prestress losses per decade. Lastly, the third case considers bending moments in determining the prestress loss. The presented methods are crucial in understanding the different aspects of prestress losses and their effect on the fatigue life of bridges.

Zero prestress losses

In the first case, the loss of prestress is not considered in the analysis, and the prestress level remains constant at $1394 N/mm^2$ throughout the bridge's life. Even though this approach is not reflective of realistic scenarios, it highlights the contribution of prestress losses in the fatigue performance of the structure and emphasizes the need for a more precise and detailed calculation of prestress loss in bridge analysis.

Calculation of prestress losses at each decade

The gradual development of prestress losses in a bridge throughout its lifespan necessitates a detailed approach for their calculation. Assuming that total prestress losses occur from the beginning of the bridge's life (instantaneous losses) is deemed conservative. However, calculating the actual prestress losses for each year would significantly increase the time required for the analysis. To address this challenge, an intermediate approach is implemented in this case. Specifically, the losses are analytically calculated every decade for the 100 years of the bridge's life when maximum losses are expected to occur. For the intermediate years, the first five years of each decade account for the losses of the previous decade, while in the last five years, the stress distribution is determined based on the prestress losses of the next decade. This approach is expected to positively affect the fatigue life of the bridge by calculating losses in prestress in a less conservative way.

It is noteworthy that the simplifications made in Appendix F.1, relating to axial loading and structural component interaction, are also applicable to this case.

Calculations, including prestress losses

In the last case, the prestress losses are calculated taking into account the bending moment caused by the prestress and permanent loads, namely, self-weight and additional dead loads. This consideration has a significant influence on the prestress losses by affecting the developed creep strain. Specifically, as outlined in Appendix F, the creep strain relies on the stress value noted at the level of the prestressing stands. Incorporating the bending moments leads to lower stress levels and, as a result, smaller creep strain development.

In composite structures erected in multiple stages, the applied loads differ during various construction stages. For the bridge under investigation, the beams are initially loaded by their self-weight and prestressing. After 28 days, the top slab is cast, and its self-weight also contributes to the structure's loads. Finally, at the third stage, the cast in-situ slab has hardened, and additional dead loads are added to the bridge. This way, the different stress distributions are considered in the calculation of prestress losses, which is described in Appendix F.2. It is noted that, in this case, the creep and shrinkage strains of the beam can be freely developed. The calculation method does not account for the interaction of the structural components, as this will be examined as a separate parameter later in this study.

Upon assessing the prestress losses calculated in this manner, it is evident that the maximum losses do not differ significantly from those computed in the basic case. Considering only the axial loads, the maximum losses are equal to $\Delta P_1 = 201.97 N/mm^2$, while also including the bending moments $\Delta P_2 = 200.36 N/mm^2$. As the two calculations yielded similar results, it is considered that accounting for the stress gradient would not significantly affect the fatigue performance of the bridge. Therefore, this third scenario was not examined as an influencing parameter in this study.

7.3   Increasing traffic rate

Bridges are analysed using loading models provided by European and National standards. These models describe the traffic volume, types of vehicles, loading patterns, and loading frequency, simulating the effect of variable actions on each structure. However, it is important to note that traffic demands are not constant. The continuous increase in transportation volume has resulted in bridges being analysed based on traffic loads that do not accurately represent their actual loading conditions.

Fatigue Load Model 4b, as reported by NEN 8701:2011+A1:2020, corresponds to the expected traffic conditions in 2050. The traffic volume can be reduced by 0.2% per year for previous years, while the number of vehicles is expected to increase annually by 0.5% after 2050.

The traffic volume is a crucial component of the fatigue analysis, as it determines the number of vehicles or loading cycles considered in the analysis. Evaluating the bridge for larger traffic

volume would lead to an underestimation of its fatigue life. Given that the bridge was erected in 1974, the load cycles accounted for in the fatigue analysis for the first 76 years of its life are smaller than those presented in Table 5.1. Therefore, a parametric study is conducted to analyse the increase in traffic rate, as it is expected that a reduction in the number of slow vehicles would have a positive impact on the fatigue life of the bridge.
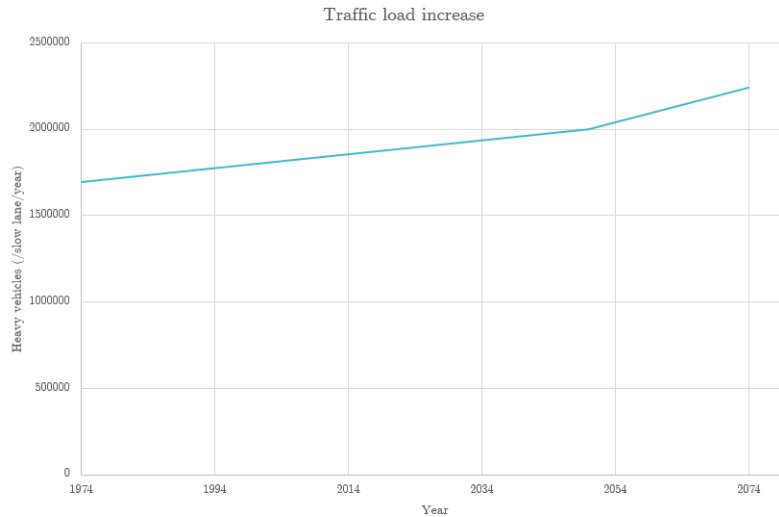
Figure 7.2: Increase of traffic volume.

7.4   Orthotropic slab properties

The material properties of the cast in-situ slab are subject to variation in different directions throughout the lifespan of a bridge. Non-uniformly distributed loads, differential deflections of beams, torsion, and transverse moment distribution can lead to cracking in the slab, resulting in a change in properties in the transverse direction that can impact the distribution of forces in the structural components.

To account for this effect, the slab is modelled using linear elastic orthotropic material properties. In the absence of cracks in the longitudinal and vertical directions, stiffness and Poison's ratio remain constant in these directions. In the transverse direction, however, the material properties are adjusted to simulate the effect of the cracked element.

The linear analysis of structures considers the relevant effects of cracking through stiffness re-

duction, as per the RTD 1006:2022-1.2.1. Orthotropic properties are calculated based on Table NB-1 of NEN-EN 1992-1-1+C2:2011/NB:2016+A1:2020. The fictitious modulus of elasticity for bending rectangular cross-sections, to which no normal forces are applied, and concrete class C25/30, is determined as follows,

$$(2.65 + 580p \cdot 10^3) \geq 3950 \tag{47}$$

where,

p $\quad = \frac{A_{st}}{A_c},$

A_{st} $\quad$ the area of the reinforcement at the most tensed side,

A_c $\quad$ the area of concrete.

Regular reinforcement of the cast in-situ slab is conducted using $\varnothing 10 - 200$ in the longitudinal direction and $\varnothing 12 - 100$ in the lateral direction at the top and bottom of the slab. Therefore, the reinforcement is calculated as,

$$A_{st} = \frac{1}{4} \cdot \pi \cdot 12^2 \cdot \frac{1000}{100} = 1131 mm^2/m \tag{48}$$

The compressive area of concrete is equal to the height of the compressive layer multiplied by a working length, which is,

$$A_c = 160 \cdot 1000 = 160000 mm^2/m \tag{49}$$

As a result, the elastic modulus in the transverse direction is,

$$(2.65 + 580 \cdot \frac{1131}{160000} \cdot 10^3) = 6749.875 N/mm^2 \geq 3950 \tag{50}$$

Finally, according to NEN-EN 1992-1-1+C2:2011/NB:2016+A1:2020, §3.1.4 (4), the Poison's ratio of cracked concrete is taken equal to 0.

7.5 Load type

The parametric study also analyses the influence of the load type utilised in modelling wheel loads. In engineering practice, simple point loads are often employed to model these loads, which are applied at the centre of the loaded area. Using area loads would increase the design and calculation type, especially in the case of fatigue loads, where three different axle types are utilised. Besides the required time, this simplification could be safely applied, as it results in a more conservative distribution of stresses.

However, in the assessment of concrete bridges, such a conservative consideration would negatively affect their fatigue life. As previously mentioned (Section 7.1), for the basic case, the heavy vehicle loads are modelled using quadrilateral force loads having the dimensions of the wheel types of Fatigue Load Model 4b (Figure 5.16).To investigate the influence of the load type, the fatigue analysis is performed by replacing the area loads with two point loads per axle positioned at the centre of the loaded area.

An additional analysis was also conducted as an intermediate solution. Specifically, in the fatigue analysis, only one of the suggested wheel types was utilized to model the moving vehicles. Wheel type A was chosen for this analysis due to its smaller area, which results in a more conservative distribution of loads. This method is frequently implemented in engineering practice, as it enables the advantages of utilizing area loads while requiring approximately the same number of load cases and analysis time as the point load analysis.

7.6 Position of traffic lanes

To create an unfavourable effect on the structure, the heaviest moving loads are often positioned closer to the free edge of the bridge. This loading configuration was also employed in the basic analysis case. However, the NEN-EN 1991-2:2003/C1:2010 standard specifies that the lanes for fatigue load models should be determined based on the actual traffic conditions of the bridge. While placing the heaviest loaded lanes close to the edge of the bridge may create the most adverse loading conditions, it may not align with the actual loads that the bridge experiences (Figure 7.1). For this reason, the location of the traffic lanes on the bridge deck is examined as

one of the influencing factors in this research.

In this assessment, the actual lane configuration of the bridge is utilised, and the vehicles traverse the bridge over two specified routes positioned in the middle of the traffic lanes (Figure 5.6). This way, the loaded lanes are shifted towards the centre of the bridge width, which is anticipated to alter the distribution of loads between the structural components.

7.7   Relative creep and shrinkage

In reinforced or prestressed concrete structures, the stress and strain undergo changes over a prolonged period due to the gradual development of creep and shrinkage in concrete, as well as relaxation in prestressing steel. The present study has performed calculations on the time-dependent effects of prestress losses for the basic analysis case and the parameters evaluated. The calculations were based on the assumption that there is no interaction between the structural components of the composite section. In this regard, the losses were computed by accounting for the creep and shrinkage strains of the beam, as those were freely developed. An overview of these values, which were calculated in Appendix F.2 for the axial loads and the bending moments applied to the beams, is presented in Table 7.1.

It is worth noting that the cast in-situ slab is also susceptible to time-dependent effects, as it undergoes shortening due to autogenous and drying shrinkage. The free strain evolution in the cast-in-situ slab has been calculated in Appendix F.3 and presented in Table 7.1.

In composite structures, such as the investigated bridge, the hardening of the slab initiates the composite action of its components, which results in the end of their free deformation. Under perfect bonding conditions, the components operate as a single cross-section, and any changes in creep, shrinkage, or relaxation of either section will impact both. Therefore, the composite action should be considered while calculating time-dependent effects. Differences in strain development can affect prestress losses, which can, in turn, influence the stress distribution of the beams. Since the stress distribution plays a crucial role in fatigue analysis, relative creep and shrinkage of the bridge components must be investigated as a parameter affecting the fatigue life of the bridge.

Prior to the casting of the top slab, the precast beam is free to deform without the constraints

Table 7.1: Free strain values of precast beams and cast in-situ slab

Age of bridge	t	28 days	56 days	10 years	20 years	30 years	40 years	50 years	60 years	70 years	80 years	90 years	100 years
						Beam							
Creep strain	$\varepsilon_{cc,b}(t)$	2.73E-04	3.46E-04	4.98E-04	5.01E-04	5.02E-04	5.02E-04	5.03E-04	5.03E-04	5.03E-04	5.03E-04	5.03E-04	5.03E-04
Autogenous shrinkage strain	$\varepsilon_{ca,b}(t)$	7.35E-05	8.73E-05	1.12E-04	1.12E-04	1.12E-04	1.12E-04	1.12E-04	1.12E-04	1.12E-04	1.13E-04	1.13E-04	1.13E-04
Drying shrinkage strain	$\varepsilon_{ds,b}(t)$	4.66E-05	7.77E-05	2.35E-04	2.39E-04	2.40E-04	2.40E-04	2.41E-04	2.41E-04	2.41E-04	2.41E-04	2.42E-04	2.42E-04
Total shrinkage strain	$\varepsilon_{cs,b}(t)$	1.20E-04	1.65E-04	3.47E-04	3.51E-04	3.52E-04	3.53E-04	3.53E-04	3.54E-04	3.54E-04	3.54E-04	3.54E-04	3.54E-04
Total free strain of the beam	$\varepsilon_{tot,b}(t)$	3.93E-04	5.11E-04	8.45E-04	8.52E-04	8.54E-04	8.55E-04	8.56E-04	8.57E-04	8.57E-04	8.57E-04	8.57E-04	8.58E-04
Beam free stain after slab casting		0.00E+00	1.18E-04	4.53E-04	4.59E-04	4.62E-04	4.63E-04	4.64E-04	4.64E-04	4.64E-04	4.65E-04	4.65E-04	4.65E-04
						Slab							
Autogenous shrinkage strain	$\varepsilon_{ca,s}(t)$	-	3.75E-05	5.75E-05	5.75E-05	5.75E-05	5.75E-05	5.75E-05	5.75E-05	5.75E-05	5.75E-05	5.75E-05	5.75E-05
Drying shrinkage strain	$\varepsilon_{ds,s}(t)$	-	7.56E-05	3.52E-04	3.56E-04	3.57E-04	3.58E-04	3.58E-04	3.58E-04	3.59E-04	3.59E-04	3.59E-04	3.59E-04
Total free strain of the slab	$\varepsilon_{cs,s}(t)$	-	1.13E-04	4.09E-04	4.13E-04	4.15E-04	4.15E-04	4.16E-04	4.16E-04	4.16E-04	4.16E-04	4.16E-04	4.16E-04
Difference		**-**	**4.82E-06**	**4.32E-05**	**4.61E-05**	**4.71E-05**	**4.76E-05**	**4.79E-05**	**4.81E-05**	**4.82E-05**	**4.83E-05**	**4.84E-05**	**4.85E-05**

created by the composite action. As a result, the strains up to this point do not affect the relative creep and shrinkage of the components. However, this effect is considered after the hardening of the slab is initiated. To investigate this phenomenon, the free strains of the precast beams after the casting of the slab are compared to those of the top slab at different stages of the bridge's life.

A comparison of the strain values provided in Table 7.1 reveals that the maximum difference occurs at the end of the bridge's service life when the strains are $4.65 \cdot 10^{-4}$ and $4.16 \cdot 10^{-4}$ for the beams and the slab, respectively. Once the slab has reached its total deformation, the beams tend to shorten more, which is partially restrained by the top slab. As a result, part of the prestress is transferred to the slab, causing it to compress and creep.

Expressing this effect as prestress losses, the constraint of the beam deformation corresponds to smaller losses than the one calculated based on the free strain of the beams. To quantify this effect, an estimation of the prestress losses accounting for the interaction between the structural members is calculated for the end of the bridge's life span at 100 years when it is considered that the maximum losses have been developed.
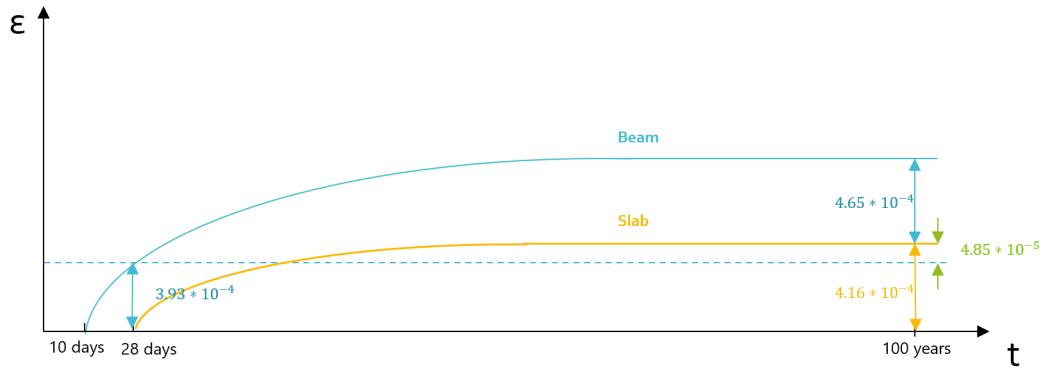
Figure 7.3: Schematic representation of free stains development for the precast beams and top slab

According to Appendix F, the prestress losses for the unconstrained creep and shrinkage of the beam $(8.58 \cdot 10^{-4})$ at the end of the bridge life are equal to $\Delta P_{c+s} = 167.22 N/mm^2$. The creep and shrinkage strain noted at the beams before the slab casting equals $3.93 \cdot 10^{-4}$, corresponding to prestress losses $\Delta P_1 = 79.57 N/mm^2$. From the point of casting of the top slab up to the point where the maximum value of the free strain of the slab is reached $(4.16 \cdot 10^{-4})$, the losses in prestress are calculated as follows, $\Delta P_2 = \frac{4.16 \cdot 10^{-4}}{8.58 \cdot 10^{-4}} \cdot 167.22 = 81.08 N/mm^2$.

The maximum remaining shrinkage is $4.65 \cdot 10^{-4} - 4.16 \cdot 10^{-4} = 4.85 \cdot 10^{-5}$. Assuming that half of the equivalent losses are restrained, $\Delta P_3 = 0.5 \cdot \frac{4.85 \cdot 10^{-5}}{8.58 \cdot 10^{-4}} \cdot 167.22 = 4.73 N/mm^2$.

Therefore, the total losses are calculated as,

$\Delta P = \Delta P_1 + \Delta P_2 + \Delta P_2 = 76.57 + 81.08 + 4.73 = 162.38 N/mm^2$.

Based on the investigated case, it is apparent that the relative creep and shrinkage of the precast beams and the cast-in-situ slab do not cause a significant difference between the calculated prestress losses. As both calculations have yielded comparable results, accounting for the interaction of the structural components is not expected to affect the fatigue life of the bridge significantly. However, it should be noted that the analysis of this particular parameter is case-dependent. Hence, its importance for the fatigue analysis must be independently assessed for each bridge under evaluation. In case studies where the effect of this parameter is more pronounced, the prestress losses and the calculated fatigue life of the structure could be highly affected.

7.8 Material degradation due to cyclic creep

Ensuring the optimal design and evaluation of concrete structures requires a detailed consideration of all potential deterioration mechanisms, including those subject to time and cycle-dependent effects. One such effect is repeated loading, which can significantly impact the performance of these structures. Concrete fatigue is a continuous and progressive process that alters the mechanical properties of concrete, increasing permanent strains while decreasing stiffness. The distribution of strains in the cross-section of eccentrically loaded concrete specimens can be affected by fatigue loading, leading to stress transfer from the most initially damaged compression zone to less fatigued areas. As a result, the specimens may exhibit an increase in the resistant number of load cycles.

In order to account for the effect of this parameter on the fatigue life of the bridge, the model proposed by Zanuy, Albajar, and De la Fuente 2009 was employed to determine the change of material properties over the beam's height. This model utilises a time-dependent material model to capture the behaviour of concrete when exposed to uniaxial compressive cyclic loading. As described in Section 2.6.10, the fatigue values of concrete under uni-axial compression can be applied to the compressive zone of the beams. This consideration is also followed in this parameter assessment to calculate the effect of the cyclic loading on the material properties of the beam.

To determine the stress-strain state of concrete at the beginning of the fatigue loading ($N = 1$) and the envelope of the fatigue process, the model utilises the $\sigma - \varepsilon$ relationship of statically loaded concrete. This relation is obtained by the normal concrete' stress-strain curve as this is given by Model Code MC90:

$$\sigma = \frac{E_c \frac{\varepsilon}{f_c} - \left(\frac{\varepsilon}{\varepsilon_c}\right)^2}{1 + \left(E_c \frac{\varepsilon_c}{f_c} - 2\right)\frac{\varepsilon}{\varepsilon_c}} f_c \tag{51}$$

$$\sigma = \left[\left(\frac{1}{\varepsilon_{lim}/\varepsilon_c}\xi - \frac{2}{(\varepsilon_{\lim}/\varepsilon_c)^2}\right)\left(\frac{\varepsilon}{\varepsilon_c}\right)^2 + \left(\frac{4}{\varepsilon_{\lim}/\varepsilon_c} - \xi\right)\right]^{-1} f_c \tag{52}$$

$$\xi = \frac{4\left[\left(\frac{\varepsilon_{lim}}{\varepsilon_c}\right)^2\left(E_c\frac{\varepsilon_c}{f_c}-2\right)+2\frac{\varepsilon_{lim}}{\varepsilon_c}-E_c\frac{\varepsilon_c}{f_c}\right]}{\left[\left(E_c\frac{\varepsilon_c}{f_c}-2\right)\left(\frac{\varepsilon_{lim}}{\varepsilon_c}\right)+1\right]^2} \tag{53}$$

where,

f_c the compressive strength of concrete,

E_c the initial value of tangent modulus of deformation,

ε_c the strain corresponding to peak stress and

ε_{lim} the strain at $0.5f_c$.
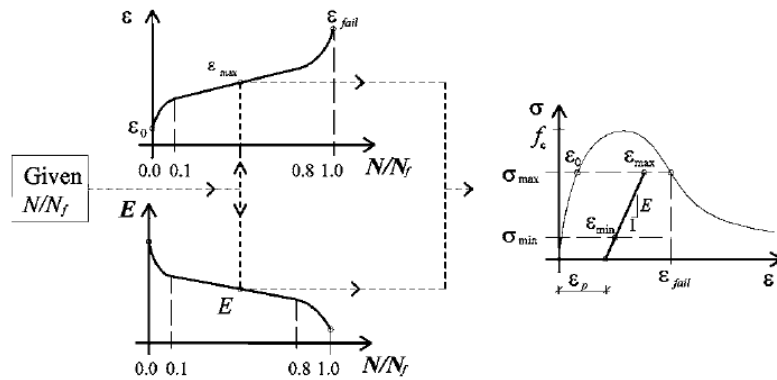
Figure 7.4: Theoretical model scheme (Zanuy, Albajar, and De la Fuente 2009).

For the time-dependent behaviour of concrete, two variables are proposed, namely the concrete stiffness E and the maximum stain ε_{max}. The two variables are employed to describe the state of the material at the investigated point of the fatigue life. It is noted that in the proposed model, each load cycle is characterised by the maximum and minimum stresses and is based on the assumption that the concrete presents a linear unloading path, as illustrated in Figure 7.4.

The model acknowledges the inefficiency of reproducing the fatigue process cycle by cycle. Thus, analytical expressions have been proposed for both the maximum strain and the modulus of deformation, considering the number of cycles and loading conditions. The proposed equations comply with the three stages of the concrete fatigue process, defined by transition points at 10% and 80% of the fatigue life. Parabolic relations are used to describe the initial and final stages of fatigue, whereas a linear expression is utilised for the intermediate stage.

The following expressions define the strain development curve, wherein the maximum strain is

determined relative to the initial strain of the first loading cycle.

$$\frac{\varepsilon_{\max}}{\varepsilon_0}\left(\frac{N}{N_f}\right) = 1 + A\frac{N}{N_f} + B\left(\frac{N}{N_f}\right)^2 ; \quad 0.0 \leq \frac{N}{N_f}0 < 0.1 \tag{54}$$

$$\frac{\varepsilon_{\max}}{\varepsilon_0}\left(\frac{N}{N_f}\right) = \varepsilon_{1-2} + \varepsilon_2\left(\frac{N}{N_f} - 0.1\right) ; \quad 0.1 \leq \frac{N}{N_f} < 0.8 \tag{55}$$

$$\frac{\varepsilon_{\max}}{\varepsilon_0}\left(\frac{N}{N_f}\right) = \varepsilon_{1-2} + \varepsilon_2\left(\frac{N}{N_f} - 0.1\right) + C\left(\frac{N}{N_f} - 0.8\right)^2 ; 0.8 \leq \frac{N}{N_f} < 1.0 \tag{56}$$

with,

$$A = 20\left(\varepsilon_{1-2} - 1\right) - \varepsilon_2 \tag{57}$$

$$B = 100\left(1 - \varepsilon_{1-2}\right) + 10\varepsilon_2 \tag{58}$$

$$C = 25\left(\frac{\varepsilon_{\text{fail}}}{\varepsilon_0} - \varepsilon_{1-2} - 0.9\varepsilon_2\right) \tag{59}$$

$$\varepsilon_{1-2} = \frac{1.184}{S_{\max}} \tag{60}$$

$$\varepsilon_2 = \frac{0.74037}{S_{\max}} \tag{61}$$

$$\varepsilon_2 \leq \frac{1}{0.9}\left(\frac{\varepsilon_{\text{fail}}}{\varepsilon_0} - \varepsilon_{1-2}\right) \tag{62}$$

where,

ε_0 the initial maximum strain,

ε_{1-2} the relative stain at the transition between stages 1 and 2 $(0.1N_f)$,

ε_2 the second domain's constant strain rate,

ε_{fail} the failure strain.

Similarly, the evolution of the concrete stiffness during the fatigue loading is given as follows.

$$\frac{E}{E_c}\left(\frac{N}{N_f}\right) = 1 + M\frac{N}{N_f} + P\left(\frac{N}{N_f}\right)^2; \quad 0.0 \leq \frac{N}{N_f} < 0.1 \tag{63}$$

$$\frac{E}{E_c}\left(\frac{N}{N_f}\right) = T + E_2\frac{N}{N_f}; 0.1 \leq \frac{N}{N_f} < 0.8 \tag{64}$$

$$\frac{E}{E_c}\left(\frac{N}{N_f}\right) = Q + R\frac{N}{N_f} + S\left(\frac{N}{N_f}\right)^2; \quad 0.8 \leq \frac{N}{N_f} < 1.0 \tag{65}$$

where,

$$M = -20 - E_2 + 20\left(\frac{E}{E_c}\right)_{1-2} \tag{66}$$

$$P = 100 + 10E_2 - 100\left(\frac{E}{E_c}\right)_{1-2} \tag{67}$$

$$T = \left(\frac{E}{E_c}\right)_{1-2} - 0.1E_2 \tag{68}$$

$$Q = A + 0.8E_2 \tag{69}$$

$$R = E_2 \tag{70}$$

$$S = 25 \left(\frac{E_{\text{fail}}}{E_c} - A - E_2 \right) \tag{71}$$

$$\left(\frac{E}{E_c} \right)_{1-2} = \begin{cases} (0.0912 + 8.19 S_{\text{min}}) + (0.8388 - 8.19 S_{\text{min}}) \, S_{\text{max}}; S_{\text{min}} \leq 0.10 \\ \\ 0.93 \quad ; S_{\text{min}} > 0.10 \end{cases} \tag{72}$$

$$\tag{73}$$

$$E_2 = \begin{cases} \frac{0.246}{1 - S_{\text{max, lim}}} \left(S_{\text{max, lim}} - S_{\text{max}} \right) ; \quad S_{\text{max}} > S_{\text{max, lim}} \\ \\ 0; \qquad\qquad\qquad\qquad S_{\text{max}} \leq S_{\text{max, lim}} \end{cases} \tag{74}$$

$$\tag{75}$$

$$\frac{E_{\text{fail}}}{E_e} = \begin{cases} 0.41 + 3.477 S_{\text{min}} ; \quad S_{\text{min}} < 0.044 \\ \\ (31.464 S_{\text{min}} - 0.8221) + (0.7758 - 17.608 S_{\text{min}}) \frac{\varepsilon_{\text{fail}}}{\varepsilon_c} ; 0.044 \leq S_{\text{min}} < 0.10 \\ \\ 2.3243 - 0.985 \frac{\varepsilon_{\text{fail}}}{\varepsilon_c} ; \quad S_{\text{min}} \geq 0.10 \end{cases} \tag{76}$$

$$S_{max,lim} = 0.3912 + S_{min} \tag{77}$$

where,

E_c \qquad the starting stiffness value,

$(E/E_c)_{1-2}$ \qquad the relative stain at the transition between stages 1 and 2 $(0.1 N_f)$,

E_2 \qquad the constant rate of stage 2,

(E_{fail}/E_c) \qquad the deformation modulus at failure.

Fatigue in concrete components leads to a redistribution of stresses, whereby each material fi-

bre undergoes a process of variable stress limits. As a result, direct application of the relevant relations is not feasible. Instead, the process is divided into shorter loading cycles, each corresponding to a specific period wherein the stress limits can be assumed as constant. To connect these cycles, the concept of the equivalent number of cycles (N_{eq}) is introduced as an accumulation rule. N_{eq} represents the number of loading cycles with constant maximum and minimum stress limits ($\sigma_{max}, \sigma_{min}$) that need to be applied in a fatigue process with constant limits to reach the total strain ε_{max}.

The method of equivalent loading cycles is demonstrated in Figure 7.5 for a loading history comprising two distinct stress level combinations ($\sigma_{max}, \sigma_{min}$). $N_{eq,1}$ is the number of load cycles required to generate a total strain $\varepsilon_{max,1}$ under stress levels ($\sigma_{max,2}, \sigma_{min,2}$). The equivalent number of cycles $N_{eq,1}$ is then combined with the last set of loading cycles N_2, and the resulting strain increment is determined.
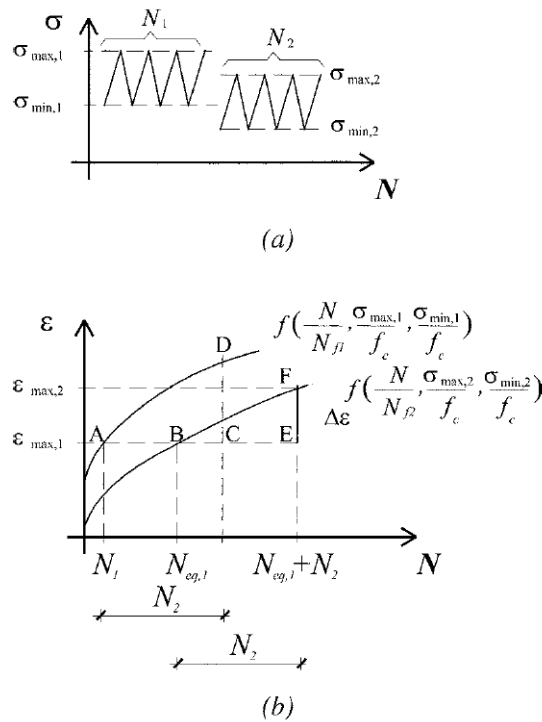
Figure 7.5: (a). Two stress level load history, and (b).strain increment based on the concept of equivalent number of cycles (Zanuy, Albajar, and De la Fuente 2009).

As part of the investigated parameters, this study aspired to investigate the effect of this material degradation on the fatigue life of the investigated bridge. Given the constraints of time,

certain simplifications have been made in the analysis process. Specifically, the analysis has been conducted by considering the loading case that results in the most significant impact on the structure, which pertains to the last vehicle of the Fatigue Load Model 4b in the scenario of two vehicles simultaneously moving over the bridge. For this load case, the effect of the first load cycle ($N = 1$) is obtained by following the analysis process described in Section 6.1. Specifically, the global and cross-sectional analyses are conducted, resulting in the stress and stress distributions that will be used to calculate the degradation of the material under cyclic loading.

As the stress distribution presents a variation over the beam height, the values of maximum and minimum stresses are different for each fibre. To account for this variation, the beam cross-section was divided into multiple layers with a height of 10mm. The maximum and minimum stress levels were considered constant along the layer height, averaging the corresponding stress values. This way, the degradation of the material was individually calculated for each layer.

As aforementioned, the fatigue process needs to be divided into shorter periods to better account for the redistribution of stresses and the variation of the stress limits during fatigue loading. The analysis time was set at five years, during which the stresses at each level were considered constant.

An additional simplification adopted in this analysis refers to the redistribution of stresses in the longitudinal and lateral directions. In a simply supported structure, the stress distribution over the beam height is not constant along the beam, being dependent on the cross-section's location in the longitudinal direction. As the maximum stress value is noted at the top compressive fibre at the midspan of the beam, the effect of material degradation is expected to be more significant at this location, resulting in a larger reduction of stiffness. Therefore, the stresses are redistributed from the most damaged part towards the stiffer lower beam layers and edges. Similarly, the stresses are redistributed in the lateral direction from the most critical beams to the adjacent less damaged beams.

Calculating the effect would require multiple calculations along the beam length, which would be further increased by the number of beams. The time required for this process would be

added to the time required to complete the finite element global analysis of the bridge using the DIANA software, which takes six hours. To reduce the analysis time and make the application feasible for practical applications, a more simple and conservative approach was followed. In this approach, it is considered that the redistribution of loads occurs only in the midspan cross-section of the most critical beam, not accounting for the redistribution in the longitudinal and transverse directions.

The global analysis was only conducted at the beginning of the analysis process to obtain the maximum and minimum moments used to calculate the stress distribution at the midspan of the beam. Starting from the initial stress, the above equations were used to calculate the change in the material properties over the beam height. The reduced stiffness of each layer was then input in IDEA Statica, where the cross-sectional analysis was performed, resulting in the new stress and strain distributions. The maximum stress and minimum stress levels, along with the maximum strains and the reduced material stiffness, were then used as starting points in calculating the material degradation occurring in the subsequent period of time. The effect of the previous set of cycles was accounted for in the subsequent calculation by employing the concept of equivalent load cycles.

This process was repeated for 30 years to determine the effect of material degradation on the fatigue life of the bridge. The stress distribution and the fatigue damage caused on the beam were compared to those determined in the basic case by the investigated vehicle.
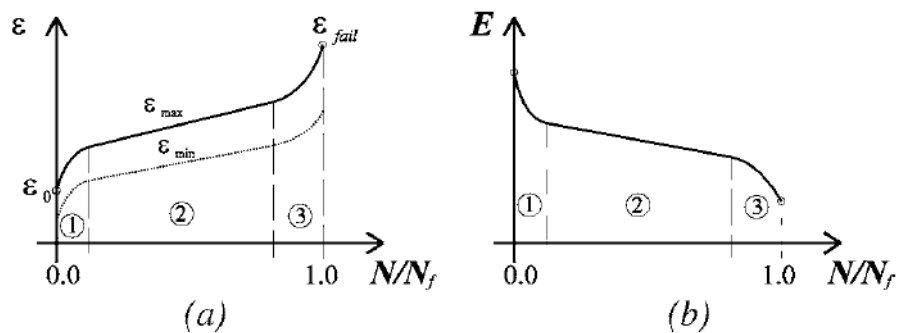
Figure 7.6: Schematic variation of (a). strains, and (b). stiffness, with the cycle ratio (Zanuy, Albajar, and De la Fuente 2009).

114

8   Results

Upon completion of the global and cross-sectional analyses of the bridge, the maximum and minimum stress distributions were determined at the midspan of the precast beams. The corresponding σ_{max} and σ_{min} were then utilised to calculate the fatigue life of each beam in accordance with the regulations of Section 3.4. The critical beam, which will fail first due to fatigue, determined the fatigue life of the bridge. It is worth noting that for each case, the critical beam corresponds to the specific analysed loading configuration, as the position of the traffic load significantly impacts the distribution of loads in the lateral direction and, thus, the stress distribution. To assess the influence of each parameter, the resulting fatigue life of its analysis was compared to the one obtained from the basic case. Moreover, the parameters were independently evaluated to determine their effect on the fatigue life of the bridge.

Basic case

The fatigue life analysis of the basic case was carried out using the parameters outlined in Section 7.1. The results of the analysis, which consider the fatigue life of each beam, have been presented in Graph 8.1. According to the results, three beams exhibit a fatigue life that is shorter than the bridge's 100-year lifespan. The critical beam, which determines the fatigue life of the structure for the applied loading conditions, is Beam 4. The fatigue failure will occur when the first beam reaches the end of its fatigue life, which, in this case, is expected to happen after 57 years. Analysing the results in the lateral direction, it is evident that the beams closest to the traffic lanes (right edge of the bridge) have a significantly shorter fatigue life. In the assessed lane configuration, girders 3 to 5 are directly located beneath the traffic lanes and are the heaviest loaded ones, presenting a shorter fatigue life. However, moving away from the traffic lanes, the fatigue life of the beams significantly increases, with the resulting value showing that these beams will practically never fail due to fatigue (for the analysed loading conditions).
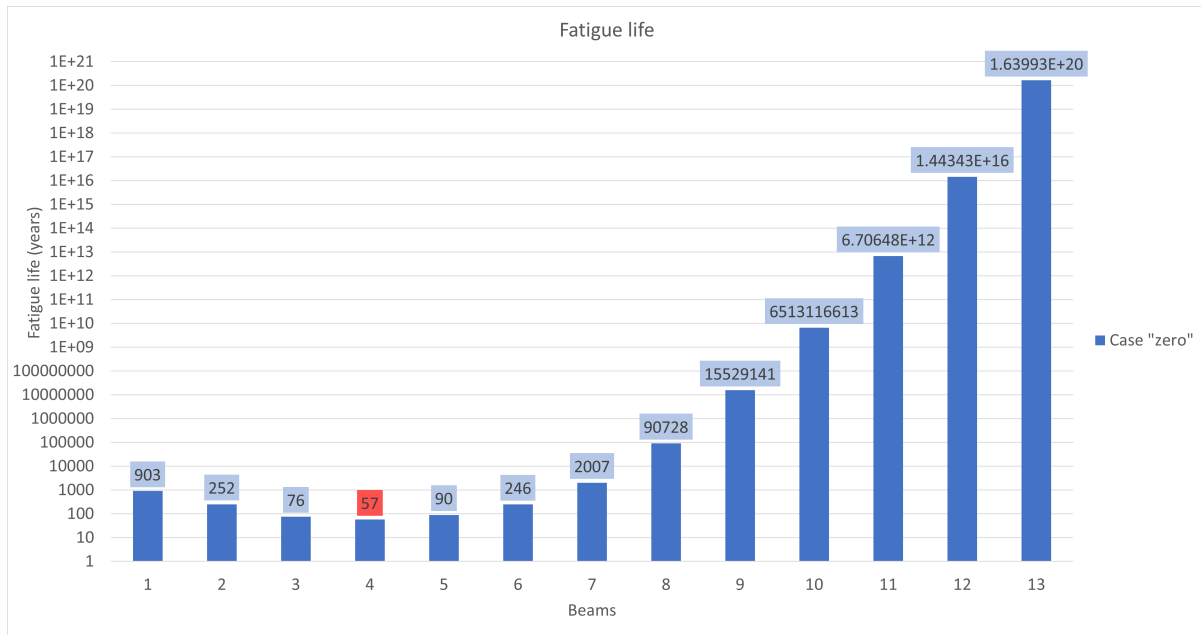
Figure 8.1: Fatigue life of the precast beams for the basic case (Case "zero").

Prestresss losses

One of the analysed cases assumed that there were no prestress losses throughout the bridge's lifespan, meaning that the prestress remained at its initial level of $1394 N/mm^2$. The resulting fatigue life of the precast beams for this scenario is 5309 years. Beam 4 was again identified as the critical beam determining the fatigue life of the bridge for the same loading configuration. The failure to account for prestress losses increased the structure's fatigue life by more than 90 times, indicating that fatigue failure is unlikely to occur. Although this analysis is not a reflection of a realistic scenario, it is valuable in demonstrating the impact of prestress losses on the fatigue assessment of the bridge and underlining the importance of precise calculations.

A more detailed analysis was conducted considering the gradual development of prestress losses at each decade, as outlined in Section 7.2. The resulting fatigue lives of the beams are presented in Graph 8.2, with Beam 4 identified as the critical beam that fails first. The prestress losses considered in this analysis are smaller than the maximum losses (basic case), resulting in a more favourable stress distribution and an 18% increase in the bridge's fatigue life from 57 to 67 years. The effect of this change is illustrated in Graph 8.2, where the most loaded beams show the most significant improvement, while the remaining beams are less affected.

Graphs 8.3 and 8.4 demonstrate the progression of the fatigue unity check over the bridge's life and the contribution of each decade to the unity check, respectively. In the basic case where instantaneous losses are taken into account from the beginning of the bridge's life, the unity check contribution remains constant at each decade. As a result, the unity check shows a steady rate of increase over time, as depicted by a straight line in Graph 8.3. Based on this, the bridge reaches its fatigue failure (UC=1) after 57 years. On the other hand, when accounting for the gradual development of prestress losses in the fatigue analysis, the fatigue unity check contribution gradually increases and reaches its maximum value at 100 years, when the maximum prestress losses have been fully developed. Consequently, the fatigue unity check line (Graph 8.3) is slightly curved and does not exhibit a constant rate of increase. The rate appears to be smaller than the one considering the instantaneous losses, and the fatigue failure of the bridge (UC=1) occurs later in its service life (after 67 years).
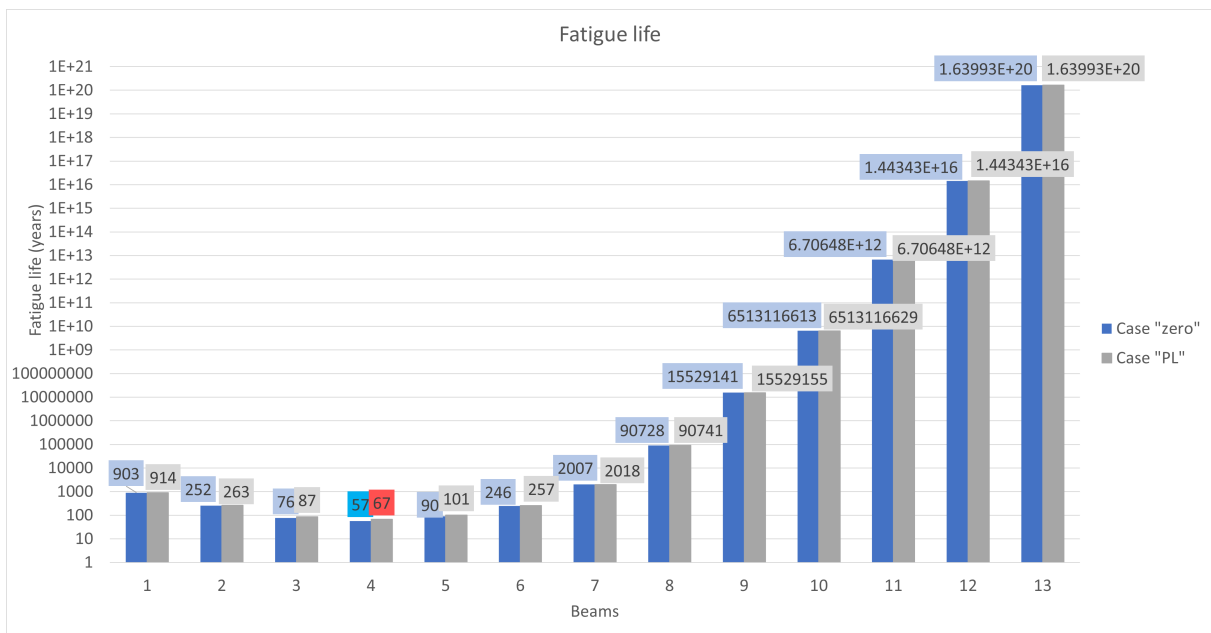
Figure 8.2: Fatigue life of the precast beams for the "Actual Prestress Losses (Case "PL")" case.
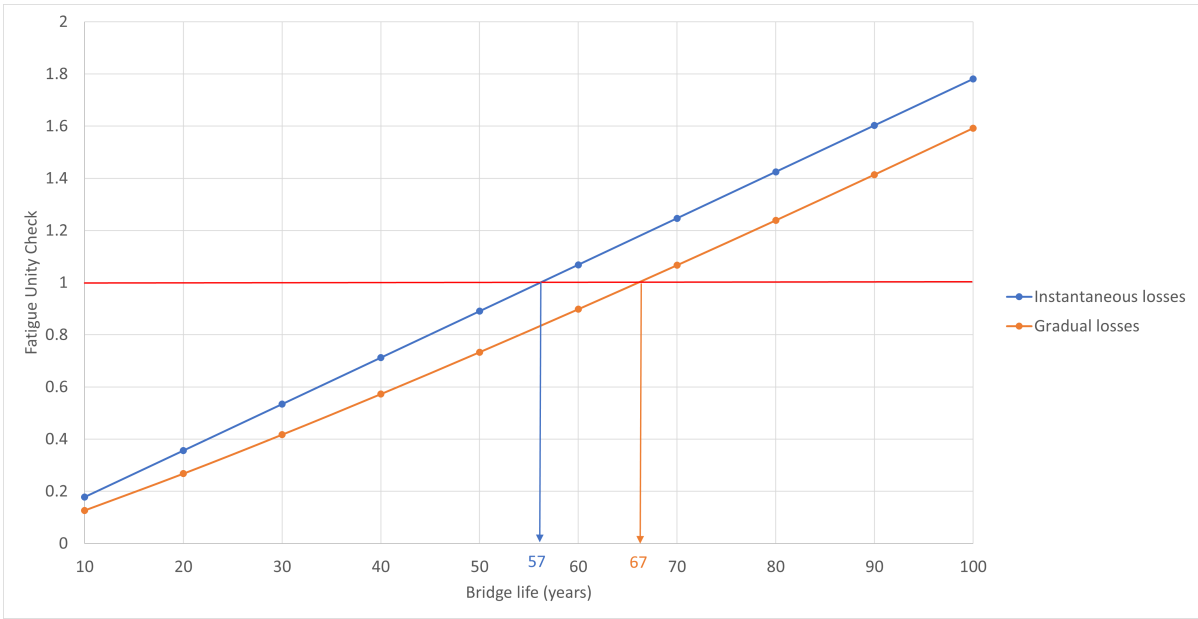
Figure 8.3: Development of the fatigue unity checks for the "Basic case" (instantaneous losses) and the "Actual Prestress Losses" case (gradual losses).
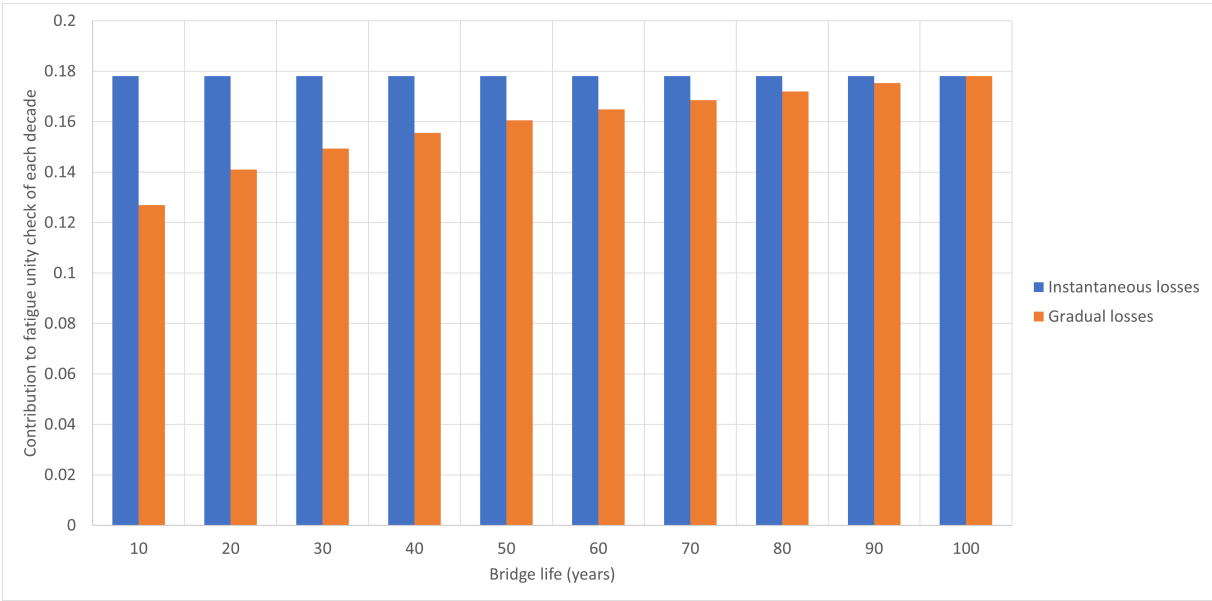
Figure 8.4: Contribution to the fatigue unity checks of the critical beam for the "Basic case" (instantaneous losses) and the "Actual Prestress Losses" case (gradual losses).

Increasing traffic volume

The increase in traffic volume over the years is an important factor that affects the fatigue life of a bridge. Graph 8.5 presents the results of the analysis conducted for the most loaded

beams. Notably, this parameter has varying impacts on the bridge girders. Specifically, beams that previously failed due to fatigue within the bridge's service life show an increase in fatigue life, with higher fatigue life values noted. Beam 4, which has the shortest fatigue life, primarily determines the fatigue life of the entire bridge. The analysis reveals a positive effect of this parameter on the fatigue life of the bridge, which has increased by 9% (from 57 to 62 years).
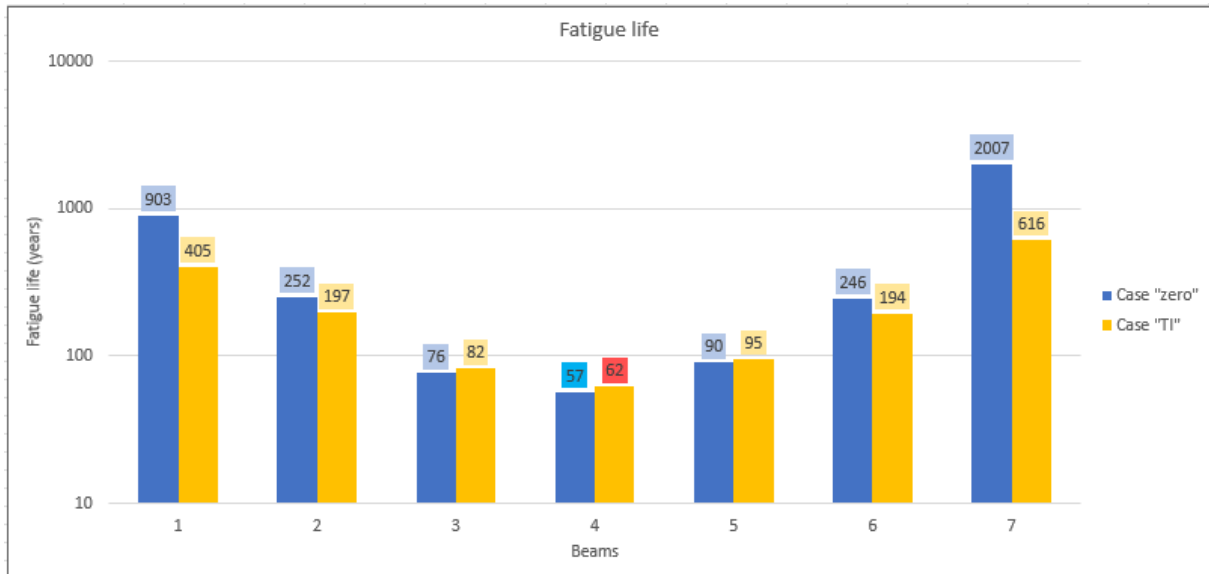
Figure 8.5: Fatigue life of the precast beams 1 to 7 for the "Increase of the traffic volume increase (Case "TI")" case.

Orthotropic slab properties

The analysis of the bridge reveals that accounting for the cracking of the slab in the transverse direction can result in a different distribution in this direction, leading to a decrease in the bridge's fatigue life. Graph 8.6 displays the resulting fatigue lives of the beams, which demonstrate that a reduction of stiffness in the lateral direction results in a smaller distribution of loads in that direction. Consequently, the most heavily loaded beams are subject to even higher loads, which significantly impacts their fatigue life, leading to a shorter lifespan of the bridge. Specifically, the fatigue life of the structure is reduced by 51%, with the fatigue failure occurring after 29 years of the bridge's life.

It's worth noting that not all beams are affected by a reduction in their fatigue life. Graph 8.6 shows that beams located under traffic lanes experience a decrease in their lives, with the

corresponding nodes of the curve moving downwards. Conversely, the opposite phenomenon is observed in the more distant beams.

In conclusion, the transverse cracking of the slab can have a significant impact on the load distribution of the bridge, leading to a decrease in its fatigue life.
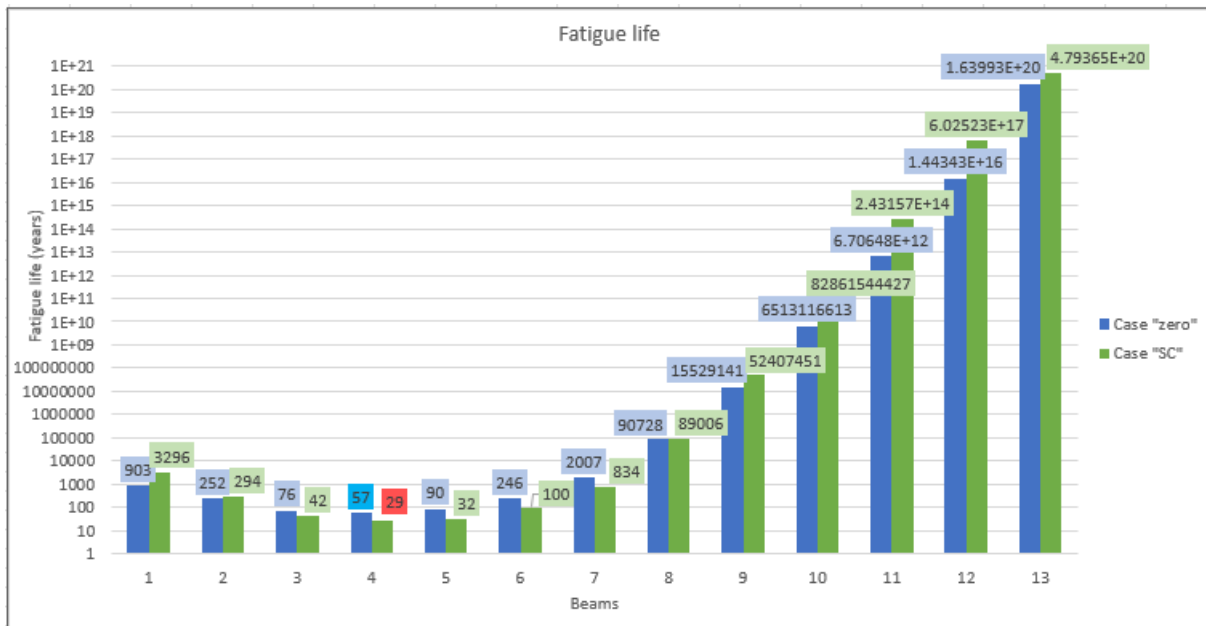
Figure 8.6: Fatigue life of the precast beams for the "Orthotropic slab properties (Case "SC")" case.

Load type

The replacement of area loads with point loads is a widely accepted engineering practice that simplifies the analysis process. Compared to area loads, point loads result in a more conservative load distribution, which can significantly impact the fatigue life of precast beams. As evidenced by Graph 8.7, precast beams located closer to the loaded lanes demonstrate reduced fatigue life. Conversely, beams located further from the traffic lanes experience a practically negligible increase in fatigue life compared to the basic case. It is worth noting that the location of the traffic lanes has not changed, making Beam 4 the critical beam in this case as well, with a fatigue life reduction of 10 years (18%).
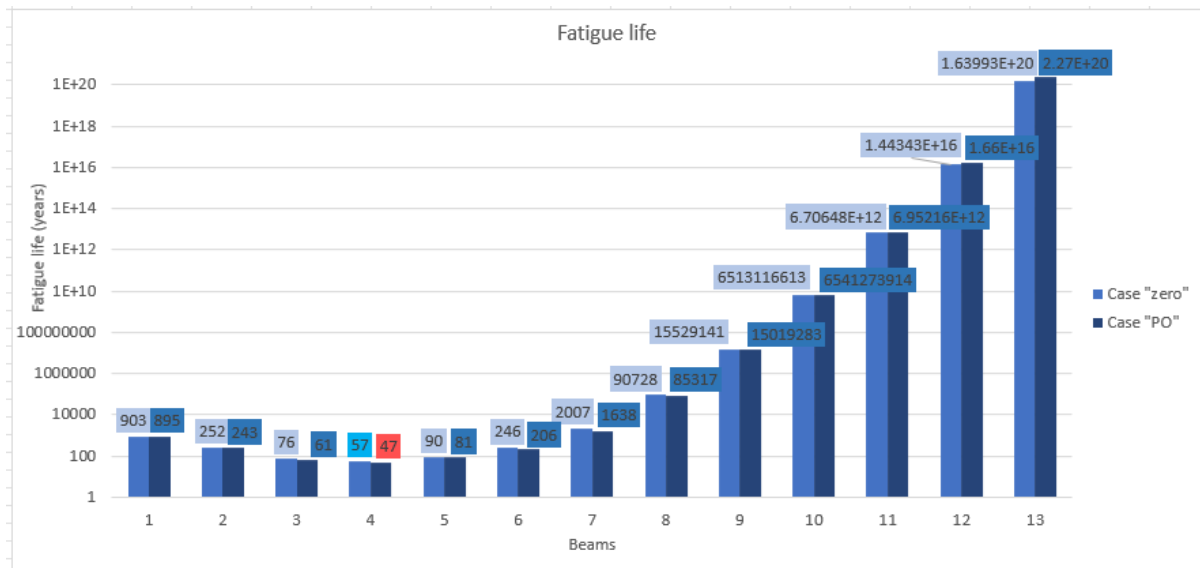
Figure 8.7: Fatigue life of the precast beams for the "Load type (Case "PO")" case.

As per the guidelines set by NEN-EN 1991-2+C1:2015/NB:2019, fatigue load vehicles are modelled using three different wheel types, which are illustrated in Figure 5.16. However, the inclusion of actual axle types during the fatigue analysis leads to a substantial increase in computational time. This consideration demands triple the number of loading cases and, in turn, triple the analysis time. Therefore, the fatigue trucks are modelled using only one wheel type in this section to investigate the influence of this simplification on the fatigue performance of the bridge.

The analysis is conducted based on the methodology followed in the analysis of the basic case and for the most critical beam, namely Beam 4. The midspan bending moments due to moving loads for both the actual wheel types of the vehicles and the single wheel type analysis are presented in Tables 8.1 and 8.2, respectively. It should be noted that wheel type A is selected for this comparison due to its smaller area, which results in a more conservative distribution of loads.

Table 8.1: Bending moments at the midspan of Beam 4 caused by moving loads - Actual wheel types analysis

Vehicle type FLM4b	Mmax [kNm]	Mmin [kNm]
Type 1 - single	194.64	-1.28
Type 1 - double	427.12	-1.19
Type 2 - single	409.92	-1.19
Type 2 - double	638.05	-1.19
Type 3 - single	394.06	-0.89
Type 3 - double	634.03	-1.53
Type 4 - single	298.12	-0.89
Type 4 - double	523.56	-1.49
Type 5 - single	329.06	-0.69
Type 5 - double	565.06	-1.19
Type 6 - single	484.16	-0.99
Type 6 - double	716.62	-1.29
Type 7 - single	585.38	-0.89
Type 7 - double	818.76	-1.19

Upon comparing the results presented in the two tables, it is evident that utilising a single type of wheel in vehicle modelling results in a slight increase in the maximum moment values. However, performing fatigue analysis based on these increased moments yields a fatigue life of 56 years, compared to 57 years in the basic case. This indicates that both methods provide almost identical predictions of fatigue life. Performing the fatigue analysis using one type of wheel would reduce the finite element analysis time to one-third while simultaneously providing the benefits of more favourable load distribution via area loads.

Table 8.2: Bending moments at the midspan of Beam 4 caused by moving loads - Single wheel type analysis

Vehicle type FLM4b	Mmax [kNm]	Mmin [kNm]
Type 1 - single	195.76	-1.28
Type 1 - double	427.93	-1.19
Type 2 - single	409.94	-1.19
Type 2 - double	637.68	-1.19
Type 3 - single	394.11	-0.89
Type 3 - double	634.08	-1.53
Type 4 - single	299.33	-0.89
Type 4 - double	524.27	-1.49
Type 5 - single	330.32	-0.69
Type 5 - double	565.98	-1.19
Type 6 - single	484.87	-0.99
Type 6 - double	716.89	-1.29
Type 7 - single	586.02	-0.89
Type 7 - double	819.07	-1.19

An overview of the resulting fatigue lives obtained from the three analyzed cases is presented in Table 8.3.

Table 8.3: Comparison of the resulting fatigue life of the bridge for the cases using different types of loads.

Case	Fatigue life (years)	Difference %
Actual wheel types	57	-
Wheel type A	56	2
Point loads	47	18

Position of traffic lanes

The assessment of fatigue life for a bridge under a different loading configuration can have a significant impact on the structure's fatigue behaviour. This is because the different loading introduces a completely different distribution of loads, causing different beams to bear greater loads. As illustrated in Graph 8.9, this effect can result in Beam 8 being the most critical component and the first to experience fatigue failure, thereby determining the overall fatigue life of the bridge. Furthermore, this altered load distribution can have a substantial influence on the bridge's fatigue life, which can be prolonged up to three times compared to the fatigue life of the basic case. In this particular case, the calculated fatigue life is 186 years, indicating that the bridge will not fail due to fatigue.
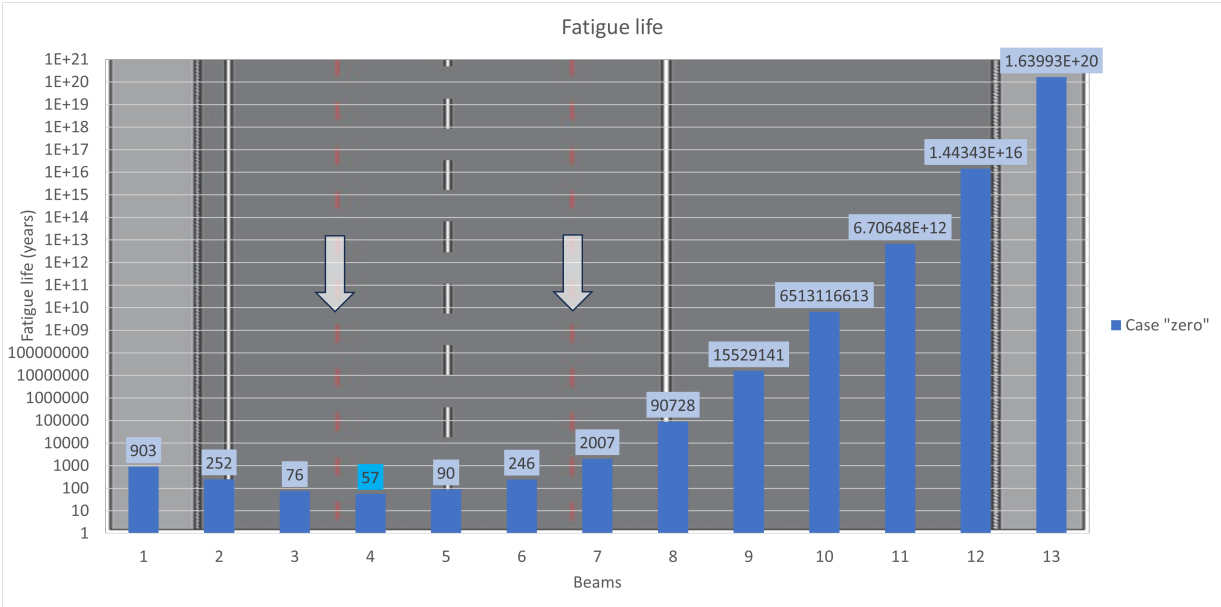
Figure 8.8: Fatigue life of the precast beams for the basic case (Case "zero") relative to the position of the traffic lanes.
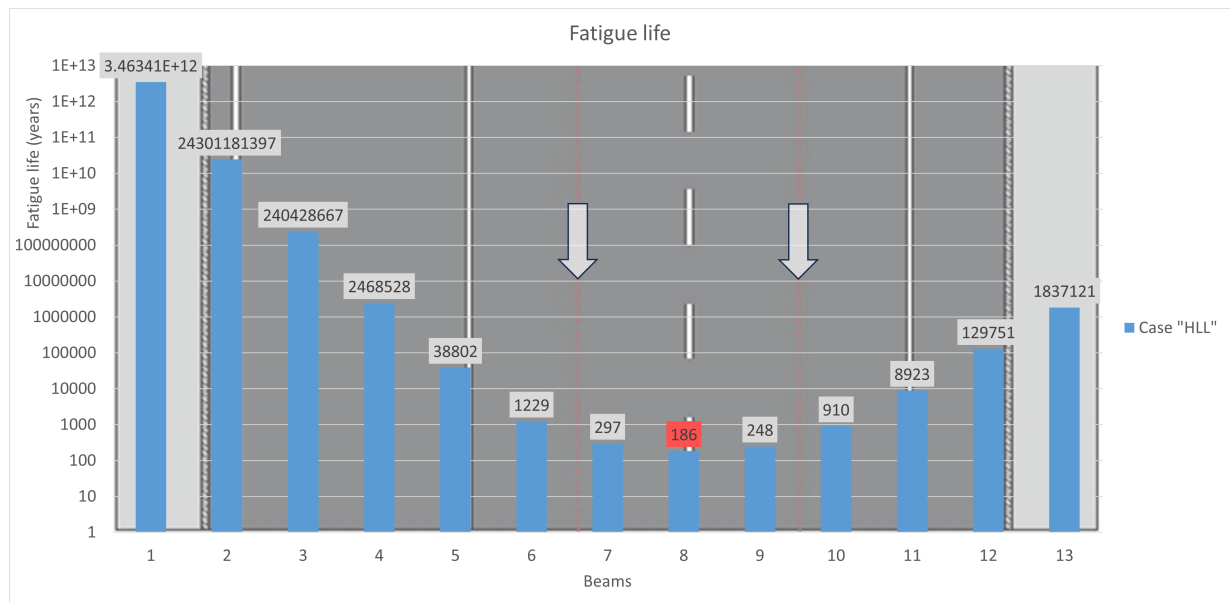
Figure 8.9: Fatigue life of the precast beams for the "Position of the traffic lanes (Case "HLL")" case relative to the position of the traffic lanes.

Fatigue load model

The Eurocode provides several fatigue load models for the fatigue analysis of bridges, as outlined in Section 5.5. The fatigue analysis of the bridge under consideration employed Fatigue Load Model 4b. This study, however, investigates the effects of using Fatigue Load Model 1 as an influencing parameter on the fatigue assessment of the structure.

The results of the fatigue life of the bridge using this loading model are presented in Graph 8.10. Each node in the graph represents the fatigue life of each beam, with the values presented in a logarithmic scale. It is clear that this loading model leads to a highly conservative analysis, causing the bridge to fail due to fatigue from the beginning of its service life. Notably, Beam 4 is the most critical beam, with a fatigue life close to zero. The fatigue life graph illustrates that the FLM1 curve is shifted downwards, with the most significant divergence in the values of the two curves occurring at the side of the bridge, which is closer to the heaviest loaded lanes. It is worth mentioning that the FLM1 presents the same loading configuration as Load Model 1, where the most unfavourable effect on the bridge occurs when the heaviest loaded lanes are positioned close to the bridge edge, as detailed in Appendix E.
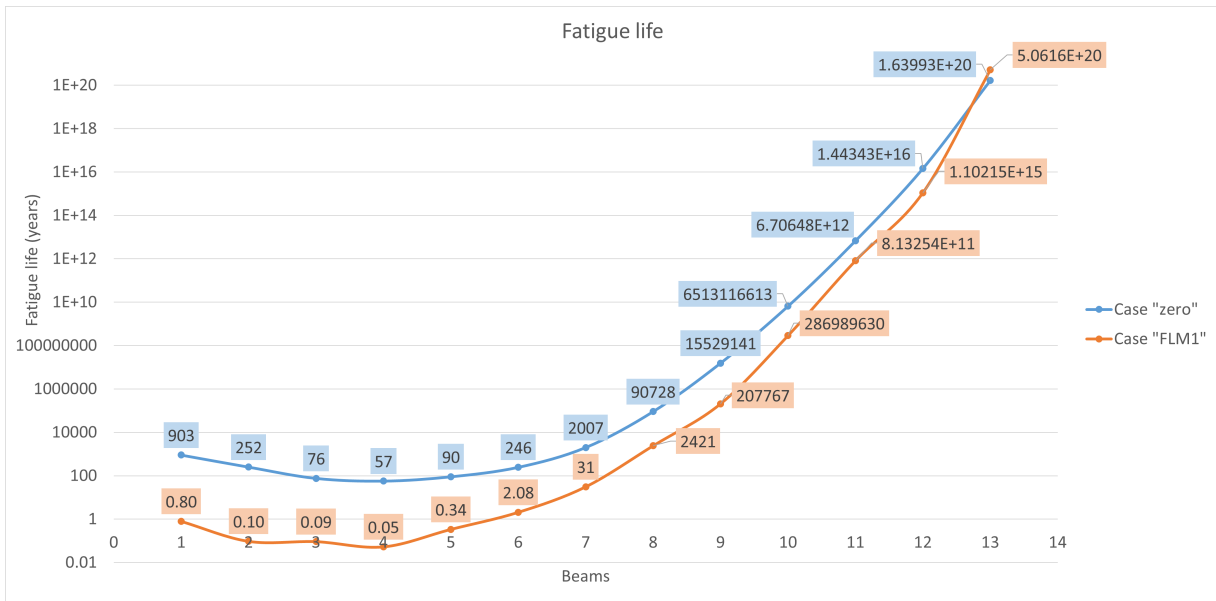
Figure 8.10: Fatigue life of the precast beams for the "Fatigue load model 1 (Case "FLM1")" case.

Graph 8.11 visually represents the impact of the parameters under investigation on the fatigue life of the bridge.
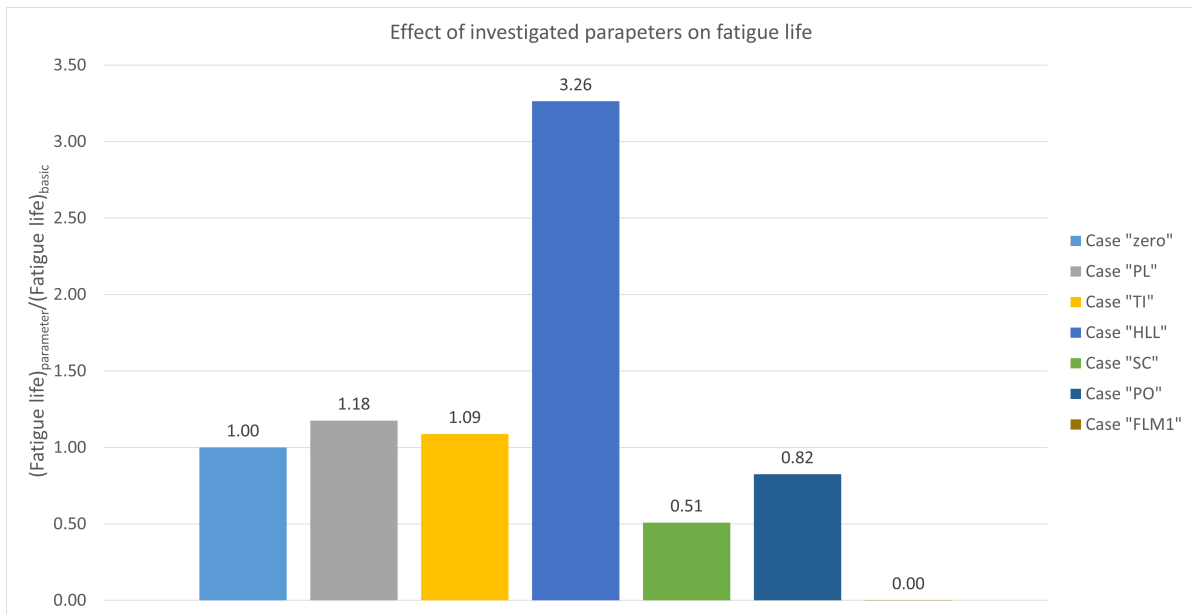
Figure 8.11: Effect of the investigated parameters on the fatigue life of the bridge.

Material degradation

As previously mentioned (Section 7.8), due to time limitations, a comprehensive analysis of the material degradation parameter for the entire lifespan of the bridge and all investigated vehicles could not be conducted. Instead, a specific period was examined, and the impact of the vehicle that had the most adverse effect on the structure was considered. The analysis of the parameter was based on the premise that the material degradation and the redistribution of stresses occurred solely at the midspan cross-section of the critical beam (Beam 4). Consequently, the results of this analysis focus on the calculated evolution of stiffness at different layers of the precast beam and the contribution of this vehicle to the fatigue unity check for the analysed period.

The material degradation was observed at the uppermost layers of the beam, where the highest stress values are noted. Table 8.4 presents the stiffness values at the top fibres of the precast beam, calculated every five years. Notably, the material degradation starts at the top of the beam and gradually extends to the lower layers. The change in material properties caused a

Table 8.4: Evolution of concrete stiffness at the top layers of the precast Beam 4

Distance from bottom fibre (mm)	Concrete stiffness					
	t=0 (N/mm^2)	t=5 years (N/mm^2)	t=10 years (N/mm^2)	t=15 years (N/mm^2)	t=20 years (N/mm^2)	t=25 years (N/mm^2)
810	38214.206	36266.617	33963.861	31736.601	29636.775	27677.340
800	38214.206	37296.994	35815.671	34046.448	32181.729	30356.395
790	38214.206	37835.444	36951.437	35447.032	33497.529	31465.339
780	38214.206	38066.851	37651.350	36697.097	35041.774	33025.027
770	38214.206	38158.972	37989.994	37522.342	36412.930	34593.237
760	38214.206	38194.116	38130.635	37938.175	37373.928	36076.253
750	38214.206	38207.106	38184.298	38112.944	37879.917	37190.272
740	38214.206	38211.771	38203.939	38178.801	38093.556	37806.045
730	38214.206	38213.397	38210.787	38202.414	38173.214	38070.197
720	38214.206	38213.947	38213.109	38210.410	38200.994	38166.555
710	38214.206	38214.126	38213.868	38213.033	38210.114	38199.391
700	38214.206	38214.183	38214.106	38213.857	38212.987	38209.777
690	38214.206	38214.200	38214.178	38214.108	38213.862	38212.954
680	38214.206	38214.205	38214.199	38214.180	38214.114	38213.867
670	38214.206	38214.206	38214.205	38214.200	38214.183	38214.120
660	38214.206	38214.206	38214.206	38214.205	38214.201	38214.186
650	38214.206	38214.206	38214.206	38214.206	38214.205	38214.203

redistribution of stresses, with the most significant stresses transferred from the most damaged part to the lower, stiffer layers of the beam. Figures 8.12 and 8.13 illustrate the evolution of the maximum and minimum stress distributions at the analysed moments, which determined the σ_{max} and σ_{min} values used to calculate the fatigue damage caused to the beam by the examined vehicle.
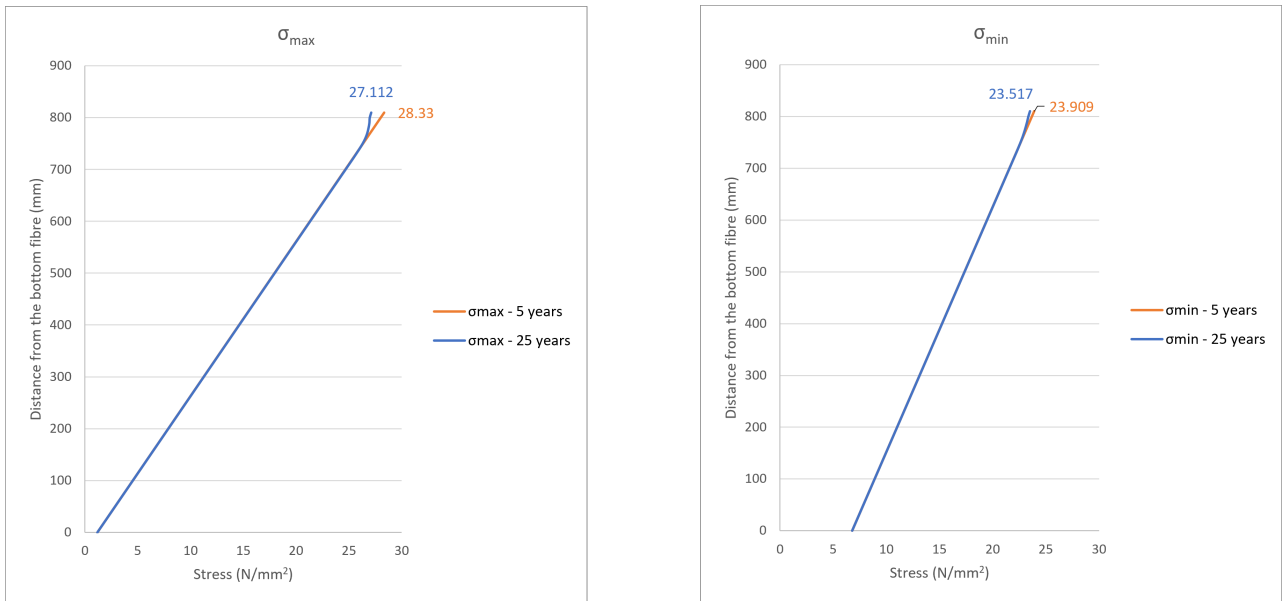
Figure 8.12: Stress distribution over the beam height at $t = 5 years$ and $t = 25 years$.
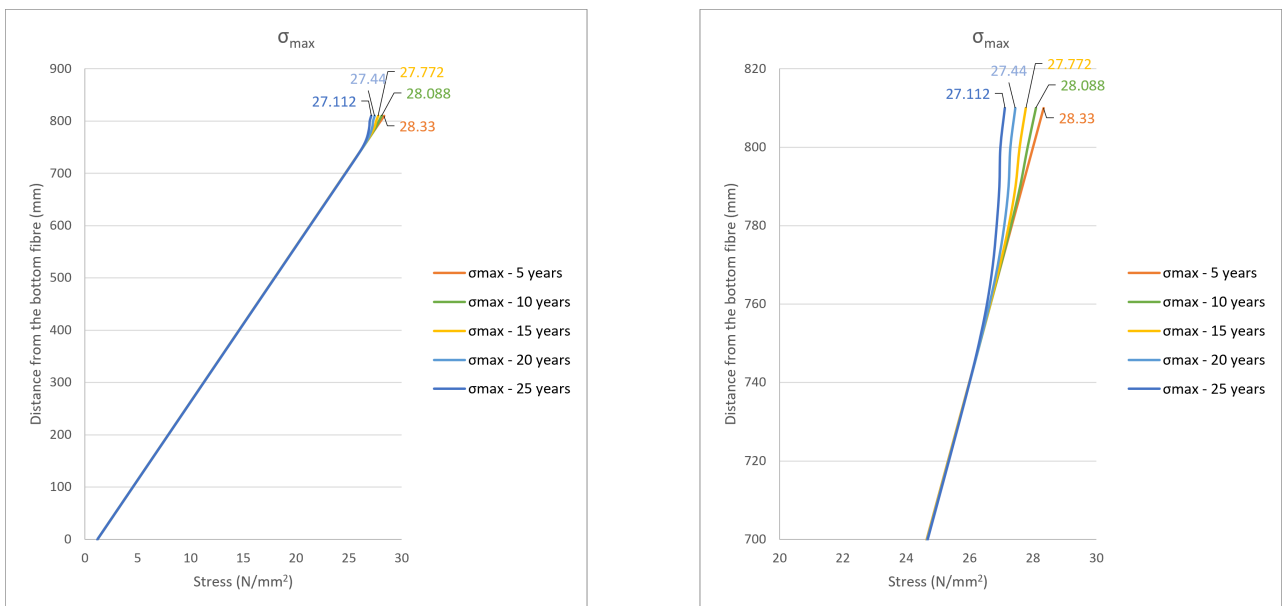
Figure 8.13: Evolution of maximum stress distribution over the beam height.

The contribution of the examined vehicle to the fatigue unity check (Equation 20) was calculated every five years. The fatigue analysis was conducted, considering that the stress levels remained constant during the examined periods. For the first five-year period, the ratio n_i/N_i was calculated based on the stress distribution of the first loading cycle $N = 1$. For the second period (5 to 10 years), the maximum and minimum stress levels were determined by the stress distributions at $t = 5 years$. The same approach was followed for the subsequent periods.

Graph 8.14 presents the calculated contribution of the investigated vehicle to the fatigue unity check over the years. It has been observed that when material degradation is taken into account, the vehicle's contribution to the fatigue check after 30 years is almost zero (0.00027). Assuming that this contribution will remain the same in the following years, the total contribution of the vehicle was calculated up to 57 years, which is the point at which the bridge will fail due to fatigue according to the basic case (Unity check $= 1$). At 57 years, the total contribution of the examined vehicle, without accounting for the material degradation due to cyclic loading (basic case), amounts to 0.5423. This implies that the contribution of the examined vehicle to the total fatigue damage is approximately 55%. However, when considering the redistribution of stresses caused by the fatigue loading, the total contribution of the vehicle is only 0.0857, representing approximately 9% of the fatigue damage. Therefore, it is evident that by totally reducing the maximum and minimum stress levels by 4.3% and 1.6% (Graph 8.14), respectively, the investigated vehicle's total contribution to the fatigue unity check can be decreased by 84%.
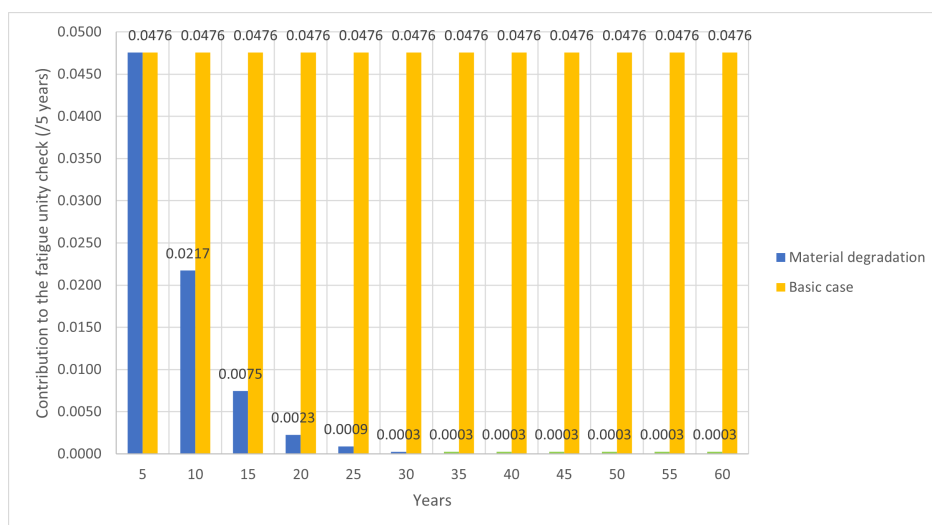
Figure 8.14: Evolution of the contribution of the investigated vehicle to the fatigue unity check.

9   Discussion

This section will present a discussion of the results obtained and the analysis considerations adopted in this study.

The findings indicate that prestress losses significantly contribute to the fatigue life of the bridge. As stress levels have an exponential impact on the fatigue life, even slight differences in stress distribution can have a significant effect on fatigue. Increasing the accuracy of prestress loss calculations by computing losses for every decade instead of using maximum losses can prolong fatigue life. For the analysed bridge, the inclusion of this parameter resulted in a considerable increase in fatigue life (18%). Incorporating this parameter in the fatigue analysis of bridges will positively affect their fatigue life. However, it is noted that the magnitude of this impact in other bridges may vary as it depends on the way that the prestress losses develop. As analytically discussed in Appendix F, the development of prestress losses depends on various parameters, such as stress level, material and geometrical properties of the structural components, age of the bridge at loading, humidity, curing time, and relaxation class of the prestressing strands. Therefore, it is clear that the gradual development of prestress losses and its impact on the fatigue life of bridges are linked to variables specific to each examined case and cannot be generalised.

Accounting for the different stress distributions of each decade can increase the post-processing effort and, consequently, the analysis time. In this study, the prestress loads are automatically calculated by IDEA Statica. Thus, this parameter's consideration influences only the time required for the cross-sectional analysis of the beams, while the more time-consuming global analysis remains unaffected. Nevertheless, accounting for the gradual development of the prestress losses in the fatigue analysis means that the cross-sectional analysis would be performed ten times.

The prestress calculation has been based on simplifications that may result in more conservative prestress losses, reducing the structure's fatigue life. Accounting for bending moments in the prestress losses calculation can result in smaller stresses at the prestressing strand level, affecting the resulting prestress losses. However, this effect is not constant along the beam length, so it

is necessary to consider different stress distributions. Such an approach would significantly increase analysis time. In this study, the calculation of the prestress losses accounting for bending moments is conducted at the most favourable cross-section. At the mid-span of the beams, the bending moment presents its highest value, reducing the stress at the prestressing level. Even for this least conservative cross-section, the consideration of bending moments was negligible and due to that, it was not accounted for in the fatigue analysis. Nonetheless, it is essential to note that this might differ in other structures assessed for fatigue. The effect of this parameter on the stress distribution depends on the magnitude of the considered moments, which in turn are determined by the construction stages, bridge geometry, material properties, the prestressing force and the height of the prestressing stands. Including the bending moments in this calculation could have a more significant effect on this calculation and, in turn, the fatigue check.

Similarly, in the case under investigation, the composite action of the structural components was found to have a minor effect and was therefore not considered in the calculation of prestress. This parameter would have increased analysis time without significantly affecting the bridge's fatigue life. However, it is necessary to note that this parameter varies for different structures. As the parameter of prestress losses, the influence of composite action on prestress losses depends on various parameters unique to each analysed case, resulting in an effect on fatigue life that can be either significant or negligible, depending on the developed strains. Generally, the consideration of composite action can result in smaller prestress losses, which, according to their magnitude, can influence fatigue. For this reason, this parameter should be evaluated on an individual basis for each structure to determine its importance and contribution to fatigue performance.

Incorporating the increase in traffic volume over the lifespan of a bridge can potentially have a positive impact on its fatigue life, as demonstrated in the investigated case. Although its consideration did not necessarily lead to a significant increase in fatigue life based on the outcome, it was still beneficial and extended the lifespan of the bridge. Accounting for this factor in the fatigue analysis does not increase the design and computational time, as it is solely related to the post-processing of the results.

However, it is essential to note that the impact of the increasing trend of traffic volume on the

fatigue analysis of the bridge depends on its construction date. Graphs 9.1 and 9.2 illustrate the effect of this parameter on a bridge built many years before 2050 and one constructed near 2050, respectively. Both bridges have a lifespan of 100 years. It is evident that when the construction date is further away from the turning point (2050), the structure is primarily affected by the positive influence of the increasing traffic rate. Conversely, for structures erected closer to 2050, the opposite holds. Therefore, the effect of the change in traffic volume on the fatigue analysis of a bridge cannot be deemed consistently positive or negative since it can either prolong or shorten the fatigue life of the structure.
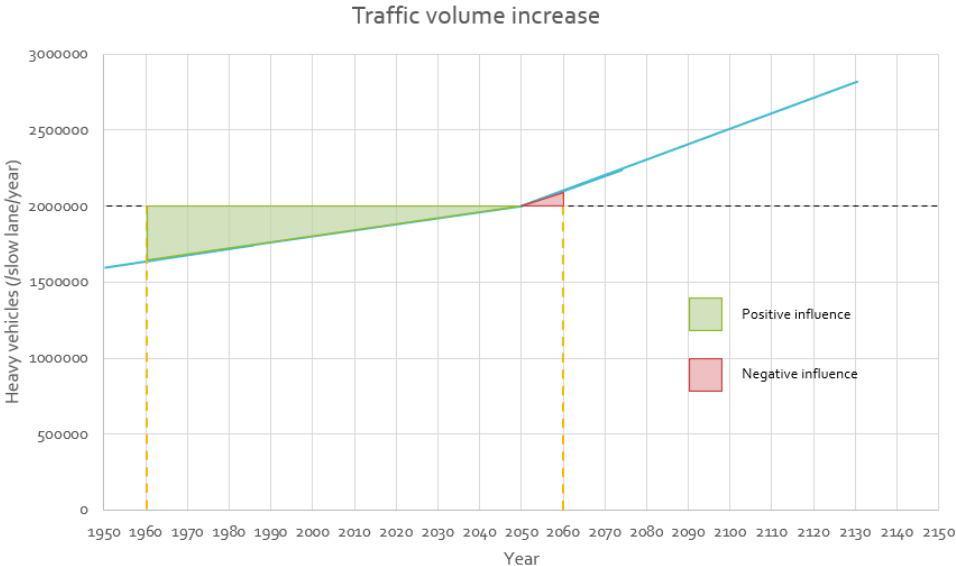
Figure 9.1: Effect of the increase of traffic rate on the fatigue life - Case 1
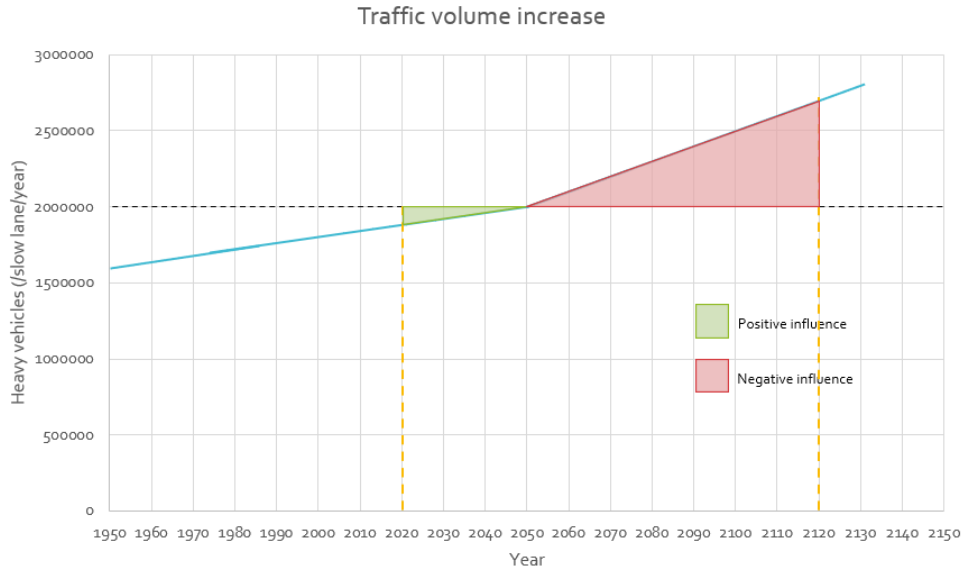
Figure 9.2: Effect of the increase of traffic rate on the fatigue life - Case 2

The fatigue check is performed using the Equation 20 (NEN-EN 1992-2:2005/C1:2008). In this relation, the percentage (p_i) of each vehicle in the total traffic volume is determined by the utilised fatigue load model. This percentage remains unaltered, provided that the fatigue assessment is conducted using the same load model. Consequently, the unity check in the fatigue analysis of a bridge with specific loading conditions is solely influenced by the traffic volume that the bridge sustains, as presented in the ensuing relation:

$$UC = V_{tot} \sum \frac{p_i}{N_i} = V_{tot} \left(\frac{p_1}{N_1} + \frac{p_2}{N_2} + ... + \frac{p_n}{N_n} \right) \tag{78}$$

As the traffic volume expands over time, the total traffic volume carried by each structure relies on the year that the bridge was constructed. The fatigue life of the bridge (d), taking into account the impact of the increasing traffic rate, can be directly determined using the ensuing equations, where x is the year of the bridge's erection and y is the fatigue life of the bridge calculated with a constant traffic volume ($V_{constant}$) per year (basic case):

(a). Bridges constructed before 2050 ($x < 2050$) and, according to the basic case, fail due to

fatigue before 2050 ($x + y < 2050$) (Figure 9.3):

$$0.001 \cdot V_{constant} \cdot d^2 + 0.002 \cdot V_{constant} \cdot d \cdot x - 3.1 \cdot V_{constant} \cdot d = V_{constant} \cdot y \qquad (79)$$
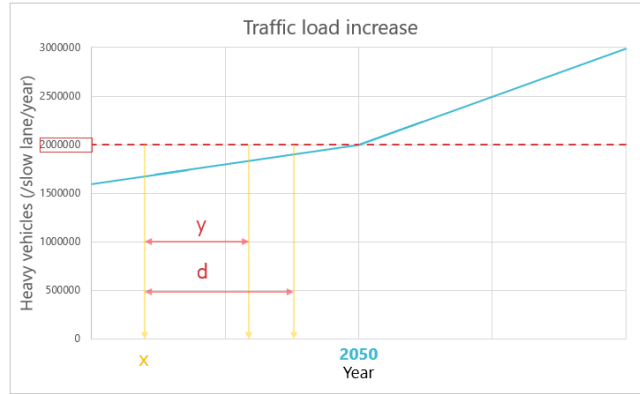
Figure 9.3: Effect of the increase of traffic rate on the fatigue life - Bridges constructed before 2050 ($x < 2050$) and, according to the basic case, fail due to fatigue before 2050 ($x + y < 2050$).

(b). Bridges constructed before 2050 ($x < 2050$) and, according to the basic case, fail due to fatigue at or after 2050 ($x + y \geq 2050$) (Figure 9.4):

$$0.0025 \cdot V_{constant} \cdot d^2 + 0.005 \cdot V_{constant} \cdot d \cdot x + 0.0015 \cdot V_{constant} \cdot x^2 - 9.25 \cdot V_{constant} \cdot d$$

$$-6.15 \cdot V_{constant} \cdot x + 6303.75 \cdot V_{constant} = V_{constant} \cdot y \qquad (80)$$
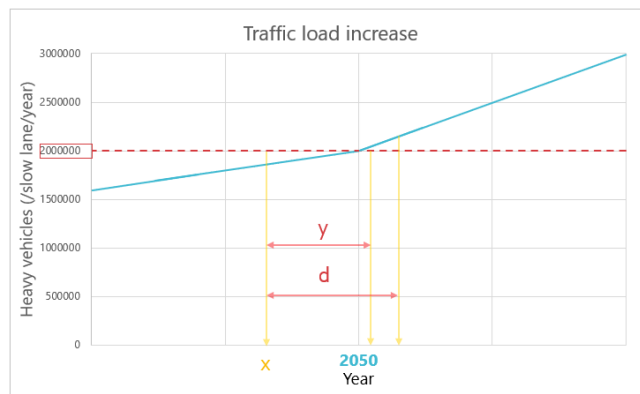
Figure 9.4: Effect of the increase of traffic rate on the fatigue life - Bridges constructed before 2050 ($x < 2050$) and, according to the basic case, fail due to fatigue at or after 2050 ($x + y \geq 2050$).

(c). Bridges constructed at or after 2050 ($x \geq 2050$) (Figure 9.5):

$$0.0025 \cdot V_{constant} \cdot d^2 + 0.005 \cdot V_{constant} \cdot d \cdot x - 9.25 \cdot V_{constant} \cdot d = V_{constant} \cdot y \qquad (81)$$
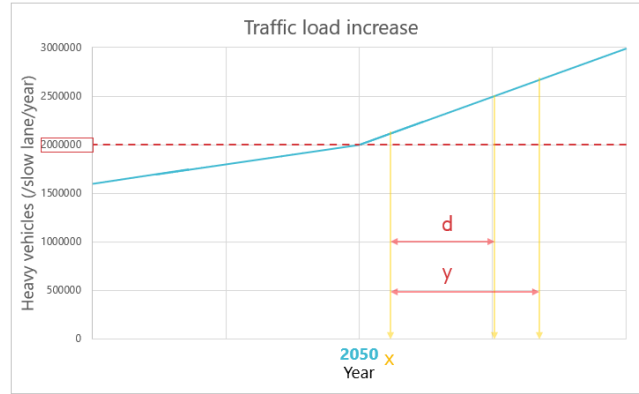
Figure 9.5: Effect of the increase of traffic rate on the fatigue life - Bridges constructed at or after 2050 ($x \geq 2050$).

An additional check should be performed for bridges of the first category. If $x + d \geq 2050$, the fatigue life accounting for the increasing rate of traffic volume should be recalculated using Equation 80.

For the investigated bridge:

$x = 1974$

$y = 57$ years

$V_{constant} = 2 \cdot 10^6$ vehicles

Using Equation 79, the following fatigue life is obtained:

$0.001 \cdot V_{constant} \cdot d^2 + 0.002 \cdot V_{constant} \cdot d \cdot x - 3.1 \cdot V_{constant} \cdot d = V_{constant} \cdot y$

$$\Rightarrow d \simeq 62 years \qquad (82)$$

It is worth mentioning that even in cases where its effect on fatigue is negative, this parameter provides valuable information on the fatigue performance of the structure based on the actual traffic conditions.

Furthermore, the cracking of the slab in the lateral direction is a parameter that has a significant impact on the fatigue life of the bridge. The reduced stiffness caused less distribution of loads in the lateral direction, which led to even higher loads being applied to the most loaded beams. This, in turn, caused a significant reduction in the fatigue life of the most loaded components (up to 51%). Considering the effect of this parameter raises questions about whether the utilised calculation is too conservative. Comparing the initial and cracked values of concrete stiffness, it can be observed that the latter is equal to one-fifth of the initial value.

In order to ascertain whether the incorporation of material properties in fatigue analysis also has the same impact on the fatigue life of other bridges, a stepwise analysis is carried out. First, as outlined in Section 7.4, the lateral stiffness of the cracked slab is dependent upon the top slab dimensions and the reinforcement amount on the most tensed side. As a result, each case will experience a unique stiffness reduction based on the specific characteristics of the bridge being examined. This stiffness reduction, in turn, affects the load distribution over the bridge. The distribution is primarily influenced by the flexural and torsional rigidities of the structure in the horizontal directions, which are defined by the material and geometrical properties of each bridge. After determining the load distribution, the stress levels of the structural components are calculated, which also depend on the structural members' characteristics and the applied loads. Finally, these stresses are used for the calculation of the fatigue life. It is evident that every step in this procedure is highly influenced by the properties of the analysed bridge. Hence, the impact of incorporating the orthotropic slab properties in fatigue analysis is not uniform for every bridge.

It is imperative to acknowledge that the reduction percentage in fatigue life that results from analysing a specific structure cannot be generalised for all bridges. However, it is expected that this parameter will have a substantial impact on the fatigue life of each structure, as it affects the stress distribution on the structural components. Excluding its effect from the fatigue assessment of a bridge would lead to an inaccurate and overly optimistic estimation of the fatigue performance.

The selection of load type used in simulating the effects of moving vehicles on bridges is a crucial factor that can significantly affect the bridge's lifespan. It has been observed that the use of

point loads does not accurately represent the actual loads and can lead to a more conservative load distribution, which can curtail the bridge's fatigue life. For the analysed bridge, replacing the are loads with point loads resulted in an 18% decrease in the fatigue life. Generally, the distribution of loads in the horizontal directions is largely dependent on the unique properties of the bridge being analysed and the size of the loaded area. It is noteworthy that the concentrated loads are dispersed horizontally through the cover layer and the concrete slab until they reach the level of the central axis of the slab, as discussed in Section 5.5.4.3. Therefore, the size of the loaded area can also be affected by the height of the top slab. Based on these factors, it is important to note that the specific influence percentage obtained in this study cannot be generalised for all bridges.

As aforementioned, the action of vehicles is modelled using the three suggested wheel types presented in Section 5.5.4.6. However, incorporating different axle types (as shown in Figure 5.16) increases the analysis type by three times, which means that triple the number of load cases needs to be analysed. For this reason, a comparison was made between the fatigue life obtained using the actual wheel types of each vehicle and using one type of wheel for all the truck axles. The results of this comparison have shown that performing the analysis using the smallest (more conservative) wheel type, namely wheel type A, yielded similar moments and fatigue life to the model utilising the exact axle types. Analysing the same wheel type for all the vehicle's axles would minimise the required load cases while providing the benefits of area loads.

For all the analysed cases, it is evident that the fatigue life of a bridge is highly dependent on the distribution of loads in the lateral direction, which determines the internal forces and, consequently, the stress distribution. The investigated bridge was analysed for fatigue using two different lane configurations. In both cases, the critical beam was identified underneath the traffic lanes, showing that changing the lane configuration can result in a completely different fatigue performance. Specifically, the analysis of the bridge using the actual lane configuration led to an increase in fatigue life by over three times as a result of the more even distribution of loads among the beams.

It is expected that positioning traffic lanes more centrally on the bridge deck will have a positive

influence on all bridges. When the lanes are located closer to the middle of the bridge width, the total load is more evenly distributed among the beams. On the other hand, when the traffic loads are applied closer to the edge of the bridge, the loads are primarily taken by the beams under the lanes. These beams are, therefore, subjected to higher loads, leading to a significant reduction in their fatigue life. It is, however, noted that even though the more centrical position of the traffic lanes is expected to have a similar effect on the fatigue performance of girder bridges, the exact percentage of this impact is not uniform. As mentioned above, the distribution of loads in the horizontal directions is linked to the flexural and torsional rigidities of the examined bridge. These are, in turn, affected by the structure's geometry, material properties and boundary conditions. Furthermore, each bridge might present a different lane configuration. As a result, the magnitude of the effect of this parameter is going to be different in each analysed bridge based on the way that the loads are applied and distributed in each particular case.

An additional point that needs to be emphasised refers to the historical lane configuration of the bridges. In the analysed case study, it is considered that the lane road configuration has remained the same throughout the service life of the bridge. For this reason, using the actual configuration is representative of the loading conditions of the bridge and can provide accurate results in determining the most critical components and the fatigue performance. However, this might not be the case in other bridges, as their lane configuration can alter over time to adjust to the traffic demands. As the fatigue life of concrete is also affected by the changes and sequence of the stress levels, these changes need to be incorporated into the fatigue analysis. Obtaining the historical data of a bridge loading is highly important for their assessment, given the large impact of this parameter on the fatigue life of the structure.

Based on the above, it is important to account for the actual loading configuration of the bridge. This consideration does not increase the design or computational time, as it merely refers to the position of traffic lanes in the transverse direction. The number of load cases and the rest of the analysis considerations remain intact. This parameter has a significant effect on the fatigue analysis of a bridge, providing essential information on the critical components.

The calculation of the bridge's fatigue life is also performed using the Fatigue Load Model 1 (Section 5.5.4.5). However, after conducting the analysis, it has been observed that the model

is excessively conservative and does not offer an accurate estimate of the bridge's fatigue life, ultimately resulting in a zero fatigue life prediction. As per the NEN-EN 1991-2:2003/C1:2010 guidelines, the model can be employed to ascertain whether the fatigue life of the specimen is unlimited, given that a constant stress amplitude limit is provided. Consequently, the model is deemed appropriate for steel structures, while it is unsuitable for other materials such as concrete. Due to this, other bridges' fatigue analysis using Fatigue Load Model 1 is expected to have a similar outcome.

Another parameter studied in this thesis refers to the material degradation caused by cyclic loading. Accounting for this effect and the resulting redistribution of stresses can significantly impact the fatigue life of the investigated structure. Even a slight reduction in stress levels can have an exponential effect on the fatigue check. Consequently, the change in the material properties significantly reduces the contribution of the investigated vehicle on the fatigue check. More specifically, as obtained from the results of this analysis, the action of the investigated vehicle affected the material properties to such an extent that its contribution to the fatigue unity check became almost zero after 30 years. Considering that the effect would be similar for the rest of the load model's vehicles, means that the fatigue life of the bridge would turn from 57 years to infinite, as the unity check would not reach one within the bridge lifespan.

Similar to other analysed parameters, the degradation of the material properties due to cyclic loading is highly dependent on case-specific parameters, such as the material properties, geometry and stress distribution of each component. Thus, the magnitude of its effect will vary not only among different bridges but also between their structural members.

As per Section 7.8, the analysis considers only the vertical redistribution of stress within the examined cross-section, without accounting for the transfer of stresses from the damaged parts to the stiffer parts of the beam and adjacent beams. Therefore, the time required for the global analysis of the bridge was not affected. The increase in the analysis time was caused by incorporating this effect in the cross-sectional analysis. Specifically, this approach requires additional time for designing the multilayered cross-section in which each layer is an individual component whose loads and properties need to be defined. Generally, considering this parameter in the fatigue analysis of a structure results in a significant increase in the time requirements.

Several considerations have also been adopted regarding the material degradation analysis. The suggested model assumes that the unloading between the maximum and minimum stresses is linear within a load cycle. In the bridge analysis, each load cycle corresponds to a crossing vehicle and is characterised by the maximum and minimum moments obtained from the influence lines. Observing the form of the influence lines (Figure 6.10), it is clear that the transition between the maximum and the minimum moment and the equivalent stresses is not linear, presenting fluctuations. These intermediate values are not accounted for in the analysis. A more accurate analysis of the stress variation could consider a more detailed approach, where the main load cycle consists of smaller cycles with corresponding stress limits.

Additionally, the model used to calculate the material degradation caused by fatigue loading has been experimentally verified using studies conducted for normal-strength concrete with characteristic strength up to $f_{ck} \leq 50N/mm^2$. In the analysed case, the concrete class of the precast beams was determined according to RBK as C55/67, which presents higher strength. It is, however, important to note that this concrete class was not utilised at the time of the bridge's construction. The original concrete strength would probably correspond to a lower concrete strength than the one of C55/67. Still, the suggestion has been made as a consideration of the strengthening of concrete caused by its ongoing hydration. Based on this, and since the characteristic strength does not significantly differ from the maximum stress limit assessed by Zanuy, Albajar, and De la Fuente 2009, it is considered that the method can be employed to sufficiently calculate the change of material properties.

A final analysis aspect that needs to be discussed refers to the consideration of concrete stiffening in the analysis process. As previously mentioned in Section 6.3, the cross-sectional analysis is performed by taking into account the increase in concrete stiffness due to ongoing hydration. Thus, the stress distributions are determined for the secant E-modulus at the analysis time. However, the global analysis of the bridge does not incorporate this stiffening effect. Instead, the linear properties outlined in Section 6.2.1 are employed to model the structural components, with the E-modulus corresponding to the stiffness of concrete at 28 days. It is essential to note that incorporating this stiffening effect would necessitate conducting the analysis for every decade, leading to a substantial increase in computational time. Considering that all the concrete

components exhibit a rise of their stiffness over time, it is assumed that this is uniform and, as a result, it does not affect the resulting moments. The stiffness evolution was, therefore, excluded from the global analysis.

10   Conclusions and Recommendations

10.1   Conclusions

The primary research question that is addressed in this thesis is

Research question:

In which way do variable analysis aspects and time-dependent parameters influence the fatigue life of an inverted T-girder bridge, and can this be used for a more sustainable fatigue assessment?

Sub-questions:

To provide an answer to the primary question, a series of sub-questions were formulated and subsequently answered.

How do the considerations taken into account for the calculation of prestress losses impact the fatigue life of a bridge?

- In this thesis, various calculations of the prestress losses were conducted to determine their effect on the fatigue life of the bridge. For the analysed case, the gradual development of prestress losses, as opposed to instantaneous losses, has been found to increase the fatigue life of the bridge by 18%.

- In general, the magnitude and the gradual development of the prestress losses depend on parameters that are unique in each case. For this reason, the above percentage cannot be generalised for all bridges. Since the prestress loss is one of the parameters that directly influence the stress distribution over the beam height, it significantly affects the fatigue life. The fatigue analysis should, therefore, be performed, accounting for the gradual loss of prestress.

- Although it is common practice to account for only the axial loads applied on the beams when calculating the losses, this approach can result in a conservative stress distribution. Considering the bending moments in the calculation of prestress losses can result in smaller stresses at the prestress level, leading to smaller losses and positively affecting fatigue performance. For the bridge under investigation, it was concluded that including bending

moments did not significantly affect the loss of prestress and, in turn, the final stress distribution. Hence, this parameter was excluded from the fatigue analysis. It should be noted that this may not be the case in all situations, as this is also a case-dependent parameter. It is essential to individually evaluate its contribution to the fatigue performance of each structure.

How does the consideration of the traffic volume increase impact the fatigue life of the bridge?

- The incessant growth of transportation has led to an upward trend in traffic volume over the years. For the examined case, accounting for the gradual increase in traffic rate in the fatigue analysis prolonged the fatigue life of the bridge by 9%.

- The effect of the increasing traffic rate on the fatigue life of a bridge can be calculated based on the following equations:

(a). Bridges constructed before 2050 ($x < 2050$) and, according to the basic case, fail due to fatigue before 2050 ($x + y < 2050$):

$$0.001 \cdot V_{constant} \cdot d^2 + 0.002 \cdot V_{constant} \cdot d \cdot x - 3.1 \cdot V_{constant} \cdot d = V_{constant} \cdot y$$

(b). Bridges constructed before 2050 ($x < 2050$) and, according to the basic case, fail due to fatigue at or after 2050 ($x + y \geq 2050$):

$$0.0025 \cdot V_{constant} \cdot d^2 + 0.005 \cdot V_{constant} \cdot d \cdot x + 0.0015 \cdot V_{constant} \cdot x^2 - 9.25 \cdot V_{constant} \cdot d$$
$$-6.15 \cdot V_{constant} \cdot x + 6303.75 \cdot V_{constant} = V_{constant} \cdot y$$

(c). Bridges constructed at or after 2050 ($x \geq 2050$):

$$0.0025 \cdot V_{constant} \cdot d^2 + 0.005 \cdot V_{constant} \cdot d \cdot x - 9.25 \cdot V_{constant} \cdot d = V_{constant} \cdot y$$

where,

x	the year of the bridge's construction
y	the fatigue life of the bridge with constant traffic volume
d	the fatigue life of the bridge accounting for the increasing traffic rate
$V_{constant}$.	the constant number of vehicles per slow lane per year

An additional check should be performed for bridges of Case (a). If $x + d \geq 2050$, the fatigue

life accounting for the increasing rate of traffic volume should be recalculated according to Case (b).

- Taking into account the increase in traffic volume leads to a more precise fatigue analysis, which accurately reflects the actual traffic conditions.

In what manner are the results of a fatigue analysis affected by the inclusion of orthotropic slab properties?

- Throughout a bridge's lifespan, the applied loads can lead to cracking on the top slab in the lateral direction, which results in a stiffness reduction in this direction. Incorporating this parameter in the fatigue analysis of the investigated bridge reduced its fatigue life by 51%.

- The orthotropic slab properties significantly impact the load distribution and, subsequently, the fatigue life of the bridge. However, the effect of this parameter is linked to the specific geometry and material properties of each structure, and therefore, the percentage of its impact will differ for each bridge.

- Taking into account this parameter is critical, despite its negative effect on the fatigue life, since excluding the orthotropic slab properties in the analysis would lead to an unrealistic stress distribution and estimation of the fatigue life.

How might the use of different load types in the modelling of fatigue moving loads influence the fatigue life of a bridge?

- In the analysis of the designed bridge, replacing the area wheel loads with point loads resulted in a more conservative load distribution, which shortened the fatigue life of the bridge by 18%. However, when the fatigue analysis was performed using wheel type A, it provided almost identical results to the analysis that took into consideration the actual wheel types of the vehicles.

- The analysis indicated that small variations in the loaded area would not have a significant impact on the fatigue performance of the bridge. Even though the exact influence percentages cannot be specified since they are dependent on the geometry and the way

the loads are distributed in each bridge, a similar magnitude effect is expected in other structures when different load types are examined.

- Based on these, it is concluded that point loads can result in a substantial reduction of the fatigue life and should not be utilised for modelling the vehicles. In contrast, using the wheel type A provides a sufficiently accurate estimation of the fatigue life without increasing the analysis time and should, therefore, be employed for the fatigue analysis.

What effect will different loading configurations have on the fatigue performance of the bridge?

- The fatigue analysis of the bridge under investigation revealed a notable increase in fatigue life when the actual lane configuration was utilised, where traffic lanes were positioned closer to the bridge's centre. Specifically, the fatigue life increased by 3.26 times compared to the scenario where traffic lanes were situated closer to the bridge's edge. Notably, the critical beams were consistently located beneath the traffic lanes, indicating that different components were identified as critical based on different loading configurations.

- The positioning of traffic lanes is a crucial factor in determining the fatigue performance and critical components of a bridge. As it is directly related to the load and stress distribution, it has a significant impact on the fatigue life of the structure. However, it is important to note that the results of this analysis cannot be generalised for other bridges, as the load distribution depends on case-specific parameters such as flexural and torsional rigidities and the lane configuration of each bridge.

- Generally, it is essential to design the loads to accurately replicate the actual conditions of the bridge, utilising historical lane configuration whenever possible. Any deviations from this would lead to an inaccurate representation of the actual situation and provide an unreliable estimation of the bridge's fatigue performance.

- The Fatigue Load Model 1 (FLM1) is not a suitable approach to evaluate concrete structures, as its primary purpose is to determine if the fatigue life of the specimen is unlimited. The recent study on this model has shown that it is overly conservative and does not provide an accurate estimate of the fatigue life of the bridge.

To what extent will the consideration of the composite action of structural components affect the fatigue life of a structure?

- In composite structures, the differential deformation of the structural components impacts the stress distribution over the beams, ultimately affecting the fatigue life of the bridge. For the studied bridge, it was observed that the composite action had only a minor impact on the calculated prestress losses, rendering it negligible. Accordingly, it was concluded that accounting for the composite action would not significantly influence the fatigue performance of the bridge, and thus, it was excluded from the analysis.

- The contribution of composite action to a bridge's fatigue life is case-specific and necessitates a separate assessment for each structure. It is essential to consider its effect on structures, where the relative creep and shrinkage of the structural members have a more critical effect on prestress losses, as this can impact the fatigue life of the structure.

How does cyclic loading influence the material properties of concrete and, consequently, the fatigue performance of the bridge?

- Repeated loading of the bridge over time degrades the concrete material properties, mainly affecting the top layers with the highest stresses. This leads to a redistribution of stresses from the most damaged parts of the beam to the stiffer areas and adjacent beams. In this study, the effect of this parameter was calculated at the midspan of the critical beam and accounting for one vehicle. After 30 years, the concrete stiffness was reduced up to 27.5% at the top fibre, which reduced the maximum and minimum stress levels by 4.3% and 1.6%, respectively.

- The stress redistribution led to a smaller contribution of a vehicle in the fatigue unity check (N_i/N_f), which is almost zero after 30 years. Ultimately, the total contribution of the vehicle to fatigue unity check was reduced by 84% compared to the analysis in which the initial stress values remained constant throughout the bridge's fatigue life. Considering that the effect will be similar for the rest of the vehicles, the bridge is no longer susceptible to fatigue failure.

- The parameter of material degradation directly impacts stress distribution, wherein is

expected to impact fatigue performance greatly. The magnitude of this influence is a function of the material and geometrical properties of the structure, as well as the stress level. As such, the current analysis results are case-specific and cannot be extrapolated to all bridges.

- Incorporating the material degradation into the fatigue analysis can be highly beneficial to the fatigue life of bridges and can potentially turn the fatigue life of a prone-to-fatigue structure into infinite.

Based on the findings of this thesis, the parameters having the most significant effect on the fatigue performance of the concrete bridge are those affecting the stress distribution over the beam height. Even slight variations in maximum and minimum stress levels can have a substantial impact on the bridge's fatigue life. Therefore, it is of utmost importance to carefully consider these factors during the fatigue assessment of concrete bridges. Among the parameters investigated in this study, the gradual prestress losses, orthotropic slab properties, loading configuration, type of loads used for modelling fatigue vehicles, and degradation of material properties due to repeated loading have the most significant influence on concrete fatigue. Conversely, parameters such as the inclusion of bending moments in the calculation of prestress losses and accounting for the composite action of the structural components have a relatively minor effect on the fatigue performance of the analysed bridge.

10.2 Recommendations

10.2.1 Recommendations for engineering practice

- Appendix C provides an overview of element types and their applications, including the types considered for the structure and the reasons for the final selection. The selection of element types for finite element analysis should be based on several factors, such as the software's modelling options, the type of analysis and the desired results, the structure's geometry and its components, and the level of accuracy required for the analysis. Based on these, the choice of elements for finite element analysis should be determined separately for each case to fit for purpose.

The general structural analysis of an inverted T-girder bridge can be performed, as suggested by current codes, using the beam elements for the precast beams' modelling, specifically when the intended outcomes involve the internal forces of the components. However, to achieve a higher degree of precision in the modelling of the bridge's geometry or include the variation of material properties, shell elements are a more suitable alternative for the beams' modelling. This approach provides an accurate depiction of the bridge's geometry and is effective in terms of both design and computational time.

- The study found that prestress losses significantly affect the fatigue life of the bridge, impacting the stress distribution over the beams. A more detailed calculation of the prestress losses can increase the fatigue life of the bridge without significantly increasing the analysis time. It is important to note that considering the composite action and the bending moments can provide a more accurate estimation of the prestress losses. However, the magnitude of their effect on stress losses and, in turn, on the stress distribution and fatigue life depends on the analysed case and should be assessed individually.

- Incorporating the time-dependent traffic volume can either positively or negatively affect the fatigue life of a bridge, depending on the date of its erection. Disregarding this factor during the analysis process can lead to an imprecise shortening or prolongation of the fatigue life. It is important to note that this parameter is not included in the global and cross-section analysis of the bridge. Instead, it is factored in the post-processing of the results, specifically on the fatigue life calculation, meaning that it does not increase the analysis time. As a result, it is highly recommended to consider its impact on the fatigue analysis as it provides a more accurate prediction of the fatigue performance.

- Excluding the orthotropic slab properties from the analysis would lead to an unrealistic and excessively optimistic stress distribution. This would result in a false calculation of the fatigue life, and therefore, it is necessary to incorporate the effect of slab cracking in the analysis.

- The study has revealed that the type of loads utilised to model moving loads can have a considerable impact on the fatigue life of the bridge. The utilisation of point loads can lead

to a more conservative load distribution, thereby reducing the fatigue life. As such, this modelling method should be avoided in the fatigue assessment. However, incorporating all of the recommended wheel types results in a threefold increase in the time required for the global analysis. Utilising area loads while using the wheel type A for all the wheel axles is an intermediate solution that results in an almost identical fatigue life without increasing analysis time It is, therefore, a preferred solution for modelling fatigued vehicles.

- Conducting the fatigue analysis of the bridge using the Fatigue Load Model 1 is highly unrecommended. As discussed in Chapter 9, this loading model is not suitable for concrete structures and can provide a very conservative estimation of the fatigue life of the bridge.

- The position of the traffic lanes is one of the main parameters determining the bridge's critical components and fatigue life. As mentioned in the analysis of the investigated parameters, the obtained results correspond to the analysed loading configuration. Consequently, it is essential to design the applied load in such a way that will accurately simulate the actual conditions existing in the bridge. The fatigue analysis should be conducted based on the historical lane configuration data when these are available. Selecting a different loading configuration may lead to a worse effect on the structure, but this would not be representative of the loading condition that the bridge exhibits. In the cases where this information is not known, the fatigue analysis should be performed using the most conservative loading configuration.

- The inclusion of the material degradation parameter in the analysis, despite the associated increase in analysis time, has a significant positive impact on the fatigue life of the bridge that cannot be overlooked. This parameter plays a crucial role in determining the distribution of stresses, which in turn greatly affects the fatigue performance of the bridge. Therefore, incorporating this parameter into the analysis process, even when using the simplest and most conservative approach, can result in a significant increase in fatigue life. Consequently, it is highly recommended to consider this parameter in the analysis process despite the considerable amount of time it entails. Automating this process could be highly beneficial in engineering practice, making it more efficient and cost-effective for the fatigue analysis of structures.

10.2.2   Recommendations for future research

- The objective of the present study was to investigate the impact of various parameters on the fatigue life of a bridge. Each parameter was analysed individually, wherein only the parameter under investigation was modified while keeping other aspects of the analysis constant. However, in reality, these parameters exist simultaneously on the bridge. Therefore, examining the interaction of these parameters and their total effect on the fatigue life of the structure appears to be an interesting proposition.

- The analysis of prestress-loss-related parameters has revealed that the approach taken during the analysis has a significant impact on fatigue performance. Notably, the analyses with instantaneous and gradual losses have produced comparable results. The difference between these analyses lies in the way the prestress losses are developed over time. If a general rule can be established that describes the relationship between this gradual development of prestress losses and fatigue unity check, it could provide valuable information on whether incorporating these gradual losses can substantially influence the fatigue life of the assessed bridge.

- In order to analyse the degradation parameter of the material, certain simplifications have been made in the method that was utilised. It is important to note that not accounting for the distribution of stresses from the most heavily loaded parts of the beams to the less damaged and stiffer parts, as well as the adjacent beams, can be considered a conservative approach. Therefore, a more detailed analysis of the phenomenon is required, which includes the longitudinal and lateral distribution of stresses to provide a more accurate view of the phenomenon's evolution. Additionally, the analysis should consider the effect of all the vehicles passing through the bridge in a random sequence, as this would be more representative of the actual traffic conditions and loads applied to the structure.

- As discussed in Section 7.8, the model employed to determine the changes in material properties due to cyclic loading has been validated for normal-strength concrete. Assessing its applicability or adjusting the existing model to properly describe the material degradation of high-strength concrete could be advantageous for fatigue analysis. As per J.-K. Kim and

Y.-Y. Kim 1996, high-strength concrete displays less strain increase and stiffness decrease than normal-strength concrete due to its stiffer monotonic response. This discrepancy may be attributed to the differences in the microcracking mechanism of high-strength concrete compared to normal-strength concrete. Specifically, in high-strength concrete, the cracking surface can also be developed through the aggregates. Given that many bridges have been constructed with high-strength concrete or have undergone strength increase over time, an appropriate material degradation model could offer a more precise understanding of the structure's condition and fatigue performance.

- One possible approach to evaluating and quantifying the impact of parameters involves conducting experimental studies.

References

Aas-Jakobsen, Knut (1970). "Fatigue of concrete beams and columns". In: *Bulletin.* 70-1.

Antrim, John D. (1967). "The mechanism of fatigue in cement paste and plain concrete". In.

Ashby, M.F. and S.D. Hallam (1986). "The failure of brittle solids containing small cracks under compressive stress states". In: *Acta metallurgica* 34.3, pp. 497–510.

Awad, Mohamed EL-Mustafa (1971). *Strength and deformation characteristics of plain concrete subjected to high repeated and sustained loads.* University of Illinois at Urbana-Champaign.

Bazant, Zdenek P. and Mija H. Hubler (2014). "Theory of cyclic creep of concrete based on Paris law for fatigue growth of subcritical microcracks". In: *Journal of the Mechanics and Physics of Solids* 63, pp. 187–200.

Bažant, Zdeněk P and Yuyin Xiang (1997). "Size effect in compression fracture: splitting crack band propagation". In: *Journal of engineering mechanics* 123.2, pp. 162–172.

Bennett, E.W. and N.K. Raju (1969). "Cumulative fatigue damage of plain concrete in compression". In: *The Proceedings of the Southampton 1969 Civil Engineering Materials Conference*, pp. 1089–1102.

Blaauwendraad, J. (2010). *Plates and FEM: Surprises and Pitfalls.* Solid Mechanics and Its Applications. Springer Netherlands. ISBN: 9789048135967.

Blasón, S. et al. (2019). "Twofold normalization of the cyclic creep curve of plain and steel-fiber reinforced concrete and its application to predict fatigue failure". In: *International Journal of Fatigue* 120, pp. 215–227.

CEB-FIP, CEBFIP (1988). "model code 1990". In: *Comite Euro-International Du Beton, Paris.*

Cornelissen, H.A.W. and H.W. Reinhardt (1984). "Uniaxial tensile fatigue failure of concrete under constant-amplitude and programme loading". In: *Magazine of concrete Research* 36.129, pp. 216–226.

DIANA Finite Element Analysis - Release Notes - Release 10.5 (Release notes). DIANA FEA BV.

Eliáš, Jan and Jia-Liang Le (2012). "Modeling of mode-I fatigue crack growth in quasibrittle structures under cyclic compression". In: *Engineering Fracture Mechanics* 96, pp. 26–36.

Fairhurst, Charles and Francois H. Cornet (1981). "Rock fracture and fragmentation". In: *ARMA US Rock Mechanics/Geomechanics Symposium*. ARMA, ARMA–81.

Fan, Ziyuan and Yongming Sun (2019). "Detecting and evaluation of fatigue damage in concrete with industrial computed tomography technology". In: *Construction and Building Materials* 223, pp. 794–805.

Fédération, Internationale du Béton (2012). *Model Code 2010 - Final draft: Volume 2*. Bulletin (fib Fédération internationale du béton). International Federation for Structural Concrete (fib): Lausanne. ISBN: 978-2-88394-106-9.

Fernández-Ordóñez Hernández, David (Jan. 2005). "Precast concrete bridges - A state of the art report". In: 71, pp. 64–65.

Galloway, J.W., H.M. Harding, and K.D. Raithby (1979). *Effects of moisture changes on flexural and fatigue strength of concrete*. Tech. rep.

Gao, Lubin and Cheng-Tzu Thomas Hsu (1998). "Fatigue of concrete under uniaxial compression cyclic loading". In: *Materials Journal* 95.5, pp. 575–581.

Hanson, John M., Craig A. Ballinger, and D. Linger (1974). "Considerations for design of concrete structures subjected to fatigue loading". In: *ACI J* 71.3, pp. 97–120.

Hilsdorf, Hubert K. and Clyde E. Kesler (1966). "Fatigue strength of concrete under varying flexural stresses". In: *Journal Proceedings*. Vol. 63. 10, pp. 1059–1076.

Holmen, Jan O. (1979). *Fatigue of Concrete by Constant and Variable Amplitude Loading*. Bulletin. Division on Concrete Structures, Norwegian Institute of Technology, University of Trondheim.

Horii, Hideyuki, Hak Chul Shin, and Tirath Manojya Pallewatta (1992). "Mechanism of fatigue crack growth in concrete". In: *Cement and concrete composites* 14.2, pp. 83–89.

Hsu, Thomas T.C. (1981). "Fatigue of plain concrete". In: *Journal Proceedings*. Vol. 78. 4, pp. 292–305.

– (1984). "Fatigue and microcracking of concrete". In: *Materiaux et construction* 17, pp. 51–54.

Ingraffea, Anthony R. (1977). *DISCRETE FRACTURE PROPAGATION IN ROCK: LABORATORY TESTS AND FINITE-ELEMENT ANALYSIS*. University of Colorado at Boulder.

Nederlandse norm, NEN 6723: Regulations for concrete - Bridges - Structural requirements and calculation methods (2009). Netherlands: NEN.

Nederlandse norm, NEN 8700:2011+A1:2020: Assessment of existing structures in case of reconstruction and disapproval - Basic rules (2011a). Netherlands: NEN.

Nederlandse norm, NEN 8701:2011+A1:2020: Assessment of existing structures in case of reconstruction and disapproval - Actions (2011b). Netherlands: NEN.

Jiang, Chao et al. (2017). "Deformation of concrete under high-cycle fatigue loads in uniaxial and eccentric compression". In: *Construction and Building Materials* 141, pp. 379–392.

Kachanov, Mark L. (1982). "A microcrack model of rock inelasticity part I: Frictional sliding on microcracks". In: *Mechanics of Materials* 1.1, pp. 19–27.

Kim, Jin-Keun and Yun-Yong Kim (1996). "Experimental study of the fatigue behavior of high strength concrete". In: *Cement and Concrete Research* 26.10, pp. 1513–1523.

Kindrachuk, Vitaliy M., Marc Thiele, and Jörg F. Unger (2015). "Constitutive modeling of creep-fatigue interaction for normal strength concrete under compression". In: *International Journal of Fatigue* 78, pp. 81–94.

Kolluru, Subramaniam V. et al. (2000). "Crack propagation in flexural fatigue of concrete". In: *Journal of Engineering mechanics* 126.9, pp. 891–898.

Lambotte, Hendrik and R. Baus (1963). *Etude expérimentale de l'effet de la fatigue sur le comportement des poutres en béton armé*. nom de l'éditeur indisponible.

Lantsoght, EOL (2014). "Fatigue of concrete under compression: Database and proposal for high strength concrete". In: *Report nr. 25.5-14-04*.

Lee, M.K. and B.I.G. Barr (2004). "An overview of the fatigue behaviour of plain and fibre reinforced concrete". In: *Cement and Concrete Composites* 26.4, pp. 299–305.

Maekawa, Koichi, Esayas Gebreyouhannes, et al. (2006). "Three-dimensional fatigue simulation of RC slabs under traveling wheel-type loads". In: *Journal of Advanced Concrete Technology* 4.3, pp. 445–457.

Maekawa, Koichi, Kukrit Toongoenthong, et al. (2006). "Direct path-integral scheme for fatigue simulation of reinforced concrete in shear". In: *Journal of Advanced Concrete Technology* 4.1, pp. 159–177.

Marco, S.M. and W.L. Starkey (1954). "A concept of fatigue damage". In: *Transactions of the American Society of Mechanical Engineers* 76.4, pp. 627–632.

Marzec, I., J. Tejchman, et al. (2019). "Fracture evolution in concrete compressive fatigue experiments based on X-ray micro-CT images". In: *International Journal of Fatigue* 122, pp. 256–272.

Miner, Milton A. (1945). "Cumulative damage in fatigue". In.

Murdock, John W. (1960). *The mechanism of fatigue failure in concrete*. University of Illinois at Urbana-Champaign.

Nemat-Nasser, S. and H. Horii (1982). "Compression-induced nonplanar crack extension with application to splitting, exfoliation, and rockburst". In: *Journal of Geophysical Research: Solid Earth* 87.B8, pp. 6805–6821.

Nordby, Gene M. (1958). "Fatigue of concrete-a review of research". In: *Journal Proceedings.* Vol. 55. 8, pp. 191–219.

Oh, Byung H. (1991). "Fatigue life distributions of concrete for various stress levels". In: *Materials Journal* 88.2, pp. 122–128.

Ople, F.S. and C.L. Hulsbos (1966). "Probable fatigue life plain concrete with stress gradient". In: *Journal Proceedings.* Vol. 63. 1, pp. 59–82.

Palmgren, Arvid (1924). "Die Lebensdauer von Kugellagern (Life Length of Roller Bearings or Durability of Ball Bearings)". In: *VDI. Z.* 68, pp. 339–341.

Petkovic, Gordana (1993). "Properties of concrete related to fatigue damage with emphasis on high-strength concrete." In.

Powers, Travel C. (1959). "Causes and control of volume changes". In: *Journal of Portland Cement Association, Research and Development Laboratories* 1.1, pp. 29–39.

Raithby, K.D. (1979). "Behaviour of concrete under fatigue loading". In: *Development in Concrete Technology, FD Lydon, Ed., Applied Science Publishers Ltd* 1, pp. 83–110.

Raju, N.K. (1970). "Small concrete specimens under repeated compressive loads by pulse velocity technique". In: *Journal of Materials.*

Richards, C.W. (1961). *Engineering Materials Science.* Engineering science series. Wadsworth Publishing Company.

Rilem Committee, 36-RDL (1984). "Long term random dynamic loading of concrete structures". In: *Materials and Constructions* 17.97, pp. 1–13.

Sammis, CG and MF Ashby (1986). "The failure of brittle porous solids under compressive stress states". In: *Acta metallurgica* 34.3, pp. 511–526.

Schulson, E.M. and O.Y. Nickolayev (1995). "Failure of columnar saline ice under biaxial compression: Failure envelopes and the brittle-to-ductile transition". In: *Journal of Geophysical Research: Solid Earth* 100.B11, pp. 22383–22400.

Shah, Surendra P. and Sushil Chandra (1970). "Fracture of concrete subjected to cyclic and sustained loading". In: *Journal Proceedings.* Vol. 67. 10, pp. 816–827.

Siemes, A.J.M. (1985). "Fatigue of concrete". In.

Singh, Avinash (2003). "Development and validation of an SN based two phase bending fatigue life prediction model". In: *J. Mech. Des.* 125.3, pp. 540–544.

Sparks, Peter R. and J.B. Menzies (1973). "The effect of rate of loading upon the static and fatigue strengths of plain concrete in compression". In: *Magazine of concrete research* 25.83, pp. 73–80.

European standard, EN 1337-3:2005: Structural bearings - Part 3: Elastomeric bearings (2005). EN. Brussels: CEN.

European standard, NEN-EN 1992-2: Eurocode 2: Design of concrete structures - Part 2: Concrete bridges - Design and detailing rules (2008). EN. Brussels: CEN.

European standard, NEN-EN 1991-1-1: Eurocode 1: Actions on structures - Part 1-1: General actions - Densities, self-weight, imposed loads for buildings (2009). EN. Brussels: CEN.

European standard, NEN-EN 1990: Eurocode - Basis of structural design (2010a). EN. Brussels: CEN.

European standard, NEN-EN 1991-2: Eurocode 1: Actions on structures - Part 2: Traffic loads on bridges (2010b). EN. Brussels: CEN.

European standard, NEN-EN 1992-1-1: Eurocode 2: Design of concrete structures - Part 1-1: General rules and rules for buildings (2010c). EN. Brussels: CEN.

European standard, National Annex to NEN-EN 1992-2: Eurocode 2: Design of concrete structures - Part 2: Concrete bridges - Design and detailing rules (2016). EN. Brussels: CEN.

European standard, National Annex to NEN-EN 1990: Eurocode - Basis of structural design (2019a). EN. Brussels: CEN.

European standard, National Annex to NEN-EN 1991-1-1: Eurocode 1: Actions on structures - Part 1-1: General actions - Densities, self-weight, imposed loads for buildings (2019b). EN. Brussels: CEN.

European standard, National Annex to NEN-EN 1991-2: Eurocode 1: Actions on structures - Part 2: Traffic loads on bridges (2019c). EN. Brussels: CEN.

European standard, National Annex to NEN-EN 1992-1-1: Eurocode 2: Design of concrete structures - Part 1-1: General rules and rules for buildings (2020). EN. Brussels: CEN.

European standard, Draft NEN-EN 1990: Eurocode - Basis of structural design (2021). EN. Brussels: CEN.

Suresh, S., E.K. Tschegg, and J.R. Brockenbrough (1989). "Fatigue crack growth in cementitious materials under cyclic compressive loads". In: *Cement and Concrete Research* 19.5, pp. 827–833.

Suresh, Subra (1998). *Fatigue of materials*. Cambridge university press.

Takhar, S.S., I.J. Jordan, and B.R. Gamble (1974). "Fatigue of concrete under lateral confining pressure". In: *Special Publication* 41, pp. 59–70.

Tepfers, Ralejs and Thomas Kutti (1979). "Fatigue strength of plain, ordinary, and lightweight concrete". In: *Journal Proceedings*. Vol. 76. 5, pp. 635–652.

Tilly, G.P. (1979). "Fatigue of steel reinforcement bars in concrete: a review". In: *Fatigue & Fracture of Engineering Materials & Structures* 2.3, pp. 251–268.

Van Leeuwen, J. and A.J.M. Siemes (1979). "MINER'S RULE WITH RESPECT TO PLAIN CONCRETE". In.

Waagaard, K (1981). "Fatigue strength of offshore concrete structures". In: *Det Norske Veritas, Hovik, Norway*.

Richtlijn Ontwerp Autosnelwegen - Veilige Inrichting van Bermen (2017). Netherlands.

RTD 1001 Richtlijnen Ontwerp Kunstwerken (ROK), Versie 2.0 (2021a). Netherlands.

RTD 1001 Standaarddetails voor Betonnen Bruggen, Versie 2.0 (2021b). Netherlands.

RTD 1006 Richtlijnen Beoordeling Kunstwerken (RBK), Versie 1.2.1 (2022). Netherlands.

Weigler, H. and D. Klausen (1979). "Fatigue behaviour of concrete effect of loading in the fatigue strength range". In: *Betonwerk Fertigteil-Technik* 4, pp. 214–220.

Zanuy, Carlos, Luis Albajar, and Pablo De la Fuente (2009). "Sectional Analysis of Concrete Structures under Fatique Loading." In: *ACI Structural Journal* 106.5.

Appendices

A Stress distribution on composite inverted T-beams

The focus of this study is an inverted T-girder bridge consisting of precast beams and a cast in-situ top layer. Erecting this type of structure involves several stages, each of which involves the application of various loads on the bridge. The thesis aims to examine the fatigue life of the concrete beams, which is contingent on the stress distribution over the beam height, particularly the maximum stress values observed.

Inverted T-girder bridges typically experience maximum stress values on the top compressive layer of the beams due to the stresses of the various load components. To provide a comprehensive understanding of the stress distribution, this appendix analyzes the stress distribution of each bridge stage.

The initial stage of the bridge's life corresponds to the initiation of the prestressing, which occurs ten days after the beams have been cast. At this stage, the stress distribution is determined by the self-weight of the beams, the axial loads, and the bending moments caused by the prestress. Thus, the stress distribution illustrated in Figure A.1 is calculated based on the following relations,

Top fibre:

$$\sigma_{top} = +\frac{F_{pi}e_p}{W_{bt}} - \frac{F_{pi}}{A} - \frac{M_g}{W_{bt}} \tag{83}$$

Bottom fibre:

$$\sigma_{bottom} = -\frac{F_{pi}e_p}{W_{bb}} - \frac{F_{pi}}{A} + \frac{M_g}{W_{bb}} \tag{84}$$

where,

M_g	the bending moment due to the self-weight of the beam,
F_{pi}	the initial prestressing force ,
e_p	the eccentricity of the prestressing strands,
A	the area of the cross section,

W_{bt} $\qquad = \frac{I}{y_{top}}$, the sectional modulus of the top fibre,

W_{bb} $\qquad = \frac{I}{y_{bottom}}$, the sectional modulus of the bottom fibre,

I $\qquad$ the second moment of inertia,

y_{top} $\qquad$ the distance of the top extreme fibre from the neutral axis,

y_{bottom} $\qquad$ the distance of the bottom extreme fibre from the neutral axis.
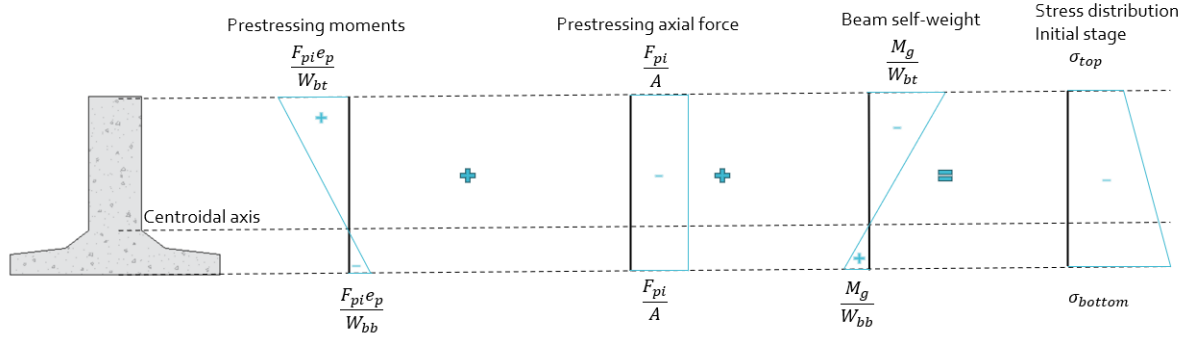
Figure A.1: Stress distribution at the initial stage

The next stage refers to the casting of the top layer prior to the hardening of the cast in-situ slab. In addition to the self-weight of the beams and prestressing loads, the beams are subjected to loading due to the self-weight of the top layer. The resulting stress distribution is presented in Figure A.2, in which the stress values at the top and bottom fibres of the beam are given as,

Top fibre:

$$\sigma_{top} = +\frac{F_{pw}e_p}{W_{bt}} - \frac{F_{pi}}{A} - \frac{M_g}{W_{bt}} - \frac{M_s}{W_{bt}} \tag{85}$$

Bottom fibre:

$$\sigma_{bottom} = -\frac{F_{pw}e_p}{W_{bb}} - \frac{F_{pi}}{A} + \frac{M_g}{W_{bb}} + \frac{M_s}{W_{bb}} \tag{86}$$

where,

M_s $\qquad$ the bending moment due to the self-weight of the cast in-situ slab,

F_{pw} $\qquad$ the prestressing force reduced by the prestress losses of the corresponding stage.
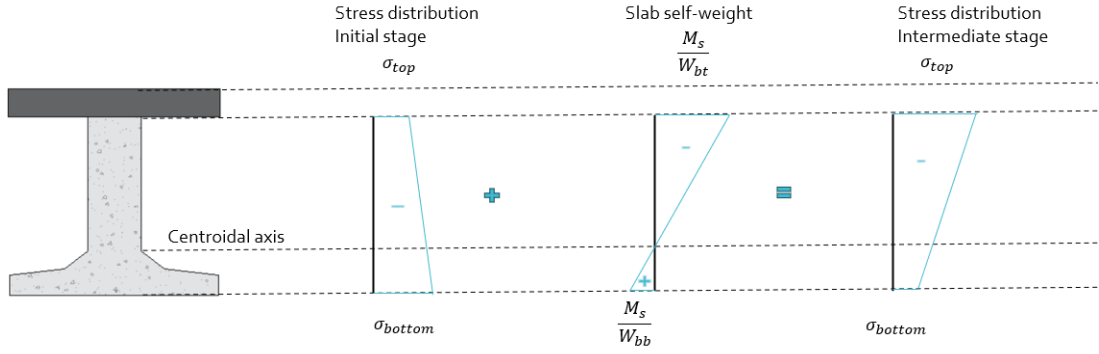
Figure A.2: Stress distribution at the intermediate stage

At the final stage, the hardening of the top slab initiates the composite action of the structural components. As a result, the components begin to work together as a single cross-section, leading to a change in the position of the neutral axis. The application of additional dead and variable loads on the bridge generates stress gradients that contribute to the final stress distribution over the beam height. Accounting for these loads, the stress distribution is depicted in Figure A.3, while the stress values of the extreme fibres are determined as,

Top fibre:

$$\sigma_{top} = +\frac{F_{pw}e_p}{W_{bt}} - \frac{F_{pi}}{A} - \frac{M_g}{W_{bt}} - \frac{M_s}{W_{bt}} - \frac{M_a + M_{ll}}{W_{bt,c}} \tag{87}$$

Bottom fibre:

$$\sigma_{bottom} = -\frac{F_{pw}e_p}{W_{bb}} - \frac{F_{pi}}{A} + \frac{M_g}{W_{bb}} + \frac{M_s}{W_{bb}} + \frac{M_a + M_{ll}}{W_{bb,c}} \tag{88}$$

where,

M_a	the bending moment due to the additional dead weight,
M_{ll}	the bending moment due to the live loads,
$W_{bt,c}$	$= \frac{I}{y_{top,c}}$, the sectional modulus of the composite section for the top fibre of the beam,
$W_{bb,c}$	$= \frac{I}{y_{bottom,c}}$, the sectional modulus of the composite section for the bottom fibre of the beam,
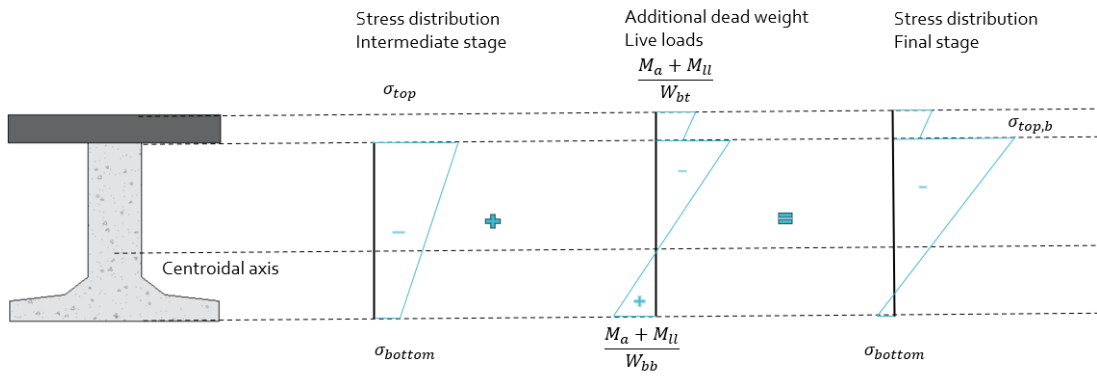
Figure A.3: Stress distribution at the final stage

B   Serviceability Limit State (SLS) - Stress control

The dimensions of the beams and the prestressing strand configuration were selected to comply with both old and current regulations, ensuring the bridge's fatigue failure within its expected lifespan. The bridge was built in 1974, meaning that its design was based on previous Dutch codes. To account for this, the stress control for Serviceability Limit State (SLS) was conducted for permanent and variable loads applied on the bridge. It is noted that the bending moment resistance of the bridge, according to the previous national regulations, is not presented. The bending moment resistance of the structure will be assessed later, based on current standards, to ensure that the bridge does not fail due to bending, which is the failure criterion.

Permanent loads applied on the structure are generated by the self-weight of the structural components, prestress and the additional dead weight applied on the bridge, as analysed in Chapter 5.5. Given the time of the bridge's erection, older traffic load models were used for its design. Specifically, with the bridge being part of the main rod network, its analysis is performed for the traffic class A/60 model. This load model consists of concentrated and uniformly distributed loads. The longitudinal and transverse configurations of the considered trucks are illustrated in Figures B.1 and B.2, respectively. For loading class 60, the traffic loads comprise three-axle loads of $200kN$ and a distributed load equal to $4kN/m^2$. Two loading cases were evaluated, one for a single vehicle and one for two vehicles simultaneously moving over the bridge. In the case of two vehicles present on the bridge, the corresponding loads are multiplied by a reduction factor of 0.8.
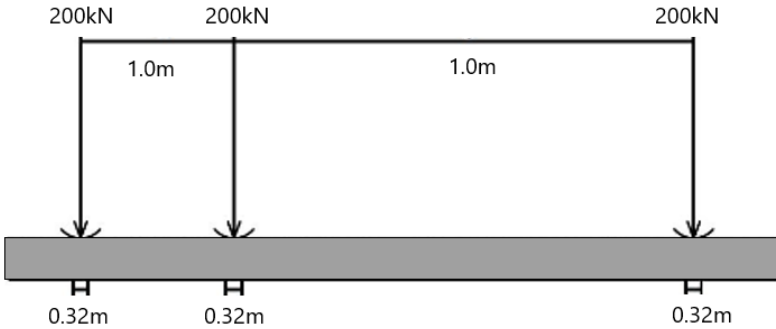
Figure B.1: Longitudinal traffic load configuration for load class A/60

164
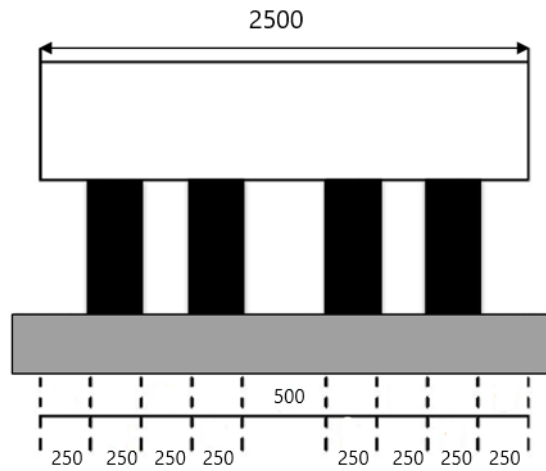
Figure B.2: Transverse traffic load configuration for load class A/60

For single-supported beams, the maximum bending moment at the midspan of the beams is noted when the vehicles are in the longitudinal position depicted in Figure B.3.
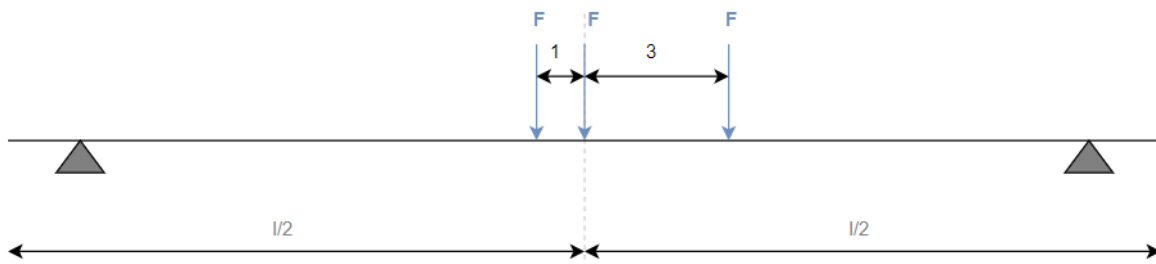
Figure B.3: Position of the vehicle in the longitudinal direction that results in the maximum bending moment.

In the bridge's design, the traffic load is modelled as static loading. However, in order to accurately account for the impact of dynamic loading on real-life traffic, a dynamic amplification factor (DAF) is applied. According to the VB 1974/1984, the DAF is given as

$$DAF(S) = 1 + \frac{3}{100L} = 1 + \frac{3}{100 \cdot 29} = 1.0 \qquad (89)$$

An additional reduction factor is also applied to the design load, which equals

$$B = 0.6 + \frac{40}{100 + L} = 0.6 + \frac{40}{100 + 29} = 0.91 \tag{90}$$

The stress control is conducted based on the following properties:

- Beam height $H_b = 810mm$

- Beam area $A_b = 375460mm^2$

- Moment of inertia of the beam $I_b = 22669278945mm^4$

- Centre of gravity of the beam (distance from the bottom fibre) $z_b = 290mm$

- Sectional modulus of the beam for the top fibre $W_{bt} = 43594767.2mm^3$

- Sectional modulus of the beam for the bottom fibre $W_{bb} = 78169927.4mm^3$

- Slab height $H_s = 160mm$

- Asphalt layer height $H_a = 140mm$

- Moment of inertia of the composite section $I_c = 63088963971mm^4$

- Centre of gravity of the composite section (distance from the bottom fibre) $z_b = 468mm$

- Sectional modulus of the composite section for the top fibre of the beam $W_{bt,c} = 184470654.9mm^3$

- Sectional modulus of the composite section for the bottom fibre of the beam $W_{bb,c} = 134805478.6mm^3$

- Initial prestress $\sigma_p = 1394N/mm^2$

- Characteristic concrete strength $f_{ck} = 55N/mm^2$

- Design concrete strength $f_{cd} = 36.7/mm^2$

- Characteristic axial tensile strength of concrete $f_{ctk0.05} = 2.95/mm^2$

- Design axial tensile strength of concrete $f_{ctd} = 1.97N/mm^2$

- Strength of fresh concrete $f_{fresh} = 45N/mm^2 (= f'_{ck,fresh})$

- Modulus of elasticity $E_{cm} = 38214.206 N/mm^2$

The stress control is conducted based on the worst loaded beam for the various construction stages of the bridge's life. The internal forces for the dead loads and the aforementioned moving loads were obtained from the Finite Element Analysis (FEA) of the structure and are equal to

- Bending moment due to the self-weight of the beam $M_g = 984.19 kNm$

- Bending moment due to the self-weight of the cast in-situ slab $M_s = 498.83 kNm$

- Bending moment due to the additional dead weight $M_a = 389.15 kNm$

- Bending moment due to the live loads $M_{ll} = 1111.70 kNm$

For the prestressing, the axial loads and bending moment caused by the prestressing strands are calculated as,

$$F_p = \sum F_{pi} = \sum n \cdot A_i \cdot \sigma_p = 6093.14 kN \tag{91}$$

$$M_{p,b} = \sum M_{pi} = \sum n \cdot F_{pi} \cdot e_{pi} = 1332.72 kNm \tag{92}$$

At the initial stage,

Top fibre:

$$\sigma_{top} = +\frac{F_{pi}e_p}{W_{bt}} - \frac{F_{pi}}{A} - \frac{M_g}{W_{bt}} = -8.25 N/mm^2 \leq f_{ctd} = 1.97 N/mm^2 \tag{93}$$

Bottom fibre:

$$\sigma_{bottom} = -\frac{F_{pi}e_p}{W_{bb}} - \frac{F_{pi}}{A} + \frac{M_g}{W_{bb}} = -20.67 N/mm^2 \geq 0.6 \cdot f'_{ck,fresh} = -27.0 N/mm^2 \tag{94}$$

where,

f'_{ck} the characteristic cubic strength

The stress control for the stages following the initial one is conducted considering prestress losses equal to 15%

At the intermediate stage,

Top fibre:

$$\sigma_{top} = +\frac{F_{pw}e_p}{W_{bt}} - \frac{F_{pi}}{A} - \frac{M_g}{W_{bt}} - \frac{M_s}{W_{bt}} = -21.83 N/mm^2 \geq 0.6 \cdot f'_{ck} = -40.2 N/mm^2 \qquad (95)$$

Bottom fibre:

$$\sigma_{bottom} = -\frac{F_{pw}e_p}{W_{bb}} - \frac{F_{pi}}{A} + \frac{M_g}{W_{bb}} + \frac{M_s}{W_{bb}} = -9.31 N/mm^2 \leq f_{ctd} = 1.97 N/mm^2 \qquad (96)$$

At the final stage,

Top fibre:

$$\sigma_{top} = +\frac{F_{pw}e_p}{W_{bt}} - \frac{F_{pi}}{A} - \frac{M_g}{W_{bt}} - \frac{M_s}{W_{bt}} - \frac{M_a + M_{ll}}{W_{bt,c}} = -29.96 N/mm^2 \geq 0.6 \cdot f'_{ck} = -40.2 N/mm^2$$

$$(97)$$

Bottom fibre:

$$\sigma_{bottom} = -\frac{F_{pw}e_p}{W_{bb}} - \frac{F_{pi}}{A} + \frac{M_g}{W_{bb}} + \frac{M_s}{W_{bb}} + \frac{M_a + M_{ll}}{W_{bb,c}} = 1.82 N/mm^2 \leq f_{ctd} = 1.97 N/mm^2 \quad (98)$$

C   Beam element types

C.1   Introduction

In order to determine the most suitable type of elements for beam modelling, a comprehensive assessment of various options was conducted. The evaluation encompassed different types of elements classified into beams, shells, and solid elements. To compare those, simply supported beam models were created and subjected to various load cases. The resulting beam models were evaluated based on deflection, moment distribution, design accuracy, node count, design and computational time. Finally, different types of elements were utilised to model the precast beams in the global models of the entire structure. The subsequent sections provide an overview of the element types analyzed in this study, based on the DIANA FEA Release notes.

C.2   Beam element types

In engineering practice, structures similar to the bridge under investigation are commonly modelled utilising beam elements for the precast beam. These beam elements are eccentrically connected to a plate or shell element, representing the cast in-situ slab.

The dimensions of the beam elements perpendicular to the bar direction are relatively smaller in comparison to their length (Figure C.1). These beam elements can exhibit axial and shear deformation, curvature, and torsion and can be used to describe axial forces, shear forces, and moments.
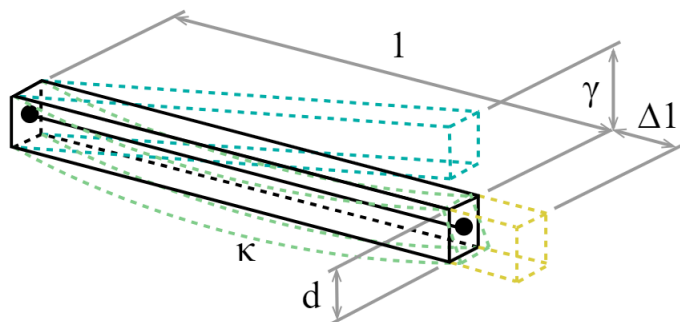
Figure C.1: Characteristics of beam element (DIANA FEA Release notes).

DIANA software offers a range of element types that are categorised into three classes.

Class I beam elements

Beams of class I can be determined by their area and moment of inertia or by defining the dimensions of predefined shapes provided by DIANA. The primary variables for this class are normal forces and moments regarding stresses, which correspond to elongation and curvature for two-dimensional beams. Torsion is also included in the primary strains of the elements for three-dimensional beams.

It is worth noting that beams of class I, by default, do not account for shear deformation, as they rely on the Bernoulli theory, where the cross-section remains plane and perpendicular to the beam's axis. However, DIANA software allows beam element models of class I to consider shear deformation by specifying a shape factor S in the material properties. Additionally, when utilising two-dimensional, three-node curved beam elements of class I, shear deformation is taken into account by default. By doing so, the deformation of the beams is regarded according to the Timoshenko theory, which considers a constant distribution of shear stresses over the cross-section.
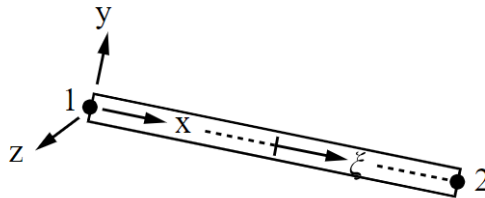
Figure C.2: Two-node straight Class I beam element - L6BEN (DIANA FEA Release notes).

This section offers a comprehensive review of two class I element types. Firstly, the two-dimensional, two-node straight beam element known as L6BEN is based on the Bernoulli theory (Figure C.2). The same element type is also analysed but with a specified shape factor of S=1.2 to account for shear deformation. The analysis of the two-dimensional, three-noded beam element (CL9BEN) is not performed as it would increase calculation time due to the p-refinement of the beam element (Figure C.3). The characteristics of the investigated class I elements are presented in Table C.2.
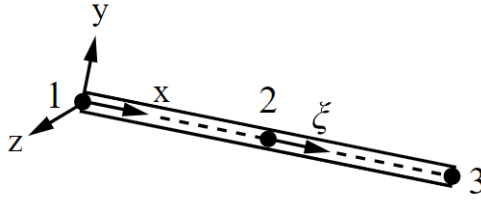
Figure C.3: Three-node curved Class I beam element - CL9BEN (DIANA FEA Release notes).

Class II beam elements

The numerical integration of DIANA's class-II Bernoulli beam elements along their cross-section and axis makes them well-suited for use in both physical and geometrical nonlinear analysis. In contrast to class-I beam elements, these beams include an additional variable, namely the relative elongation of the beam - Δu_x. The primary variables for class-II beams comprise Cauchy stresses and Green-Lagrange strains, which are derived directly from node displacements. It is important to note that the primary strains and stresses of class-II beams are not calculated with consideration to the distributed load or self-weight on the beam element. Given these characteristics, class-II beam elements are deemed unsuitable for the current investigation and, therefore, are not included in the analysis.

Class III beam elements

DIANA software employs class-III beams, which consist of both straight and curved elements. These elements undergo numerical integration along their axis and cross-section and are based on the Mindlin-Reissner theory, which accounts for shear deformation. The class-III beam elements differ from the classical beam elements of class-I and class-II, using an isoparametric formulation. This formulation allows the beam axis normals' displacements and rotations to be mutually independent and interpolated from the nodal displacements and rotations. The cross-sectional geometry of the beams is determined through predefined shapes of DIANA FEA that do not, however, include a geometry similar to the investigated beam. As a result, the precast beam cannot be accurately represented by class-III beam elements, and consequently, this beam element type is excluded from the analysis.

C.3 Plates and shells

The modelling of the precast beams can also conducted using plate or shell elements, whose configuration and thickness have been properly determined to match the geometry of the beams. These elements are characterised by a relatively small out-of-plane thickness in comparison with their in-plane dimensions. They can have a quadrilateral or triangular shape, while their displacement field can present a linear, quadratic or cubic interpolation function. Within the DIANA software, three types of plate or shell elements are available, including the plate bending element, the flat shell element, and the curved shell element.

Plate elements

The design of plate-bending elements necessitates their adherence to specific shape and loading criteria. These elements must exhibit a flat configuration, with the node coordinates situated on the xy plane of the element. Force loading (F) must act perpendicularly to the element plane, while moment loading (M) must act around an axis situated in the element plane (Figure C.4). The plate-bending elements are characterised by a zero direct stress component perpendicular to the plane, which satisfies the plane stress condition. The normals of the element plane remain straight post-deformation, and the displacement perpendicular to the plane remains consistent throughout the thickness.

Two categories of plate-bending elements are available, namely, Discrete Kirchhoff plate elements based on the Discrete Kirchhoff theory and Mindlin plate elements based on the Mindlin-Reissner theory. Both kinds of plate-bending elements are numerically integrated. These elements are typically employed in analysing two-dimensional structural components that are not subject to in-plane forces. However, due to the geometry of the examined structure, precast beams are mostly subjected to in-plane loading, rendering plate-bending elements unsuitable for their modelling.
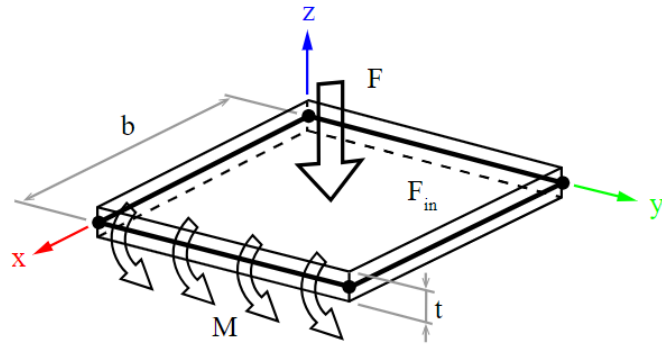
Figure C.4: Characteristics of plate bending element (DIANA FEA Release notes).

Flat shell element

Flat shell elements combine the characteristics of both plane and plate-bending elements. However, in contrast to plane stress elements, forces are the fundamental variables instead of Cauchy stresses. To qualify as a flat shell element, the element must meet specific shape and loading criteria, including being planar and having its nodes' coordinates lying in a flat plane. If these criteria are not met, the element can be replaced by curved shell elements.

It is worth noting that force loads (F) can act in any direction, either out or in the plane, while moments (M) only act within the flat shell element's plane (Figure C.5). After deformation, the plane normals remain straight, and there are no variations in the perpendicular displacement's thickness direction.

Flat shell elements are unique in that they do not exhibit coupling between the membrane and bending behaviour despite being a combination of plane stress and bending plate elements. The membrane behaviour is similar to that of a plane stress element, except that the primary stresses are defined in terms of forces and moments instead of Cauchy stresses.
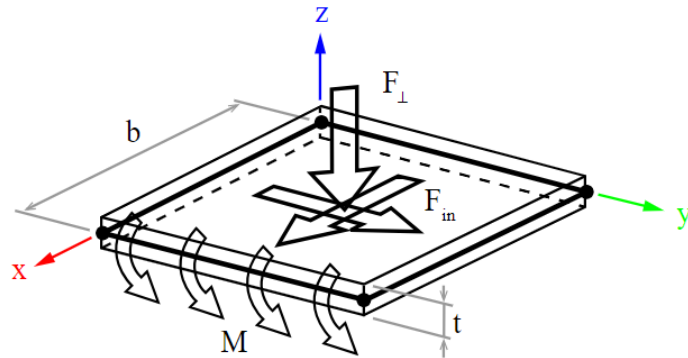
Figure C.5: Characteristics of flat shell element (DIANA FEA Release notes).

Diana provides two distinct categories of flat shell elements, namely regular elements and elements with drilling rotation (Figure 6.4). The regular elements offer three degrees of freedom for translation and two degrees of freedom for in-plane rotation at each node. Conversely, elements with drilling rotation offer an additional degree of freedom for rotation (ϕ_z) perpendicular to the plane at each node, commonly known as the "drilling rotation".

In this analysis, the modelling of the precast beams is conducted using the Q24SF element type (Figure 6.19), whose characteristics are presented in Table C.1. This type refers to a quadrilateral, four-node flat shell element with drilling rotation. The beam models analysed in this section are intended to be used in the global analysis model. As analytically explained in Chapter 6, the configuration of the structural components may result in incompatibility at their connection points. Therefore, These elements are selected to prevent such problems and ensure that they will have the same degrees of freedom at their shared nodes.

Curved shell elements

Diana's curved shell elements employ an isoparametric degenerated-solid approach that comprises two shell hypotheses, namely the straight-normals and zero-normal stress hypotheses. The straight-normals hypothesis assumes that the normals are straight, though not necessarily normal to the reference surface, and accounts for transverse shear deformation based on the Mindlin-Reissner theory. Meanwhile, the zero-normal-stress hypothesis enforces a zero normal stress component in the normal direction ($\sigma_{zz} = 0$).

Each shell point is equipped with a local Cartesian coordinate system (xy_{local}) corresponding to a lamina basis and spanning the element tangent plane. The x_l and y_l local directions are tangent to the $\xi\eta$ plane, while the z_l direction is perpendicular. The curved shell elements exhibit strains characterised by linear variation in the thickness direction for in-plane strains such as ε_{xx}, ε_{yy}, and γ_{xy}. In contrast, transverse shear strains γ_{xz} and γ_{yz} remain constant in the same direction.

Like flat shell elements, each node of curved shell elements has five defined degrees of freedom, encompassing three translations and two rotations. The degrees of freedom per node can be increased by the rotation perpendicular to the plane, utilising the curved shell elements with drilling rotation. Figure C.6 illustrates that force loads are present in any direction in and out of the shell plane, while moment loads act around the in-plane axis of the element.

When comparing the two types of shell elements, it is worth noting that flat shell elements are a more cost-effective choice, particularly in situations where the desired results are forces and moments. As a global analysis model is utilised to obtain bending moments at the midspan of the beam for various loads, flat shell elements have been selected for precast beam modelling.
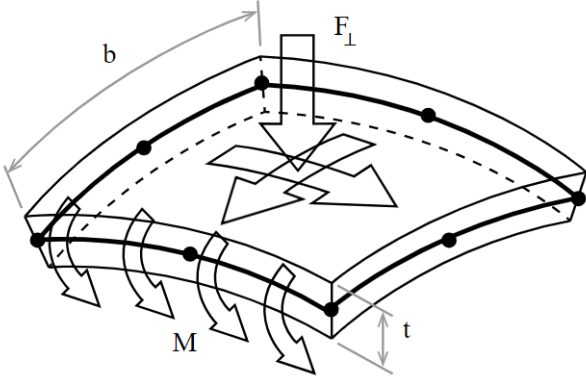
Figure C.6: Characteristics of curved shell element (DIANA FEA Release notes).

Shell element design versions

As aforementioned, the precast beams can be modelled using shell elements, provided their configuration and thickness are accurately determined to correspond to the beams' geometry. In

this beam model analysis, two model versions of the precast beams are examined, one including both vertical and horizontal shell elements and one utilising only vertical shells to model the beams.

As illustrated in Figure C.7, the flat shell element thickness can be either constant throughout the whole element or tapered. The variation of the thickness can be accomplished using spacial functions depending on one, two or three global coordinate components. This DIANA feature has been utilised in both model versions described below.
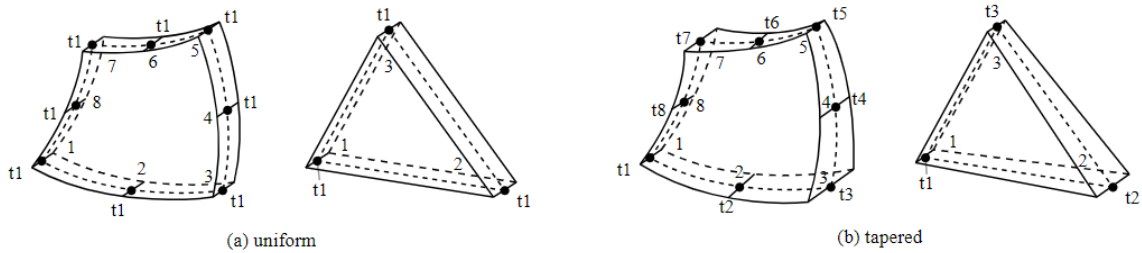
Figure C.7: Shell element thickness: (a).uniform and (b). tapered (DIANA FEA Release notes).

In the first Version (Figure C.8), shell elements were arranged both vertically and horizontally to represent the web and the flange of the inverted T-beam, respectively. Both varying and constant thickness elements have been used. A combination of varying and constant thickness elements was utilised. However, this configuration led to a problem of overlapping elements at the intersection of shell elements for the web and flange. To address this issue, the geometry of some shells is eccentrically positioned. Each beam was modelled using nine shells, trying to model the cross-sectional properties of the beam with the most possible accuracy.

In a simpler approach, the beams were modelled using only vertical shell elements. In this version, the geometry and the properties of the beams are defined by the assigned thicknesses to the shells, as presented in Figure C.9.

Both designs were used to create simply supported beam models that were later analysed to determine the element type and beam design finally used in the global analysis.
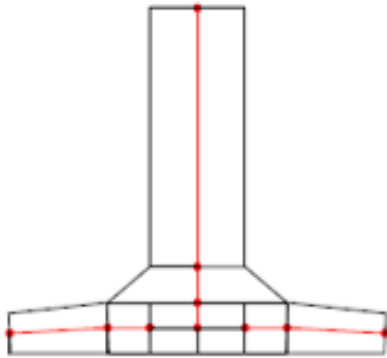
Figure C.8: Shell element design - Version 1
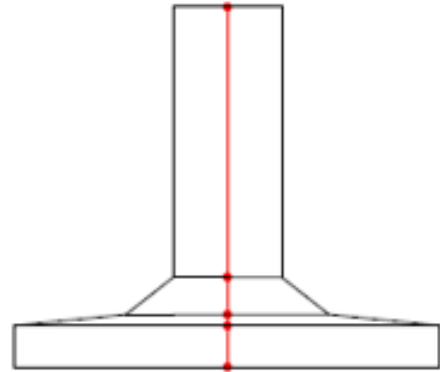
Figure C.9: Shell element design - Version 2

C.4 Solid elements

Solid elements are a highly versatile and general-purpose type of element that can be used to model complex geometries without the need for engineering considerations and simplifications of the real element geometries during analysis. In the past, these elements were not frequently employed due to their tendency to produce large systems of equations. However, modern advancements have allowed for their efficient use in situations where other elements may be unsuitable or produce inaccurate analysis results.

These elements are characterised by their three-dimensional stress situation, arbitrary loading, and dimensions in the three axial directions (x, y, and z) being of the same order of magnitude. They are often employed for analysing voluminous structures.
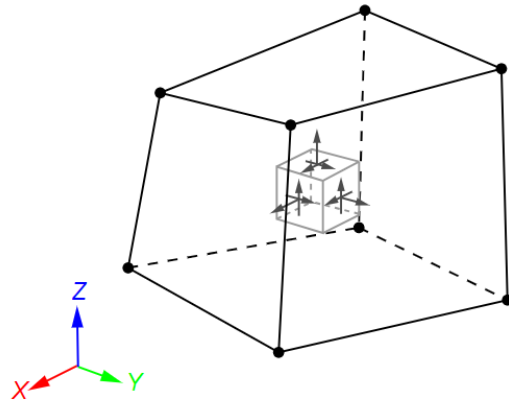
Figure C.10: Characteristics of solid element (DIANA FEA Release notes).

DIANA provides a wide range of regular three-dimensional structural element types for bodies, including tetrahedrons, pentahedrons, and hexahedrons. Furthermore, the elements may feature linear, quadratic, or cubic interpolation functions for the displacement field, depending on the specific requirements of the analysis.

In this analysis, the beams are modelled using tree-dimensional, eight-node (brick) and six-node (wedge) elements, whose characteristics are overviewed in Table C.1.

Table C.1: Characteristics of the element types (DIANA FEA Release notes)

	L6BEN	CL9BEN	Q24SF	T18SF	HX24L	TP18L
	2-nodes bending beam	3-nodes bending beam	4-nodes flat shell element with drilling rotation	4-nodes flat shell element with drilling rotation	8-node brick solid element	6-node wedge solid element
Finite Element Type						
DOFs (per node i)	Three per node: $u_x^i,\ u_y^i,\ \varphi_z^i$	Three per node: $u_x^i,\ u_y^i,\ \varphi_z^i$	Six per node: $u_x^i,\ u_y^i,\ u_z^i,\ \varphi_x^i\ \varphi_y^i\ \varphi_z^i,$	Six per node: $u_x^i,\ u_y^i,\ u_z^i,\ \varphi_x^i\ \varphi_y^i\ \varphi_z^i,$	Three per node: $u_x^i,\ u_y^i,\ u_z^i$	Three per node: $u_x^i,\ u_y^i,\ u_z^i$
Interpolation Scheme	Linear	Linear	Linear	Linear	Linear	Linear
Shape Dimensions	2D	2D	3D	3D	3D	3D
Topological Dimensions	1D	1D	2D	2D	3D	3D
Stress Components	Normal stress: σ_{xx} Shear stress: σ_{xy}	Normal stress: σ_{xx} Shear stress: σ_{xy}	Normal stress: $\sigma_{xx},\ \sigma_{yy},\ \sigma_{zz}$ Shear stress: $\sigma_{xy},\ \sigma_{xz},\ \sigma_{yz}$	Normal stress: $\sigma_{xx},\ \sigma_{yy},\ \sigma_{zz}$ Shear stress: $\sigma_{xy},\ \sigma_{xz},\ \sigma_{yz}$	Normal stress: $\sigma_{xx},\ \sigma_{yy},\ \sigma_{zz}$ Shear stress: $\sigma_{xy},\ \sigma_{xz},\ \sigma_{yz}$	Normal stress: $\sigma_{xx},\ \sigma_{yy},\ \sigma_{zz}$ Shear stress: $\sigma_{xy},\ \sigma_{xz},\ \sigma_{yz}$
Inclusion of Shear Deformation	No	Yes	Yes	Yes	Yes	Yes

C.5 Comparison of the element types

The simply supported beam models created were analysed for the following load cases:

- Load case 1: Point load ($1kN$) at the midspan of the beam

- Load case 2: Point load ($1kN$) at the $l = \frac{l}{4}$

- Load case 3: Point load ($1kN$) at the $l = \frac{l}{8}$

- Load case 4: Uniformly distributed load

- Load case 5: Self-weight of the beam

For the above loads, the deflection and bending moment at the midspan of the beams are presented in Table C.2.

Table C.2: Results of simply supported beam models for different elements

		Beam element Class I		Shell elements		Solid elements
		Bernoulli	Shape Factor	Version 1	Version 2	
Point load	$u_z[*10^{-4}m]$	-5.87	-5.88	-5.99	-5.88	-5.87534
at l/2	$M_y[kNm]$	7.25	7.25	7.25	7.25	7.25
Point load	$u_z[*10^{-4}m]$	-3.92	-3.92	-4.00	-3.92	-3.92
at l/4	$M_y[kNm]$	3.50	3.50	3.50	3.50	3.50
Point load	$u_z[*10^{-4}m]$	-1.94	-1.94	-1.96	-1.94	-1.94
at l/8	$M_y[kNm]$	1.63	1.63	1.63	1.63	1.63
Disrtibuted	$u_z[*10^{-4}m]$	-3.98	-3.99	-4.06	-3.99	-3.99
load	$M_y[kNm]$	3.94	3.94	3.94	3.94	3.94
Selfweight	$u_z[m]$	-0.10	-0.10	-0.10	-0.10	-0.10
	$M_y[kNm]$	985.58	985.58	985.58	985.58	985.58
Duration	t [sec]	1	1	8	3	11
Nodes	N	906	906	37650	16850	62420

Based on the results of the analyses, it is observed that the different element types did not result in significant differences in terms of deflection and bending moment. As expected, the deflection of the Bernoulli beam is smaller compared to the rest of the elements, which also accounts for shear deformation. However, this deference caused by the shear deformation is very small. The response of the beam models is highly affected by their slenderness, with shear deformation being negligible in slender beams. One exception was the Version 1 shell element beam model, which was found to have larger deflections compared to the other models. The larger deflections can be attributed to the design of the beam, which could not provide a completely accurate representation of the beam's cross-sectional properties.

Besides the deformation and internal forces resulting from the analyses, plenty of other parameters contribute to the selection of the element type finally used for the bridge model. Starting from the time required for the design of the models, beam elements are, without a doubt, the simplest design method offered. The beam element models were created through a straightforward method, making them efficient in terms of design time and an attractive solution for engineering practice. The solid element model also presented a simple design process. The design complexity was significantly increased for the Version 1 shell element model. Its design process required careful consideration of the shells' configuration, thicknesses and geometries. For this reason, the simpler approach followed in the Version 2 shell element model is considered more efficient, requiring a relatively small design time and employing a simpler model geometry.

During the design process, it is imperative to consider the computational time required for the analysis. Table C.2 shows that beam elements are the most cost-effective solution, requiring the least number of nodes and shortest calculation time. On the other hand, the solid element model is the least efficient, significantly increasing the number of calculated elements and, consequently, the analysis time. The shell type is often used as an intermediate design solution as it results in a more efficient model compared to the solid element model. It is noted that the effects of the more complex geometry of the Version 1 beam are also evident in this parameter.

In the analysed cases using shell and solid elements, the results were obtained using a composed line feature offered by DIANA, described in Chapter 6. This way, the resulting concentrated forces and moments were easily obtained without requiring a complicated post-processing of the

results.

An additional parameter that needs to be considered is the compatibility of utilised elements. As discussed in Chapter 6, the top slab was modelled using shell elements with drilling rotation, which offer six degrees of freedom per node, including three translational and three rotational degrees of freedom. This element type is compatible with both beam and shell elements of the same type used for the precast beam modelling. Solid elements, conversely, only account for three translations and no rotations at their nodes (Figure C.11). In case solid elements are used for precast beams, the same element type should also be used for all other structural components, which would significantly increase computation time.
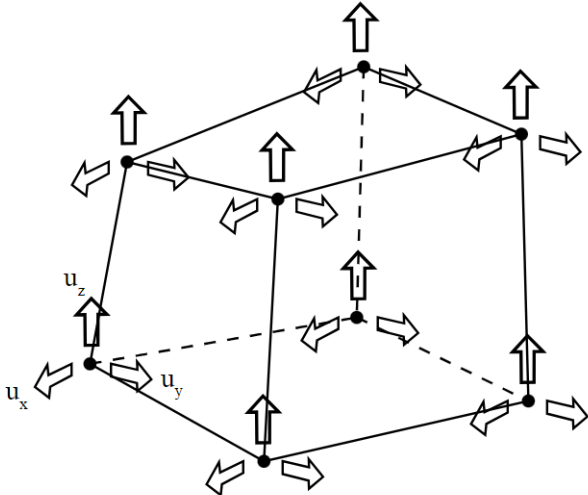
Figure C.11: Veriables of solid element (DIANA FEA Release notes).

The selection of element type depends on several factors, including the design's accuracy, the characteristics that need to be modelled, and the results that need to be obtained from the analysis. Beam elements are efficient and accurate in simulating the cross-sectional properties of beams, making them ideal for internal force calculations. However, beam elements are unsuitable when modelling characteristics that vary over the beam directions. In this element type, the properties of the beam are concentrated in a single line. This way, the variation of these properties, for example, the stiffness reduction over the beam height caused by cycling loading, cannot be simulated using this element type. In addition, beam elements cannot provide results

such as the strain and stress distribution or the distributed forces. On the other hand, these options are available for both shell and solid element types.

As analysed in Chapter 7, cyclic loading can cause material degradation of the precast beam, which is translated with the reduction of their stiffness. As this degradation is highly dependent on the applied stresses, its effect is more evident at the top layer of the beams, where the highest stresses are noted. As a result, this stiffness reduction is not constant over the beam height. To simulate this effect, an element type that allows the variation of properties over the beam height needs to be employed. Even though this feature was finally not utilised in the analysis due to time limitations, the model was initially designed to offer this design option.

Finally, considering the accuracy of the bridge design, using bream elements for the precast beam means that the cross beams are also modelled using beam elements. This way, the connection of the two elements is conducted to a single point, which cannot accurately represent the confinement offered by the diaphragm beam. The same problem is also met when modelling the cross beams using shell elements. Even though this approach can ensure an over-the-height connection of the two beams, it does not accurately model the cross-beam connection in the beams in the longitudinal direction. To mitigate this issue, alternative solutions can be employed, as described in Section 6.2.1.3. The most accurate approach would include modelling all the structural components using solid elements, which, however, would significantly impact the model's effectiveness.

Taking the above into consideration, it has become clear that different element types may be used to study the structure. Each type presents its own advantages and disadvantages in the analysed domains. In linear structure analysis, beam elements provide sufficiently accurate results for the internal forces on structural components. However, in studies where nonlinear analysis is conducted, the stresses, strains or distributed forces and moments are studied, localised effects are analysed, or the variation of the properties needs to be modelled, a different type of element might regarded as more appropriate.

Comparing the two beam versions using shell elements, it is noted that the Version 2 model provided more accurate results and modelling of the beam properties. Furthermore, the Version

1 model requires a substantially longer time for both its design and analysis, with a calculation time of more than twice that of Version 2. This difference would significantly impact the computational time required for analysing the bridge.

It could be argued that the beam model, including the beam flanges, better represents the torsional behaviour of the beam, as flanges contribute to its torsional stiffness. To investigate the influence of this effect on the beams, the two beam models were analysed for eccentrically located point loads, for which the resulting torsional moments are presented in Table C.3. Based on these results, it is evident that the torsional stiffness of Version 1's beam is slightly larger, resulting in smaller torsional moments caused by the same loads. However, the obtained values do not present a significant divergence, and therefore, we consider that Version 2's shell element model sufficiently simulates the torsional stiffness of the beam.

Table C.3: Torsional moments at the midspan of the simply supported beam models modelled with shell element

		Shell elements	
		Version 1	Version 2
Ecc.Point load (1kN) at l/2	$M_x[Nm]$	11.60	11.55
		-11.60	-11.55
Ecc.Point load (1kN) at l/4	$M_x[Nm]$	33.75	34.79
		33.83	34.83
Ecc.Point load (1kN) at l/8	$M_x[Nm]$	15.79	15.93
		15.80	15.94

A last comparison is conducted between the Version 2 shell element model and the solid element model. For this analysis, the different elements are used to model the precast beam in the global analysis model. The response of the bridge model is examined for the self-weight loads, for which the obtained bending moments at the midspan of the beams are presented in Table C.4. Notable, the divergence of the resulting moments is smaller than 0.15% and is therefore considered negligible.

Table C.4: Comparison of the global models modelled using shell and solid elements.

| | Element type | | Difference |
| Beam | Shell | Solid | |
	$M_y(kNm)$	$M_y(kNm)$	%
1	1481.17	1482.76	0.11
2	1483.26	1484.41	0.08
3	1484.59	1485.02	0.03
4	1488.04	1487.69	0.02
5	1491.61	1490.56	0.07
6	1494.08	1492.81	0.08
7	1494.95	1493.56	0.09
8	1494.08	1492.81	0.08
9	1491.61	1490.56	0.07
10	1488.04	1487.69	0.02
11	1484.59	1485.02	0.03
12	1483.26	1484.41	0.08
13	1481.17	1482.76	0.11

Summarising, based on the above analyses, it has been determined that the shell Version 2 element beam design is the most suitable choice for the present study. This model offers an accurate representation of the beam and bridge geometry, along with a diverse range of modelling possibilities. Moreover, the design proves to be highly efficient in terms of both computational time and practicality.

D   Model validation

The precision of the constructed models was validated for both beam models examined in Appendix C, as well as for a model of the composite beam and the global analysis model. It is noteworthy that for this validation, the beams were modelled as simply supported using regular supports.

Beam models

Point load at the midspan In statically determined beams, whose supports are located at a distance $d = 0.5m$ from its edges, the bending moment at the midspan of the beam for a point load ($F = 1kN$) applied at $x = \frac{l}{2}$ is given as,

$$M_{pointload} = \frac{F}{2}\left(\frac{l}{2} - d\right) = \frac{1}{2}\left(\frac{30}{2} - 0.5\right) = 7.25kNm \tag{99}$$

Furthermore, the effect of the self-weight of the beam is calculated as a distributed load, whose resulting moment at the midspan of the beam equals,

$$q_{beam} = A_{beam} \cdot \gamma_{concrete} = 375460 \cdot 10^{-6} \cdot 25 = 9.39kN/m \tag{100}$$

$$M_{beam} = \frac{q_{beam}l}{2}\left(\frac{l}{2} - d\right) - \frac{q_{beam}(\frac{l}{2})^2}{2} = \frac{9.39 \cdot 30}{2}\left(\frac{30}{2} - 0.5\right) - \frac{9.39(\frac{30}{2})^2}{2} = 985.58kNm \tag{101}$$

Composite beam model

For the composite section consisting of the beam and the equivalent parts of the cast in-situ slab and the cross-beams, the validation is again conducted regarding the resulting bending moment at $x = \frac{l}{2}$. The section is analysed for the self-weight of its structural components. Specifically, the self-weight of the beam and the slab are accounted as distributed loads, while for the weight of each cross-beam, point loads were applied at the locations of the shell elements representing the diaphragm beams (Figure D.1). As explained in Chapter 6, the diaphragm beam is modelled

using two shell elements having half its thickness. The bending moment at the beam midspan is calculated as,

$$q_{slab} = A_{slab} \cdot \gamma_{concrete} = (1200 \cdot 160) \cdot 10^{-6} \cdot 25 = 4.80 kN/m \tag{102}$$

$$M_{slab} = \frac{q_{slab}l}{2} \left(\frac{l}{2} - d \right) - \frac{q_{slab}(\frac{l}{2})^2}{2} = \frac{4.80 \cdot 30}{2} \left(\frac{30}{2} - 0.5 \right) - \frac{4.80(\frac{30}{2})^2}{2} = 504.00 kNm \tag{103}$$

$$F_{cross-beam} = \left[(H_{cross-beam} \cdot \frac{t_{cross-beam}}{2} \cdot b_{equivalent}) - (A_{beam} - (1.18 \cdot 0.115)) \right] \cdot \gamma_{concrete} \tag{104}$$

$$= \left[(0.695 \cdot 0.4 \cdot 1.2) - (375460 \cdot 10^{-6}) - (1.18 \cdot 0.115)) \right] \cdot \gamma_{concrete} = 5.94 kN \tag{105}$$

$$M_{cross-beam} + F_{cross-beam} \cdot (x - 0.6) + F_{cross-beam} \cdot (x - 0.2) - 2F_{cross-beam} \cdot (x - 0.5) = 0 \tag{106}$$

$$\Rightarrow M_{crossbeam} = -0.2 \cdot F_{cross-beam} \tag{107}$$

$$\Rightarrow M_{cross-beam}(\frac{l}{2}) = -0.2 \cdot F_{cross-beam} = -1.19 kNm \tag{108}$$

Therefore, the resulting bending moment at the midspan of the beam is

$$M_{Total} = M_{beam} + M_{slab} + M_{cross-beam} = 1488.39 kNm \tag{109}$$

This result was also obtained by the numerical analysis of the composite cross-section.
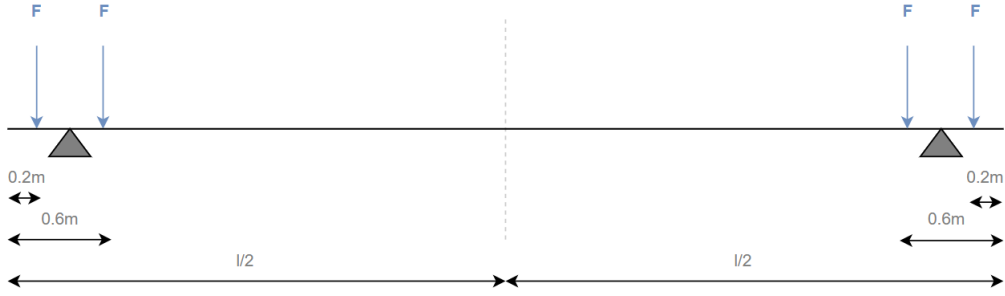
Figure D.1: Equivalent loads from the self-weight of the cross-beams.

Global model

The validation of the global analysis model was also conducted for the self-weight of the structure, calculating the total reaction force of the model and the total bending moment at the midspan of the bridge.

The structural components of the bridge contribute to its total weight, which is calculated as follows,

$$F_{beam} = 13 \cdot L_{bridge} \cdot A_{beam} \cdot \gamma_{concrete} = 13 \cdot 30 \cdot (375460 \cdot 10^{-6}) \cdot 25 = 3660.74kN \tag{110}$$

$$F_{slab} = L_{bridge} \cdot W_{bridge} \cdot H_{slab} \cdot \gamma_{concrete} = 30 \cdot 15.58 \cdot 0.16 \cdot 25 = 1869.60kN \tag{111}$$

$$F_{cross-beam} = [2 \cdot (W_{bridge} \cdot t_{cross-beam}) - 13 \cdot (A_{beam \cdot cross-beam})] \cdot \gamma_{concrete} \tag{112}$$

$$= [2 \cdot (30 \cdot 0.8) - 13 \cdot (375460 \cdot 10^{-6} \cdot 0.8)] \cdot 25 = 308.45kN \tag{113}$$

$$F_{Total} = F_{beam} + F_{slab} + F_{cross-beam} = 5838.78kN \tag{114}$$

The total weight of the bridge should be equal to the summation of the reaction forces presented

187

in Table D.1.

Table D.1: Reaction forces due to self-weight

Reaction	F_z [kN]
1	254.08
2	244.52
3	221.78
4	223.38
5	218.64
6	221.73
7	218.38
8	220.60
9	218.60
10	219.98
11	218.79
12	219.70
13	218.90
14	219.63
15	218.80
16	219.70
17	218.60
18	219.98
19	218.37
20	220.58
21	218.70
22	221.80
23	221.71
24	223.35
25	254.10
26	244.51
Total	5838.80

As previously calculated, the bending moment at the midspan of the cross-section is $1488.39 kNm$ for the intermediate beams (Beams 2-12) and $1484.21 kNm$ for the edge beams (as the considered width equals 1.19m instead of 1.2m). For the total bridge,

$$M_{Total} = (13 \cdot 1488.39) + (2 \cdot 1484.250) = 19340.7 kNm \tag{115}$$

The total moment should be equal to the summation of the model bending moments presented in Table D.2. Table D.2 provides an overview of the model and calculated values, establishing

that the analytical calculations confirm the numerical results. It is worth noting, however, that the model moments of the composite section do not align with the analytically calculated values. Instead, they display variation in the transverse direction. Specifically, the middle beam exhibits the highest bending moment, while the values decrease towards the edge beams. This variation can be explained by the lateral bending and load distribution, as well as the torsional stiffness of the structural components, factors that were not accounted for in the analytical calculations.

Table D.2: Summation of the total bending moments at the midspan of the bridge due to self-weight.

Beam	$M_y(kNm)$
1	1481.17
2	1483.26
3	1484.59
4	1488.04
5	1491.61
6	1494.08
7	1494.95
8	1494.08
9	1491.61
10	1488.04
11	1484.59
12	1483.26
13	1481.17
Total	19340.45

E Ultimate Limit State - Bending moment capacity

As previously stated, this study employs the failure criterion due to bending. One of the criteria in the selection of the beam dimensions and configuration of the prestressing strands is to ensure that the bridge does not fail due to bending moment. Otherwise, in case of failure, the analysis would not proceed with assessing the fatigue life of the bridge.

In the composite structure, the failure can occur if:

- The strain at the top of the compressive zone of the precast beam exceeds the concrete ultimate strain: $\varepsilon_c \geq \varepsilon_{cu3}$,

- The strain at the top of the compressive zone of the top slab exceeds the concrete ultimate strain: $\varepsilon_c \geq \varepsilon_{cu3}$,

- The strain at the prestressing reinforcement level exceeds its ultimate value: $\varepsilon_p \geq \varepsilon_{pu3}$.

Given that the depth of the cast in-situ deck is relatively small ($160mm$), it is considered that the strains in this part are larger than the yield strain. Therefore, the developed stresses of the deck can be viewed as uniform all over its height and equal to the design strength of the concrete (C25/30).

For the Ultimate Limit State, the prestressing strands present prestress losses of 15%. The figure below shows the distribution of forces for ULS, with a compression zone of depth h_i.

By applying the equilibrium of forces,

$$N_b + N_d - \Delta F_p = F_{pw} \tag{116}$$

$$ab_b x_u F_{cd,b} + b_d h_d F_{cd,d} - A_p 0.85 \frac{f_{pk}}{1.1} - \sigma_{pm\infty} = F_{pm\infty} \tag{117}$$

$$x_u = \frac{A_p 0.85 \frac{f_{pk}}{1.1} - b_d h_d F_{cd,d}}{ab_b F_{cd,b}} = 603mm \tag{118}$$

As $x_u > H_{slab}$, is located in the web of the beam

For the bending moment resistance,

$$M_{Rd} = N_d z_d + N_b z_b + (F_{pw} + \Delta F_p)e_p = 4557.80 kNm \qquad (119)$$

The bending moment capacity of the bridge is assessed for the permanent and variable loads acting on the structure. For the Ultimate Limit State, the acting moment is obtained by the load combinations of Table 5.7. For the traffic loads, two loading configurations were examined, as depicted in Figure E.1. Positioning the heaviest loaded lane close to the bridge resulted in the most adverse effect. The check is performed for the critical beam of the bridge, which in this case is Beam 4. The maximum design moment is obtained for the 6.10b - gr1a load combination as

$$M_{Ed} = 1.15 M_{Ed,G} + 1.25 M_{Ed,Q} = 4396.21 kNm \qquad (120)$$

Therefore,

$$UC = \frac{M_{Ed}}{M_{Rd}} = 0.96 \qquad (121)$$
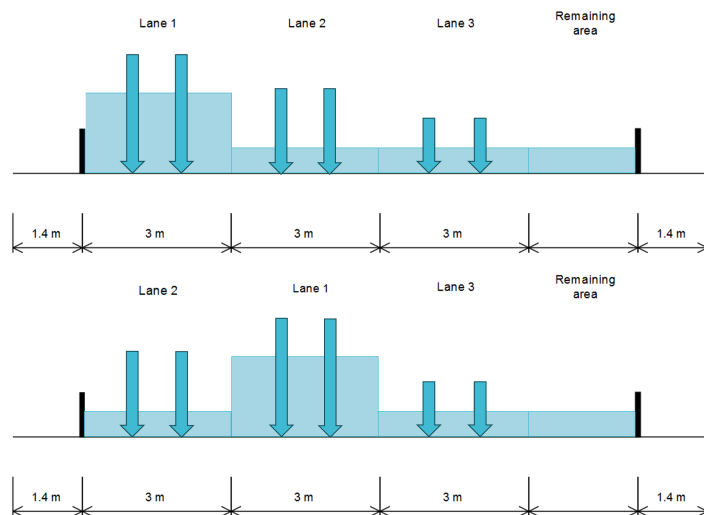
Figure E.1: Loading configurations analysed for traffic loads (Load Model 1).

F Prestress losses

F.1 Prestress losses accounting for axial loads

Various simplifications have been taken into consideration while calculating the prestress losses. The calculation presented here takes into account the development of creep and shrinkage strains in the beam, along with relaxation losses. It is noteworthy that the beam's creep and shrinkage were considered to develop independently of its interaction with the cast-in-situ slab.

In order to determine the creep strain, only axial loads were considered, while bending moments were excluded. This is a common practice as the stress value at the prestress level is not uniform along the length of the beam. Bending moments cause a stress gradient, leading to smaller stress values at the level of the strands. However, this is not constant for the entire length of the beam. Therefore, focusing solely on axial loads might be a more conservative approach, as higher stress levels lead to larger prestress losses in the analysis.

Creep

The creep and shrinkage of concrete are influenced by the ambient humidity, composition of the concrete, and dimensions of the element. The magnitude and duration of the loading, as well as the maturity of the concrete at the time of the initial application of the load, can also affect the amount of creep.

To determine the creep deformation of concrete $\varepsilon_{cc}(t, t_0)$ at a given time t under a constant compressive stress σ_c applied at the age t_0 of the concrete, the following formula can be utilized,

$$\varepsilon_{cc} = \varphi\left(t, t_0\right) \frac{\sigma_c}{E_c} \tag{122}$$

where,

$\varphi\left(t, t_0\right)$	the final creep coefficient,
t_0	the age of concrete at the loading time (10 days),
E_c	$1.05 \cdot E_{cm}$, the tangent modulus and
σ_c	the compressive stress

The creep coefficient is given as,

$$\varphi\left(t, t_0\right) = \varphi_0 \cdot \beta_c\left(t, t_0\right) \tag{123}$$

with, the notional creep coefficient before the casting of the slab:

$$\varphi_0 = \varphi_{RH} \cdot \beta\left(f_{cm}\right) \cdot \beta\left(t_0\right) = 1.27 \tag{124}$$

and $\varphi_0 = 1.26$ after the slab casting,

To account for:

the effect of relative humidity (80%)on φ_0 coefficient,

$$\varphi_{RH} = \left[1 + \frac{1 - \frac{RH}{100}}{0.1 \cdot \sqrt[3]{h_0}} a_1\right] a_2 = 1.09 \quad \text{for} \quad f_{cm} > 35 MPa \tag{125}$$

the effect of concrete strength

$$\beta\left(f_{cm}\right) = 16.8/\sqrt{f_{cm}} = 2.12 \tag{126}$$

and the effect of concrete age at loading

$$\beta\left(t_0\right) = \frac{1}{0.1 + t_0^{0.2}} = 0.55 \tag{127}$$

The notional size of the member is

$$h_o = \frac{2A_c}{u} = 195.4mm \tag{128}$$

before the top layer is cast, and $h_0 = 210.8mm$ after the slab casting.

The coefficient that describes the degree of creep development that occurs over time after loading is calculated as,

$$\beta_c\left(t, t_0\right) = \left[\frac{\left(t - t_0\right)}{\left(\beta_{\mathrm{H}} + t - t_0\right)}\right]^{0,3} \tag{129}$$

with, β_H a coefficient that depends on the relative humidity and the notional member size, which equals to

$$\beta_H = 1,5 \left[1 + (0,012RH)^{18}\right] h0 + 250a_3 = 187.84 \leq 1500a_3 = 1118 \quad \text{for} \quad f_{cm} \leq 35MPa \tag{130}$$

The following coefficients take into consideration the effect of concrete strength as,

$$a_1 = \left[\frac{35}{f_{cm}}\right]^{0.7} = 0.66 \tag{131}$$

$$a_2 = \left[\frac{35}{f_{cm}}\right]^{0.2} = 0.89 \tag{132}$$

$$a_3 = \left[\frac{35}{f_{cm}}\right]^{0.5} = 0.75 \tag{133}$$

The creep coefficient of concrete can be modified by adjusting the age of loading with respect to the type of cement used.

$$t_0 = t_{0,T} \left(\frac{9}{2 + t_{0,T}^{1.2}} + 1\right)^a 15.02 \geq 0.5 \tag{134}$$

where,

a $= 1$ for cement class R

$t_{0,T}$ the temperature corrected age of concrete in days, given by

$t_T = \sum_{i=1}^n \Delta t_i e^{13.65 - \frac{4000}{273 + T(\Delta t_i)}}$, with

Δt_i : the number of days with temperature T

$T(\Delta t_i)$: the temperature during time period Δt_i

Based on the above the time-dependent values of the creep coefficient $\varphi_0(t, t_0)$, $\beta_c(t, t_0)$ and finally the creep strain $\varepsilon_{cc}(t, t_0)$ are presented in Table F.1

Shrinkage

Concrete's total shrinkage strain is composed of two main components - drying shrinkage strain and autogenous shrinkage strain. Drying shrinkage strain occurs slowly over time as water migrates through the hardened concrete, while autogenous shrinkage strain develops during the

hardening process of concrete.

In order to determine the values of total shrinkage strain, both drying and autogenous shrinkage strains need to be taken into consideration, as follows

$$\varepsilon_{cs} = \varepsilon_{cd} + \varepsilon_{ca} \tag{135}$$

where,

ε_{cd} the drying shrinkage and

ε_{ca} the autogenous shrinkage.

For the drying shrinkage ε_{cd},

$$\varepsilon_{cd,} = \beta_{ds}\left(t, t_s\right) k_h \varepsilon_{cd,0} \tag{136}$$

with,

$$\beta_{ds}\left(t, t_s\right) = \frac{t - t_s}{\left(t - t_s\right) + 0.04\sqrt{h_0^3}} \tag{137}$$

The basic drying shrinkage strain is determined as

$$\varepsilon_{cd,0} = 0.85 \left[\left(220 + 110 a_{ds1}\right) \exp\left(-a_{ds2}\frac{f_{cm}}{f_{cm0}}\right)\right] = 2.83 \cdot 10^{-4} \tag{138}$$

where, for the cement type CEM42.5R:

$$a_{ds1} = 6 \tag{139}$$

$$a_{ds2} = 0.11 \tag{140}$$

and

$$\beta_{RH} = 1.55 \left[1 - \left(\frac{RH}{RH_0} \right)^3 \right] = 0.76 \tag{141}$$

The value of k_h is determined based on the notional size of the cross-section (h_0) and equals to $k_h = 0.86$ and $k_h = 0.84$ before and after the slab casting, respectively.

The autogenous shrinkage strain ε_{ca} is calculated as,

$$\varepsilon_{ca}(t) = \beta_{as}(t) \varepsilon_{ca,\infty} \tag{142}$$

with

$$\varepsilon_{ca,\infty} = 2.5 \left(f_{ck} - 10 \right) 10^{-6} \tag{143}$$

$$\beta_{as}(t) = 1 - \exp\left(-0.2 t^{0.5} \right) \tag{144}$$

The time-dependent values that have been calculated are listed in Table F.1.

Relaxation

The relaxation loss can be determined either by referencing the manufacturer's test certificates or by calculating it as a percentage of the variation between the prestressing stress and the initial prestressing stress. For this study, the relaxation losses are calculated according to Class II, based on the following expression,

$$\frac{\Delta \sigma_{\mathrm{pr}}}{\sigma_{\mathrm{pi}}} = 0.66 \rho_{1000} \mathrm{e}^{9.1\mu} \left(\frac{t}{1000} \right)^{0.75(1-\mu)} 10^{-5} \tag{145}$$

where,

$\mu \qquad = \frac{\sigma_{\mathrm{pi}}}{\mathrm{f}_{\mathrm{pk}}}$,

$\rho_{1000} \qquad = 8\%$, the value of relaxation loss (in %), at 1000 hours after tensioning and at

mean temperature of 20°C,

t the time after tensioning,

σ_{pi} absolute initial prestress

Relaxation losses have been computed for every decade, and the obtained results are presented in Table F.1.

Based on the above, the total prestress losses are given as

$$\Delta\sigma_{\mathrm{c+s+r}} = \Delta\sigma_{\mathrm{c+s}} + 0.8\Delta\sigma_{\mathrm{pr}} = \varepsilon_{\mathrm{tot}}(\mathrm{t}) * \mathrm{E}_{\mathrm{p}} + 0.8\Delta\sigma_{\mathrm{pr}} \tag{146}$$

Table F.1: Time-dependent parameters for prestress losses accounting for axial loads

			10 years	20 years	30 years	40 years	50 years	60 years	70 years	80 years	90 years	100 years
Age of concrete (days)	t	28	3650	7300	10950	14600	18250	21900	25550	29200	32850	36500
Creep												
Creep development coefficient	$\beta_c(t,t0)$	0.4396	0.9850	0.9924	0.9949	0.9962	0.9969	0.9974	0.9978	0.9981	0.9983	0.9985
Creep coefficient at t	$\varphi(t,t0)$	0.5583	1.2458	1.2551	1.2583	1.2599	1.2608	1.2615	1.2619	1.2623	1.2626	1.2628
Creep strain	$\varepsilon_{cc}(t)$	2.26E-04	5.05E-04	5.09E-04	5.10E-04	5.10E-04	5.11E-04	5.11E-04	5.11E-04	5.11E-04	5.12E-04	5.12E-04
Shinkage												
Autogenous shrinkage												
Autogenous shrinkage coefficient	$\beta_{as}(t)$	0.6530	1.0000	1.0000	1.0000	1.0000	1.0000	1.0000	1.0000	1.0000	1.0000	1.0000
Autogenous shrinkage strain	$\varepsilon_{ca}(t)$	7.35E-05	1.12E-04	1.12E-04	1.12E-04	1.12E-04	1.12E-04	1.12E-04	1.12E-04	1.13E-04	1.13E-04	1.13E-04
Drying shrinkage strain												
Drying shrinkage coefficient	$\beta_{ds}(t,t_s)$	0.1922	0.9675	0.9835	0.9889	0.9917	0.9933	0.9944	0.9952	0.9958	0.9963	0.9967
Drying shrinkage	$\varepsilon_{ds}(t)$	4.66E-05	2.35E-04	2.39E-04	2.40E-04	2.40E-04	2.41E-04	2.41E-04	2.41E-04	2.41E-04	2.42E-04	2.42E-04
Total shrinkage	$\varepsilon_{cs}(t)$	1.20E-04	3.47E-04	3.51E-04	3.52E-04	3.53E-04	3.53E-04	3.54E-04	3.54E-04	3.54E-04	3.54E-04	3.54E-04
Total strain	$\varepsilon_{tot}(t)$	3.46E-04	8.52E-04	8.60E-04	8.62E-04	8.63E-04	8.64E-04	8.65E-04	8.65E-04	8.65E-04	8.66E-04	8.66E-04
Relaxation												
Relaxation losses N/mm^2	$\Delta\sigma_{pr}$	9.90	26.86	30.60	33.03	34.87	36.36	37.63	38.73	39.72	40.61	41.42
Total prestress losses	$\Delta\sigma_{c+s+r}$	**75.37**	**187.63**	**192.11**	**194.55**	**196.27**	**197.62**	**198.73**	**199.69**	**200.53**	**201.29**	**201.97**

F.2 Prestress losses accounting for axial loads and bending moments

In the above section, the calculation of the prestress losses was conducted considering only the axial loads applied on the beams. This simplification affects the development of the creep strain, the considered loads determine the stress value at the prestressing stands level. For this section, the bending moments caused by permanent loads are also accounted for in the calculation of prestress losses.

In composite bridges, the structure is erected in multiple stages, and different loads are applied

to the structural components. This results in a different stress distribution over the beams, which also affects the stress value used for the calculation of the creep strain. Figure F.1 illustrates the various stress distributions and stress values at the prestressing level for the different construction stages. These stresses were utilized to calculate the creep strains that are presented in Table F.2, along with the equivalent total prestress losses. It is important to note that the contribution of shrinkage and relaxation is not affected by the bending moments, and thus their values remain the same as those calculated in the previous section.
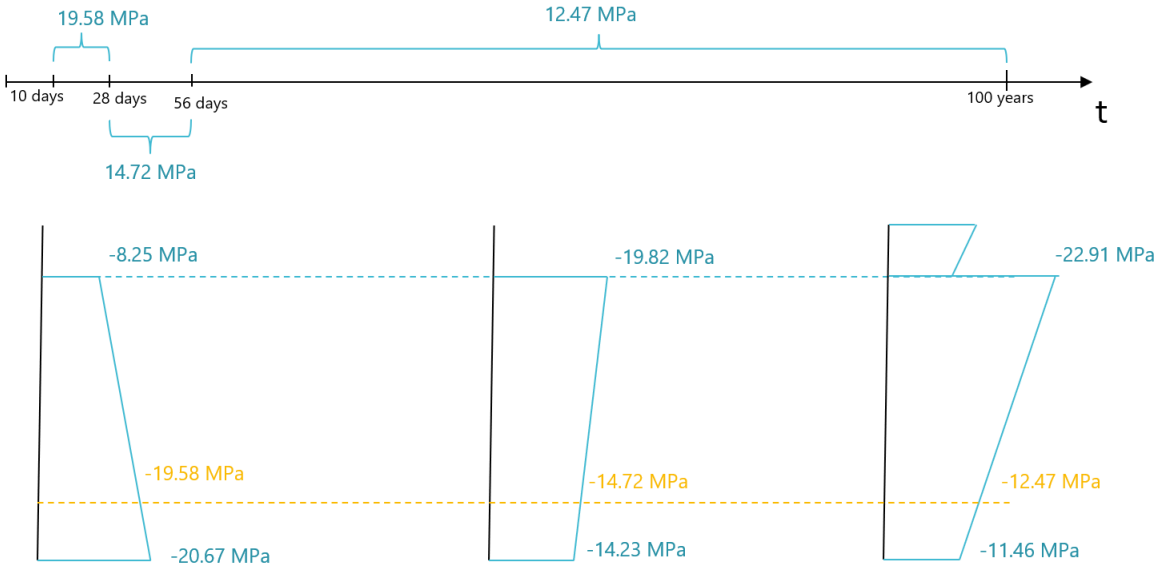

Figure F.1: Stress distributions for the different constraction stages.

Table F.2: Time-dependent parameters for prestress losses accounting for axial loads and bending moments

				10 years	20 years	30 years	40 years	50 years	60 years	70 years	80 years	90 years	100 years
Age of concrete (days)	t	28	56	3650	7300	10950	14600	18250	21900	25550	29200	32850	36500
Creep													
Creep strain	$\varepsilon_{cc}(t)$	2.73E-04	3.46E-04	4.98E-04	5.01E-04	5.02E-04	5.02E-04	5.03E-04	5.03E-04	5.03E-04	5.03E-04	5.03E-04	5.03E-04
Total prestress losses	$\Delta\sigma_{c+s+r}$	**84.49**	109.01	**186.33**	**190.63**	**193.02**	**194.71**	**196.04**	**197.14**	**198.09**	**198.93**	**199.68**	**200.36**

F.3 Slab shrinkage

Upon completion of the casting process and the subsequent 7-day curing period ($t_s = 7$), the cast in-situ slab undergoes shrinkage. Following the same methodology used in the previous sections, the resulting shrinkage strains have been calculated and are presented in Table F.3.

Table F.3: Development of slab shrinkage strains

		56 days	10 years	20 years	30 years	40 years	50 years	60 years	70 years	80 years	90 years	100 years
Age of concrete slab (days)	t	28	3622	7272	10922	14572	18222	21872	25522	29172	32822	36472
Autogenous shrinkage												
Autogenous shrinkage coefficient	$\beta_{as}(t)$	0.6530	1.0000	1.0000	1.0000	1.0000	1.0000	1.0000	1.0000	1.0000	1.0000	1.0000
Autogenous shrinkage strain	$\varepsilon_{ca}(t)$	3.75E-05	5.75E-05	5.75E-05	5.75E-05	5.75E-05	5.75E-05	5.75E-05	5.75E-05	5.75E-05	5.75E-05	5.75E-05
Drying shrinkage												
Drying shrinkage coefficient	$\beta_{ds}(t, t_s)$	0.2101	0.9786	0.9892	0.9928	0.9946	0.9957	0.9964	0.9969	0.9973	0.9976	0.9978
Drying shrinkage	$\varepsilon_{ds}(t)$	7.56E-05	3.52E-04	3.56E-04	3.57E-04	3.58E-04	3.58E-04	3.58E-04	3.59E-04	3.59E-04	3.59E-04	3.59E-04
Total shrinkage	$\varepsilon_{cs}(t)$	1.13E-04	4.09E-04	4.13E-04	4.15E-04	4.15E-04	4.16E-04	4.16E-04	4.16E-04	4.16E-04	4.16E-04	4.16E-04